Comparaison et développement de méthodes avancées de détection de défauts sur des câbles coaxiaux

Ihssane Bzikha

Doctorate thesis

Université de Limoges

Université de Limoges
ED 610 - Sciences et Ingénierie des Systèmes, Mathématiques, Informatique (SISMI)
Xlim Laboratory – UMR CNRS n° 7252

Thesis to obtain the degree of
Doctor of Limoges' University

High Frequency Electronics, Photonics and Systems Engineering

Presented and submitted by

BZIKHA Ihssane

December 17, 2019

Comparison and development of advanced wiring fault detection methods on coaxial cables

Supervised by Alain REINEIX

JURY :

Chairperson
Ms. Valérie MADRANGEAS, Professor, Limoges University.

Reviewers
Mr. Pierre BONNET, Professor, Clermont Auvergne University.
Mr. Lionel PICHON, CNRS Research director, research institute Geeps.

Examiners
Ms. Valérie MADRANGEAS, Professor, Limoges University.
Mr. Fabrice AUZANNEAU, Engineer, CEA Paris-Saclay.
Mr. Alain REINEIX, CNRS Research director, research institute Xlim.

Acknowledgment

First, I would like to thank my committee members, in particular the both reviewers; the professor Pierre Bonnet and the CNRS research director Lionel Pichon for their good comments which have improved the quality of my work. I would like also to thank the Professor Valérie Mandrageas and Mister Fabrice Auzanneau to accept to be examiners of my PHD work, and, of course, thank you Alain Reineix who allows the improvement of my technical skills. Thank you for your support. I will miss you, and I will miss working with you.

Then, I would like to thank the XLIM EMC team. Thanks to Alain, Christophe, Guillaume, François, Omar, Nadine, Paul, Nicolas and all the PHD students. Thank you for the excellent working atmosphere in which I was glad to participate. Thank you all for your support and your help.

I will never forget my first day in France. It was 21 August, and it was a windy and a cold day regarding to the weather that I left behind me in my sweet country Morocco. I said oh my Gosh, how can I live in this weather. For me, August equals 47 °C or at least 45 °C. Day after day, I become loving spending the summer in France not because I habituate but because the temperature increases to 40 °C, Yeah, I know it is not 45 °C but it is Ok for me. In 21 august, when my foot touch for the first time the France land, I was afraid. A lot of questions come to my mind about cultures, integration etc. By time, I was astonishing how France welcome everyone from different countries with different religious and give them the opportunity to integrate the society and learn from its universities, companies and research centers. Thank you, France, for choosing me to come and continue my studies in one of your best engineering schools. Thank you for accepting me to be officially French citizen. Thank you for giving me the opportunity to see the development and learning from you to be open-minded, and to accept the others regardless their countries, religious and sex. Thank you for everything my country France.

Thank you for my parents who encourage and help me to come to France. Thank you for believing in me. I learned and I continue learning from my mother how to become an independent woman and love myself. Thank you my mom, the best mother ever, to teach me all what you know, and pushing me to not be afraid to discover new countries and new cultures. Thank you dad for teaching me how balance the feelings and the emotions and how choosing my friends. All the time, my dad told me that my best friend is ….Sorry I cannot tell you, is a secret between me and my dad. Thank you daddy for the advice. When I need someone to listen to me, I cannot find better that my sister Ilham, and my two brothers Reda and Amine. Thank you Ilham, Reda and Amine to be here for me whenever the time is.

Calm down Paul, I did not forget you, only I cannot find words to thank you for your help, encouraging and spending the nights in the hospitals sometimes for you, sometimes for me. Thank you a lot for obliging me to support PSG football team and teaching me fishing. Thank you for everything. But if you think that by finishing my thesis, you will never see me again. I am afraid to tell you that you will never get rid of me because I am following you whenever you go and keeping my eyes on you. Thank you. I would also thank your family Claire, Mami, Jean-charles, Papi, Farah, Julien, Aicha, Marius and Tonton Jean-Christophe for supporting me, encouraging and believing in me, and give me their hands when I need them. Thank you a lot.

The friendship is the hardest thing in the world to explain. It's not something you learn in school. But, if you haven't learned the meaning of friendship, you really haven't learned anything because you do not meet Chaimaa, Ikram and Kamila. Thank you to all of you for being my friends, and for accepting me how I am.

Table of Contents

Table of figures

Table of tables

Introduction

Introduction

Issues and context

Electrical cables are used in many fields, such as transportation systems, industrial machinery, power plants, and infrastructure in order to connect devices for energy or data transmission. Hence, these cables guarantee good performance of a system. In recent decades, the increasing use of electrical components has increased the demand for electrical cables. For instance, the cumulative length of the electrical wires installed in a typical civil aviation aeroplane is more than 400 km, and a modern train contains around 200 km of wire. Consequently, electrical wires have become important subsystems in critical systems. However, these subsystems have a lifespan. Indeed, over time, due to either external reasons, such as chemical contamination or mechanical stress, or internal causes manifested in manufacturing defects or temperature increases, a cable breaks down partially or entirely. Increasing the number of cables can also increase the wiring fault risk. Wiring faults are classified into two categories: hard, which refers to open circuits that completely interrupt the transmission of energy or data in the cable and are easy to detect, and soft, which refers to insulation damage, cracks, and frays that are difficult to detect and, over time, become hard defects. Wiring faults have been considered a major cause of safety and control problems. In particular, the Boeing 747 TWA Flight 800 disaster in 1996 and the crash of a Swissair MD-11 in 1998 that took the lives of hundreds of passengers were caused by electrical wiring faults, according to the U.S. National Transportation Safety Board (NTSB). Accordingly, the importance of electrical wires in daily life requires rigorous fault detection methods able to detect wiring defects before systems are put in jeopardy. It suggests an industry spends a significant amount of money each year at the operational level to troubleshoot and repair wiring system problems.
Two types of wiring fault detection methods are used: techniques relying on direct observation by human senses (visual inspection, X-ray methods, and so on), which are time consuming, expensive, and inefficient in most cases, and techniques based on mathematical and physics concepts, such as low-frequency and direct current (DC) methods, capacitive method and inductive method, and medium-frequency approaches, in addition to several other techniques. Despite the evolution of these methods over time, reflectometry-based techniques are at the centre of industrial research applications in the signal processing domain. The reflectometry relies on testing the propagation of an electromagnetic waveform in the wire network and then monitoring its reflection to detect and localize an impedance discontinuity. There are two main reflectometry families: time domain reflectometry (TDR) and frequency domain reflectometry (FDR). They are efficient in detecting hard faults due to the high reflection coefficients of such faults, but they are less reliable in detecting soft faults. In fact, soft faults are usually associated with reflectiveness so weak it can pass unnoticed because of junctions and noise level. Additionally, these methods are inefficient to detect fault in complex networks.

Thesis objective

The objective of this thesis is to propose new approaches to locate single or multiple chafing faults in networks of varying complexity. Time domain reflectometry, standing for the reflection coefficient, was originally developed for diagnostic and monitoring purposes for fault detection in electric wires in buildings, aircraft, and transportation systems. Basically, it allows high versatility and accuracy with relatively low implementation costs, providing a visual method for inferring chafing fault positions. When moving from a simple cable to a

wire network, however, this is no longer true. Multiple chafing faults cannot be resolved separately, because of their reflection coefficient.
The denoising method decomposes the signal in the time domain and allows for removing noise from signals before applying fault detection methods. Three well-known methods are used to reduce noise: empirical mode decomposition (EMD), local mean decomposition (LMD), and the discrete wavelet transform (DWT). These denoising methods already exist in the literature, but they were limited only to denoise signals. In this work, these denoising methods are used to denoise signals and detect chafing faults.
Providing a denoised signal, the time–frequency analysis is reviewed for inferring the chafing fault's position. These Time Frequency methods was already used in different literature. However, in this thesis, we compare between them in terms of their sensitivity regarding chafing fault position. These methods concern the analysis and processing of signals with time-varying frequency content. Such signals are best represented by time–frequency transforms, which depict the signal energy over the two-dimensional time–frequency space instead of only the one dimension of time or frequency. However, conventional representations of a signal in the time domain or frequency domain do not facilitate the signal's interpretation because of the noise level.
To overcome this, a Bayesian approach is used. In the research, the Bayesian method solved by the Nested Sampling method was already used to detect the wiring fault. However, in this thesis, the Bayesian method is solved via Nested Sampling and Gauss Newton in order to overcome some limitations of the Nested Sampling method and compare between them. In the Bayesian approach, test signals are obtained from the network's scattering matrix that once injected into the network model will make it possible to locate the position of the chafing fault. Notably, this novel approach allows extracting the signature of each chafing fault characterized by its posterior parameters. Additionally, converging the network model to the measurement allows a clear identification of the chafing fault and reduces the probability of false alarms. This method gives credibility to critical real-life configurations that are not well addressed in current literature. In addition, the proposed procedure allows an accurate estimate of the severity of a chafing fault, a feature of practical interest when monitoring the state of a cable in a wiring network. Notably, the proposed method has shown a remarkable robustness in the presence of noise, and this efficiency improves when the network's complexity increases. However, the approach is less stable because it depends on estimations of prior parameters estimations and prior distribution. It is also time-consuming and costly.
To address these challenges, we use chaos time domain reflectometry (CTDR) based on time-domain analysis. In the literature, the CTDR was used only for hard fault detections by using only the simulations. In this thesis, we develop the CTDR to detect chafing faults by using measurements and simulations. This method shares the same foundations as other TDR-based methods – namely, the characterization of the wiring network. However, the difference is that in the CTDR approach, the injected signal is a chaotic signal. Therefore, its resolution is limited by bandwidth, as with any other time-domain method. In addition, a correlation process between the injected and the received signal is defined to detect and locate single and multiple chafing faults in different network configurations. Experimental and simulated results confirm the practical potential of this novel approach. It is important to point out CTDR has also shown a great robustness with noisy measured scattering data, proving its feasibility for working in noisy environments.

Thesis organization

The following thesis is composed of five chapters. Chapter 1 presents an overview of the context of our study, starting with defining electrical cables, their types, and their fields of

application, followed by an introduction of the main causes behind the appearance of wiring faults. After that, we list some of the consequences that these cable defects can lead to and introduce the most common methods used for investigating cables. The general principles of reflectometry techniques are presented with their different varieties, along with an illustration of their major advantages and limitations. The bases that allow understanding of the proposed methods, namely, the principles of wave propagation along transmission lines, are represented, and the concepts and tools used to model and simulate a cable are described. We review the transmission line theory tools needed for our study, and multiport modelling with the S-parameter matrix that is used to define our model. Finally, the chapter content is illustrated with an application.

Chapter 2 is dedicated to denoising a signal and detecting a chafing fault. Three denoising methods are proposed: EMD, LMD, and the DWT. To denoise a signal, different threshold filtering algorithms are used. In the present study, we investigate which method provides coherent denoised data. For that, we compare the proposed methods applied to some examples by studying their sensitivity regarding chafing fault detection.

Chapter 3 focuses on the concepts of time–frequency analysis while presenting three of its major approaches. We address the theoretical bases of these three methods, their areas of applications, and the merits and demerits of each.

Chapter 4 addresses the Bayesian approach applied to transmission lines. This Bayesian approach is reviewed, and its feasibility in locating single soft faults in cables of different complexity is addressed. This method is solved via two statistical methods: The Gauss–Newton algorithm and nested sampling. Based on these two statistical methods, we examine the Bayesian approach while showing its different steps, which allow for detecting and locating multiple soft faults in various cables. This is validated numerically, and results are presented of computations of the severities of the soft faults of the tested cables.

Chapter 5 deals with the application of CTDR to transmission lines and the high-resolution results obtained with continuous wave excitation signals for the accurate detection and location of single and multiple soft faults in different networks under test. A numerical and experimental study validates the novel approach. This is accompanied by a presentation of the process. The faults' reflection coefficients are computed, and corresponding results are presented. Finally, the robustness of CTDR to noise is examined.

Chapter 1: State of Art

1 State of the art

1.1 Introduction

The increasing of embedded electronic devices is responsible of the increasing number of electrical wires connections. Therefore, the importance of electrical wires and their reliability has dramatically risen over the last decade. The explosion of the electrical link number can be observed in different domains that concern our daily life. This is mainly:

- The telecommunications that was one of the first area where cables are essential used to transmit information from one point to another,
- The aeronautic and automotive domains where the number of embedded sensors and calculators has submitted an exponential increasing these last years because of the various safety and comfort functions that they are used for. In the future, the evolution toward autonomous vehicles will also increase the need of cables for data transmissions,
- The power feeding where high voltage cables transport the energy from the production centres to the customer.

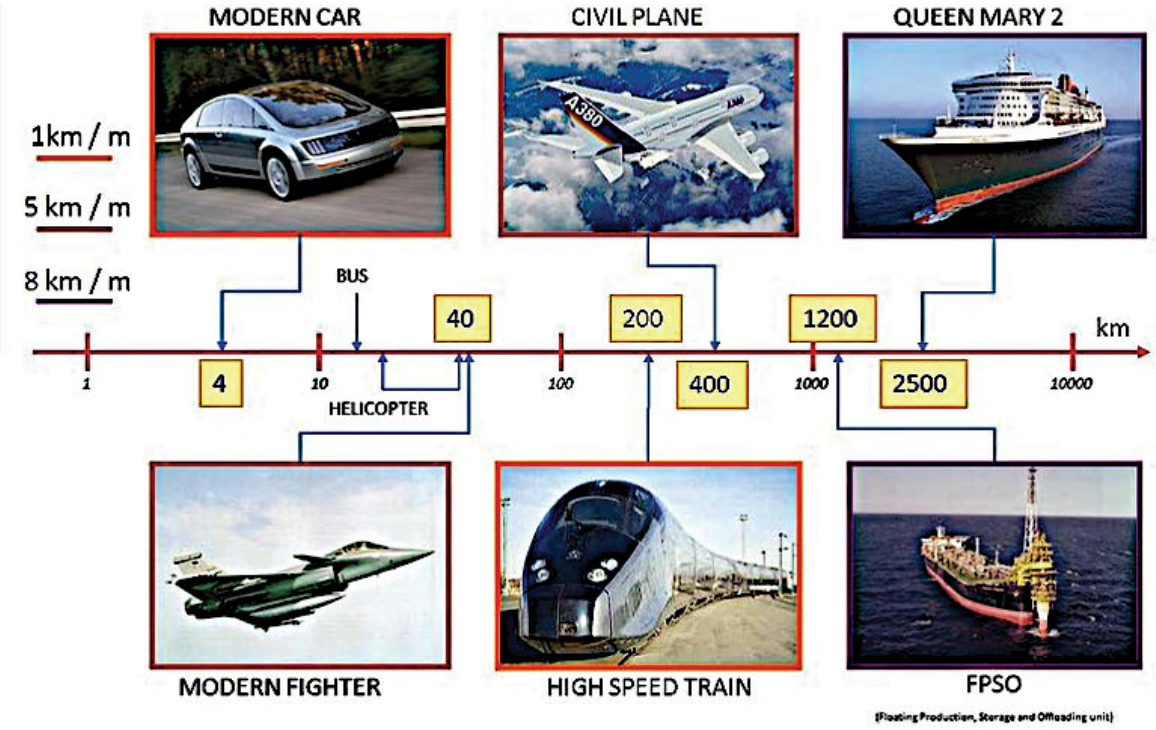

Figure 1-1. The cumulative length of the wiring in different industrial applications [1].

In some of these domains, the quality of the cables (ex: telecommunication) is need and their dysfunctions are not permitted (aeronautic and automotive). Indeed, the cables are primarily responsible, contributing to 29% of aircraft accidents, while connectors contribute to 14% of them as illustrated in Figure 1-2. Thus, they generate safety issues and increase maintenance costs [2]. In 2010, in Spain, a Bombardier flight was cancelled because of an autopilot control cable breakdown. In 1998, Swiss Air flight 111 experienced smoke and fire caused by cable failures, as was the case with the Apollo accident in 1970 [3] because over time, wires' characteristics change, particularly in response to cyclic temperature variations, ageing, in the presence of corrosive media or due to vibrations. As a result, some wiring parts are

prematurely. Therefore, optimal operational conditions require regular monitoring of wear and tear.

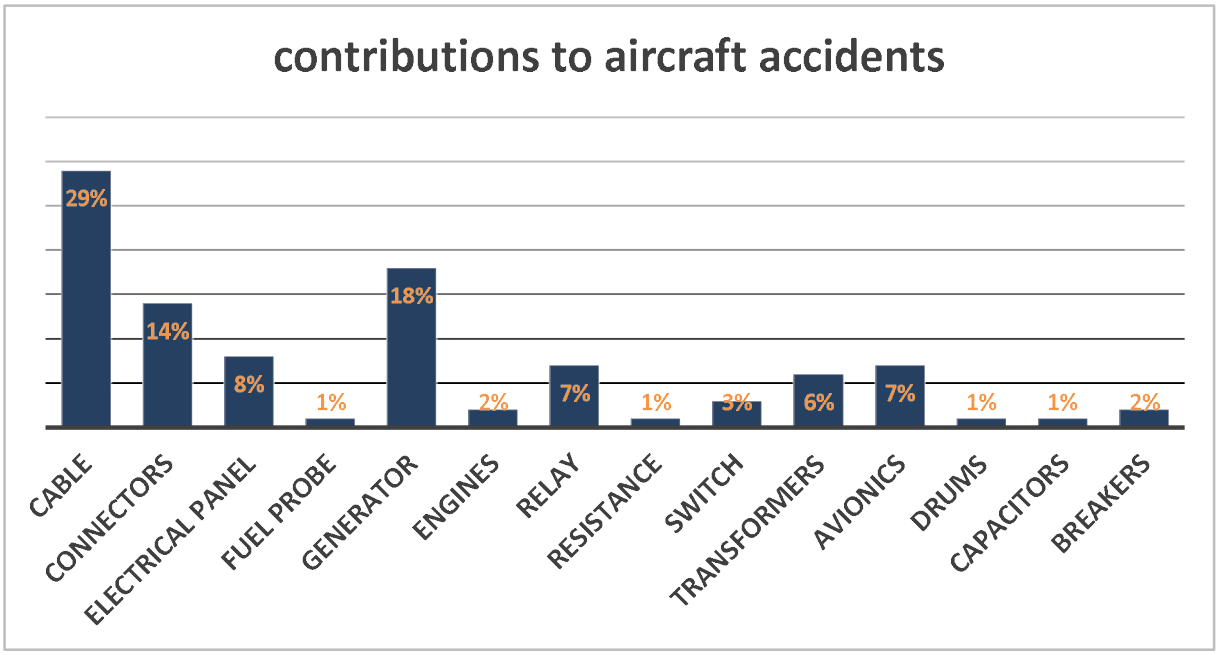

Figure 1-2. Breakdown of components contributing to aircraft accidents according to data collected by AFSA[4].

To sum up:

- The choice of a cable depends on the application that it is used for. As the constrains are different from one domain to another, specific kind of cables have been developed. Main categories will be described below,
- It is important to detect wiring defects. For that, first, we will define what kind of defect can arise on a cable, and then some techniques for the wiring fault detection will be described later in details.

The importance of electrical wires has risen dramatically over the past decade. As technologies, electrical wires play a significant role in our daily lives and are widely used in almost all fields, such as aeronautics, telecommunications, and electronics. They enable the transfer of electrical signals or power from one device to another. Several systems use transmission lines, such as transportation systems [5], reactor machinery [6], modern industrialized systems [7], and telecommunications [8]. The optimal use of these transmission lines depends on the target function and can include both technical and economic aspects; the frequency bandwidth; the transmitted signal, which can be either analogue or digital [9]; and the cable's environment, such as the sea, the air, or the ground [10].

In recent years, many new methodologies have been developed to determine the new optimum sophisticated cables. One of these cables is the ethernet cable, which is assumed to have good reliability, good propagation characteristics (linear attenuation and signal distortion as frequency function), and improved ability to carry information. It is widely accepted that the cumulative length of the wiring used in different industrial fields must increase to supply the increased electric loads, as shown in Figure 1-1. For instance, last-generation cars use many kilometres of cables, and this use is expected to increase in electric autonomous cars, which require many sensors to relate to the embedded computers. In addition, the introduction of sensors such as radars and lidars can provide great benefits for system safety, which is the priority in all fields. However, construction and connection of electrical wires cannot be done

without considering the impact they will have on the system. For instance, the National Transportation Safety Board (NTSB) investigation revealed that it was electrical wiring faults that caused the Long Island TWA Flight 800 crash and the Cincinnati Air Canada Flight 797 crash [11]. In fact, the optimum reliability related to safety will depend on the optimal operating modes, which must be considered in he operating frequency bands, particularly for data transfers, and The working environment that may be responsible for performance degradation (underground cables, submarines, and so on).
In recent years, many new methodologies have been developed to detect the wiring problem. Indeed, there are some wiring faults that are undetectable at first appearance but whose impact can grow with time. However, over time these faults could lead to system breakdowns. This chapter is summarized as follows. First, we present different kind of cables and their application domains, and we define cable modelling methods: 3D approaches, transmission line theory, and scattering parameters. Second, wiring faults are presented. Notably, we present different kind of defects, their origins, and two main approaches of fault detection methods, including the well-known reflectometry-based methods and others that are not reflectometry based. Third, we introduce methods for modelling wiring faults and we define network modelling. Finally, among the cable configurations used all along this thesis, the two simplest cable configurations with soft fault are depicted. In particular, the analysis of the reflected signals leads to use and/or develop advanced method for the soft fault detection.

1.2 The cable: features, models, applications

As shown above, over the past decade, cables have become increasingly popular due to their reliability, safety, and physical characteristics. With technological advances and various objectives and constraints in different fields, the process of choosing cables has become more economical and efficient, as illustrated in Figure 1-3. Although electrical cables perform numerous functions such as supplying electricity to motors, transformers, and heaters, they can also affect the performance of systems by creating fire, or breakdowns. The dependable operation of electrical cables is essential to safe operations in different fields. For instance, to ensure an increases of the throughput in digital transmissions, cables with low attenuation over a wide frequency band are required. Cables that typically consist of one or more metallic conductors with insulation, filler, shielding, sheaths, and jacket [12] - [13] can be modelled as impedances [14]. In addition, for electric equipment EMC, it is necessary to not only reduce the electromagnetic waves radiated from the equipment but also raise the resistance against external electromagnetic waves. For that, the cable pairs must be isolated. The insulation is often considered the single most important component of the cable and cable categories are indicated by their insulation use.
Ranked by increasing shielding efficiency for the transmission of the information, the categories are shielded, unshielded, and foiled twisted pair cables (Figure 1-4).

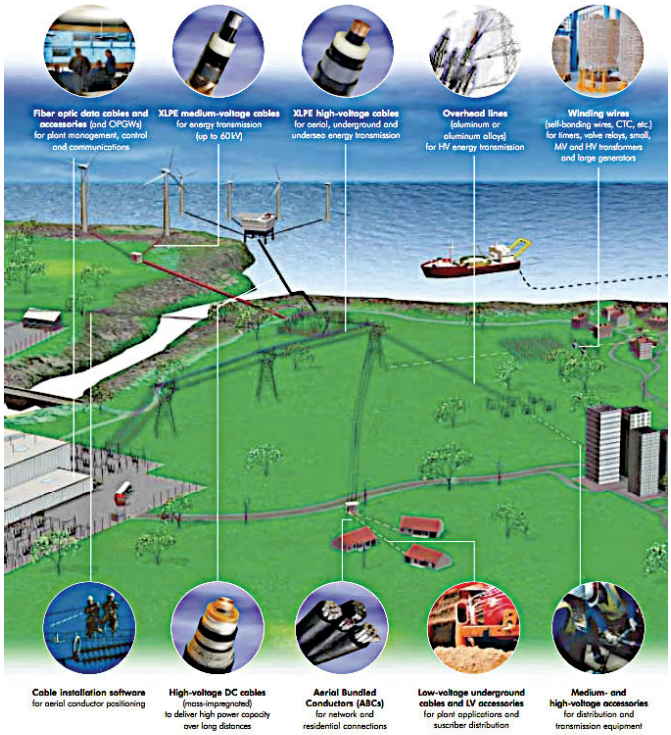

Figure 1-3. Different cables and their areas of application [15].

- Twisted pair cable:

Twisted pair (TP) cables (Figure 1-4) are composed of two conductors twisted together to eliminate internal and external electromagnetic interference. For instance, in computer networking, two pairs of twisted-pair cables are typically used for transmitting data, while other pairs receive data. Three main twisted-pair cable types exist: shielded twisted pair (STP, its impedance $Z = 100\Omega$), unshielded twisted pair (UTP, its impedance $Z = 100\Omega$), and foiled twisted pair (FTP, its impedance $Z = 100\Omega$) [16]. While even unshielded UTP cables reduce electromagnetic interference, shielded STP cables eliminate it more effectively. In addition, UTP cable is used more often than FTP in Europe, and especially in France, in Ethernet networking. In addition, for RJ45 cable [17], the twisted pair cables are classified into three standards: Category 5, Category 6, and Category 7, according to theoretical data speed and the frequency range [18]. For instance, Category 5e (Class D) transmits data with a theoretical data speed of 1,000 Mb/s at frequencies up to 155 MHz, while Category 7 (Class F) transmits data at theoretical speeds of 10 Gb/s with frequencies up to 600 MHz. Moreover, the greater the number of twists, the lower the crosstalk.

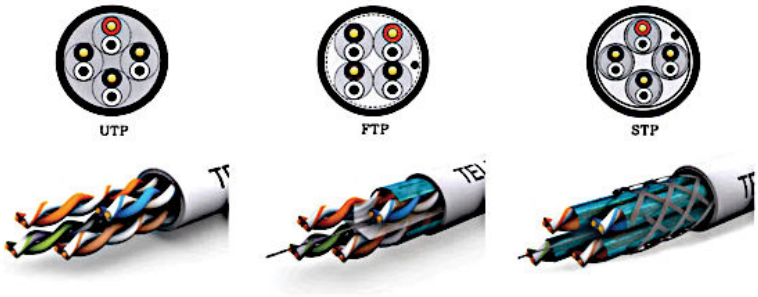

Figure 1-4. Twisted pair cable [18].

- Coaxial cable

Coaxial cables carry electrical signals using an inner conductor (usually copper wire), as seen in Figure 1-5. They are surrounded by three layers, which are, from the internal to the external, an insulating layer, a shield layer, and an outer insulation layer [19]. Usually, the ground potential is connected to the shield, while the voltage is applied to the internal copper wire to carry a signal. The advantage of a coaxial cable is that the electromagnetic fields are kept in the dielectric with low leakage outside the shield. Besides, this cable type is protected from external interferences, which makes it useful for carrying weak signals that cannot tolerate any interference from the environment. Furthermore, using coaxial cable is relevant for higher power signals that must not be allowed to radiate or couple with adjacent structures or circuits [20]. Moreover, the losses are highly dependent on the quality of the dielectric used. To avoid microwave attenuation (for example up to 40 GHz), expensive special dielectrics are used. In addition, coaxial cable is used in computer science and low-frequency electronics but also in the field of radio frequency (RF) and microwaves up to several tens of gigahertz [21]. The present work depicts experimental measurements made with coaxial cables to compare with simulated data to validate our new fault detection methods (Chapters 1, 1, and **Error! Reference source not found.**).

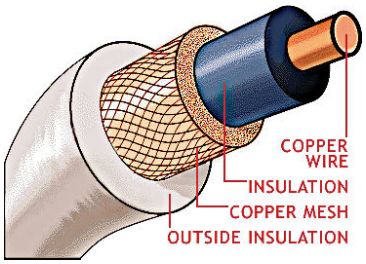

Figure 1-5. Example of a coaxial cable, showing four parts: copper wire, insulation, copper mesh, and outside insulation [22].

- Power cables

Power cable is used for high-voltage signals. It is covered by a metallic shield layer, which is kept at earth ground and designed to equalize the dielectric stress on the insulation layer. Figure 1-6 depicts a high-voltage power cable. The inner conductor must tolerate stresses during cable laying, while the metallic layer contributes to the mechanical protection. Power cables come in a variety of materials, sizes, and types depending on the application they are

used for. These cables sometimes use large insulated conductors to protect the cable from the surrounding medium circumstances as the heating causing by the joule's losses [15].

Figure 1-6. Power transmission cables [15].

In this section, we introduced some cable types, their features, and their applications. We now define different cable modelling methods.
In all the following sections, coaxial cables are considered when applying the processing techniques developed.

1.3 Cable modelling

Several EMC issues (shielding, electromagnetic coupling…) concerns cables. The electronic devices connected to cable leading to complex system are more and more increasing. Thus, the EMC study is becoming increasingly difficult. This is one of the main reasons why interest in modelling cables has increased considerably. Because of the expansion of transmission lines, it is necessary to have accurate simulation models [23].
To understand the modelling used for transmission lines, this section provides an analysis of many methods to model a cable. These include methods based on the resolution of Maxwell's equations without approximation, methods based on transverse electromagnetic (TEM) mode propagation (transmission line theory), and methods based on scattering parameters.

1.3.1 3D approaches

As the electrical properties differ considerably from one cable to another, the modelling and studies of cables are considered very challenging. To model a cable, it is necessary to have a good knowledge of the physical structure of the cable and of the electrical characteristics of the material as well as the variation of losses (in the dielectric and the conductor) versus frequency. For this, 3D modelling methods can be used [24]. These methods are numerical approaches consist in a resolution of Maxwell equations after their discretization. Two main categories of approach can be distinguished: the first one consists in the resolution of the problem in a three-dimensional volume by decomposing it into elementary cells. In this case, the electromagnetic fields are computed in each elementary cell by the discretized Maxwell equations which allow the propagation of the energy from one cell to the adjacent one. The second category consists in, first, deriving an integral formulation of the Maxwell's system, then a surface resolution that consists in the surface currents calculation is made [25].
The finite element method (FEM) is one of the most useful approaches in many fields [26]. It is a mathematical technique used to solve partial differential equations that depict physical problems. Approximating functions in finite elements solve the Maxwell equations in a

domain of interest. Additionally, this approach consists of discretizing a physical problem. Thus, the most important properties of the FEM are worth mentioning [27]:

- Decomposition of the three-dimensional computational volume into elementary volumes, that generally have a tetrahedral shape,
- Discretization of an integral formulation of the Maxwell's equation in each cell. For that, two main approaches can be used: the nodal FEM method where the unknowns are the fields at the nodes of the discretized volume, and, the edge method where the integral formulation of the electromagnetic fields along edges of the cells is derived.
- Thanks to the discretization, a submatrix can be obtained on each cell, and then the following operation consists in the integration of all these matrices into a general matrix containing all unknowns. This general matrix is a sparse matrix that can be constructed and solved by using an appropriate method.
- The approximation of physical fields on finite elements to simple approximating functions provides good precision.
- In discretizing problems, approximation leads to sparse equation systems which lead to large numbers of nodal variables (when considering nodal finite elements).

There are five steps to model a cable via the FEM.

- First, the cable's region is divided into elementary volumes. Then, the Maxwell equations are discretized in each cell.
- Second, this discretization of the Maxwell equation in each cell can be solved by two main approaches: the nodal FEM method or the edge method.
- Third, due to this discretization, a submatrix can be obtained on each cell, and then the following operation consists in the integration of all these matrices into a general sparse matrix containing all unknowns.
- Fourth, imposition of the boundary conditions and element connectivity to assemble the element equations that defining the sparse matrix.
- Finally, resolution of the global equation system that is sparse, symmetric and positive definite. The study of a large frequency band requires building the system and its resolution as many times as the frequencies be considered.

These steps are used in the High Frequency Structure Simulator (HFSS) commercial software that discretizes the cable undertest via FEM, as shown in Figure 1-7.

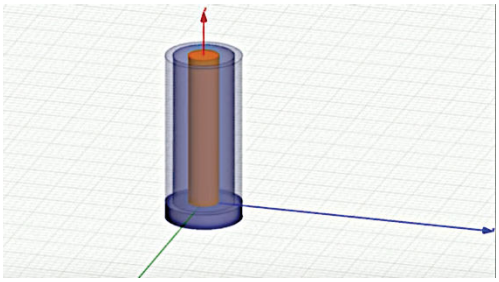

Figure 1-7. Coaxial cable model via HFSS [28].

There are also other approaches, matched to broadband problems, for solving Maxwell's equations in the time domain, such as the finite-difference time-domain (FDTD) method. The FDTD method is simple in terms of implementation to solve electromagnetics problems. In some cases, the FDTD simulator models the cable on the order of a wavelength. The smaller the wavelength compared to the physical features of interest, the faster the FDTD method solves the problem. The FDTD method consists in a decomposition of the three-dimensional

space into elementary parallelepipeds cells by positioning the electric and magnetic field points interlaced in each cell in order to have a second order accuracy in the spatial derivatives that appear in the curl operator of the Maxwell's equation. In order to get a second order accuracy in the time domain, the electrical field and magnetic field components are interlaced and separated of half one-time step. As a result, the global scheme is of second order, this accuracy is attained simply using central derivatives in time and space, obtained by using only two separated of one space or time step [29]. Moreover, the interlaced calculation instants of the electric and the magnetic fields lead to an explicit problem resolution without any matrix inversion. The main constraint is the Courant Fredrich Levy (CFL) criterion that constraints the time step to be lower than a given value depending on the space increments $(\Delta x, \Delta y, \Delta z)$. Physically, the numerical propagation should be lower than the speed of light c, if it is not the case, a divergence can be observed.

$$\Delta t < \frac{1}{c\sqrt{\left(\left(\frac{1}{\Delta x}\right)^2+\left(\frac{1}{\Delta y}\right)^2+\left(\frac{1}{\Delta z}\right)^2\right)}}. \qquad (1.1)$$

In the FEKO commercial software, by contrast, the moment method is used [30]. Using Computer Aided Drafting (CAD), the software carries out a superficial discretization, usually in triangles, and calculating the normal currents at the edges of each triangle (Rao–Glisson–Wilton functions). Based on the Maxwell's equations, this method leads to a large full matrix unlike the FEM. Its only difficulty lies in the system resolution, which is now accelerated by recent approaches such as the Fast Multipole method (FMM) or the Adaptive Cross Approximation (ACA) method. Besides, there are four steps to model the cable. First, building geometry for the cable. Second, building a geometry to represent surrounding geometry. Third, meshing the created cable. Finally, solving the Maxwell's equation via the method of moments.

It is important to notice that the FDTD or the MoM methods do not need a discretization of the section of the wire, only segmentation is necessary. In this case the longitudinal current component is computed. On the contrary, the FEM method needs a discretization of the length as well as the section of the wire, as a result, it cannot be used in cables modeling (but only for short section of cables or for fault modeling)

In the next section, we present the transmission line method, which is an easier and useful tool for studying propagation inside wires.

1.3.2 Transmission line theory

The rigorous formulation methods seen above will give precise answer if all parameters of the problem to be modelled are well known. In particular, on a cable or a transmission line, they are able to take radiation phenomena into account. In the present work, we will concentrate on the flowing current along a transmission line, if the frequency is not two high, the radiation phenomena can be neglected in a first approximation. Then, in this case, we can only consider the TEM mode. Consequently, it is possible to use the transmission line method (TLM) for this kind of problem because of its short computational time. The TLM principle will now be described more in details [31].

The lines theory is based on a quasi-TEM approximation of the propagation between at least two conductors. The Maxwell's system approximation assumes a potential difference in any section of the cable based on the following constraints:

- The distance between the cables or between a cable and a ground plane must be small (typically lower than $\lambda/10$); and
- The cable geometry is invariant all along the direction of propagation.

The transmission line method consists of solving two coupled equations on voltage and current either in time or in frequency [32]. Moreover, the transformation from one to the other can be achieved using the Fourier transform [33].
A simple transmission line is represented as a two-wire line (multiconductor transmission line will not be used in this work). By considering equation (1.2), the piece of line of infinitesimal length dx can be modelled as an RLCG circuit [34] as shown in Figure 1-8.

$$dx \ll \lambda. \tag{1.2}$$

The parameters are as follows:

- λ: wavelength.
- L: linear inductance (henry/m) is divided into two kinds: an inner inductance which is due to the magnetic field inside the conductors and an outer inductance that is due to the magnetic field between conductors.
- C: linear capacitance (farad/m) depends on the permittivity of the insulator.
- G: linear conductance (siemens/m) represents a current flow between two conductors.

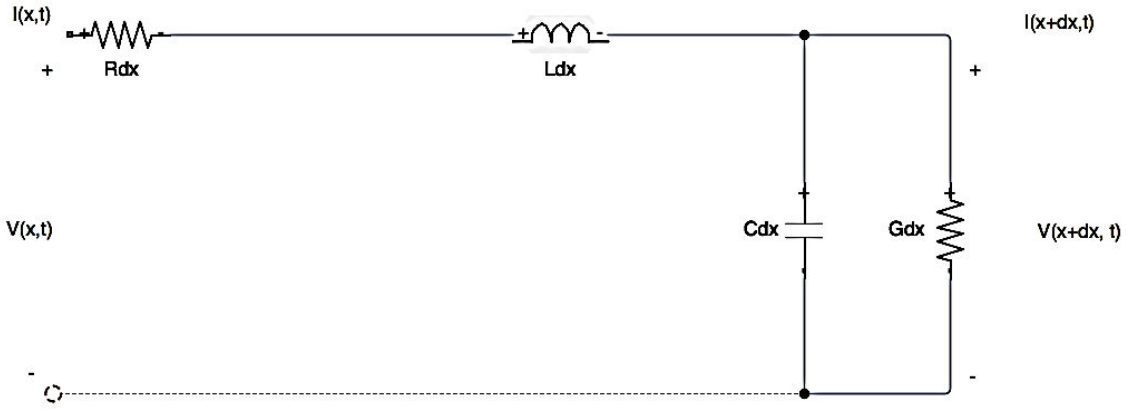

Figure 1-8. A scheme of an RLCG equivalent model of a segment of a transmission line.

By the application of Kirchhoff's laws, the equations (1.3) and (1.4) are obtained:

$$v(x + dx, t) - v(x, t) = -Rdxi(x, t) - Ldx\frac{\partial i(x, t)}{\partial t}, \tag{1.3}$$

$$i(x + dx, t) - i(x, t) = -Gdxv(x, t) - Cdx\frac{\partial v(x, t)}{\partial t}. \tag{1.4}$$

where v and i are the voltage and the current, respectively, at the instant t in a segment dx of the line.
In addition, by deriving the equations (1.3) and (1.4), we get the telegraphist equations [2]:

$$\frac{\partial v(x,t)}{\partial x} = -Ri(x,t) - L\frac{\partial i(x,t)}{\partial t}, \tag{1.5}$$

$$\frac{\partial i(x,t)}{\partial x} = -Gv(x,t) - C\frac{\partial v(x,t)}{\partial t}. \tag{1.6}$$

By considering a sinusoidal wave as an excitation, the current and voltage waves are given in the harmonic regime as shown below:

$$v(x,\omega,t) = V(x,\omega)e^{j\omega t}, \tag{1.7}$$

$$i(x,\omega,t) = I(x,\omega)e^{j\omega t}. \tag{1.8}$$

where $V(x,\omega)$ and $I(x,\omega)$ represent the complex amplitudes associated with the voltage $v(x,\omega,t)$ and current $i(x,\omega,t)$, respectively.
By replacing the equations (1.7) and (1.8) in the equations (1.5) and (1.6), we obtain

$$\frac{\partial V(x,\omega)}{\partial x} = -(R + j\omega L)I(x,\omega), \tag{1.9}$$

$$\frac{\partial I(x,\omega)}{\partial x} = -(G + j\omega C)V(x,\omega). \tag{1.10}$$

Deriving the equation (1.10) with respect to x, we get

$$\frac{\partial^2 I(x,\omega)}{\partial x^2} = -(G + j\omega C)\frac{\partial V(x,\omega)}{\partial x}. \tag{1.11}$$

Then, by replacing equation (1.9) in equation (1.11), we can write

$$\frac{\partial^2 I(x,\omega)}{\partial x^2} = (G + j\omega C)(R + j\omega L)I(x,\omega). \tag{1.12}$$

In the same way, we can obtain equation (1.13):

$$\frac{\partial^2 V(x,\omega)}{\partial x^2} = (G + j\omega C)(R + j\omega L)V(x,\omega). \tag{1.13}$$

Finally, the two propagation equations are thus obtained:

$$\frac{\partial^2 I(x,\omega)}{\partial x^2} - \gamma^2 I(x,\omega) = 0, \tag{1.14}$$

$$\frac{\partial^2 V(x,\omega)}{\partial x^2} - \gamma^2 V(x,\omega) = 0. \tag{1.15}$$

where γ is the propagation constant defined as follows:

$$\gamma = \sqrt{(G + j\omega C)(R + j\omega L)} = \alpha + j\beta \ . \tag{1.16}$$

with α the attenuation constant and β the phase constant.
As a result, the solutions of equations (1.14) and (1.15) are written as

$$V(x,t) = V^{+}e^{-\gamma x} + V^{-}e^{\gamma x} \ , \tag{1.17}$$

$$I(x,t) = I^{+}e^{-\gamma x} + I^{-}e^{\gamma x} \ . \tag{1.18}$$

Equation (1.17) shows that the voltage and the current can be written as the summation of two waves:

- $V^{+}e^{-\gamma x}$ is a progressive wave which propagates towards the load impedance Z_L (in the direction of the *x*-axes) and
- $V^{-}e^{\gamma x}$ is a regressive wave that propagates towards the generator (in the opposite direction of the *x*-axes).

The equations (1.17) and (1.18) are connected by the characteristic impedance Z_c expressed in (1.19).

$$Z_c = \sqrt{\frac{R + j\omega L}{G + j\omega C}} \ . \tag{1.19}$$

In the case of a lossless transmission line, (R = 0 and G = 0), the propagation constant becomes

$$\gamma = j\omega\sqrt{CL} = j\beta \ . \tag{1.20}$$

In addition, in this case, the characteristic impedance is

$$Z_c = \sqrt{\frac{L}{C}} . \tag{1.21}$$

At a distance x from the origin, the reflection coefficient $\Gamma(x)$ is defined by the ratio of a reflected wave on an incident wave as follows:

$$\Gamma(x) = \frac{V^{-}e^{\gamma x}}{V^{+}e^{-\gamma x}} . \tag{1.22}$$

In nutshell, this section introduces that while the cable does not radiate, the Transmission Line Theory model it as RLCG circuit. As consequence, it defines how waves propagate into a cable in quasi TEM mode in order to analyze the information that they carry. The concepts of describing cables in terms of the S-matrix and related matrices are defined in the next section.

1.3.3 Modelling a cable by its scattering matrix

The TLM is a numerical way to solve efficiently the propagation along transmission lines, but a simpler way to consider simple configurations consists in modelling the cable seen from its two extremities. As it will be recalled after, the scattering matrix is an efficient way to solve the problem. In the case of serial fault present along the line, we will see that the transformation into a chain matrix and the multiplication of these matrix give directly the behaviour of the damaged cable.

As all along this thesis only coaxial cables will be considered, we will focus on this kind of cable in the following of this part.

A coaxial cable symmetric with respect to the *x*-axis and invariant in the x direction will now be considered. Its cross-section in the transverse plane is given in Figure 1-9.

Figure 1-9. Coaxial cable.

As seen above, this cable is characterized either by its primary parameters (RLCG) or by its secondary parameters: complex propagation constant and characteristic impedance. Considering these last two quantities, the voltage and current are written as [35]

$$V(z) = Ae^{-\gamma x} + Be^{\gamma x}, \tag{1.23}$$

$$I(z) = \frac{1}{Z_c}(Ae^{-\gamma x} - Be^{\gamma x}). \tag{1.24}$$

The outgoing waves b and the incoming waves a, which are linked by the S parameters, are defined in terms of the current and the voltage, where Z_r is the reference impedance.

$$a = \frac{V + Z_c I}{2\sqrt{Z_r}}, \tag{1.25}$$

$$b = \frac{V - Z_c I}{2\sqrt{Z_r}}, \tag{1.26}$$

$$b = Sa. \tag{1.27}$$

We are interested in the matrix representation because of its ability to characterize the system from its ports.

$$S = \begin{bmatrix} S_{11} & S_{12} \\ S_{21} & S_{22} \end{bmatrix}, \tag{1.28}$$

$$S_{ij} = \frac{b_i}{a_j}, i,j \in [1,2]. \quad (1.29)$$

where b_i and a_j are the reflected wave and the incident wave, respectively and when $a_k = 0$ with $k \neq j$.

The S-parameters for a lossy symmetric transmission line are given by Equations (1.30), (1.31) where Z_c is the characteristic impedance of the transmission line, γ is the propagation constant of the line, l is the length of the line, and Z_S is the port impedance of the generator.

$$S_{11} = S_{22} = \frac{(Z_c^2 - Z_S^2)sinh(\gamma l)}{(Z_c^2 + Z_S^2)sinh(\gamma l) + 2Z_c Z_S cosh(\gamma l)}, \quad (1.30)$$

$$S_{12} = S_{21} = \frac{2Z_c Z_S}{(Z_c^2 + Z_S^2)sinh(\gamma l) + 2Z_c Z_S cosh(\gamma l)}. \quad (1.31)$$

Moreover, if a cable is matched at the input and the output port, the scattering parameters become

$$S_{11}=S_{22}=0\,, \quad (1.32)$$

$$S_{21} = S_{12} = e^{-i\gamma l}\,. \quad (1.33)$$

Although the S-matrix is efficient for characterizing a two-port transmission line, it is also a very convenient way to describe an n-port line in terms of waves. A straightforward approach to the problem is possible with the T-matrix (transfer matrix), which directly relates the waves to the input and to the output [36]. Although in the literature various uses of the T-matrix and the S-matrix can be found, the most important one for this work is detecting wiring faults, which are defined in the next section.

1.4 Wiring faults

1.4.1 Types of wiring faults

Generally, faults are classified into two main categories:

• Hard faults: open and short circuits. They are caused by a broken connection in the system.

• Soft faults: insulation damage (Figure 1-11) , cracks, frays, the pinch defect which reflects a variation of a section of the cable over a length L_f (Figure 1-11) and the chafing fault, which indicates the tearing of the shield at an angle $\theta_f$and a length L_f (Figure 1-11). They are caused by a weak impedance discontinuity along the cable [41]. Figure 1-10 depicts the different fault types that occur in naval and aircraft equipment. Different types of soft faults [166] are shown, as well as their significant percentage of occurrence compared to hard faults.

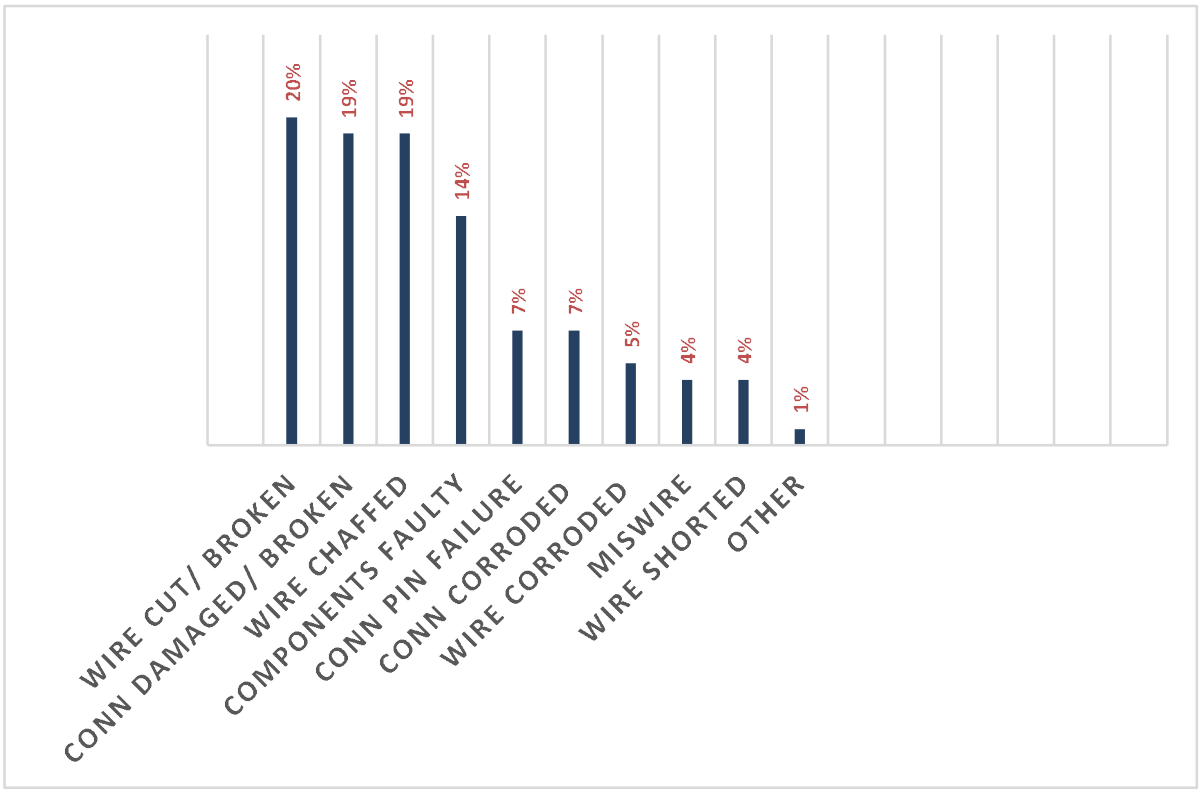

Figure 1-10. Wire fault types and their percentage of occurrence [39].

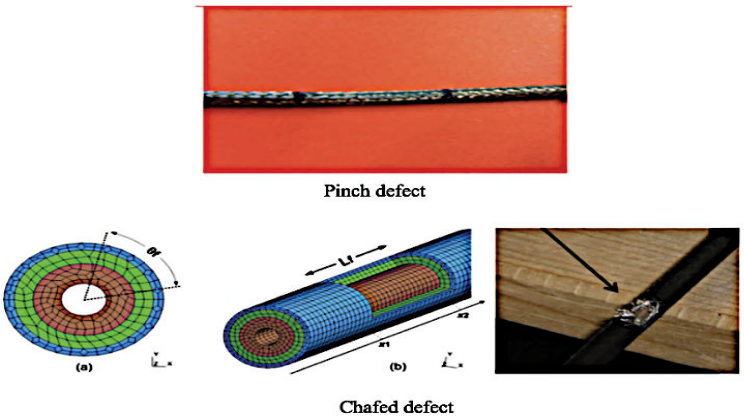

Figure 1-11. Different kinds of chafing faults [166].

Soft wiring faults, especially chafing faults (Figure 1-11) result from either external or internal causes:

- External causes can result from chemical contamination (fuel oil or corrosion), mechanical stresses [43] such as vibrations, or inappropriate application of the cable linked. For example, to an underestimation of the rim, tensions, or thermal resistance of the environment.
- Internal causes include design defects not detected during post-manufacturing testing and cable ageing.

At the end, a chafing fault is a defect that can lead to dramatic consequences, since it induces the breaking of the bond [42]. It is generally an emerging defect which should be detected early, before it turns into a hard defect. Thus, in this work, we are interested in chafing faults, because hard faults are easier to detect.

1.4.2 Wiring fault detection method

In the previous section, we described different types of defects that can appear along a cable. Each type of defect has its own characteristics (type, origin, consequences, and so on). Several methods have been developed to realize a diagnostic and to detect faults. These methods can be divided into two classes: reflectometry and others [44] - [45]. The visual inspection method, the X-ray method, the capacitive method and the inductive method are usually listed as the non-reflectometry-based methods. Although the visual inspection method is the most used, it is inefficient due to the complexity of cable networks. In addition, it detects only 25% of the defects present in an aircraft [46]. X-ray inspection requires the use of heavy equipment, direct access to cables, and human intervention for post-acquisition data analysis. However, it does not detect all types of wiring defects [47]. Both the capacitive and inductive methods are effective in hard fault detection in a simple cable [48], however, their use remains limited in cable networks. In the present work, only in reflectometry-based methods will be studied.

1.4.3 The reflectometry-based method

Reflectometry is a high-frequency method. It is an industrial standard approach based on the transmission of an incident signal in the conductor. If there are impedance discontinuities, the incident signal (V_i) will be reflected back to the source (Figure 1-12) [45]. Reflectometry has been used in the characterization of rheological properties [49], in geotechnology [50], hydrology [51], and telecommunication networks [52]. It is also widely used in determining the properties of cables. In particular, it allows the detection, location, and characterization of electrical defects [5]. The reflectometer setup is composed of a wave generator, the tested cable, and the load, as shown in Figure 1-12. The reflected signal, V_r, is referred to as the reflectogram and can be measured by an oscilloscope (for time domain reflectometry as explained below).

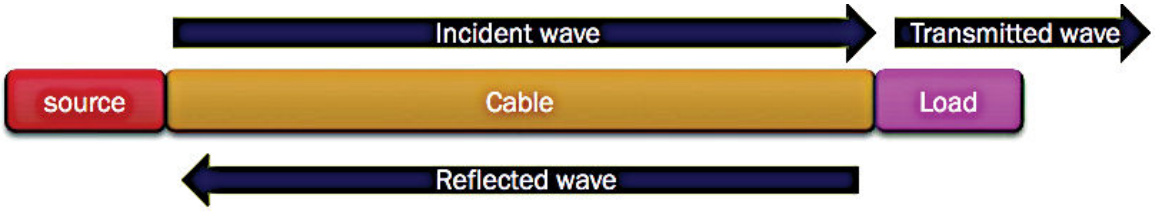

Figure 1-12. A scheme showing the principal of reflectometry.

There are two well-known reflectometry based-methods: frequency domain reflectometry (FDR) and time domain reflectometry (TDR).

1.4.3.1 Frequency domain reflectometry

FDR, which is also called swept frequency reflectometry (SFR), sends a set of stepped-frequency waves along the cable under test in order to analyze the changes in frequency domain between the incident wave and the reflected one [56]. To measure the reflected signal at the cable entry, we use a VNA instrument to determine the characteristics of the line (length, hard fault location, and so on).

Three main types of FDR are commonly used:

1. Standing wave reflectometry (SWR) [57] is the simplest FDR method. It is based on measuring the maxima and the nulls in the standing wave causing by the constructive and destructive interferences of the transmitted and reflected waves.
2. The frequency modulated carrier wave (FMCW) method measures the frequency shift ΔF between the incident and reflected signals to calculate the distance d (1.34) to the fault [58].

$$d = \frac{v_p T \Delta F}{2\delta F}, \tag{1.34}$$

with δF being the bandwidth of the injected signal, v_p the velocity of wave propagation, and T the signal's period.

3. Phase detection frequency domain reflectometry (PD-FDR) measures the phase shift between the transmitted and reflected waves [59].

1.4.3.2 Time domain reflectometry

TDR is widely used in detecting and locating faults. In its standard form, it is based on emitting a train of fast voltage pulses and analysing the magnitude, duration, and shape of the reflected pulses. Consequently, the position of the fault d (1.36) is retrieved from the round-trip time t, the velocity of wave propagation (v_p) of the cable given by equation (1.35), and the distance running by the signal onto the conductor.

$$v_p = \frac{c}{\sqrt{\varepsilon_r}}, \tag{1.35}$$

$$d = v_p \frac{\mathrm{t}}{2}. \tag{1.36}$$

Three main types of TDR are commonly used:

1. Online TDR (OTDR) [60] applies the TDR technique while the system is functioning by using high-power signals which are limited by the cable's propagation attenuation. Notably, this requires the use of a binary pseudorandom signal and calculating the correlation of the measured signal to the injected one to obtain the reflectogram [61].
2. Sequence TDR (STDR) [62] uses pseudo noise (PN) as testing signals, which have small magnitudes and are well-suited to use in aircraft applications. The combination of incident and reflected waves is correlated with a test copy of the PN code, and the distance to the fault is easily determined from the correlation data.
3. Spread spectrum TDR (SSTDR) follows the same principal as STDR. The difference is that SSTDR leads to sharper correlation peaks than those obtained with STDR, leading to more accurate estimates of the fault's position. Indeed, as shown in Figure 1-13, the STDR or SSTDR creates first a PN code depending on the application that they are used for. Second, a signal is injected onto the PN Sequence block in order to generate the waveform of PN sequence. Finally, in STDR, this signal is transmitted along the cable. However, SSTDR, the PN sequence passes through the BPSK block to perform the Direct Sequence Spread Spectrum Signal.

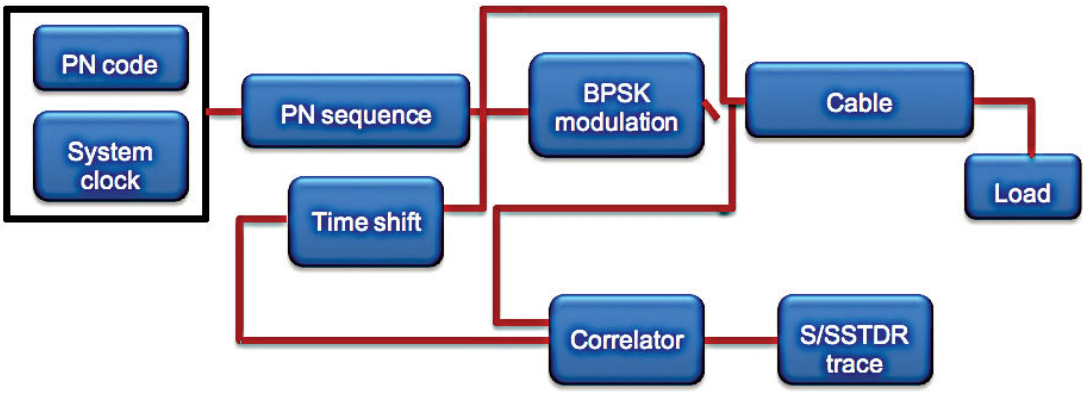

Figure 1-13. S/SSTDR schematic setup.

The objective of TDR is to look for V_r. To this end, a model is made to look for S-parameters by using the reflection coefficient $\Gamma(x)$, which is defined as the ratio of a reflected wave v^- on an incident wave v^+ as follows:

$$\Gamma(x = l) = \frac{v^-}{v^+} = \frac{Z_L - Z_c}{Z_L + Z_c} \quad . \tag{1.37}$$

Hard-fault detection using equation (1.37) is efficient due to the higher impedance discontinuity at the load Z_L.

- If short circuit $Z_L = 0$, which makes $\Gamma(x) = -1$, the reflected signal has the same magnitude as the incident signal with an opposite direction.
- If open circuit $Z_L = \infty$, which makes $\Gamma(x) = 1$, the reflected signal has the same magnitude as the incident signal.
- If $Z_L = Z_c$, which makes $\Gamma(x) = 0$, there is no reflected signal.

Moreover, the reflection coefficient at the first interface of a soft fault encountered by the incident wave:

$$\Gamma(x = d_f) = \frac{Z_f - Z_c}{Z_f + Z_c}. \tag{1.38}$$

Equation (1.38) shows that the magnitude of the reflected signal depends on the value of the fault impedance Z_f. If the fault signature is small, TDR generally fails to detect it in practice for at least several reasons such as the noise level.

1.5 Wiring faults modelling

Previously, several defect types are presented. In this thesis, and especially in this section, only the chafing defect will be studied. The chafing defect is the chafing of the shield and insulator as shown in Figure 1-14. A damaged cable with this defect is named the chafe model. To model this damaged cable, a circuit diagram of impedances is used as shown in Figure 1-15. This scheme will always be used to make a simple model of a coaxial cable with the chafing defect.

Figure 1-14. The chafing fault.

Figure 1-15. Modeling of a damaged coaxial cable called the chafe model with Z_f is the fault's impedance.

1.5.1 Theory

In this section, we look for the chafe model that will be defined in the section 1.5.2. As a defect is an impedance discontinuity, two cables with different characteristic impedances are first studied, as seen in Figure 1-16.

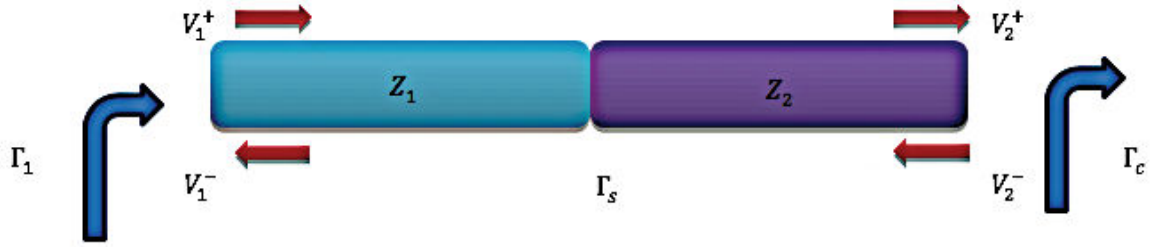

Figure 1-16. Scheme of the impedance step.

The objective is to find Γ_1. First, the reflection coefficient Γ_s and the transmission coefficient τ_s caused by the impedance discontinuities are defined at the discontinuity level.
For waves moving to the right:

$$\Gamma_s=\frac{Z_2-Z_1}{Z_1+Z_2}=\left[\frac{V_1^-}{V_1^+}\right]_{V_2^-=0} , \tag{1.39}$$

$$\tau_s=1+\Gamma_s . \tag{1.40}$$

For waves moving to the left (from the second cable to the first), the reflection coefficient Γ_{s2} at the discontinuity level is defined as

$$\Gamma_{s2}=\frac{Z_1-Z_2}{Z_1+Z_2}=-\Gamma_s , \tag{1.41}$$

Then, the transmission coefficient is

$$\tau_{s2}=1-\Gamma_s . \tag{1.42}$$

Combining the equations (1.39), (1.40), (1.41), and (1.42), we get

$$\begin{bmatrix} V_1^- \\ V_2^+ \end{bmatrix} = \begin{bmatrix} \Gamma_s & 1-\Gamma_s \\ 1+\Gamma_s & -\Gamma_s \end{bmatrix} \begin{bmatrix} V_1^+ \\ V_2^- \end{bmatrix} . \quad (1.43)$$

As consequence, we get

$$V_1^- = \Gamma_s V_1^+ + (1-\Gamma_s) V_2^- , \quad (1.44)$$

$$V_2^+ = (1+\Gamma_s) V_1^+ - \Gamma_s V_2^- . \quad (1.45)$$

Combining equations (1.44) and (1.45), the desired result is

$$\Gamma_1 = \frac{\Gamma_s + \Gamma_c}{1+\Gamma_s \Gamma_c} . \quad (1.46)$$

Where $\Gamma_1 = \frac{V_1^-}{V_1^+}$; $\Gamma_C = \frac{V_2^-}{V_2^+}$.

1.5.2 Chafe model

Consider a chafe placed at a distance d_f on a coaxial cable of length ℓ, having width $w_f = r_i \Delta\varphi_f$, length ℓ_f , and angular position φ_f, as depicted in Figure 1-18(a). It is represented by a modified characteristic impedance Z_f (1.38), as indicated in Figure 1-18(b). To calculate the fault impedance Z_F, numerical methods can be used, such as FDTD, electromagnetic modelling via HFSS (Figure 1-17), or the capacitive and inductive method [62].

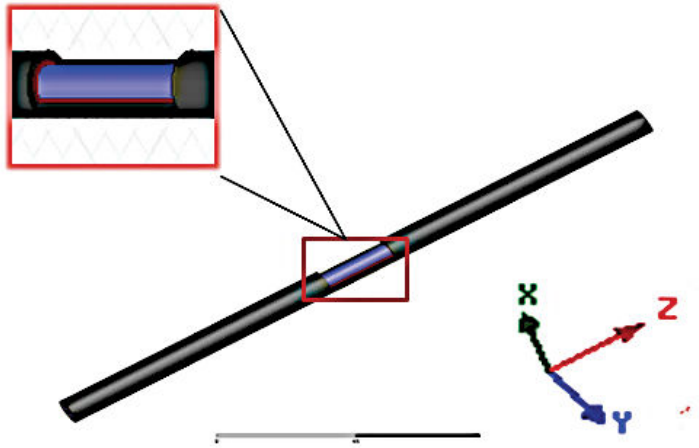

Figure 1-17. 3D chafed RG-58 modelling via HFSS.

However, these methods are time-consuming and expensive, and they need a large system storage size. In order to simplify the problem, the fault will be supposed to have the same geometry along the x axis, therefore, a two-dimensional problem can be solved. The fault region will be a kind of line having a short length (Figure 1-18). In order to have a good approximation, we neglect the capacitive effect at the beginning and at the end of this short line. Moreover, as the impedance of this short line is very close to the impedance of the

nominal transmission line part, we can consider the speed of light in this part is the same as in the rest of the line. With these approximations, the problem will now be solved. First, we need to find the linear characteristics of the fault. It is classically made by calculating the linear capacitance in the static approximation case.

This computation for a nonstandard geometry is made by using a numerical approach to solve the Laplace equation. In the present case, the computation of the electric potential is made using a finite difference scheme. It consists in discretizing the cable and surrounding space in a Cartesian grid. To make such a computation, the following rules should be considered:

- The computation surface border is situated sufficiently far from the cable to avoid potential lines perturbations,
- A zero potential is considered on the external part of the coaxial,
- A unity potential is applied on the internal conductor.

With these considerations, the charge on the internal conductor can be expressed in two different ways.

First, the charge can be expressed by the internal linear capacitance as

$$Q = CV. \tag{1.47}$$

As V=1 V, we have C=Q

Moreover, this charge equals the integral of the charge density all around the conductor. In addition, this density is connected to the potential V and to the normal electric field E_n. Finally, we have:

$$Q = C = \oint \varepsilon E_n dc = -\varepsilon \oint \nabla_n V dc. \tag{1.48}$$

If the integral negative term is denoted τ_f, then, we have:

$$C = \varepsilon \tau_f. \tag{1.49}$$

As the speed of light is

$$v = \frac{1}{\sqrt{L_0 C_0}} = \frac{1}{\sqrt{\varepsilon \mu}}. \tag{1.50}$$

Where: ε is the permittivity, μ is the permeability, L_0 is the inductance, and C_0 is the capacitance.

If C is multiplied by a factor τ_f compared to C_0, L is devided by the same factor, therefore, the impedance is divided by this factor:

$$Z_f = \frac{1}{\tau_f}\sqrt{\frac{\mu}{\varepsilon}}. \tag{1.51}$$

As we must consider different chafing faults, with different angles, τ_f can be stored in a lookup table using a polynomial interpolation.

$$\tau_f = C_0 + C_1 w + C_2 w^2 + C_3 w^3. \tag{1.52}$$

Therefore, in our work, the efficient approach used is to approximate the fault equivalent impedance to a polynomial whose coefficients are calculated from a lookup table via Matlab.

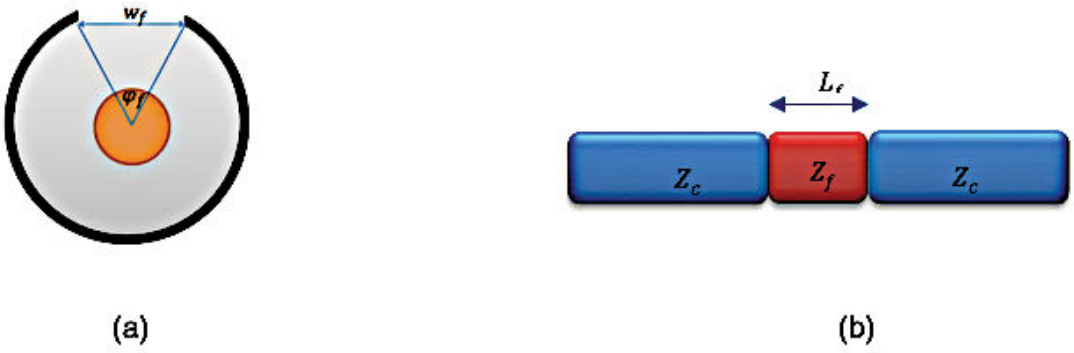

Figure 1-18. Scheme of a chafed cable.

After τ_f is calculated, it is substituted into equation (1.51). From this, the value of the fault impedance Z_f is calculated.
Since the chafe model is symmetric with respect to the cable axis, the fault S matrix is defined as

$$S^f = \begin{bmatrix} S_{11}^f & S_{12}^f \\ S_{21}^f & S_{22}^f \end{bmatrix}. \tag{1.53}$$

Moreover, the incident wave travels the default length, reflects from the discontinuity, and travels back. As consequence, the reflection coefficient is $\Gamma_2 e^{2i\gamma_f l_f}$,
Where

$$\Gamma_2 = \frac{Z_f - Z_c}{Z_f + Z_c}. \tag{1.54}$$

γ_f is the attenuation in this fault, which for our model equals the attenuation γ of the nominal cable.
Furthermore, the incident wave is delayed by $e^{i\gamma_f l_f}$ because of its transmission through the impedance discontinuity.
Consequently, the transmission coefficient is $(1 - \Gamma_2)e^{i\gamma_f l_f}$.
Noting from Figure 1-16, that $\Gamma_1 = -\Gamma_2$, and by replacing $\Gamma_1 = -\Gamma_2$ and $\Gamma_c = \Gamma_2 e^{2i\gamma_f l_f}$ in equation (1.46), we obtain

$$S_{11}^{f} = \frac{\Gamma_2(e^{2i\gamma_f l_f} - 1)}{1 - \Gamma_2^2 e^{2i\gamma_f l_f}}, \tag{1.55}$$

$$S_{21}^{f} = \frac{e^{i\gamma_f l_f}(1 - \Gamma_2^2)}{1 - \Gamma_2^2 e^{2i\gamma_f l_f}}. \tag{1.56}$$

Notice that we have calculated the scattering parameters of the nominal cable (§1.3.3) as that of the fault (1.55) and (1.56). To get the total scattering parameters of the chafed cable, we should transform each S-parameters matrix to a T-parameters matrix. Then, we multiply these T-parameters matrices to obtain the T-parameters matrix of the chafed cable. At the end, we switch to the S-parameters matrix.
Finally, the composite S-parameters matrix for a chafed cable may be written as

$$S = \begin{bmatrix} S_{11}^{f} e^{i2\gamma d_f} & S_{12}^{f} e^{i2\gamma(l-l_f)} \\ S_{21}^{f} e^{i2\gamma(l-l_f)} & S_{22}^{f} e^{i2\gamma(l-l_f-d_f)} \end{bmatrix}. \tag{1.57}$$

1.5.3 S-scattering parameters of the whole system

In the previous sections, the S-matrix of the chafed cable was obtained. In this paragraph, we look for the total S-matrix of the entire system, taking into consideration the VNA's impedance Z_S and the load's impedance Z_L, which is infinite, as shown in Figure 1-12.
To get the total S-matrix, Mason's Rule [64] was applied (Figure 1-19),

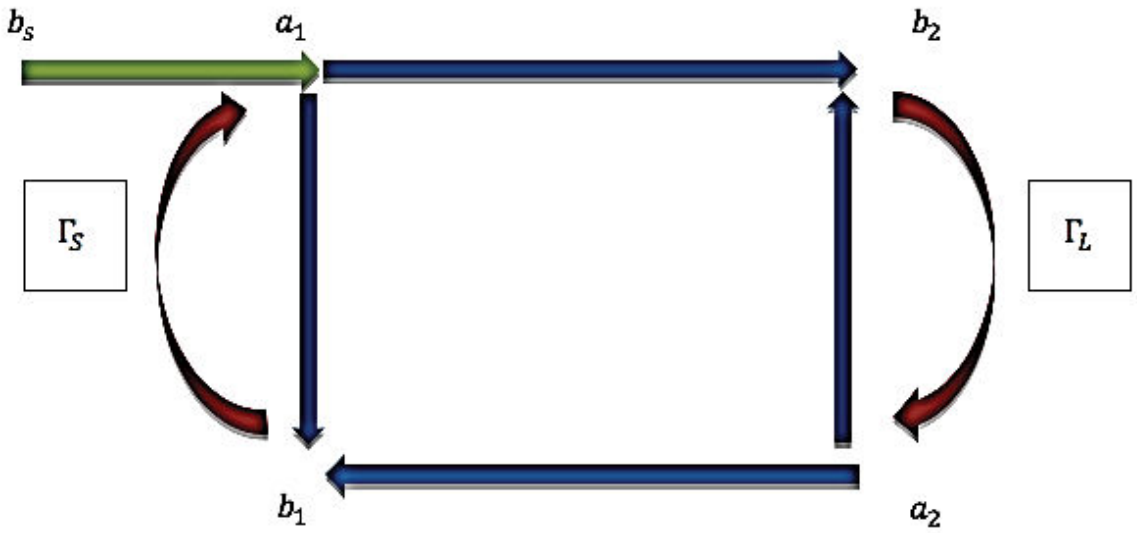

Figure 1-19. Scheme of Mason's Rule.

where Γ_S is the reflexion coefficient between the first nominal section of the cable and the VNA, and Γ_L is the reflexion coefficient between the second nominal section of the cable and the load.

$$\Gamma_s = \frac{Z_c - Z_s}{Z_c + Z_s} \quad , \tag{1.58}$$

$$\Gamma_L = \frac{Z_L - Z_c}{Z_c + Z_L}. \tag{1.59}$$

Using Mason's Rule, we calculate the transfer function T for a signal flow graph (Figure 1-19).

$$T = \frac{P_1\left(1 - \sum L(1)^{(1)} + \sum L(2)^{(1)} - \ldots\right) + P_2\left(1 - \sum L(1)^{(2)} + \sum L(2)^{(2)} - \ldots\right) + \cdots}{1 - \sum L(1) + \sum L(2) - \ldots}. \tag{1.60}$$

P_i is the product of the coefficients of the directed route from the input to the output signal.
$\mathcal{L}(1)^{(j)}$ represents the sum over all j order loops.
Applying Mason's Rule to our system, S parameters are written as

$$S_{11\_system} = \frac{S_{11} + \Gamma_S - \Gamma_S\Gamma_L S_{22} - (S_{11}S_{22} - S_{21}S_{12})\Gamma_L}{1 + S_{11}\Gamma_S - \Gamma_L S_{22} - (S_{11}S_{22} - S_{21}S_{12})\Gamma_L\Gamma_S} \quad , \tag{1.61}$$

$$S_{12\_system} = \frac{S_{12}(1 + \Gamma_S)(1 + \Gamma_L)}{1 + S_{11}\Gamma_S - \Gamma_L S_{22} - (S_{11}S_{22} - S_{21}S_{12})\Gamma_L\Gamma_S}. \tag{1.62}$$

1.6 Network modelling

Having found S-parameters for a simple faulted cable, we look now for S-parameters for a bifurcation. Three sets of cables were designed for this research work. The cables were grouped into three types:
Type A: nominal coaxial cable (L_1: *length*).
Type B: nominal coaxial cable (L_2: *length*).
Type C: chafed coaxial cable (L_3: *length*).

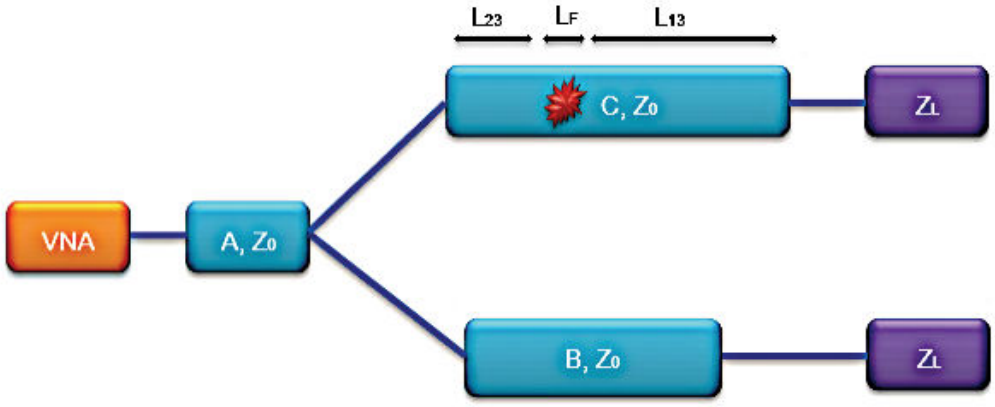

Figure 1-20. This network cable has one fault placed in cable C. Z_L is equal to the cable impedance Z_0.

In the literature, there are several methods to model transmission lines. The objective is to look for S_{11} at the cable entry. We choose to work with the easiest one, namely the reduced

impedance [65]. It implies that by knowing the impedance at a point of this cable (e.g., at the end), we can determine the impedance back to any point of the cable.
The considered transmission line (Figure 1-20) has a fault with two sections attached to it. For each section, the reduced impedance at its entry was calculated. Moreover, the fault is a straightforward variation in impedance, denoted Z_F.
For the last part in cable C, the reflected impedance Z_{in1} is

$$Z_{in1} = Z_0 \frac{Z_L + Z_0 \tanh(\gamma L_{13})}{Z_0 + Z_L \tanh(\gamma L_{13})}. \quad (1.63)$$

where γ is the propagation constant.
We then recalculate the new reflected impedance Z_{in2} at the fault entry.

$$Z_{in2} = Z_F \frac{Z_{in1} + Z_F \tanh(\gamma L_F)}{Z_F + Z_{in1} \tanh(\gamma L_F)}. \quad (1.64)$$

Afterward, Z_C will be reflected at cable C as

$$Z_C = Z_0 \frac{Z_{in2} + Z_0 \tanh(\gamma L_{23})}{Z_0 + Z_{in2} \tanh(\gamma L_{23})}. \quad (1.65)$$

The reflected impedance Z_B at the cable B entry is

$$Z_B = Z_0 \frac{Z_L + Z_0 \tanh(\gamma L_2)}{Z_0 + Z_L \tanh(\gamma L_2)}. \quad (1.66)$$

Therefore, as B and C come in parallel at the end of the line A, the equivalent impedance at D is written as

$$Z_{inBC} = \frac{Z_B * Z_C}{Z_B + Z_C}. \quad (1.67)$$

As a result, the reflected impedance at the cable A entry is

$$Z_{in} = Z_0 \frac{Z_{inBC} + Z_0 \tanh(\gamma L_1)}{Z_0 + Z_{inBC} \tanh(\gamma L_1)}. \quad (1.68)$$

Finally, the reflected coefficient at the cable entry is

$$S_{11} = \frac{Z_{in} - Z_S}{Z_{in} + Z_S}. \quad (1.69)$$

Moreover, S_{11} is in the frequency domain. To get the reflected signal S, we convert S_{11} to the time domain by using the inverse Fourier transform (IFT).

$$S = \mathrm{IFT}(S_{11}). \quad (1.70)$$

1.7 Application

A coaxial cable with length $\boldsymbol{l}$ and characteristic impedance Z_c which equals 50 Ω, as shown in Figure 1-21 will be now considered. The shield has the outer radius $r_s = 1.5$ mm. The conductor, having the latter radius $r_w = 0.3$ mm, is symmetric with respect to the cable axis. The area between the shield and the conductor is a homogeneous, isotropic insulator of radius $r_i = 1.35$ mm, having permittivity $\varepsilon = 2.3\,\varepsilon_0$, permeability $\mu = 1.0\,\mu_0$, conductivity shield σ_s=60 MS/m, conductivity insulator $\sigma = 0$S/m, and conductivity conductor σ_w=60 MS/m. Moreover, the attenuation constant of the nominal coaxial cable is written as [63]

$$\gamma_c = w\sqrt{\mu\varepsilon} + \frac{1}{2\ln\left(\frac{r_i}{r_w}\right)}\sqrt{\frac{w\varepsilon}{j\sigma}}\left(\frac{1}{r_w}+\frac{1}{r_i}\right). \tag{1.71}$$

where w is the pulsation:

$$w = 2\pi f\,, \tag{1.72}$$

where f is the frequency.

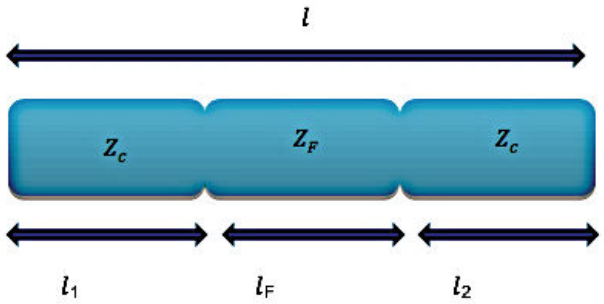

Figure 1-21. Cable with a characteristic impedance Z_c and a length l.

In this section, the coaxial cable with respect to the *Z*-axis is treated as a two-port device with a 2 × 2 matrix of S-parameters (1.28). By replacing $\gamma = \gamma_f$, $x = l_2$, and $x = l_1$ in equation (1.26), we obtain the scattering parameters of the both nominal sections of the cable.
This cable is matched at the input port $Z_s = Z_c$, where Z_s is the generator impedance. For conventional TDR, a Gaussian injected signal is used (1.73). In this work, the frequencies range is $[1MHz, 4GHz]$.

$$f(x) = e^{-\frac{(x-\mu)^2}{2\sigma_g^2}}. \tag{1.73}$$

Where $\mu = 0$, corresponds to the mean, and σ_g the standard deviation.

To calculate Z_f, a look-up table that is described in (§1.5.1) is made. For this, we select a set of fault widths within the range $(0, \pi r_i)$. For w_f, the 2D Laplace's equation $(\nabla^2_{\perp}\varphi_f = 0)$ is numerically solved by a finite difference approach using boundary conditions. At the end, an outer surface is used to not disturb the fields leaking out through the chafe.

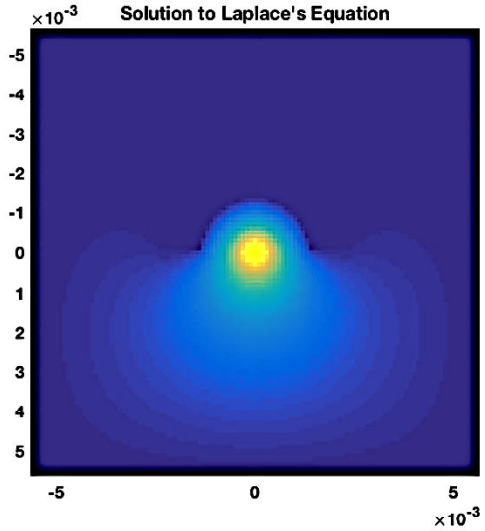

Figure 1-22. Numerical solution to Laplace's equation for the angular fault position π/2 and the width πri. ri is the inner radius of the coaxial cable conductor.

After getting the Laplace's equation solution (Figure 1-22), τ_f is calculated by using an interpolating function (1.52). Then, τ_f is introduced into equation (1.51). As a result, the value of the fault impedance is $Z_f = 62.56\Omega$. This fault impedance will be used for all the applications shown in this thesis.
By replacing $\gamma = \gamma_c$ in equation (1.57), we obtain the scattering parameters of the fault.
Using Mason's Rule defined in Section 1.5.3, the scattering parameters of the whole system are calculated. The simulated reflected signal at the three meters cable entry with one chafing fault at 1 m is depicted in Figure 1-23. This signal has $SNR_{noisy\_f} = 10\ dB$.

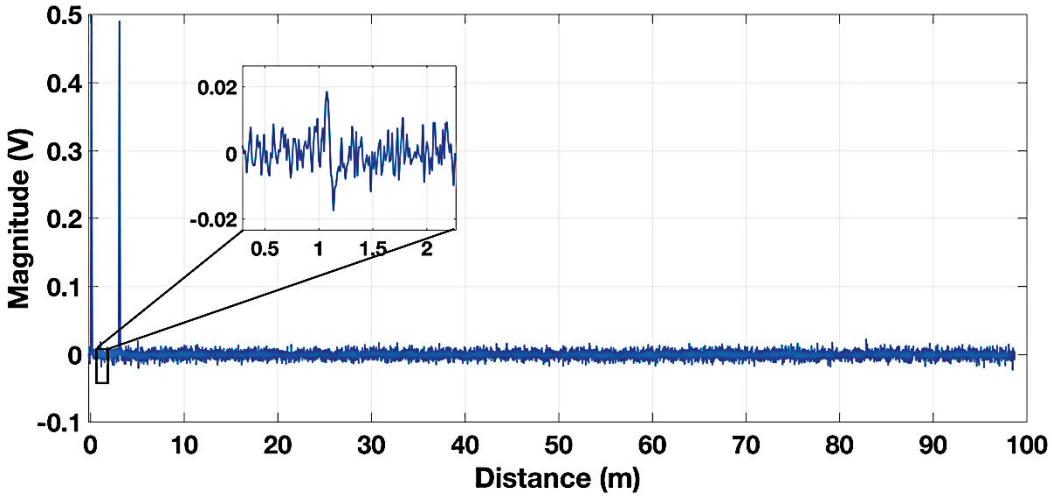

Figure 1-23. The simulated reflected voltage at the 3 m coaxial cable with one chafing fault at 1 m and l_f = 0.014 m.

For 10 m coaxial cable with two chafing faults at 3 m and 8 m, the simulated reflected signal at this cable entry whose $SNR_{noisy\_f} = 10\ dB$ is depicted in Figure 1-24.

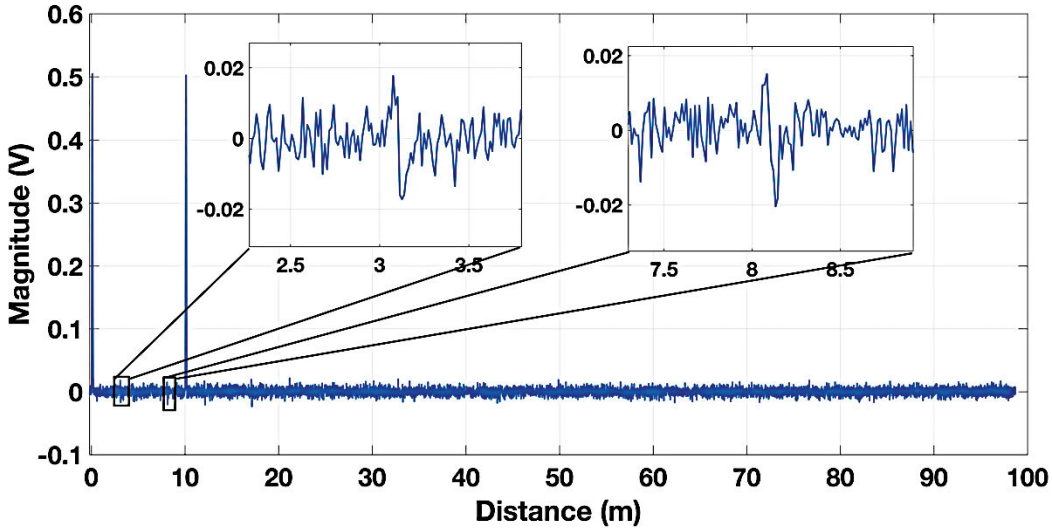

Figure 1-24. The simulated reflected voltage in the 10 m coaxial cable with two chafing faults at 3 m and 8 m and $l_f = 0.014$ m.

All the results and figures in this thesis are generated for these two coaxial cables via Matlab. These systems are open circuit. For these two signals whose $SNR_{noisy\_f} = 10dB$ shown in Figure 1-23 and Figure 1-24, the chafing faults are barely identified because they are drown in the noise. As a result, the objective of this thesis is to detect these chafing faults' characteristics. For this reason, before the post-treatment of these two simulated signals shown in Figure 1-23 and Figure 1-24, we denoise them in the next section using sophisticated denoising methods. Then, we detect the chafing faults via some advanced fault detection methods. In addition, because the TDR has some difficulties to detect the chafing fault in simple cables, there is no necessity to try it on the network cable at the moment.

1.8 Conclusion

In this chapter, we presented an overview of electrical cable types widely used today. Their cumulative length can increase the probability of wiring faults which cause safety problems. Two kind of fault have been identified: Hard faults which are open or short circuits. Soft faults, such as chafing faults, still allow signals to propagate along a cable, but over time they can lead to hard faults. We then illustrated some of the fatal consequences that a wiring breakdown can lead to and presented statistical examples of the losses such breakdowns have caused, particularly in the avionics industry. Because detecting and locating soft faults is a necessity, we highlighted two main groups of fault detection and location methods: reflectometry-based methods and other methods. We have seen that the reflectometry-based techniques, which have formed the pivot of nearly all modern studies in this field, can be distinguished according to the analysis domain of the reflected signals: time domain (TDR) methods and frequency domain (FDR) methods.

We reviewed the primary well-known reflectometry-based methods developed in recent decades. These have shown great performance but also some limitations. Most are unable to produce efficient results with simple cables involving multiple faults, and noise.

To sum up, we adopted a frequency domain analysis to implement our simulation, based on the S-matrix approach, due to its simplicity and ease of implementation. The transmission line theory and the reduced impedance allowed us to represent the studied cables in a simple

manner to give insight into the voltage propagation. We also showed that reflectometry methods are highly sensitive for detecting chafing faults but only under perfect conditions that are not feasible in practical applications. One idea is to denoise the signal before post-treatment and combine TDR with sophisticated denoising approaches. For that, multiple methods are used in the next chapter. These denoising methods were already used to denoise signals in different literature. However, in this work, we use them as denoising methods and also as chafing fault detection methods. In chapter 3, the Time Frequency is introduced in order to compare between them in terms of chafing fault position. In Chapter 4, Bayesian approach is represented. The Bayesian method exists in the literature, but it is limited to be solved by Nested Sampling. In this work, we solve it by the Nested Sampling and Gauss Newton approach in order to overcome some limitations of the Nested Sampling. In Chapter 5, chaos time domain reflectometry (CTDR) based on time-domain analysis is performed. In the research, this approach was used only for hard fault detections by using only the simulations. In this thesis, we develop the CTDR to detect chafing faults by using measurements and simulations.

Chapter 2: Denoising Methods

2 Denoising methods

2.1 Introduction

In this thesis, we concentrate mainly on the Time Domain Reflectometry. The signals are often disturbed by an undesirable perturbation which is superimposed on the useful data, in a transmission line or in a system. This disturbance is called the noise that is created by the environment where the system is, or by the measurement set-up (measurement dynamics, measurement devices' noise …). To enhance the quality of the reflected signal produced by wiring faults, advanced denoising methods are required. In general, denoising methods impose a compromise between noise reduction and preserving significant signal details [66]. To achieve good performance in this respect, a denoising algorithm has to be adaptative in order to take into account the signal discontinuities, particularly strong variations.

The denoising approach generally compresses the essential information in a signal into relatively few, large coefficients, which represent signal details at different resolution levels. In fact, this approach, which generally consists in suppressing rapid signal changes versus time, performs low-frequency filtering that can be performed delicately [67]. Two main things are important in the choice of the denoising parameters. First, the choice of a low cut-off frequency can be excessive and eliminate low-amplitude signals that correspond to the soft fault reflectometry pulses that are the subject of this work. Second, the choice of too high a cut-off frequency may not be sufficient to eliminate unwanted signals. Then, it will always be difficult to extract the real signal from the noise. The filtering process consists in eliminating as much noise as possible while preserving as much information as possible and involves selecting and strengthening certain frequency bands that provide interesting information [68]. There are three types of such filtering:

- Linear filtering, such as spatial linear filtering, frequency filtering, differential filtering, and wavelet transform [69], is one of the most powerful signal-enhancement methods. It is a process in which part of the signal frequency spectrum is modified by the transfer function of the filter [70]. In general, the filters under consideration are linear and shift-invariant, and thus, the output signals are characterized by the convolution between the input signal and the filter impulse response.
- Non-linear filtering, such as median filters [71], Perona–Malik model [72], Wiener filtering [73], EMD [74], and LMD [75], is not based on linear relationships between an input and an output via a system function. Instead, these filters represent a much broader class of operations that do not have any explicit frequency domain transfer function [76]. Non-linear filters find applications in a range of signal processing and coding applications such as denoising, edge preserving operations, and some forms of prediction.
- Variational filtering [77] suggests variational methods based on Bayesian interference combined with an efficient importance-sampling procedure to obtain the required filtering estimates to minimize errors between the original and reconstructed signals. These methods include the Rudin–Osher–Fat model [78], and the Kalman filter [79].

Given a great variety of denoising methods, we decided to limit our research to three relevant techniques:

- the EMD method (empirical mode decomposition) based on intuitive signal processing and used particularly for non-stationary signals;

- the LMD method (local mode decomposition), which is an improvement on the EMD method and considers local signal variations;

- DWT method (discrete wavelet transform) [80].

Efficient denoising is a challenge. These methods are difficult to apply, and they do not always attain the desired result because they can create artefacts or remove signal structures. The basic challenge in this section is to correctly denoise the signal before applying any post-treatment. For this purpose, there are some classical denoising methods such as filter-bank techniques based on the Fourier transform [81] and the bandpass filter [82]. The literature abounds with methods that can denoise signals that have relatively little background noise. There are also the three well-known methods identified above: EMD, LMD, and DWT. These methods, based on the Fourier, are used for denoising non-linear and non-stationary signals. Moreover, they have been applied in various applications such as industrial machine monitoring, medical signal analysis, and signal processing [83]-[84]-[85]-[86]-[87]-[88]-[89]. Compared to classical approaches where the extracted modes are thresholded in the time domain, in the proposed methods, especially DWT [90] -[91]- [92], the thresholding can be done in the frequency domain. Each mode divides signals into blocks of equal length, and the frequency content of each is analysed. The denoised signal is obtained by the superposition of the thresholded modes.

This section aims to define a general mathematical methodology for EMD, LMD, and DWT algorithms and to analyse, and compare between them. The mathematical analysis is based on the difference between a signal and its denoised version. In this work, the denoising performances of all considered methods are compared using two approaches: quantitative simulation, which compares the denoised version with the original signal and perceptual-mathematical, which looks at the soft fault amplitude regarding the noise level.

2.2 Empirical mode decomposition (EMD)

EMD is the fundamental part of Hilbert Huang transforms (HHT) [93]. It is like filter bank decompositions [84], which makes it an efficient method for non-stationary signal analysis and, specifically, for signal denoising [94]. The EMD is the construction of some intrinsic mode functions (IMFs) [93] that are constructed through a sifting process. This sifting process is an iterative process based on an interpolation approach and a stopping criterion. Various interpolation approaches are proposed, such as thin-plate splines [95]-[96]-[97]. However, this interpolation method is too time-consuming.

EMD is a decomposition of signal f in IMFs that are defined as follows [96]- [98]:

- A function f is an IMF if
  - the number of extremities and the number of zeroes must be equal or must have a difference of at least 1.
  - its average envelope is defined by the envelope of local maxima and the envelope of local minima.
- A IMF should correspond at least to $f \in C^2$ ($f \in C^2$ means that f can be derivative twice).

Moreover, a function $f \in C^2$ is IMF if it has zero local mean. Conversely, a single-component signal is not necessarily an IMF although it has positive maxima and negative minima. In addition, the first IMF contains the most oscillatory component which could be rejected during the signal reconstruction in the interest of smoothing.

The EMD algorithm for a one-dimensional signal $f(n)_{0\leq n\leq N-1}$ is defined below in Figure 2-1. N being the number of points constituting the signal.

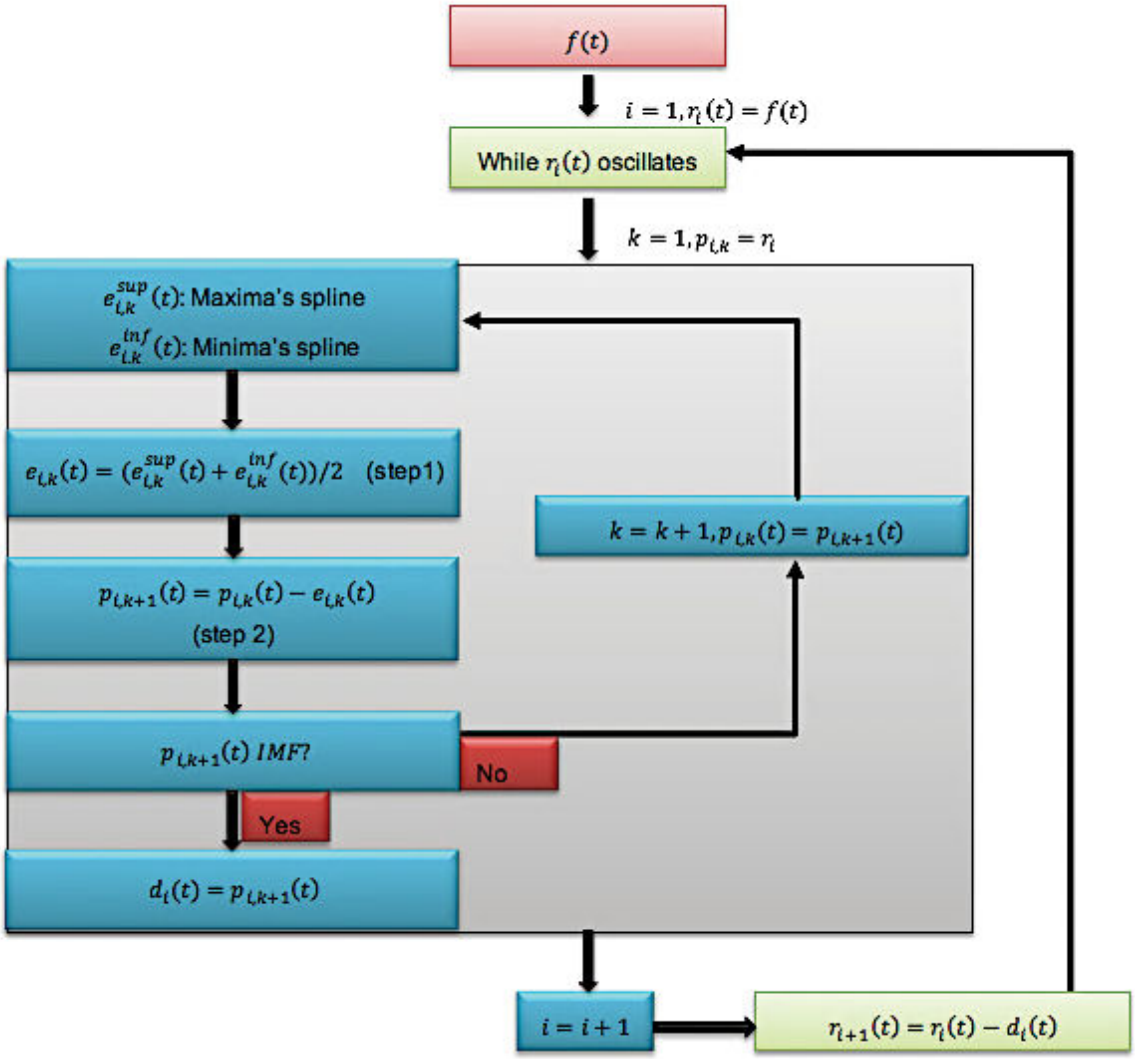

Figure 2-1. EMD algorithm for a signal f.

The EMD decomposes a given signal $f(t)$ into a series of IMFs, through the sifting process, each with a distinct time [98]. This decomposition is made by adaptive basis functions on each local time slice of the signal. First, throughout an IMF, the number of extrema and the number of zero crossings must either be equal or differ by one at most. Second, at any data location, the mean values of the local maxima envelope and the local minima envelope must be zero. Given these properties, the sifting process for extracting an IMF from $f(t)$ is employed. Third, the mean of these two envelopes is subtracted from the data to get their difference: Let $r_i(t)$ be the data and repeat steps 1 and 2 iteratively until the envelopes are symmetric with respect to zero mean under certain stopping criteria. Moreover, the choice of a relevant stopping criterion is the most important factor in improving the EMD algorithm [99]. Four stopping criteria are given in the literature [93]- [83]:

- Standard deviation

This method is proposed by HUANG et al.; the process stops if the SD is less than a given value.

- Threshold method

This method uses two thresholds to guarantee the fluctuations around the low average.

- Different Energy Tracking

This approach calculates the energy according to a decomposed orthogonal signal.
Our work uses the standard deviation stopping criterion, which is based on the standard error between two successive iterations of the signal $p_{i,k}(t)$ (2.1) [93]. As a result, $p_{i,k}(t)$ is an IMF if $\sigma_{i,k} < 0.3$ and $\sigma^*_{i,k} < 0.0003$.

$$\sigma_{i,k}=\sum_{t}\frac{|p_{i,k-1}(t)-p_{i,k}(t)|^2}{p^2_{i,k-1}(t)} \tag{2.1}$$

$$\sigma^*_{i,k}=\frac{||p_{i,k-1}(t)-p_{i,k}(t)||^2}{||p_{i,k-1}(t)||^2} \tag{2.2}$$

Once the stopping criterion is selected, the first IMF, $p_{1,1}$, is obtained. Then, the final $r_i(t)$ is designated as $d_i(t)$ and the first IMF satisfies the criteria of an intrinsic mode function. The residue $r_{i+1}(t) = r_i(t) - d_i(t)$ is then treated as the new data subject of the sifting process as described above. The procedure continues until either the recovered IMF or the residual data are small enough. Finally, when the decomposition is complete, the function is written as follows:

$$f(n)=\sum_{k=1}^{K} d_k(n)+r(n), \quad K\in N^* \tag{2.3}$$

In brief, the main advantage of the EMD approach compared to other decompositions is that it is fully adaptive. However, the interpolation method used in the construction of envelopes (spline interpolation) and the mathematical analysis of the sifting process are very expensive. In particular, the mode mixing is the major drawback. Indeed, a detail related to one scale can appear in two different intrinsic modes. This makes an individual IMF devoid of physical meaning.
To illustrate the sifting process, a harmonic signal is considered (2.4).

$$f(t) = \sin(2\pi t) + \sin(6\pi t) * \sin(2\pi t)^2 + \cos(6\pi t), \tag{2.4}$$

where t is the time.
Figure 2-2 illustrates the signal $f(t)$ over the time interval $t \in [0 - 10\,s]$.

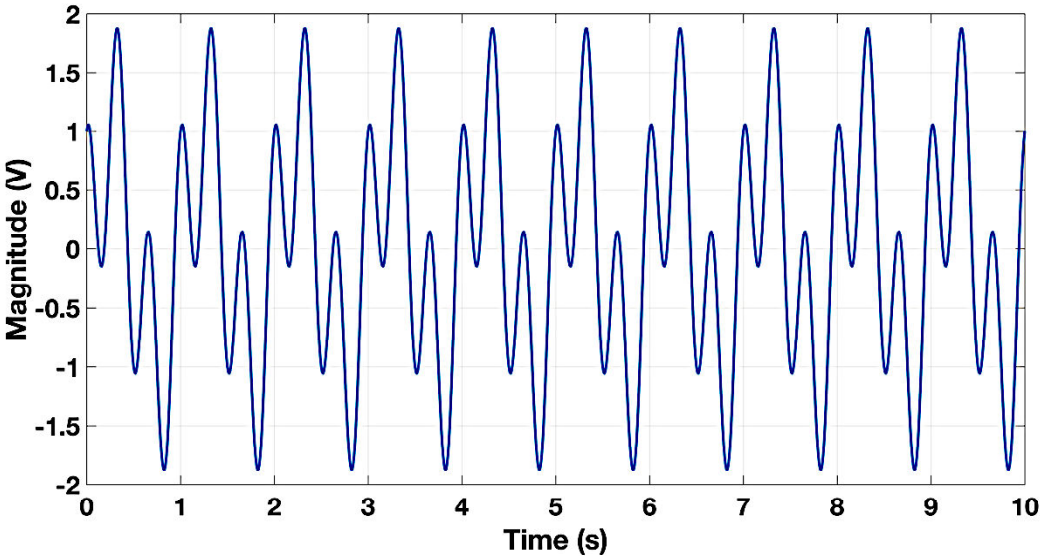

Figure 2-2. Harmonic signal over time interval [0 − 10 s].

For the EMD algorithm shown in Figure 2-1, we consider the signal $f(t) = p_{1,1}$ illustrated in Figure 2-2 as the input signal. At the first iteration, we calculate its lower and upper envelope as they are illustrated in the Figure 2-3 with the black line. Then, we calculate the mean envelope as it is illustrated in the Figure 2-3 with the red line. After that, we subtract the mean envelope from the input signal $f(t)$, as it is shown in the Figure 2-4. we noted the resulting signal $p_{1,2}$. At that point, we test if $p_{1,2}$ is IMF, wich mean if $\sigma_{1,1} < 0.3$ and $\sigma^*_{1,1} < 0.0003$. If yes, then we subtract the $p_{1,2}$ from the input signal. The result is considered as the new input signal for the next iteration. The algorithm continues running until there is no IMF. If not, the algorithm stops. For our signal $f(t)$, Figure 2-5 depicts five IMF sub-blocks of the signal $f(t)$ decomposed by EMD. It shows that the side effects are perceptible over a short time interval at each extremity of the IMF signals. Moreover, it illustrates that the signal oscillations decreases as the number of decomposition cycles increases. In short, Figure 2-5 depicts that EMD efficiently decomposes the signal to several IMFs, however, it generates side-effects at the IMFs extremities.

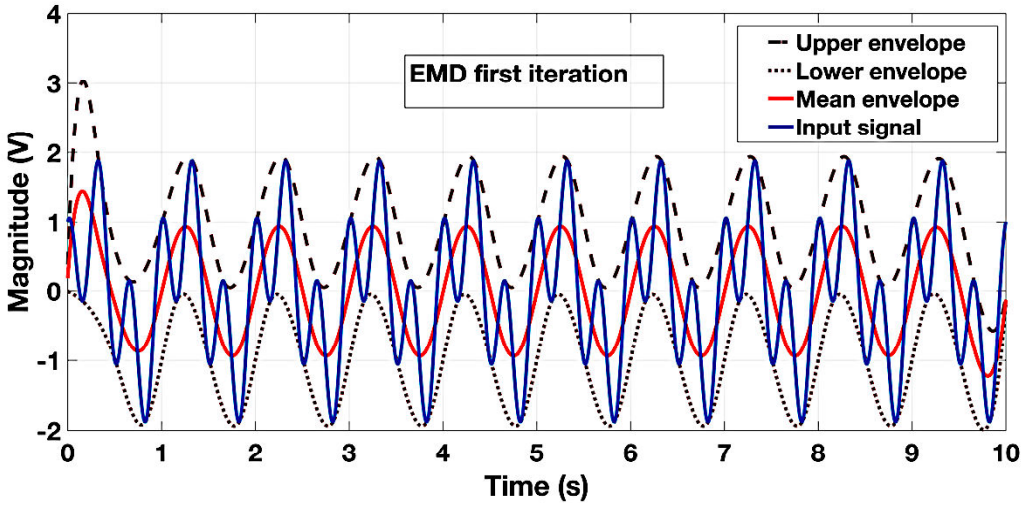

Figure 2-3. First iteration of the EMD Decomposition. The calculation of the lower envelope, upper envelope and mean envelope of the harmonic signal.

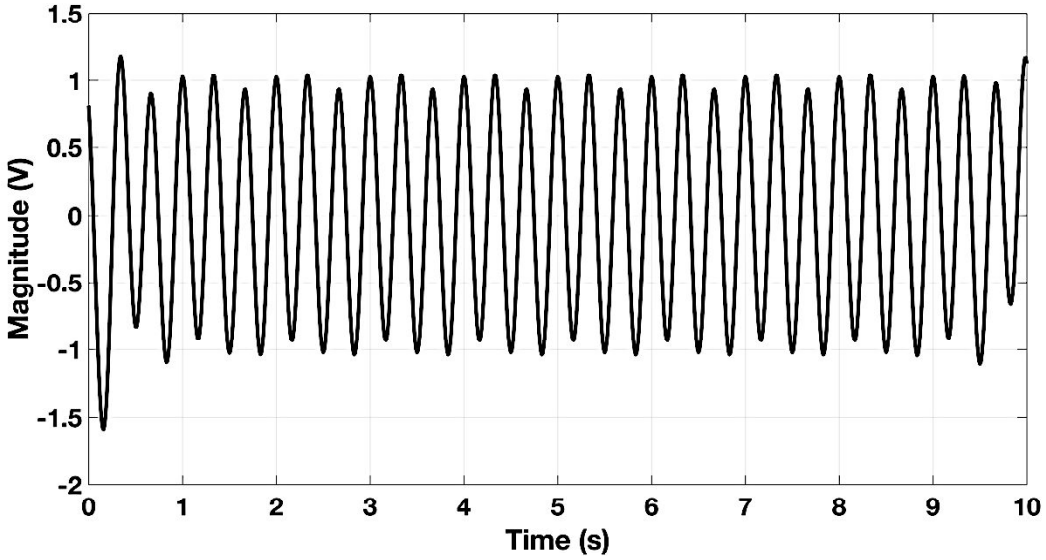

Figure 2-4. First iteration of the EMD Decomposition. The subtraction of the mean envelope from the harmonic signal.

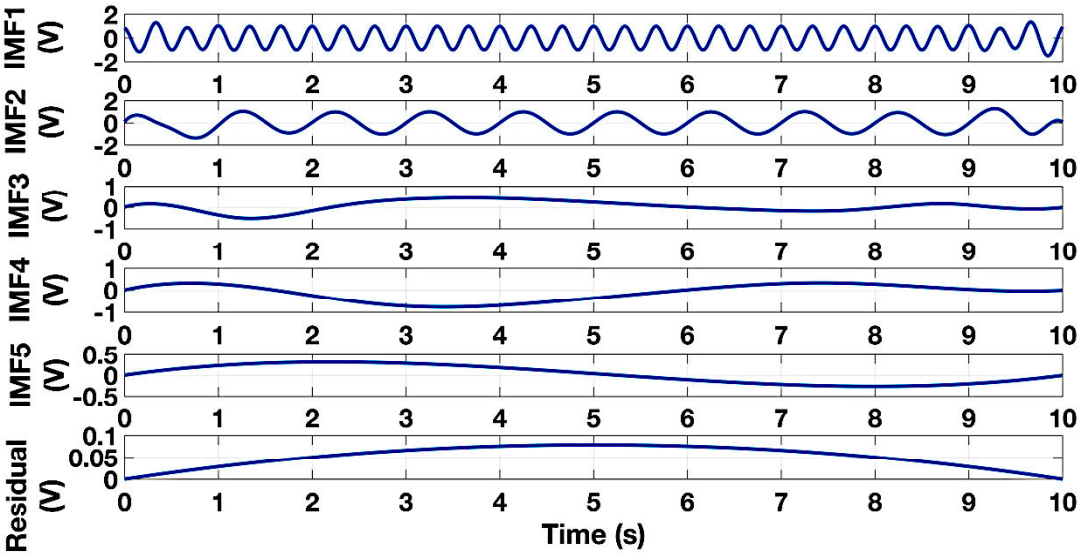

Figure 2-5. Decomposition of the harmonic signal over time (seconds) by EMD.

2.3 Local mean decomposition (LMD)

In the present work, the second method chosen for denoising signals is the Local Mean Decomposition (LMD). LMD is an adaptive method originally introduced by Smith [75] and applied in signal processing. It replaces EMD with another type of decomposition, as detailed in this section. LMD comprises a decomposition of the signal $f(t)$ into a sum of IMF [89]. LMD eliminates the negative instance frequency [100] because it can generate instantaneous amplitude and frequency data. However, LMD has two major drawbacks, which are end effect and mode mixing. It is notable that these two LMD disadvantages are associated with boundary conditions, envelope estimation, and the sifting stopping criterion. Therefore, LMD performance is based on the setting of these three properties [93]. The LMD sifting process is similar to that used for EMD; however, several new methods have been used in determining the sifting stopping criterion. Zhang et al. [101] introduced an orthogonality criterion into LMD, and Cheng et al. [102] proposed a two-condition criterion. In the present work, the algorithm is repeated as long as the signal modulated in frequency and amplitude does not have a constant envelope equal to 1.

LMD is an iterative signal process which consists in extracting a set of product functions (PFs) of a signal [98]. The algorithm for LMD is based on a nested loop structure that calculates PFs and signal envelopes. In the following, we briefly introduce the LMD process, as shown schematically in Figure 2-6.

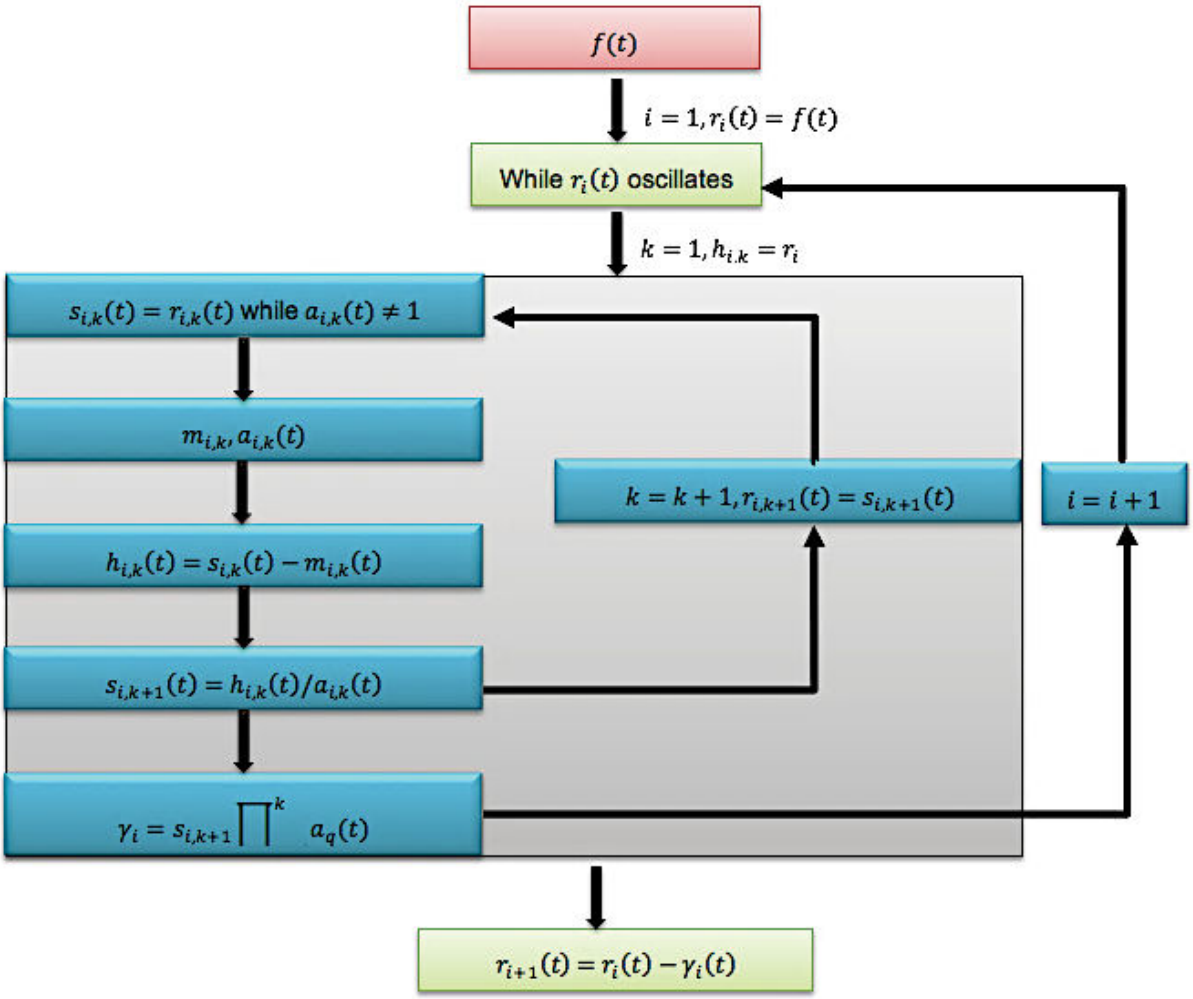

Figure 2-6. LMD algorithm for a signal 〖f(n)〗_(0≤n≤N-1).

The first step of the robust LMD is to initialize $r_i(t)$ of the sifting process as ($i = 1, r_i(t) = f(t)$) to obtain the $\gamma_i(t)$ PF. The local extrema of $r_i(t)$, noted as $n_{i,1}$, are determined. These extrema are then used to calculate local means $m_{i,1}$ (2.5) and local magnitudes $a_{i,k}$ (2.6) denoted by the following formulas **Error! Reference source not found.**.

$$m_{i,1}=\frac{n_{i,1}+n_{i+1,1}}{2} \quad , \qquad (2.5)$$

$$a_{i,1}=\frac{|n_{i,1}-n_{i+1,1}|}{2} \quad . \qquad (2.6)$$

The local mean and magnitude are extended to form stepped continuous magnitude and mean functions. The width of the steps is determined by the abscissa separating two consecutive extrema. These functions are smoothed by a slippery average whose window is between the two most distant extrema. The result of smoothing provides the mean $m_{i,1}(t)$ and the envelope $a_{i,1}(t)$. Then, the signal $r_i(t)$ is subtracted from its mean $m_{i,1}(t)$ and the result is divided by the envelope $a_{i,1}(t)$:

$$h_{i,1}(t)=r_i(t)-m_{i,1}(t) \quad , \qquad (2.7)$$

$$s_{i,1}(t)=h_{i,1}(t)/a_{i,1}(t) \quad . \tag{2.8}$$

where $s_{i,1}(t)$ is a signal modulated in frequency and amplitude. The algorithm is repeated as long as the resulting signal $s_{i,k}(t)$ does not have a constant envelope equal to 1.
Then, if $s_{i,k}(t) \in [-1,1]$, the sifting process stops. As a result, we write

$$s_{i,k}(t)=\cos\left(\phi_{i,1}(t)\right) \quad , \tag{2.9}$$

$$\phi_i(t)=\arccos\left(s_{i,k}(t)\right) \quad . \tag{2.10}$$

$\phi_i(t)$ is the instantaneous phase of the analytic signal $s_{i,n}(t)$. The instantaneous frequency is deduced immediately from expression (2.11):

$$\omega_i(t)=\frac{d\phi_i(t)}{dt} \quad . \tag{2.11}$$

Finally, PF ($\gamma_i(t)$) is written as

$$\gamma_i(t)=s_{i,k}(t)\prod_{q=1}^{k} a_{i,q}(t) \quad , \tag{2.12}$$

$$r_{i+1,1}(t)=r_i(t)-\gamma_i(t) \quad . \tag{2.13}$$

The procedure is iterated for calculating $\gamma_{i+1}(t)$ until the residual signal $r_{i+1}(t)$ is monotonic or non-oscillating.
To better understand the LMD method, an academic signal is considered (2.14).

$$f(t) = 2 + \cos(\pi t) * \cos(10\pi t + 15t^2) + \cos(4\pi t), \tag{2.14}$$

where t is the time.
Figure 2-7 illustrates the signal f over the time interval $t \in [0 - 3\,s]$.

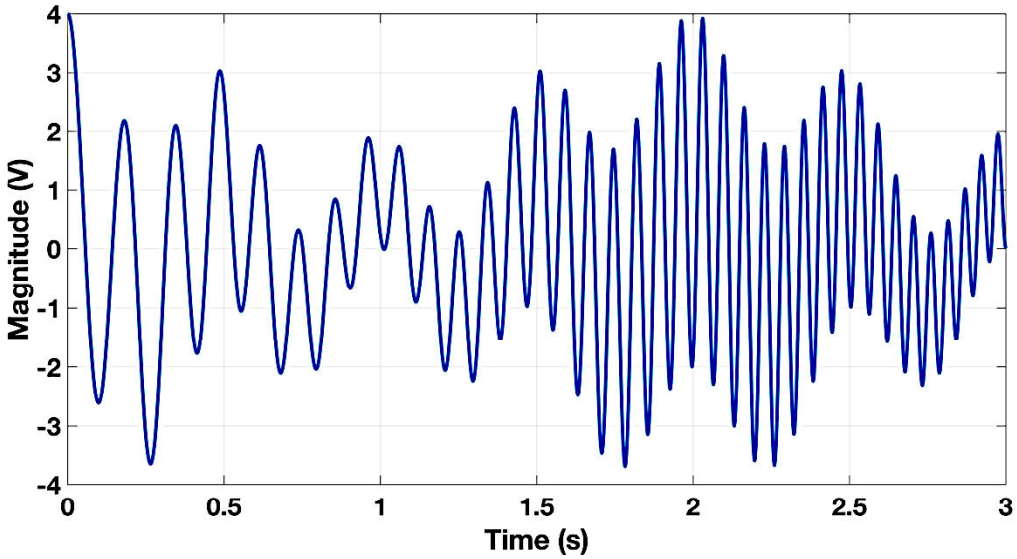

Figure 2-7. Harmonic signal $f(t)$ over time interval $[0 - 3\ \mathrm{s}]$.

The signal $f(t) = S_{1,1}$ illustrated in Figure 2-7 is considered as the input signal for the LMD algorithm. At the first iteration, we calculate local means and local magnitudes of the signal $f(t)$. The width of the steps is determined by the abscissa separating two consecutive extrema. These local mean and local magnitudes functions are smoothed by a slippery average whose window is between the two most distant extrema. The result of smoothing provides the mean $m_{1,1}(t)$ as it is illustrated in the Figure 2-8 by the red line and the magnitude envelope $a_{1,1}(t)$ illustrated by the black line. After that, we subtract the mean envelope from the input signal. As a result, we get the signal $h_{1,1}$that is illustrated in Figure 2-9 by the blue line. Then, we divided it by the envelope in order to get the signal $S_{1,2}$ that is illustrated in Figure 2-9 by the black line. At that point, we test if $S_{1,2}$ has a constant envelope equal to 1. If yes, the algorithm stops. If not, then we subtract the $S_{1,2}$ multiplied by the envelope $a_{1,k}(t)$ calculated from the input signal. The result is the new input signal. The algorithm continues running until $S_{i,k}$ has no constant envelope equal to 1. The signal f (2.4) represented in Figure 2-7 is broken down by LMD into two PFs and residual as depicted in Figure 2-10. Overall, the PFs stands for the product function. They are calculated by multiplying the last frequency demodulated signal $S_{1,k}$ by allthe magnitude envelope calculated during the LMD decomposition. Moreover, these PFs obtained by LMD have the same problem as EMD regarding the side effects. However, LMD converges more quickly than EMD. PF_1 is called the first PF component of signal $f(t)$ and contains the highest frequency component of the original signal, which is a single-component AM-FM signal. The residual signal is monotonic or non-oscillating which stops the LMD algorithm after two iterations.

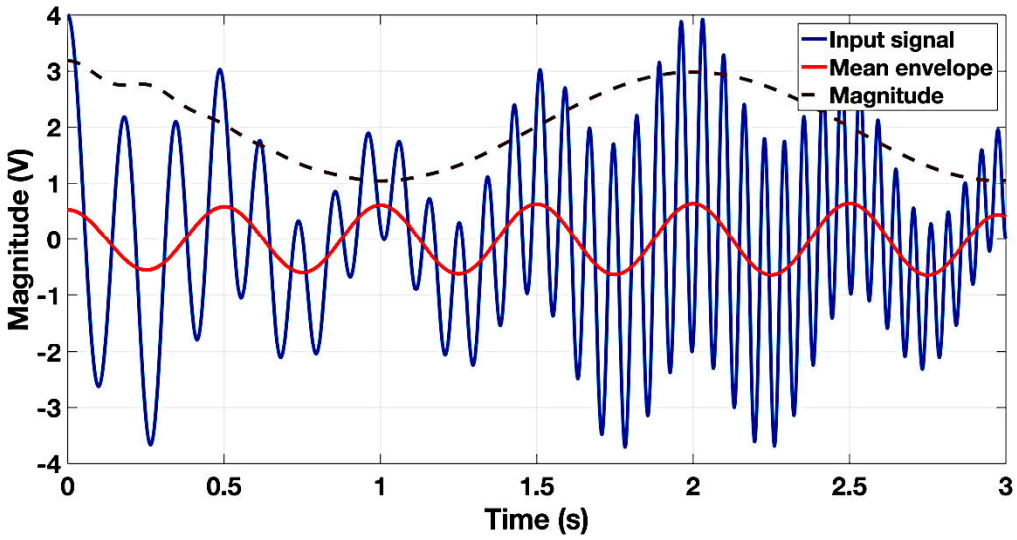

Figure 2-8. First iteration of the LMD Decomposition. The calculation of the mean envelope, and the magnitude envelope of the harmonic signal.

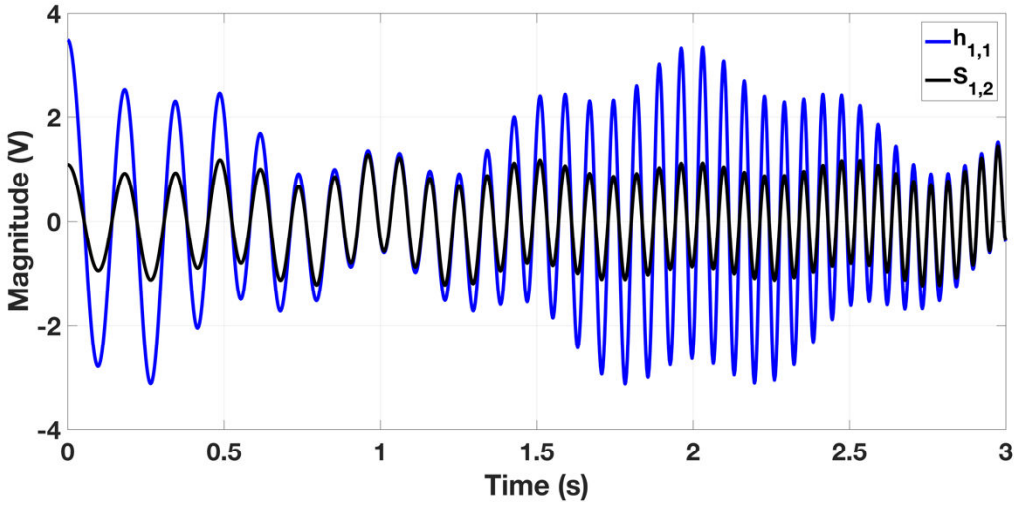

Figure 2-9. First iteration of the LMD Decomposition. The subtraction of the mean envelope from the harmonic signal ($h_{1,1}$). $S_{1,2}$ results in the frequency demodulation of $h_{1,1}$.

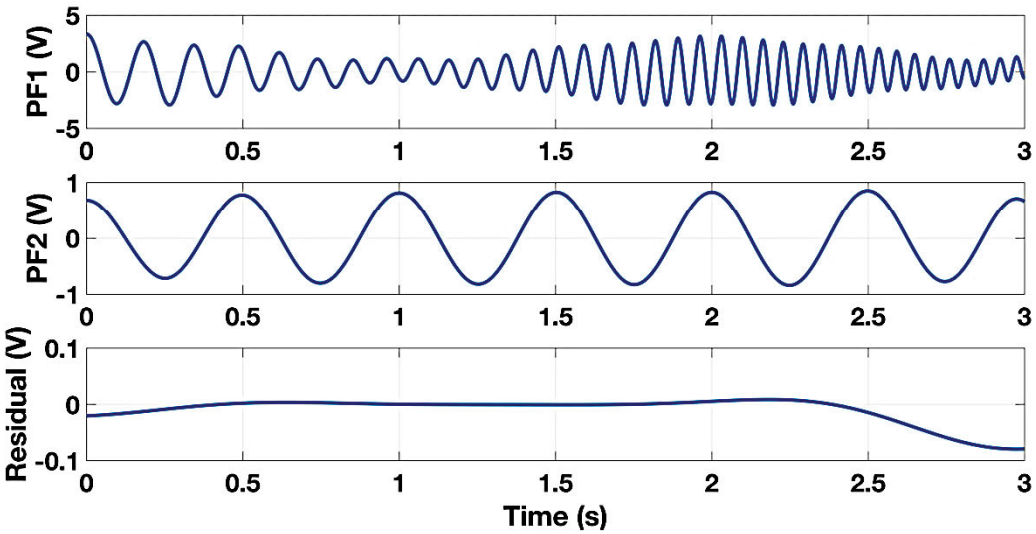

Figure 2-10. Decomposition of the harmonic signal $f(t)$ over time via LMD.

2.4 Discrete wavelet transform (DWT)

The third method chosen to denoise a signal is the Discrete Wavelet Transform (DWT). The wavelet transform has been recently used for analysing and denoising signals and images. There are two wavelet transforms types: continuous (Section 3.5) and DWTs. These transforms differ based on the application. This section focuses only on the Discrete Wavelet Transform. The DWT uses a discrete wavelet scales and translations. It decomposes the signal into mutually orthogonal sets of wavelets, which is its main difference from the continuous wavelet transform (CWT).

Generally, a wavelet is a wave with zero mean and a finite duration. Mathematically, it is

$$\int_{-\infty}^{+\infty} \psi(t)dt = 0 \quad , \tag{2.15}$$

There are many types of wavelets with different sizes and shapes, as shown in Figure 2-11.

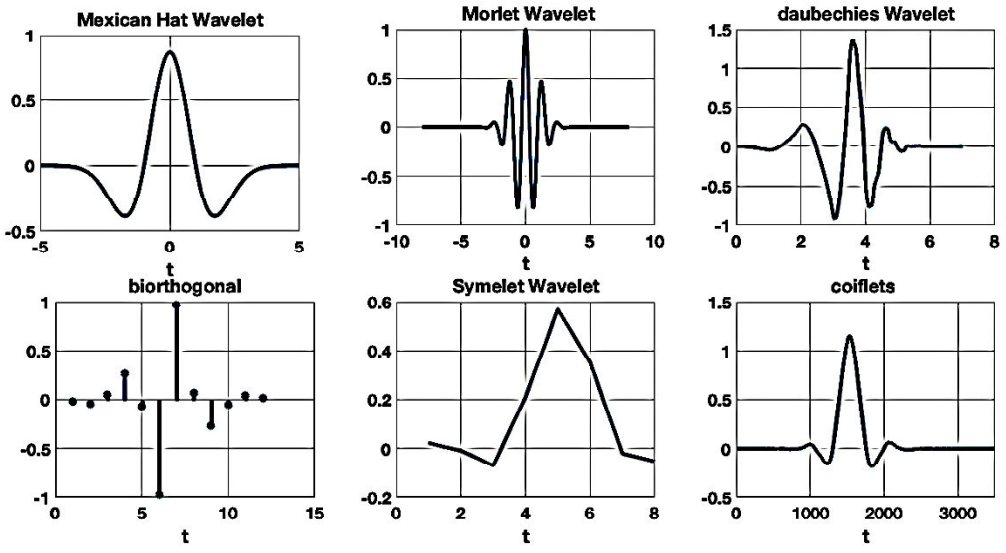

Figure 2-11. Well-known wavelet types.

The robustness of the wavelet is in its wide range. The chosen wavelet is called the mother wavelet. In addition, the wavelet has two important wavelet components: scaling and shifting. s, the scaling factor which is a positive value, is stretching or shrinking the signal in time, which is expressed by (2.16). It is used to capture the slowly and abrupt changes in a signal. This scaling factor is proportional to the frequency (2.17), because of the bandpass wavelet characteristic in the frequency domain.

$$\psi\left(\frac{t}{s}\right), s>0. \tag{2.16}$$

$$F_{eq}=\frac{F_c}{s\Delta t}, s>0. \tag{2.17}$$

where F_c is the central frequency of the wavelet, s is the wavelet scale, and Δt is the sampling step.
The second important wavelet component is shifting u, which is delaying or advancing the wavelet along a signal to align with its feature sought for in it (2.18).

$$\psi(t-u), u>0. \tag{2.18}$$

Using the translation and dilation properties, the mother wavelet becomes:

$$\psi_{s,u}(t)=\frac{1}{\sqrt{s}}\psi\left(\frac{t-u}{s}\right). \tag{2.19}$$

where $u, s \in \mathbb{R} * \mathbb{R}^+$, s is the scale coefficient, and u is the translation coefficient.
The DWT is split into three major steps [90]-[91]-[103]-[104]:
1. Look for the approximation and detail coefficients by splitting the signal into a low-pass sub-band ('approximation level') and a high-pass sub-band ('detail level').
2. Analyse the wavelet decomposition and identify a threshold.
3. Apply the threshold and reconstruct the signal.
The DWT splits the noisy signal into n levels. The first level represents the noisy part of the signal which could carry some important information that we want to retain. We remove the noise using a threshold. Although there are different threshold types [105], the universal threshold which is used in all our applications used in the DWT method, is the simplest to compute (2.20). Moreover, there are two kinds of thresholding techniques: soft (2.21) and hard (2.22).

$$\text{Threshold universal}=\frac{\sqrt{2(\text{length(signal)})*\text{median}|D|}}{0.6745}. \tag{2.20}$$

where D is a set of first detail coefficients.

$$f(x)=\begin{cases}x-\text{sign}(x)T \text{ if } |x|\geq T,\\ 0 \text{ otherwise}\end{cases} \tag{2.21}$$

$$f(x)=\begin{cases}x \text{ if } |x|\geq T,\\ 0 \text{ otherwise}\end{cases} \tag{2.22}$$

Where T is the threshold.

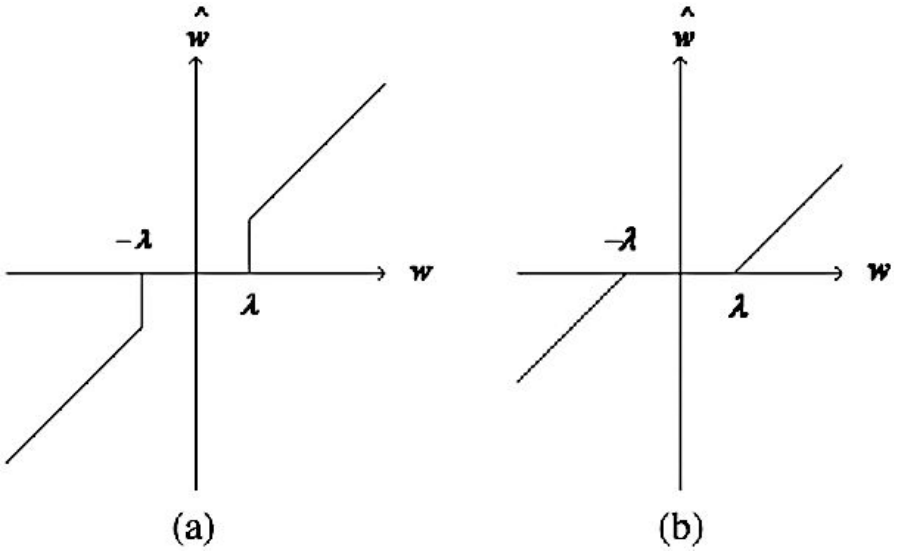

Figure 2-12. The (a) hard and (b) soft threshold methods to estimate wavelet coefficients [106].

Figure 2-12 depicts when the coefficient magnitudes are less than T, they are set to zero for both thresholdings. Otherwise, for soft thresholding the coefficients are shrunk towards zero by subtracting the threshold value from the coefficient value; for hard thresholding they are unchanged.
Finally, before reconstructing the signal, it is decomposed into multiple levels to compute and thresholded the detail coefficients.

2.4.1 The construction of the approximation and detail coefficients

As the DWT breaks down the signal into bi-orthogonal wavelets, the DWT is subdivided into several transforms; the difference between them lies in the number of low-pass and high-pass filter coefficients and the decomposition of a signal into a set of bi-orthogonal wavelets. The decomposition of a signal represents the construction of wavelet coefficients [107]-[108]. To carry out this construction, it is necessary to construct the wavelet tree that is based on the pyramid algorithm or Mallab's algorithm [109].

- ***Bi-orthogonal Basis definition***

Two families $(u_1, \cdots, u_k)$ and $(v_1, \cdots, v_k)$of E are biorthogonal, if they are:

$$1 \leq i,j \leq k, < u_i, v_i > = 1, \tag{2.23}$$

and for $1 \leq i,j \leq k$,

$$(i \neq j) < u_i, v_j > = 0 \quad , \tag{2.24}$$

In all that follows, we work in a Hilbert space with bi-orthogonal basis (w_n, ϕ_n).
Where ϕ_n is the detail basis, and w_n is the approximation basis.

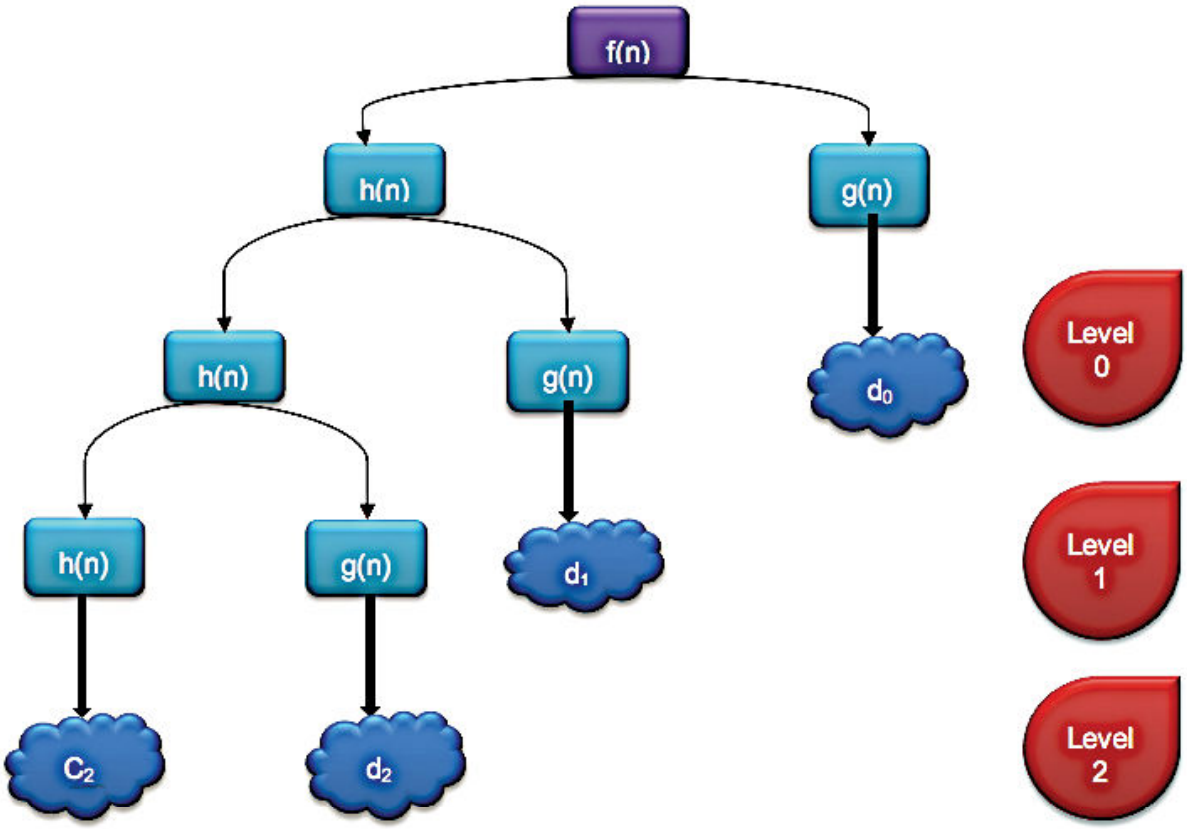

Figure 2-13. DWT tree.

f is a function defined in Hilbert space.

Figure 2-13 depicts the decomposition of f in the high-pass g(n) (2.29) and low-pass h(n) (2.28) filters. This decomposition produces details d_n and approximations C_n, coefficients that are referred to as the wavelet coefficients. The approximations are the output of the low-pass filter; conversely the details are the output of the high-pass filter. In each level, the approximations are separated and used for another decomposition filtering, and only the approximations of the last level are kept. In addition, the number of levels M is defined by (2.30). This also determines the number and the length of detail coefficients; for instance, for level 0, the length of the detail coefficient is one-half of the initial function f length, due to decimation. Consequently, d_1 has one-fourth the number of coefficients, and so on.

$$e_0 = f \quad , \tag{2.25}$$

$$e_{i+1} = h * e_i, i \in [0,1] \ , \tag{2.26}$$

$$d_k = g * e_k, k \in [0,2], \tag{2.27}$$

$$h(n) = \sum_{j=0}^{n} \sum_{i=0}^{m} <(f)_{ij} , \ \Phi_i > \Phi_i \quad , \tag{2.28}$$

$$g(n)=\sum_{j=0}^{n}\sum_{i=0}^{m}<(f)_{ij}\,,\ w_i>w_i \quad , \tag{2.29}$$

$$M=E(\log_2 N) \quad , \tag{2.30}$$

Where:

$$\text{length}\,(f)=N \quad . \tag{2.31}$$

In this section, we have seen the DWT's construction, starting by choosing filters, then calculating levels, and finally decomposing the signal on a biorthogonal basis. Now, we proceed to the reconstruction process.

2.4.2 Wavelet synthesis

In the reconstruction or synthesis process, after thresholding the levels, the detail and approximation coefficients are assembled back into the original signal f with no loss of information. The mathematical method that effects synthesis is the inverse discrete wavelet transform (IDWT). Figure 2-14 illustrates the synthesis procedure. The detail and approximation coefficients are up-sampled and filtered with the resynthesis low-pass $rh(n)$ (2.32) and high-pass $rg(n)$ (2.33) filters. The sum gives the approximation coefficients for the next level. The process is repeated until level 0 has been resynthesized.

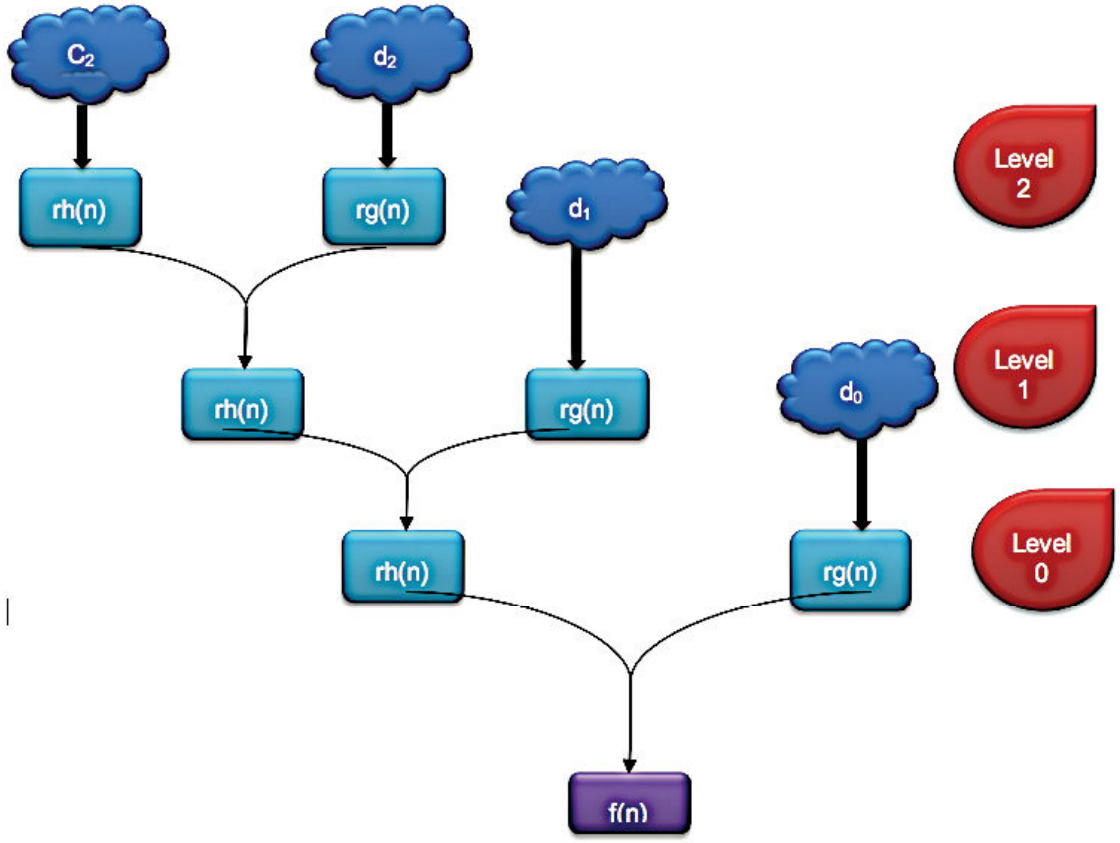

Figure 2-14. Resynthesis wavelet tree.

$$rh(n) = h(n)^T, \tag{2.32}$$

$$rg(n) = g(n)^T, \tag{2.33}$$

To better illustrate the discrete wavelet transform, the sinusoidal signal $f(t)$ (2.34) illustrated in Figure 2-15 is considered.

$$f(t) = \cos\left(\frac{1}{64}\pi t\right), \tag{2.34}$$

Where t is the time.

We add to the signal $f(t)$ a white gaussian noise ϑ whose signal noise ratio (SNR) equals 5 dB.

$$X(t) = \cos\left(\frac{1}{64}\pi t\right) + \vartheta, \tag{2.35}$$

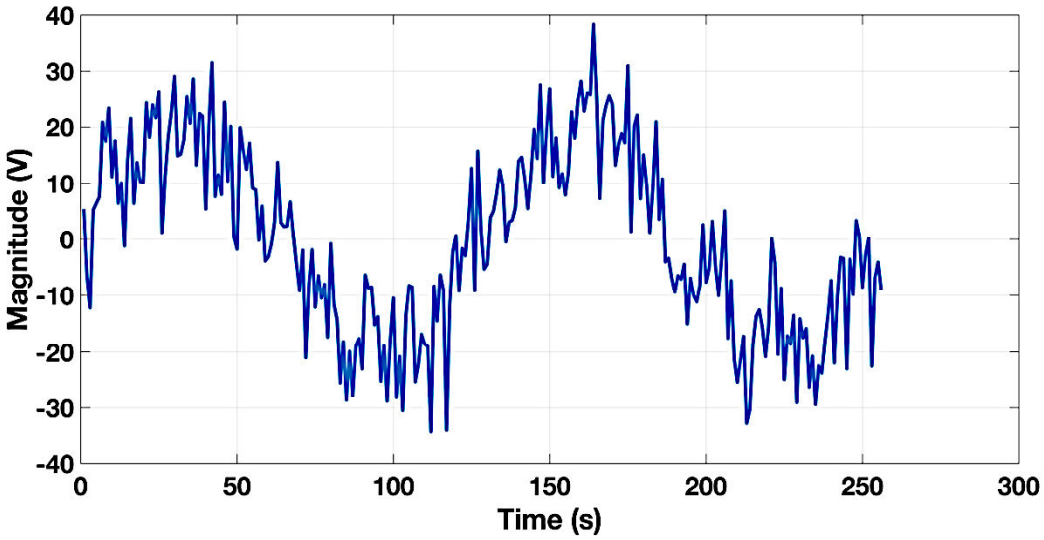

Figure 2-15. Noisy sinusoidal signal X(t) over time interval (SNR = 5 dB).

The aim of this section is to denoise the signal $X(t)$ by using the DWT. For that, before the wavelet decomposition, we select the wavelet basis which is called the mother wavelet. In this example, daubechies (db13) wavelet, which has thirteen vanishing moments, is used to decompose the noisy signal down to three levels (Figure 2-16). In fact, the Daubechies wavelet family with fewer vanishing moments would fail to suppress the noise. The wavelet decomposition consists in decomposing the signal $X(t)$ into low-pass h and high-pass filter g. In Figure 2-16, D1 which is the first detail coefficient, corresponds to the decomposition of the signal by the first high-pass filter. D2 which is the second detail coefficient, corresponds to the decomposition of the signal by the first low-pass filter and then by the high-pass filter. D3 which is the third detail coefficient, corresponds to the decomposition of the signal by the two low-pass filter and then by the high-pass filter. A3 is the result of decomposition of the signal by the three low-pass filters. Moreover, these details coefficients (D1, D2, D3) take into account primarily the fluctuations of the function around its mean value. After decomposing the signal, it is the time to reconstruct it. However, before reconstructing it, we should denoised it. For that, a threshold should be selected. In our work, to denoise the signal $X(t)$, the soft universal threshold (2.20) is applied to each detail coefficient (Figure 2-17). The signal is then reconstructed with the thresholded detail coefficients (Figure 2-18). The signal noise ratio of the denoised signal equals 8.40 dB which is higher than the signal noise ratio of the noisy signal X(t).

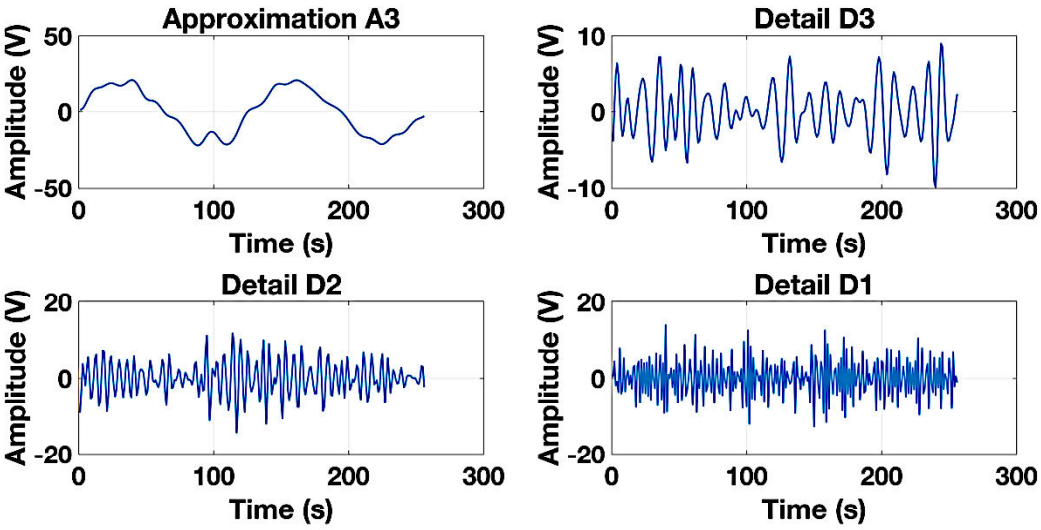

Figure 2-16. Decomposition of noisy signal X(t) by DWT into three levels.

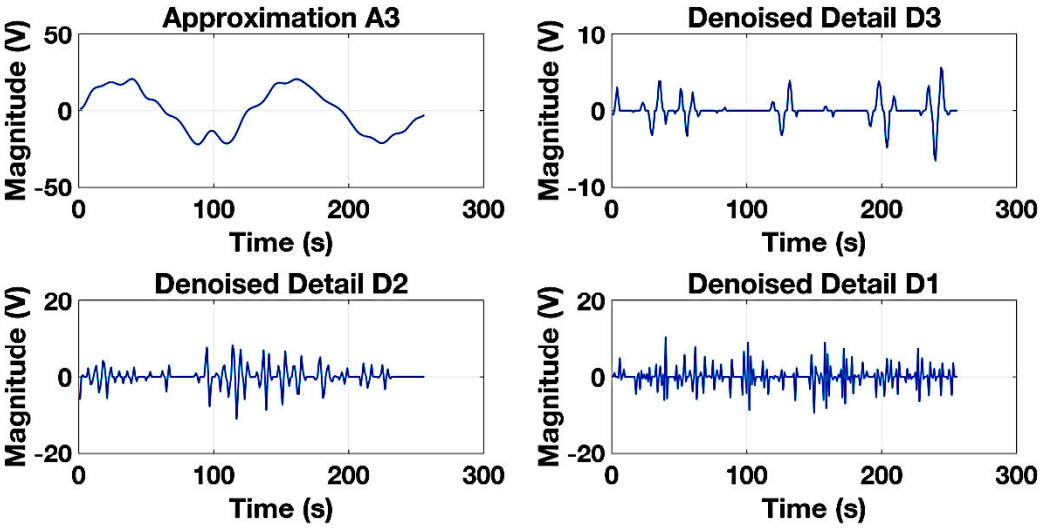

Figure 2-17. The denoised detail coefficients by the universal threshold.

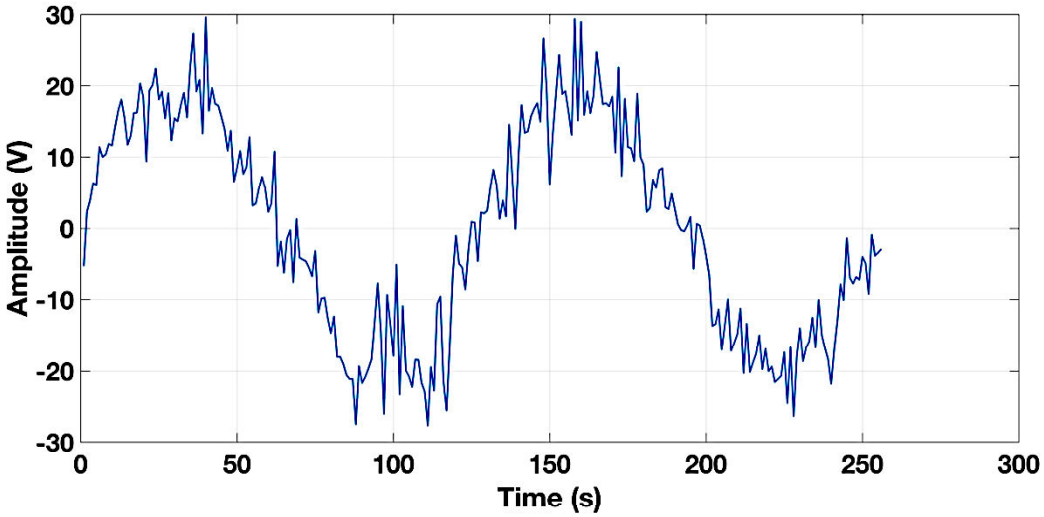

Figure 2-18. The denoised signal via DWT approach (SNR = 8.40 dB).

2.5 Application

The performances of the three methods will now be compared with test cases defined in the first part that will be used along this thesis. A cable with non-fault and a cable with one fault will be tested.

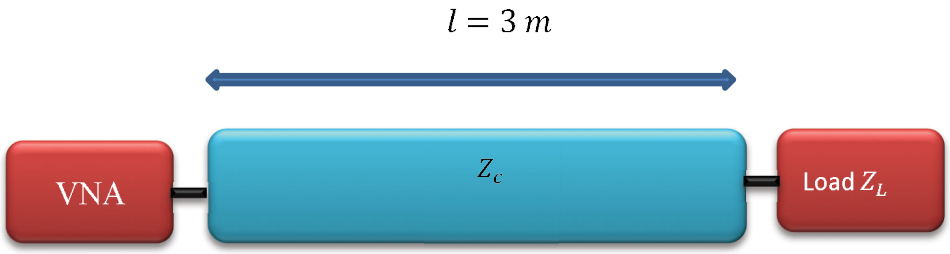

Figure 2-19. An open circuit with three meters nominal cable.

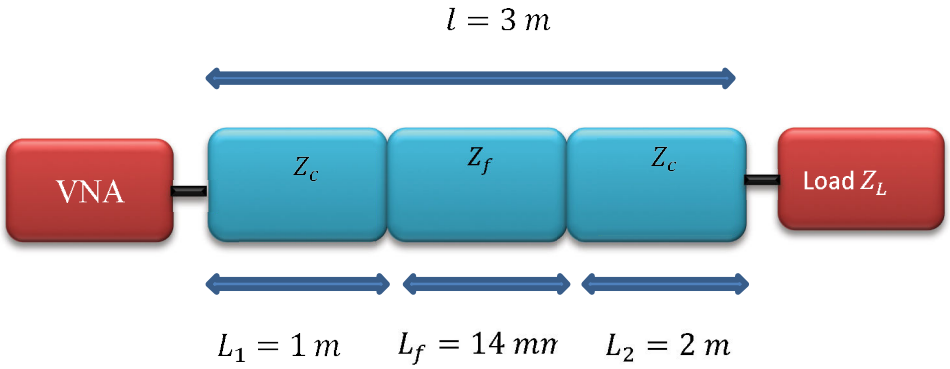

Figure 2-20. An open circuit with three meters cable with one fault at 1 m.

EMD

To test the EMD, the LMD, and the DWT denoising methods, we performed numerical simulations for the reflected test signal obtained from the coaxial cable with one chafing fault as shown in Figure 1-23, and Figure 2-20. First, we test the EMD method. For that, we apply the algorithm shown in Figure 2-1. Our input signal is the reflected signal (Figure 1-23)

whose $SNR_{noisy\_f} = 10\ dB$ and the $SNR_{noisy\_interval\_f} = 2.77\ dB$ which represents the SNR for the fault interval defined as [0.5-1.6] m. The EMD method decomposes this signal into eleven Intrinsic Mode Function (IMFs), because after eleven iterations, the residual is non-oscillating signal which stops the EMD algorithm. In Figure 2-21, one can remark that the first IMF corresponds to fast oscillation while the eleventh IMF corresponds to slow oscillation. As a reminder, the proposed method is divided into three steps. First, the signal is decomposed into different IMFs. Second, the first IMF is eliminated because it contains the maximum of the noise. Finally, the signal is reconstructed after removing the first IMF. Figure 2-22 displays the outcomes of applying the EMD denoising scheme to the one-fault reflected signal after eliminating the First IMF. Its $SNR_{denoised\_EMD} = 13\ dB$ which is obviously higher than $SNR_{noisy\_f} = 10\ dB$. Therefore, using the EMD method, The SNR has 3 dB improvement. In addition, in order to examine and improve the EMD performances, we consider a 3-m nominal cable (Figure 2-19) which has the same topology as the one-fault cable illustrated in Figure 2-20. In this time, for the EMD decomposition, our input signal is the reflected signal at the entry of the three meters nominal cable. Its signal noise ratio SNR_{noisy} equals the signal noise ratio of the one-fault cable, $SNR_{noisy} = SNR_{noisy\_f} = 10\ dB$. Moreover, the generated noise is the same than the one with the one-fault cable. We apply the algorithm shown in Figure 2-1 to our new input signal. After that, we reconstruct the signal by removing the first IMF as depicted in Figure 2-23. Then, we subtract the reconstructed reflected signal at the entry of the 3 meters one-fault cable (Figure 2-22) from this reconstructed signal. We obtain the signal shown in Figure 2-24. After that, we calculate the signal noise ratio SNR_{subs_EMD} of this signal only for the fault interval defined as [0.5-1.6] m in order to extract and detect the soft fault regarding the noise. The $SNR_{subs\_EMD} = 23\ dB$, as a result, the fault amplitude is higher than the noise level. Therefore, we detect the fault better than using only the time domain reflectometry without the denoising methods. Besides, the EMD method creates some side effects at the beginning and the end of each signal's peak. However, if $SNR_{noisy\_f} = 5\ dB$, there is no way to denoise satisfactorily the soft fault as it is illustrated in Figure 2-25 because the $SNR_{denoised\_EMD} = 5.81\ dB$. Although if we subtract this denoised signal from the denoised signal of the nominal cable, we detect the fault as shown in Figure 2-26 because the $SNR_{subs\_EMD} = 24.15\ dB$, this substraction is not realisable in real time because we could not generate the same noise for the both signals (nominal cable, and one-fault cable). Nevertheless, the solution could be measuring the reflected signal of the nominal cable several times. Then, we calculate the mean amplitude of the signal which is decomposed and reconstructed, after that, by the EMD algorithm. After that, we subtract it from the reconstructed reflected signal at the one fault cable entry.

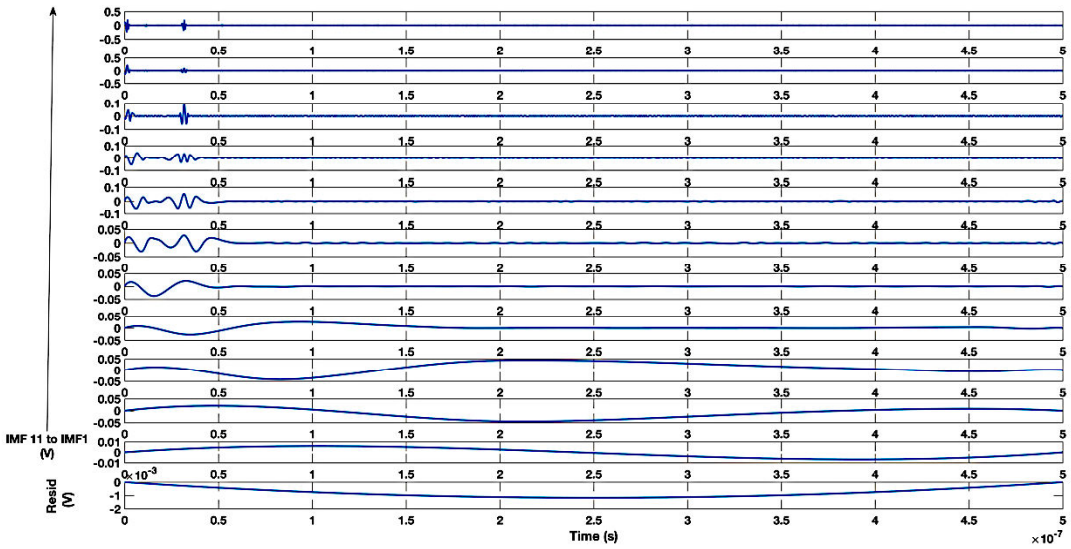

Figure 2-21. EMD decomposition over the time into eleven levels (IMFi, i∈[1,11]) of noisy reflected signal in 3 m coaxial cable with one chafing fault at 1 m ($SNR_{noisy\_f} = 10\ d\ B$).

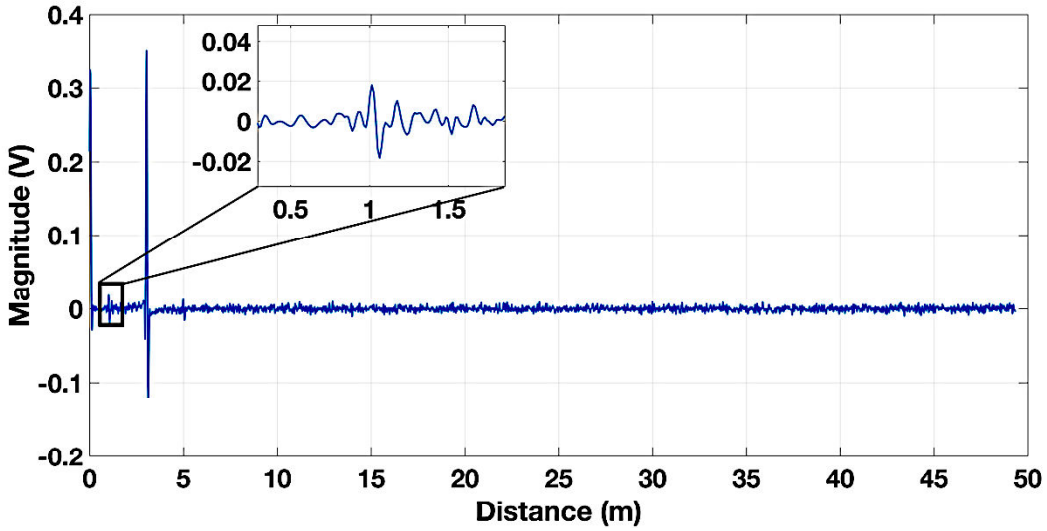

Figure 2-22. The denoised signal of 3 m coaxial cable with one chafing fault at 1 m via EMD method ($SNR_{noisy\_f} = 10\ dB, SNR_{denoised\_EMD} = 13\ dB$).

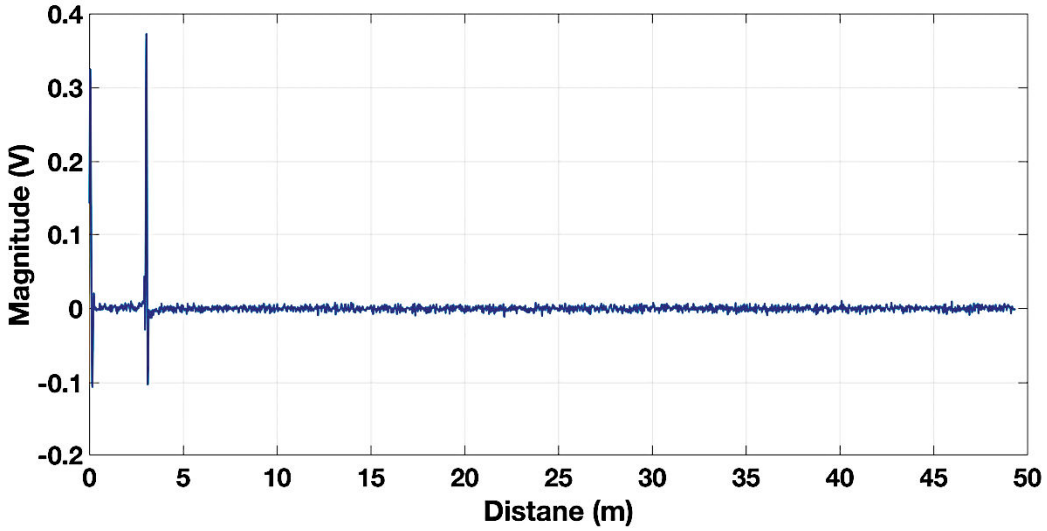

Figure 2-23. The denoised signal of 3 m nominal coaxial cable via EMD method ($SNR_{noisy\_f} = 10\,dB$).

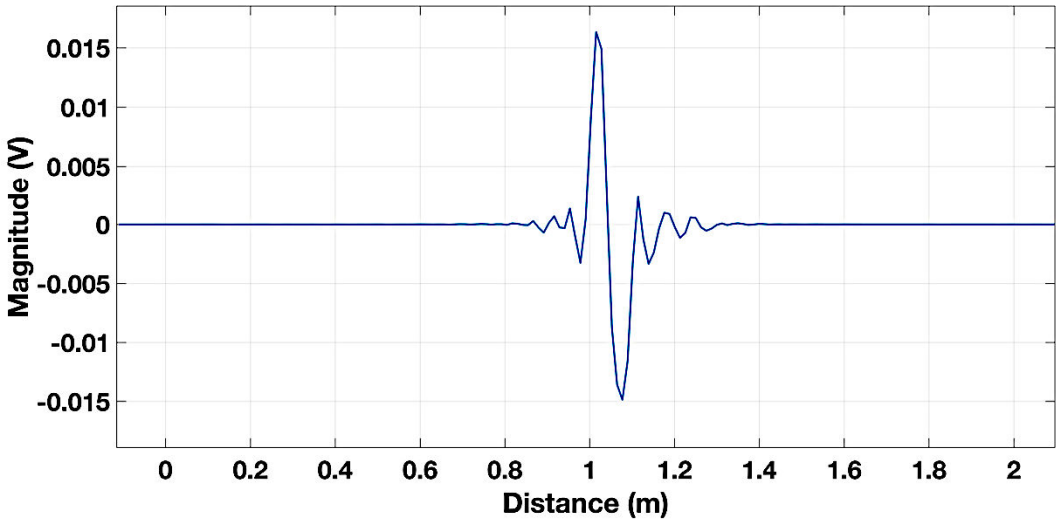

Figure 2-24. The subtraction between the reconstructed reflected signal at the entry of the 3 meters faulty cable and the reconstructed reflected signal at the entry of the 3 meters nominal cable ($SNR_{noisy\_f} = 10\,dB, SNR_{subs\_EMD} = 23\,dB$).

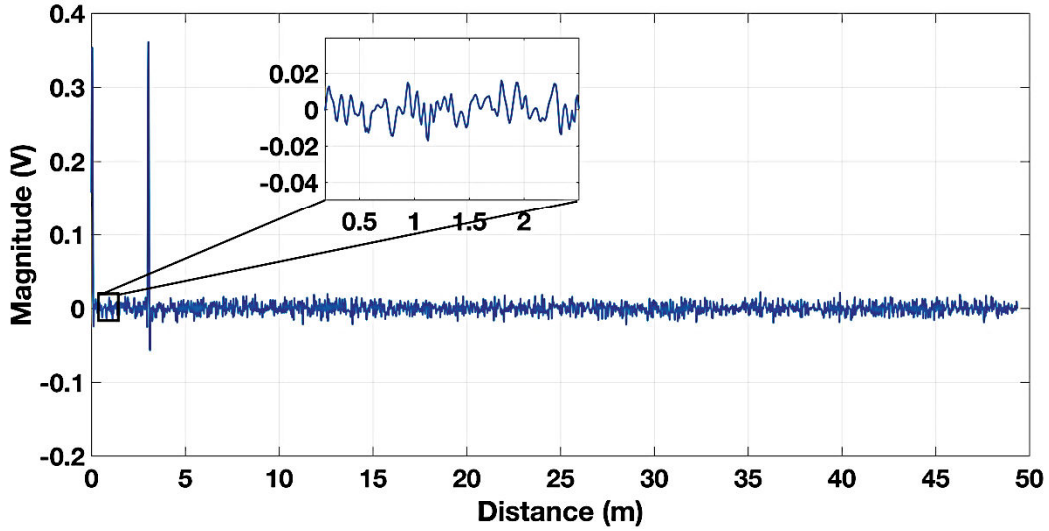

Figure 2-25. The denoised signal of 3 m coaxial cable with one chafing fault at 1 m whose $SNR_{noisy\_f} = 5\,dB$ via EMD method ($SNR_{denoised\_EMD} = 5.81\,dB$).

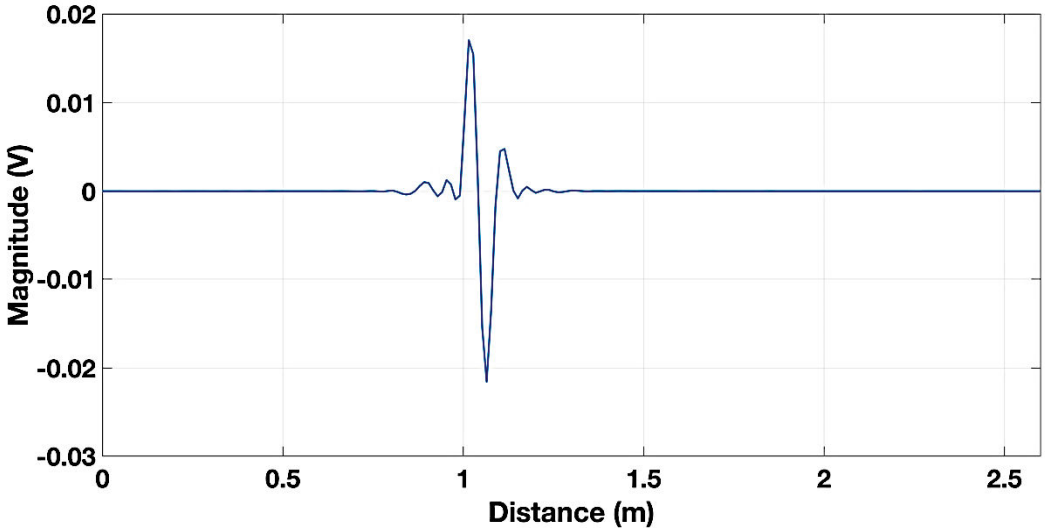

Figure 2-26. The subtraction between the reconstructed reflected signal at the entry of the 3 meters faulty cable and the reconstructed reflected signal at the entry of the 3 meters nominal cable ($SNR_{noisy\_f} = 5\,dB, SNR_{subs\_EMD} = 24.15\,dB$).

LMD

In this section, LMD was employed to the reflected test signal obtained from the coaxial cable with one chafing fault as shown in Figure 1-23, and Figure 2-20. For that, we apply the algorithm shown in Figure 2-6. Our input signal is the reflected signal (Figure 1-23) whose $SNR_{noisy\_f} = 10\,dB$ and the $SNR_{noisy\_interval\_f} = 2.77\,dB$ which represents the SNR for the fault interval defined as [0.5-1.6] m. The LMD method decomposed this signal into six product functions (PFs), because after six iterations, the residual is monotonic and non-oscillating signal which stops the algorithm. In Figure 2-27, the first PF corresponds to fast oscillation while the sixth PF corresponds to slow oscillation. The LMD follows the same process as the EMD. It is divided into three steps. First, the decomposition of the signal into different PFs. Second, the elimination of the first PF because it contains the maximum of the

noise. Finally, the reconstruction of the signal after removing the first PF. Figure 2-28 displays the outcomes of applying the LMD denoising scheme to the one-fault reflected signal after removing the First PF. Its $SNR_{denoised\_LMD} = 12.62\,dB$ which is higher than SNR_{noisy_f} but lower than the one computed by the EMD method ($SNR_{denoised\_EMD} = 13\,dB$). As the EMD method, in order to examine and improve the LMD performances, we consider also a three meters nominal cable (Figure 2-19) which has the same topology as the one-fault cable illustrated in Figure 2-20. We apply the same process and the same signal with the same noise used in the EMD method. After subtracting the reconstructed reflected signal at the entry of the 3 meters one-fault cable from the reconstructed reflected signal at the entry of the 3 meters nominal cable. We obtain the signal shown in Figure 2-29. Its $SNR_{subs\_LMD} = 7.35\,dB$, as a result, the fault amplitude is higher than the noise level. Therefore, we detect the fault better than using only the time domain reflectometry ($SNR_{noisy\_interval\_f} = 2.77\,dB$). However, it is worse than SNR_{subs_EMD}.

However, if $SNR_{noisy\_f} = 5\,dB$, there is no way to denoise satisfactorily the soft fault as it is illustrated in Figure 2-30 because the $SNR_{denoised\_LMD} = 6.32\,dB$. Indeed, if we subtract this denoised signal from the denoised signal of the nominal cable, we detect the fault as shown in Figure 2-31 because the $SNR_{subs\_LMD} = 5.46\,dB$.

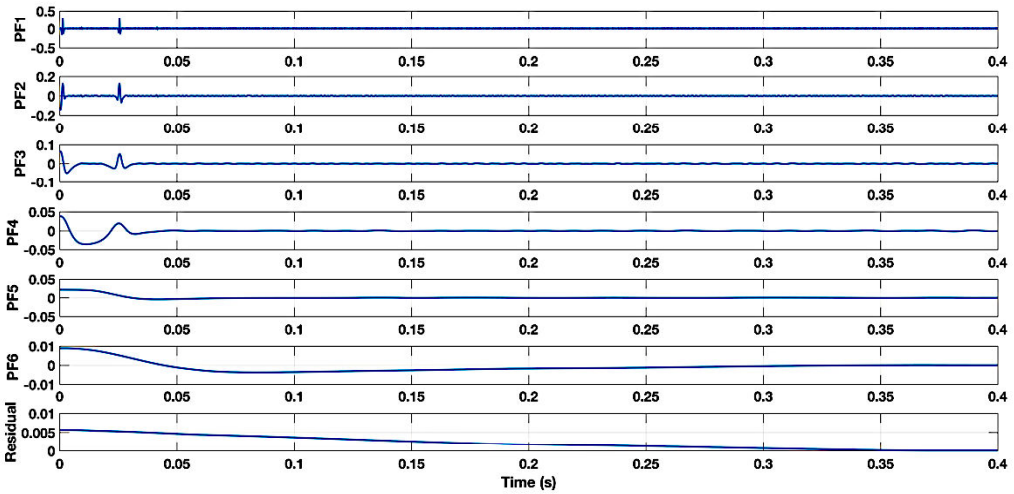

Figure 2-27. LMD decomposition of noisy reflected signal in 3-m coaxial cable with one chafing fault at 1 m into five levels (PFi, i∈[1,6]) and the residue coefficient ($SNR_{noisy\_f} = 10\,dB$).

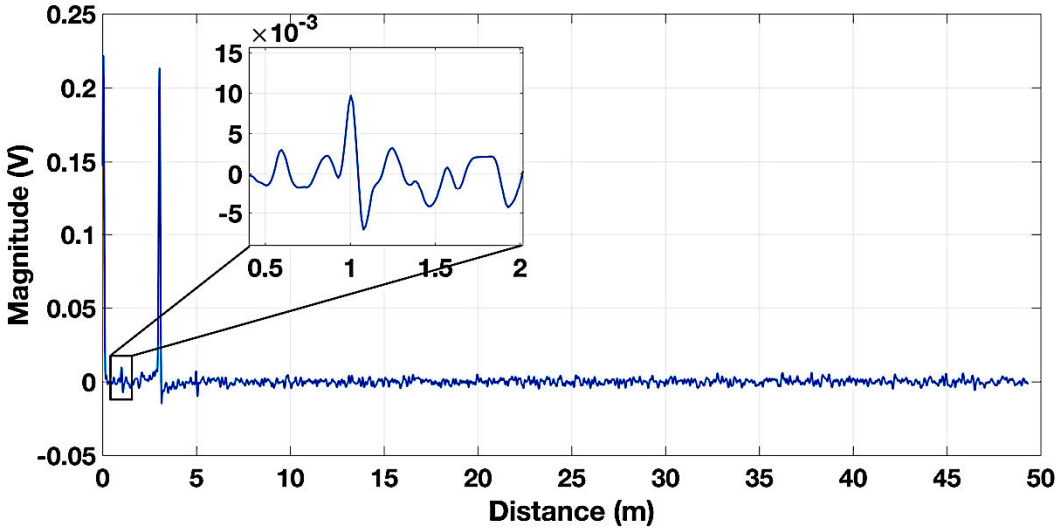

Figure 2-28. The denoised signals of 3 m coaxial cable with one chafing fault at 1 m via LMD method ($SNR_{noisy\_f} = 10\,dB, SNR_{denoised\_LMD} = 12.62\,dB$).

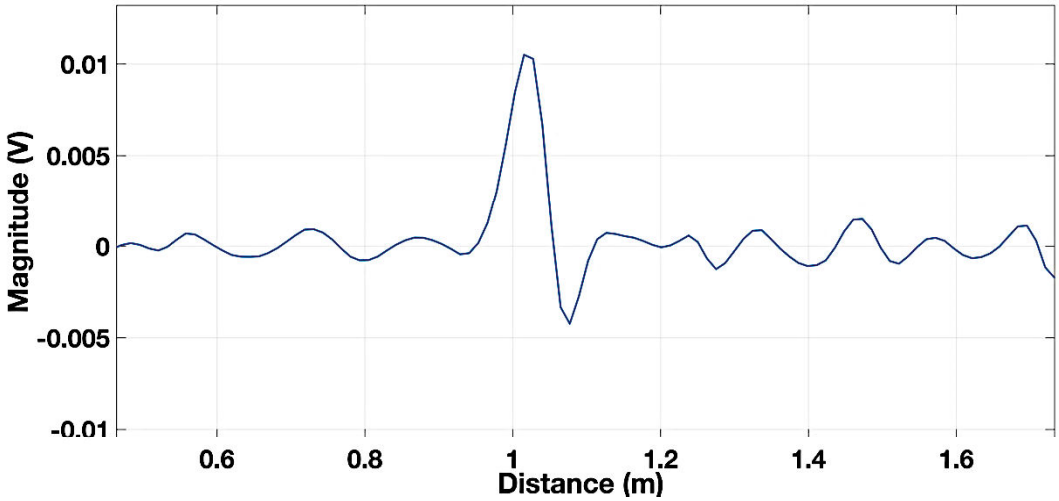

Figure 2-29. The subtraction between the reconstructed reflected signal at the entry of the 3 meters faulty cable and the reconstructed reflected signal at the entry of the 3 meters nominal cable ($SNR_{noisy\_f} = 10\,dB, SNR_{subs\_LMD} = 7.35\,dB$).

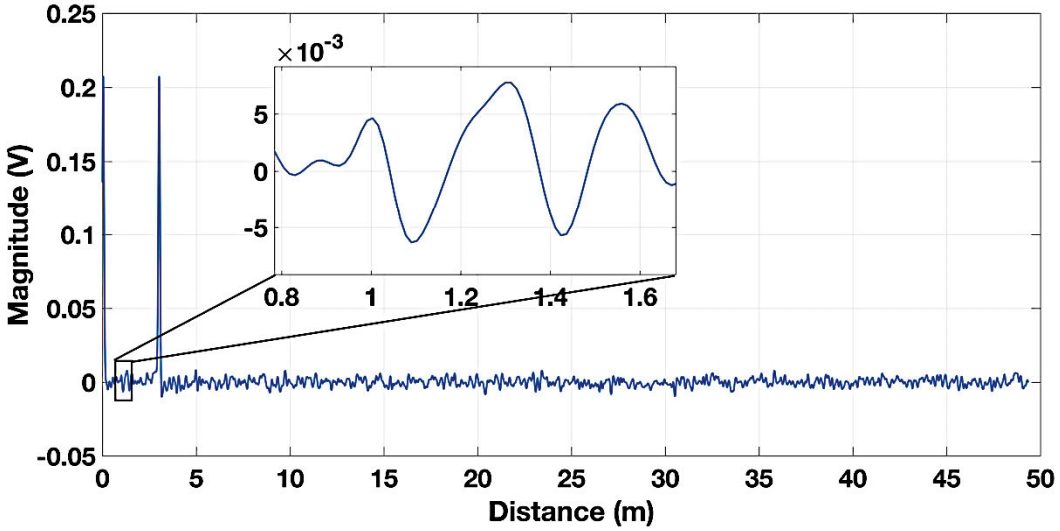

Figure 2-30. The denoised signals of 3 m coaxial cable with one chafing fault at 1 m via LMD method ($SNR_{noisy\_f} = 5\ dB, SNR_{denoised\_LMD} = 6.32\ dB$).

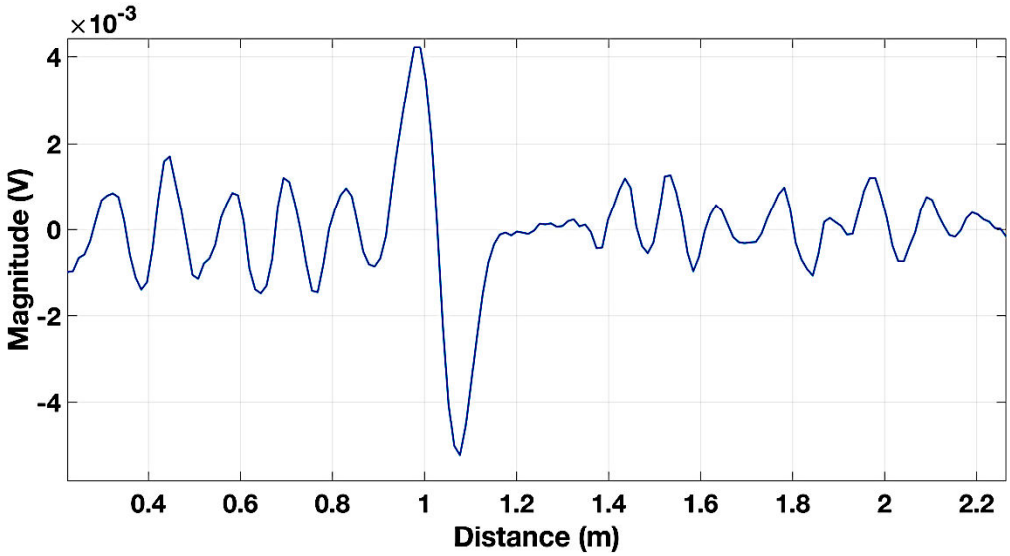

Figure 2-31. The subtraction between the reconstructed reflected signal at the entry of the 3 meters faulty cable and the reconstructed reflected signal at the entry of the 3 meters nominal cable ($SNR_{noisy\_f} = 5\ dB, SNR_{subs\_LMD} = 5.46\ dB$).

DWT

After tested the LMD and the EMD on the cable with one fault, The DWT operated on the reflected test signal obtained from the coaxial cable with one chafing fault as shown in Figure 1-23, and Figure 2-20. For that, we choose the Daubechies with thirteen moments as the mother wavelet. The wavelet decomposition consists in decomposing the tested signal into low-pass h and high-pass filter g. In Figure 2-32, D1 which is the first detail coefficient, corresponds to the decomposition of the signal by the first high-pass filter. D2 which is the second detail coefficient, corresponds to the decomposition of the signal by the first low-pass filter and then by the high-pass filter. D3 which is the third detail coefficient, corresponds to the decomposition of the signal by the two low-pass filters and then by the high-pass filter. A3 is the result of decomposition of the signal by the three low-pass filters. This method aims to

denoising the signal. For that, the process splits into three steps: First, we choose the mother wavelet, then the signal is decomposed into different detail coefficients. Second, we choose the threshold and apply it to all detail coefficients. Finally, reconstruct the signal after thresholding it. Figure 2-33 displays the outcomes of applying the DWT denoising scheme to the one-fault reflected signal after thresholding the detail coefficients (D1, D2, D3) by the universal threshold defined in (2.14). Its $SNR_{denoised\_DWT} = 10.20\,dB$ which is higher than SNR_{noisy_f} but lower than $SNR_{denoised\_EMD} = 13\,dB$ and $SNR_{denoised\_LMD} = 12.62\,dB$. As the previous methods, in order to examine and improve the DWT performances, we consider also a three meters nominal cable (Figure 2-19). We apply the same process and the same signal with the same noise used in the previous methods. After subtracting the reconstructed reflected signal at the entry of the 3 meters one-fault cable from the reconstructed reflected signal at the entry of the 3 meters nominal cable. We obtain the signal shown in Figure 2-34. Its $SNR_{subs\_DWT} = 0\,dB$, which means that the DWT method considers this chafing fault as a noise that it should remove.

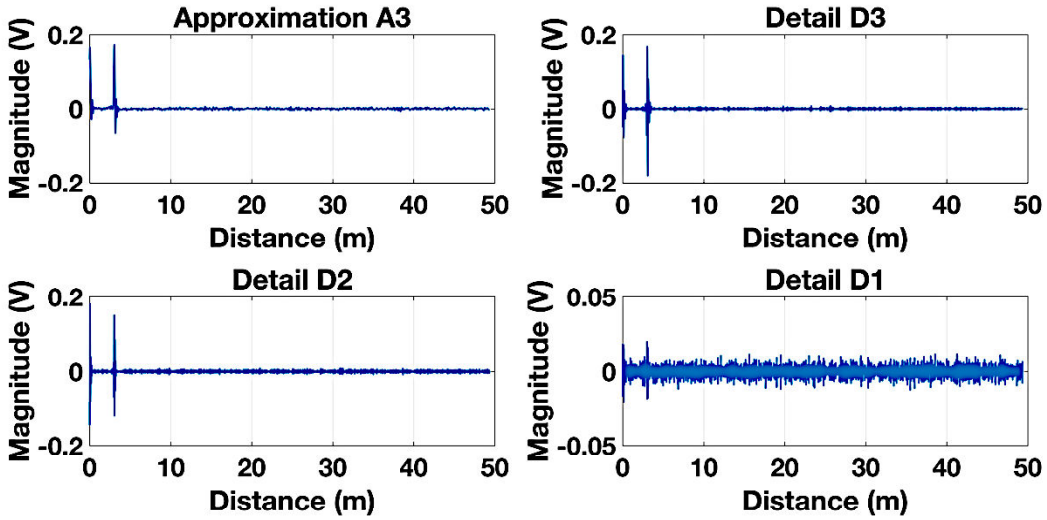

Figure 2-32. The DWT decomposition into three levels (Di, i∈[1,3]) of the noisy reflected signal from 3 m coaxial cable with one chafing fault at 1 m ($SNR_{noisy\_f} = 10\,dB$).

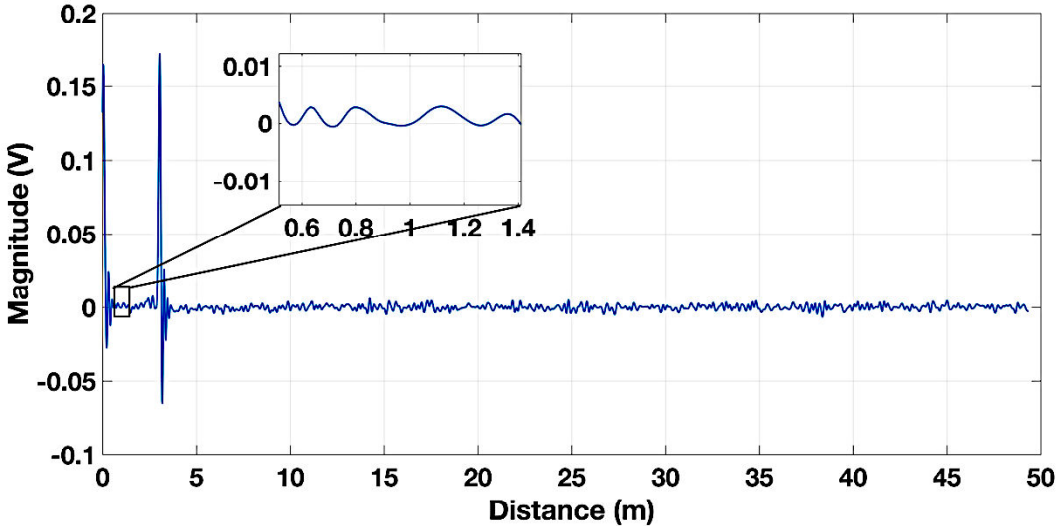

Figure 2-33. The denoised signal from 3 m coaxial cable with one chafing fault at 1 m via DWT method ($SNR_{noisy\_f} = 10\,dB, SNR_{denoised\_DWT} = 10.20\,dB$).

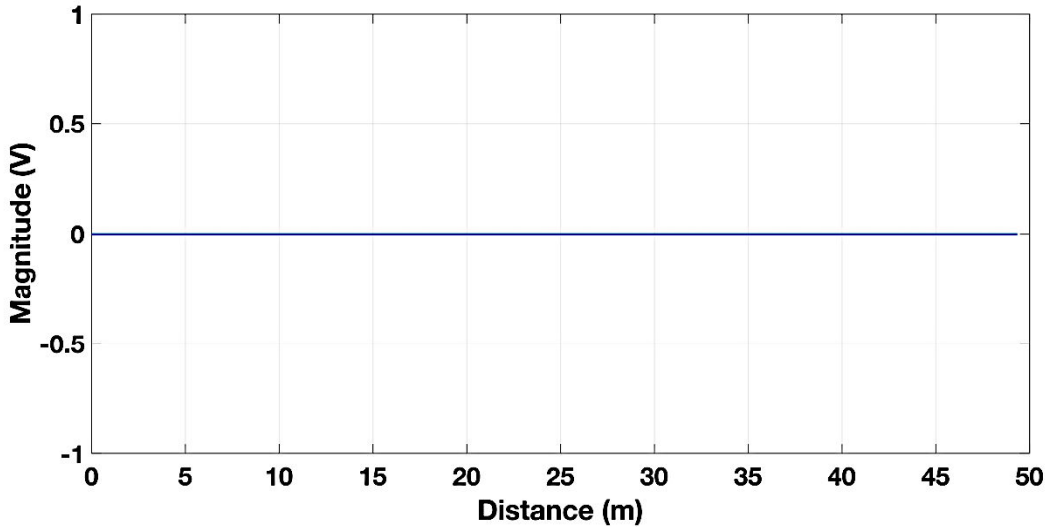

Figure 2-34. The subtraction between the reconstructed reflected signal at the entry of the 3 meters faulty cable and the reconstructed reflected signal at the entry of the 3 meters nominal cable ($SNR_{noisy\_f} = 10\ dB, SNR_{subs\_DWT} = 0\ dB$).

To compare between the EMD, the LMD, and the DWT denoising methods, we tested them on a complicated case regarding the first one. We performed numerical simulations for the reflected test signal obtained from the coaxial cable with two chafing faults, as shown in Figure 2-35 and, for the three methods, our input signal that is the reflected signal illustrated in Figure 1-23 whose $SNR_{noisy\_f} = 10\ dB$ and $SNR_{noisy\_interval\_f}[2,9] = 2.5\ dB$. For this signal, we apply the EMD algorithm, the LMD algorithm and the DWT. Figure 2-36 displays the outcomes of applying the EMD denoising scheme whose $SNR_{denoised\_EMD} = 15.32\ dB$ after removing the first IMF. Figure 2-38 depicts the reconstructed reflected signal via the LMD method after removing the first PF, $SNR_{denoised\_LMD} = 13.6\ dB$ which is lower than $SNR_{denoised\_EMD} = 15.32\ dB$.

For the DWT method, Figure 2-40 displays the outcomes of applying the DWT denoising scheme to the two-faults reflected signal after thresholding the detail coefficients (D1, D2, D3) by the universal threshold. Its $SNR_{denoised\_DWT} = 10.18\ dB$. Which is lower than $SNR_{denoised\_EMD} = 15.32\ dB$. As a consequence, we detect the fault better than using only the time domain reflectometry but barely which confirm that the refelectometry is a limited method to detect the soft fault. In order to compare between the three methods' detection performances, we apply the same process used in the cable with one fault. We consider a 10 m nominal cable which has the same topology as the two faults cable. Its signal noise ratio SNR_{noisy} equals the signal noise ratio of the one-fault cable, $SNR_{noisy} = SNR_{noisy\_f} = 10\ dB$. Moreover, the generated noise is the same than the one with the one-fault cable. We apply the three approaches to our new input signal. After that, we reconstruct the signal by eliminating the first IMF for EMD, the first PF for LMD and filtered the DWT's detail coefficients by the universal threshold. Then, we subtract the reconstructed reflected signal at the entry of the 10 m two-faults cable of each method from the reconstructed reflected signal at the entry of the 10 m nominal cable of each method. for DWT, the signal noise ratio $SNR_{subs\_DWT} = 0\ dB$ of the signal shown in Figure 2-41, as a consequence, we cannot detect

the soft fault. For LMD, and EMD, the signal noise ratio $SNR_{subs\_LMD} = 17\,dB$, and $SNR_{subs\_EMD} = 24\,dB$, respectively, of the signal shown in Figure 2-39, and Figure 2-37 respectively. As a result, for the both methods, the fault amplitude is higher than the noise level, however EMD is better than LMD because $SNR_{subs\_LMD} < SNR_{subs\_EMD}$.

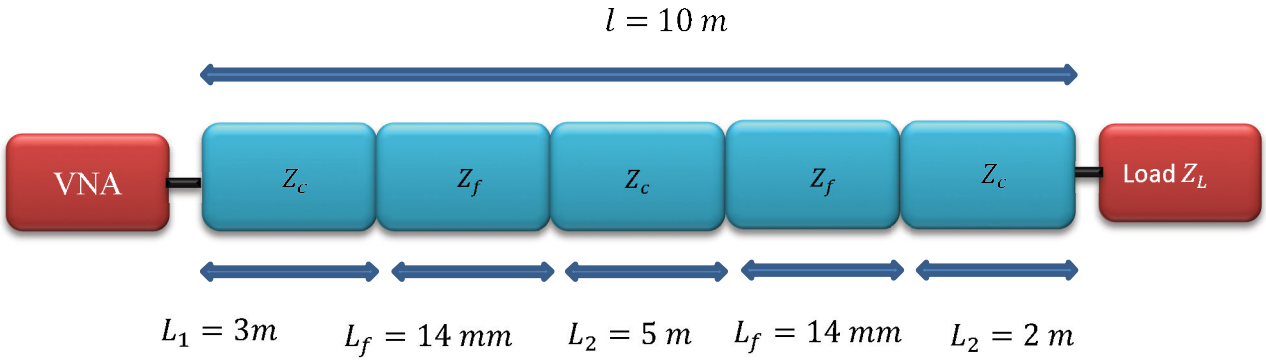

Figure 2-35. Ten meters cable with two faults with 14 mm length at 3 m and 8 m. It is an Open circuit.

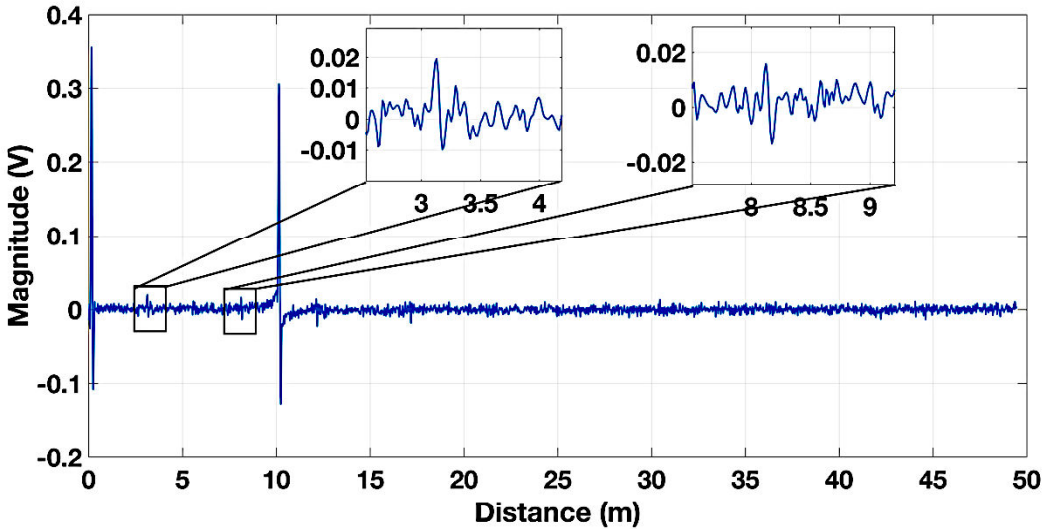

Figure 2-36. The denoised signal from 10 m coaxial cable with two chafing faults at 3 m and 8 m via EMD method ($SNR_{noisy\_f} = 10\,dB$, $SNR_{denoised\_EMD} = 15.32\,dB$).

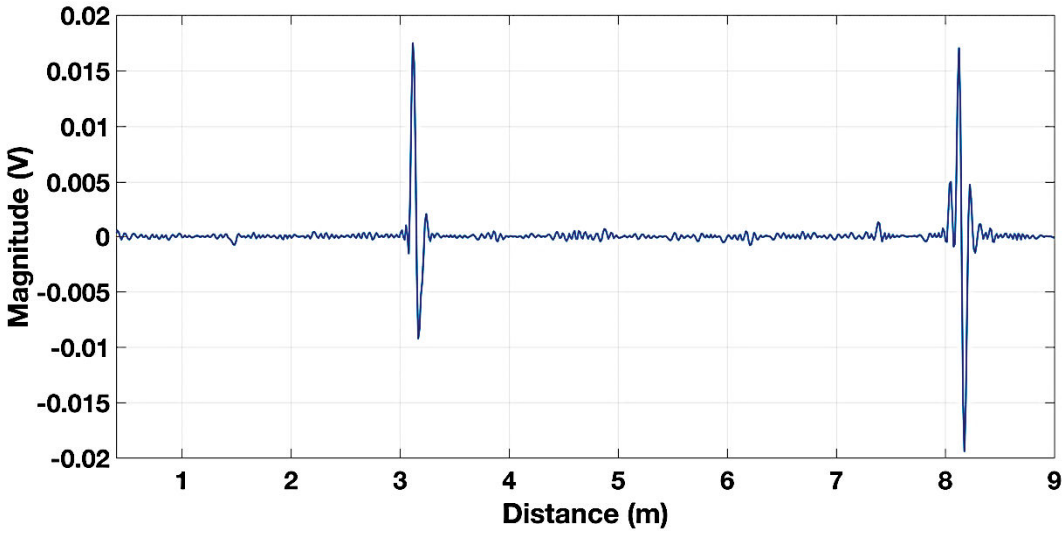

Figure 2-37. The subtraction between the reconstructed reflected signal via EMD at the entry of the 10 meters faulty cable and the reconstructed reflected signal via EMD at the entry of the 10 meters nominal cable ($SNR_{noisy\_f} = 10\,dB, SNR_{subs\_EMD} = 24\,dB$).

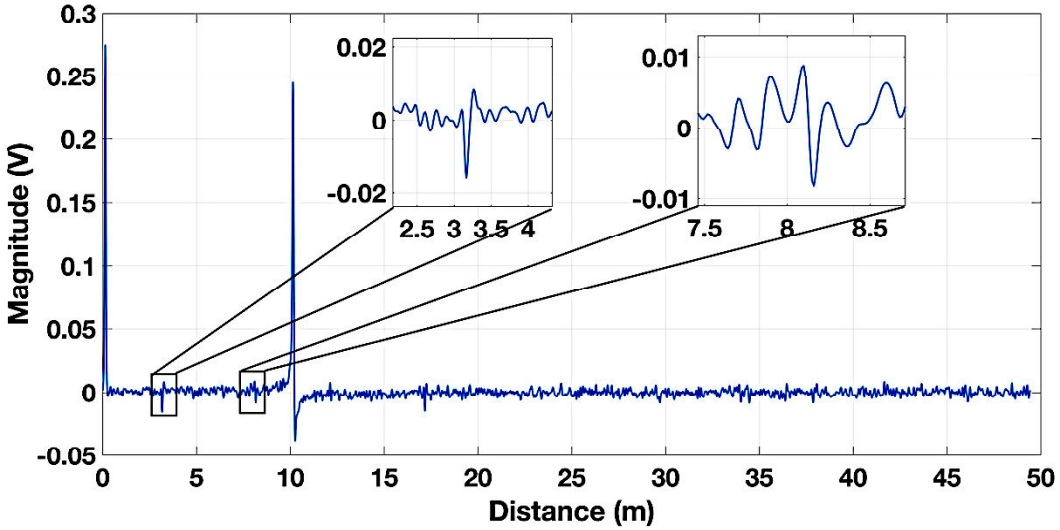

Figure 2-38. The denoised signal from 10 m coaxial cable with two chafing faults at 3 m and 8 m via LMD method ($SNR_{noisy\_f} = 10\,dB, SNR_{denoised\_LMD} = 13.6\,dB$).

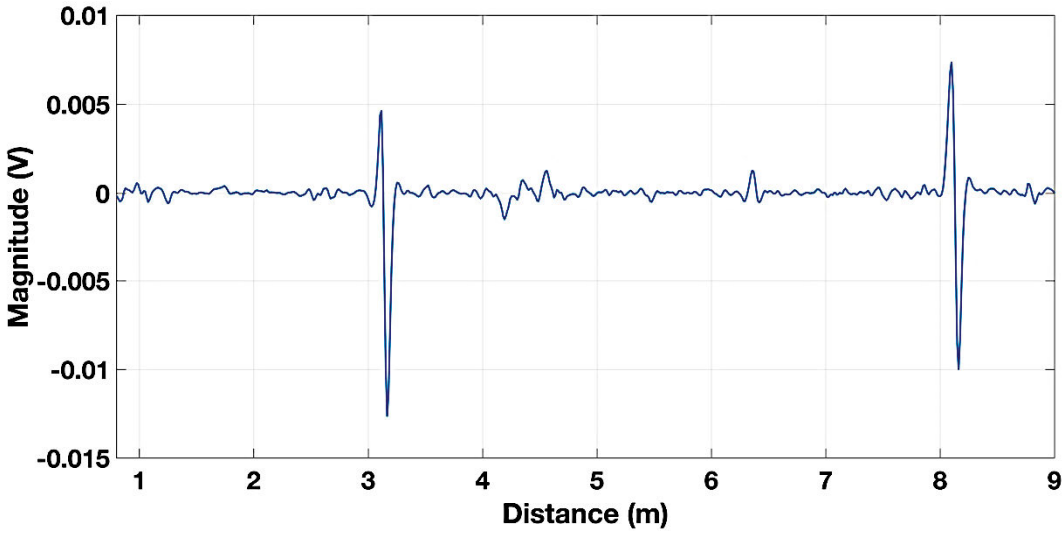

Figure 2-39. The subtraction between the reconstructed reflected signal via LMD at the entry of the 10 meters faulty cable and the reconstructed reflected signal via LMD at the entry of the 10 meters nominal cable ($SNR_{noisy\_f} = 10\,dB, SNR_{subs\_LMD} = 17\,dB$).

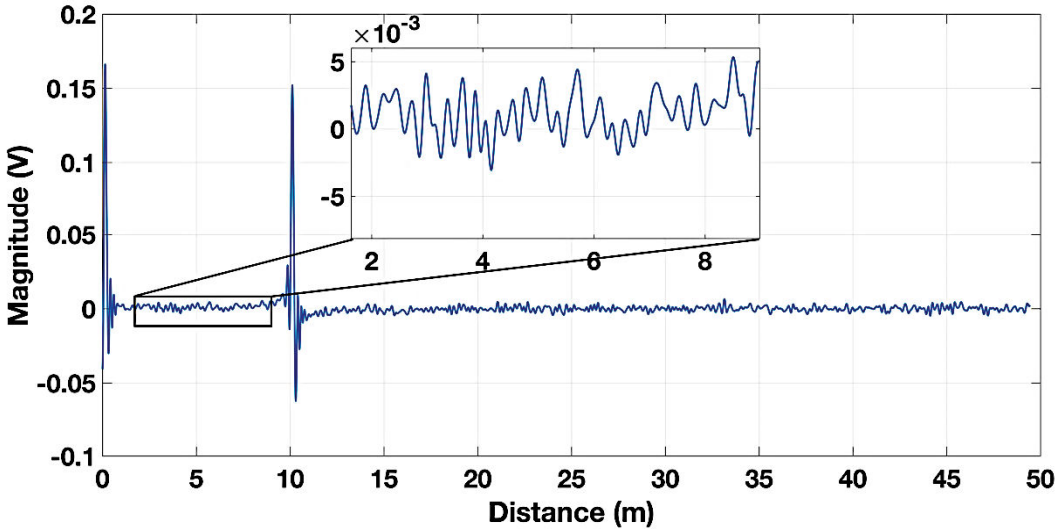

Figure 2-40. The denoised signal from 10 m coaxial cable with two chafing faults at 3 m and 8 m via DWT method ($SNR_{noisy\_f} = 10\,dB, SNR_{denoised\_DWT} = 10.18\,dB$).

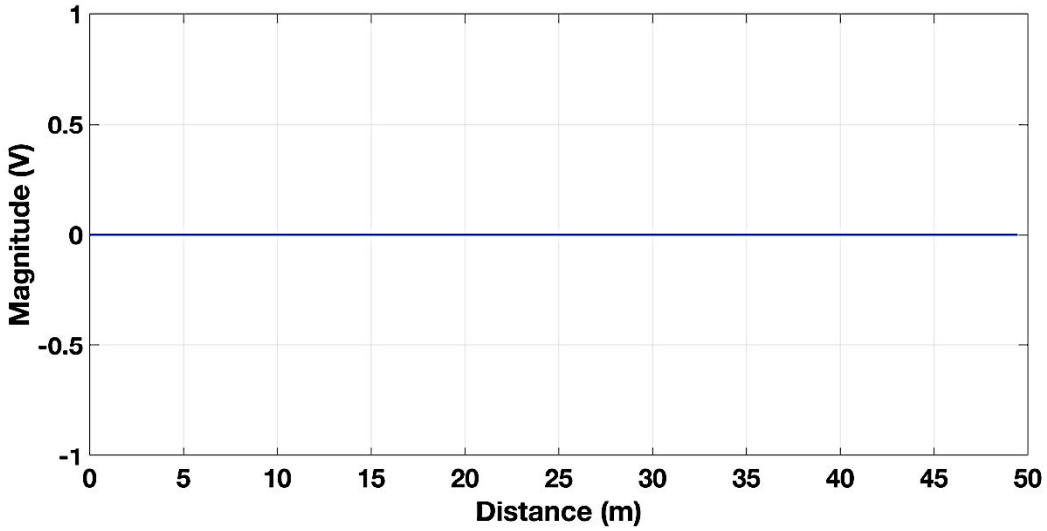

Figure 2-41. The subtraction between the reconstructed reflected signal via DWT at the entry of the 10 meters faulty cable and the reconstructed reflected signal via DWT at the entry of the 10 meters nominal cable ($SNR_{noisy\_f} = 10\,dB, SNR_{subs\_DWT} = 0\,dB$).

To sum up, In this section, first, we applied the EMD, LMD and the DWT on a signal for several SNR ($SNR_{noisy\_f} = 10\,dB$, $SNR_{noisy\_f} = 5\,dB$). Second, we decompose it into several blocks as IMFs for EMD, and PFs for LMD, or to several detail coefficients for DWT. Third, we threshold these sub-functions, either by remove the first IMF or PF for EMD and LMD, respectively, or by filtering all the detail coefficients for DWT by the universal threshold. After that, we reconstruct the reflected signal after filtering. For $SNR_{noisy\_f} = 10\,dB$, using EMD, $SNR_{denoised\_EMD} = 13\,dB$ for one fault cable, and $SNR_{denoised\_EMD} = 15.32\,dB$ for two faults cable. Using LMD, $SNR_{denoised\_LMD} = 12.62\,dB$ for one fault cable, and $SNR_{denoised\_LMD} = 13.6\,dB$ for two faults cable. For DWT, $SNR_{denoised\_DWT} = 10.20\,dB$ for one fault cable, and $SNR_{denoised\_DWT} = 10.18\,dB$ for two faults cable. For $SNR_{noisy\_f} = 5\,dB$, using EMD, $SNR_{denoised\_EMD} = 5.81\,dB$ for one fault cable. For LMD, $SNR_{denoised\_LMD} = 6.32\,dB$ for one fault cable. For DWT, $SNR_{denoised\_DWT} = 5.43\,dB$ for one fault cable. Fourth, for each method, we subtract this reflected signal from the reconstructed reflected signal of a nominal cable whose topology is the same as the faulty cable. Finally, for each method, we calculate the SNR of the result as shown in Table 2-1. For both case, the cable with one fault and the cable with two faults, SNR_{subs_EMD} is higher than SNR_{subs_LMD} and the SNR_{subs_DWT}. As a result, for the EMD, the fault amplitude is higher than the noise level. Consequently, we detect the fault better than using only the time domain reflectometry or LMD or DWT. However, this subtraction is not realisable in real time because we could not generate the same noise for the both signals (nominal cable, and fault cable). Nevertheless, the solution could be measuring the reflected signal of the nominal cable several times. Then, we calculate the mean amplitude of the signal which is decomposed and reconstructed, after that, by the EMD algorithm. After that, we subtract it from the reconstructed reflected signal at the fault cable entry.

Table 2-1. The comparison between the $SNR_{denoised}$ for different SNR_{noisy}.

	EMD	LMD	DWT
Coaxial cable with one chafing fault. $SNR_{noisy\_f} = 10\ dB$	$SNR_{denoised\_EMD} = 13\ dB$	$SNR_{denoised\_LMD} = 12.62\ dB$	$SNR_{denoised\_DWT} = 10.20\ dB$
	$SNR_{subs\_EMD} = 23\ dB$	$SNR_{subs\_LMD} = 7.35\ dB$	$SNR_{subs\_DWT} = 0\ dB$
Coaxial cable with one chafing fault. $SNR_{noisy\_f} = 5\ dB$	$SNR_{denoised\_EMD} = 5.81\ dB$	$SNR_{denoised\_LMD} = 6.32\ dB$	$SNR_{denoised\_DWT} = 5.43\ dB$
	$SNR_{subs\_EMD} = 24.15\ dB$	$SNR_{subs\_LMD} = 5.46\ dB$	$SNR_{subs\_DWT} = 0\ dB$
Coaxial cable with two chafing faults. $SNR_{noisy\_f} = 10\ dB$	$SNR_{denoised\_EMD} = 15.32\ dB$	$SNR_{denoised\_LMD} = 13.6\ dB$	$SNR_{denoised\_DWT} = 10.18\ dB$
	$SNR_{subs\_EMD} = 24\ dB$	$SNR_{subs_{LMD}} = 17\ dB$	$SNR_{subs\_DWT} = 0\ dB$

2.6 Conclusion

This chapter investigated noise models and included an in-depth literature survey of denoising based on level decomposition. Desirable features and complexities of denoising algorithms were discussed. In addition, common mechanisms used to evaluate the performance of denoising algorithms were explained. According to the current literature, denoising algorithms based on EMD are the best choice for achieving the desired performance. However, the computational complexity must also be considered.

The EMD decomposition can be determined approximately by calculating the mean of two curves generated by local maxima and local minima of the signal. The decomposition performance of EMD is improved by the movement of any extremum point involved in the first IMF in the iteration process. It can be found that the residual tends to zero with the increase of iteration times, which makes the process converge quickly. With this consideration, the EMD algorithm has good robustness. EMD does, however, have a major drawback: the side effects.

LMD is an adaptive method of signal processing like EMD. The difference is in the behaviour of the IMF at each level. LMD has shown promising results in convergence but failed to denoise the soft fault signal properly. This method has the same drawbacks as EMD.

Thresholding techniques using the DWT are the simplest to implement. DWT decomposition is the construction of the detail and approximation coefficient. The wavelet transform provides a high degree of flexibility in its properties and performance. Fixing the wavelet and its parameters would eliminate this flexibility.

To sum up, in this study, the denoised results of the proposed algorithms are compared under different cable models. The evaluation methods introduced above indicated that the DWT and LMD failed to denoise properly the reflected signals, while EMD shows promising results with some limitations. As a result, EMD is the method that we retain at the following. With this in mind, the next chapter recalls the basic principles of detecting wiring faults via time–frequency analysis and presents some of the simulation results. Accordingly, the limitations of time–frequency methods in detecting multiple faults are illustrated.

Chapter 3: Time-Frequency Analysis

3 Time–frequency analysis

3.1 Introduction

As discussed in previous sections, the signals carrying information into transmission lines can be classified into two categories: stationary and non-stationary signals [110]. In the first type, the signal frequency content does not change over time, while it is not the case in the second kind, non-stationary signals can be encountered in speech and vibrations. Because of the non-stationary characteristic of these latter signals, a Fourier transformation cannot be performed. Moreover, a frequency domain analysis would not provide information about the changing frequencies over time [111].

Representations of the stationary noisy signals can be carried out in two ways: in the time domain, in which voltage or current levels are represented versus time or in the frequency domain by replacing oneself by the spectral domain. The relation between the two combined domains is the Fourier transform [111]. In our case, our signals do not evolve over time on the scale of observation, which means they can be considered as stationary. However, some interesting properties of non-stationary signal processing techniques may be used to have a better detection of soft faults. The recently developed field of time–frequency signal analysis (TFA) provides suitable tools for analysing non-stationary signals occurring in many fields of engineering [112], such as telecommunications, radar, sonar, vibration analysis, biomedicine, speech, and seismic exploration [118]. This chapter approaches such signals using a TFA approach; it outlines many of the important concepts underpinning TFA. The work represented in this chapter is based on some researches made to detect the wiring faults such as [113]-[114]-[115]-[116]-[117]. In addition, the chapter builds upon and refines concepts and results that were originally reported in [119]. Major theoretical breakthroughs in the field of time–frequency methods were accomplished via the Short-Time Fourier transform (STFT), the Wigner–Ville Transform (WVT), and the Continuous Wavelet Transform (CWT) in the context of fault detection. The STFT consists in a segmentation of a signal into narrow time intervals and takes the FT of each one [120]. Each FT provides the spectral information of a separate time-slice of the signal, providing simultaneous time and frequency information. The WVT provides high spectral resolution and is optimal [121] in the sense of energy concentration around the signal instantaneous frequency (IF), for linear frequency modulated (FM) signals. The CWT is a formal tool that provides an overcomplete representation of a signal by letting the translation and scale parameters of the wavelets vary continuously [122].

To understand the effects of time–frequency transforms in detecting wiring faults, this chapter describes the FT and derives the STFT, the WVT, and the CWT. These three time–frequency methods allow us to project the reflected signal at the cable entry in a bidimensional space, the time and frequency domains, as explained in the next sections.

3.2 The Fourier transform

To obtain the frequency content of the electrical signal, we should use many narrow bandpass filters, which is equivalent to modulating the signal in the frequency domain and using one low-pass filter. This is the idea behind frequency analysis and Fourier expansion [123].

Arthur Schuster observed that there were some periodicities in sunspot numbers using Fourier series. This observation in turn helped James Cooley to develop the fast Fourier transform (FFT), the algorithm for which was developed in 1805 by Carl Friedreich Gauss. The FFT is useful for calculating the discrete Fourier series [124]. The Cooley-Turkey algorithm is frequently used for calculating the Fourier Transform in a fast version. It is based on a "divide and rule" approach through recursion. It subdivides a discrete Fourier transform into several discrete Fourier transforms of smaller sizes. This evolution of frequency representation makes the FT an efficient tool for understanding stationary signals.

The FT (3.1) is used to pull original signal frequencies from their combined sum.

$$FT(\omega) = \int_{+\infty}^{-\infty} s(t)e^{-i\omega t}\, dt, \tag{3.1}$$

Where s is an integrable function defined on $\mathbb{R}$. FT is the complex Fourier Transform. As the time signal is generally causal, the integration can only be made from 0 to the infinity.
This representation (3.1) corresponds to a signal expansion into the orthogonal family of complex exponentials called FTs. It is a representation of the signal spectrum.
Although the FT is the most useful mathematical tool of signal analysis, it has some limitations, such as not representing the signal in both the time and frequency domains, as shown in the equation (3.1). Moreover, as explained above the FT is not efficient for analysing non-stationary signals, which are considered as the most common signals.
One of the well-known methods used to overcome the FT restrictions is time–frequency analysis using the STFT, the CWT, or the WVT. These approaches are described in the next paragraphs. Then, these methods are applied to a cable under test to evaluate their performance.

3.3 The Short-Time Fourier Transform (STFT)

The STFT (3.2) is a windowed FT [125]. It represents the signal in both time and frequency domains. This method is based on two steps (Figure 3-1): First, dividing the signal in the time domain into sub-sequences dt multiplied by a temporal window w(t). Second, calculating the spectrum for each sub-sequence. The time and frequency resolution are limited by the window length. Indeed, a wide window w gives better frequency resolution but poor time resolution; on the other hand, a narrower window w gives better time resolution but poor frequency resolution. They are different kinds of the temporal window as Gaussian, rectangular, Hanning, hamming and Blackman Harris. In this work, we use the hamming window (3.3) because it minimises the side-effects and gives an accurate result regarding the other windows. After choosing the window and applying the STFT, the spectrogram is depicted. The spectrogram is a three-dimensional graph of power, frequency, and time. There are several advantages to use the spectrogram: fast implementation using the FFT and easy interpretation.

$$STFT(f,w) = \int_{-\infty}^{+\infty} f(\tau)\, w(t-\tau) e^{-i2pif\tau} d\tau, \tag{3.2}$$

$$w(n) = \begin{cases} 0.54 - 0.46\cos\left(2\pi\frac{n}{N}\right) & if\ n \in [0,N] \\ 0 & if\ not \end{cases}, \tag{3.3}$$

Where N+1 is the samples' number chosen in terms of the width of the filter used in the applications. Indeed, the higher the samples' number, the largest the frequency band of the filter.

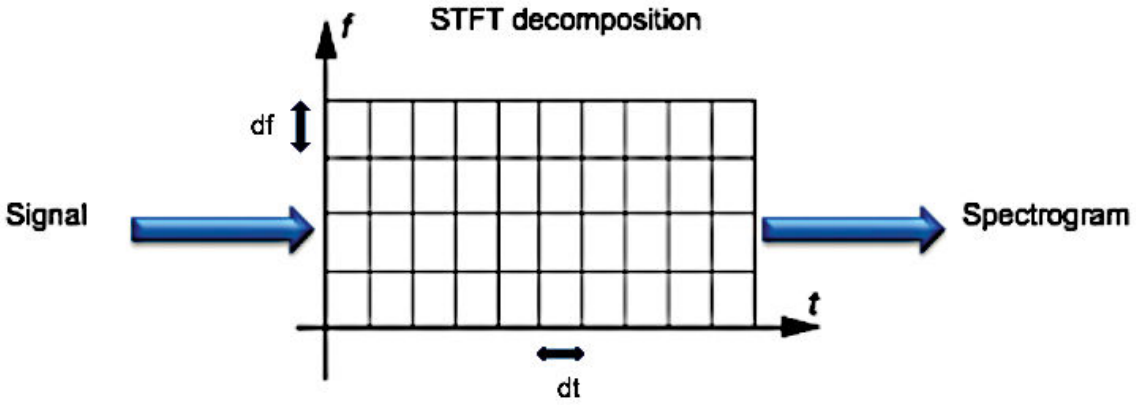

Figure 3-1. The short-time Fourier transform decomposition over the time and frequency domains [108].

The STFT will be more obvious with an illustrating example. The reflected signal at the cable with one fault denoised by the EMD ($SNR_{noisy\_f} = 10\,dB, SNR_{denoised\_EMD} = 13dB$) as defined in the chapter 2 (Figure 3-2) is considered.

First, the hamming window defined in (3.3) is used in the STFT with N=64. The denoised reflected signal is divided into shorter sub-sequences, and the periodogram is calculated for each one, giving frequency spectra for all sub-sequences. Then, we obtain the spectrogram (Figure 3-3) which has slow power variations in terms of frequency. Indeed, in Figure 3-3, there is almost no variation regarding the frequency because we look for a better time resolution or variation. Consequently, we lose the frequency resolution. In Figure 3-3, STFT was able to localize the fault interval [1-1.2] m for a range frequency range [3-4] GHz but not the fault accurate position because of its time resolution. Finally, the STFT lacks the precision and the accuracy to detect the chafing fault. In addition, the second drawback is the colour-code. For instance, in Figure 3-3, the intensity of the colours is near to each other because of the value of the power/frequency. For 1 GHz, at 1 m, the power/frequency equals -20.52 dB/GHz and at 0.4 m, the power/frequency equals -23 dB/GHz. As a result, it can be confusing to distinguish between them and to conclude in which position the chafing fault is. As regards the hard fault which is the open circuit in this case, the STFT is able to detect its interval [2.9-3.1] m at 3 GHz. In addition, it is clearer than the chafing fault because of the value of the power 18 dB/GHz in this interval.

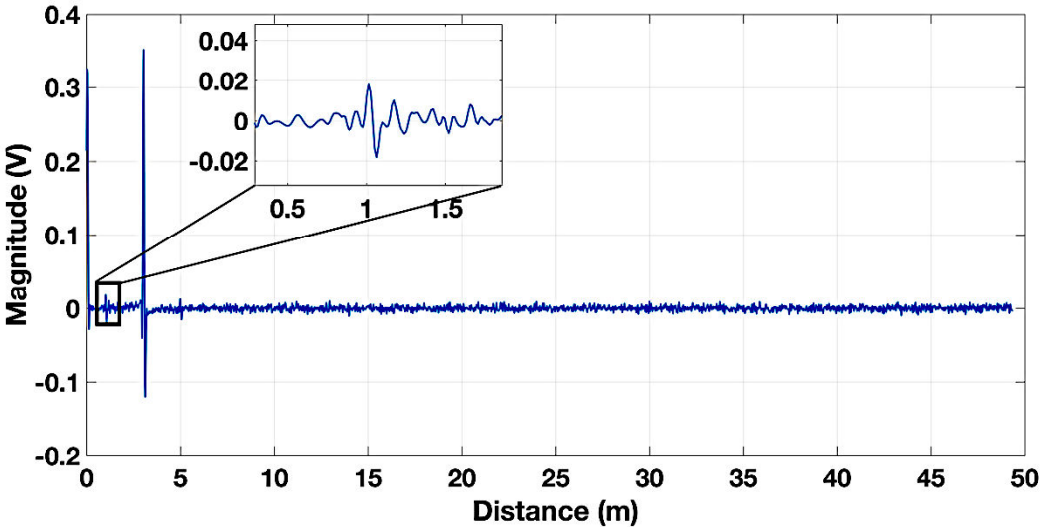

Figure 3-2. The denoised signal of 3 m coaxial cable with one chafing fault at 1 m via EMD method ($SNR_{noisy\_f} = 10\ dB, SNR_{denoised\_EMD} = 13\ dB$).

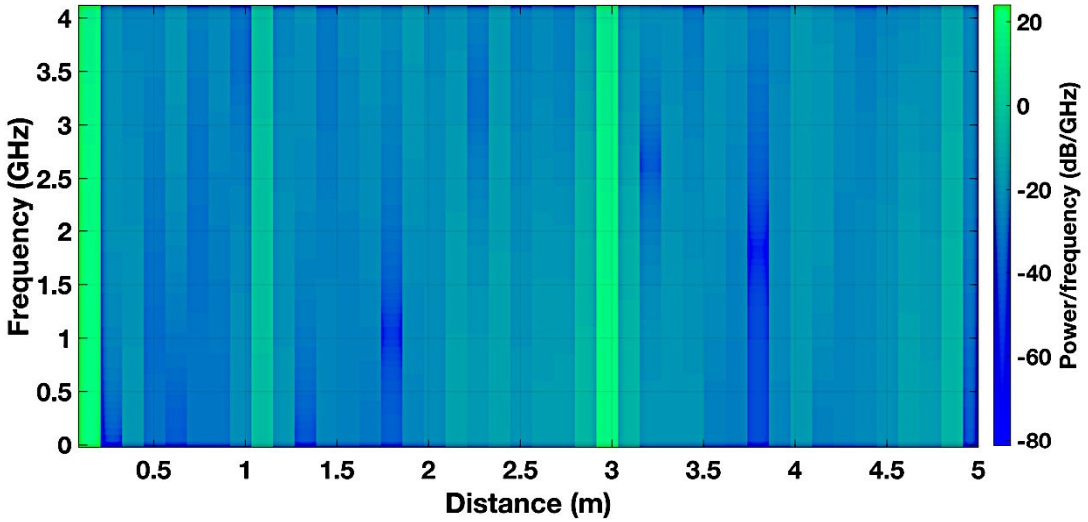

Figure 3-3. The spectrogram of the reflected signal with the Hamming window.

3.4 The Wigner–Ville Transform (WVT)

The WVT [121] represents the signal in frequency versus time by calculating the power spectrum via the local autocorrelation. The autocorrelation (3.4) means that the signal is compared to itself for all possible relative shifts or lags.

$$r_{xx}(t) = \int x(\tau)\, x(t+\tau) d\tau. \tag{3.4}$$

where τ is the delay time of the signal regarding itself.
The WVT uses the instantaneous autocorrelation function R_{xx}.

$$R_{xx}(t,\tau) = x(t+\tau/2) x^{*}(t-\tau/2). \tag{3.5}$$

where τ is the time lag, and x^{*} represents the complex conjugate of the signal x.

The Wigner–Ville transform is defined as

$$WVT(t,\omega) = \frac{1}{2\pi}\int x\left(t+\frac{\tau}{2}\right)x^{*}(t-\tau/2)e^{-i\omega\tau}d\tau. \tag{3.6}$$

The WVT has some properties, such as marginal energy-preserving properties (3.7), shifting properties (3.8),(3.9), and a time delay property (3.10) which are not present with the STFT.

$$|x(t)|^2 = \int_{-\infty}^{+\infty} WVT(t,\omega)d\omega, \tag{3.7}$$

$$if\ y(t) = x(t-\tau), then\ WVT_y(t,\omega) = WVT_x(t-\tau,\omega), \tag{3.8}$$

$$if\ y(t) = x(t)e^{-i\omega_0 t}, then\ WVT_y(t,\omega) = WVT_x(t,\omega-\omega_0), \tag{3.9}$$

$$\Delta t = \frac{1}{2\pi}\frac{d}{dt}\arg\left(X(\omega)\right) = \frac{\int_{-\infty}^{+\infty} tWVT(t,\omega)\,dt}{\int_{-\infty}^{+\infty} WVT(t,\omega)dt}, \tag{3.10}$$

The principle of the WVT will be more obvious with an illustrating example. The reflected signal at the cable with one fault denoised by the EMD ($SNR_{noisy\_f} = 10\ dB, SNR_{denoised\_EMD} = 13\ dB$) as defined in the chapter 2 (Figure 3-4) is considered. Figure 3-5 depicts a three-dimensional picture, distance, frequency, and power. The frequencies are ordered on a corresponding time-scale. The WVT does not suffer from leakage effects as the STFT does. Even though the WVT provides the best spectral resolution than the STFT, it gave the two signal's components at 0 m and 3 m, and one interference at 1.5 m. This interference is due to the cross terms that appears while calculating the autocorrelation function of the signal. For that reason, the interference appears in the middle of the cable. These cross terms which are the major drawback of the Wigner distribution, can be partly suppressed by extending the WVT or simply by using a smoothed pseudo WVT (SPWVT). As consequence, the WVT is not able to detect the chafing fault for the frequency range [3-4] GHz which is worse than the STFT which detects this fault at [1-1.2] m for the same frequency range. As regards the hard fault which is the open circuit in this case, the WVT can detect its position 3.1 m at 3 GHz. As a result, the WVT is more accurate than the STFT regarding the hard fault.

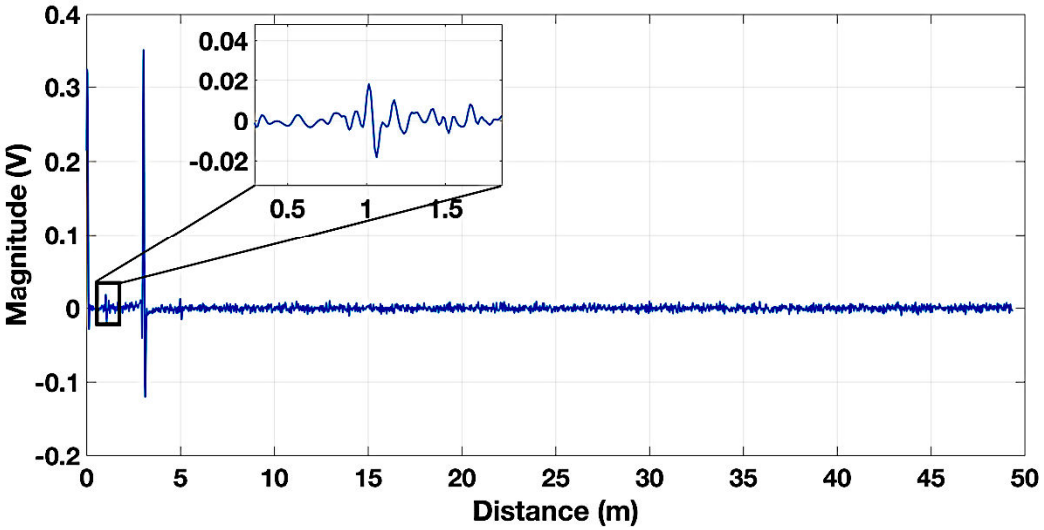

Figure 3-4. The denoised signal of 3 m coaxial cable with one chafing fault at 1 m via EMD method ($SNR_{noisy\_f} = 10\ dB, SNR_{denoised\_EMD} = 13\ dB$).

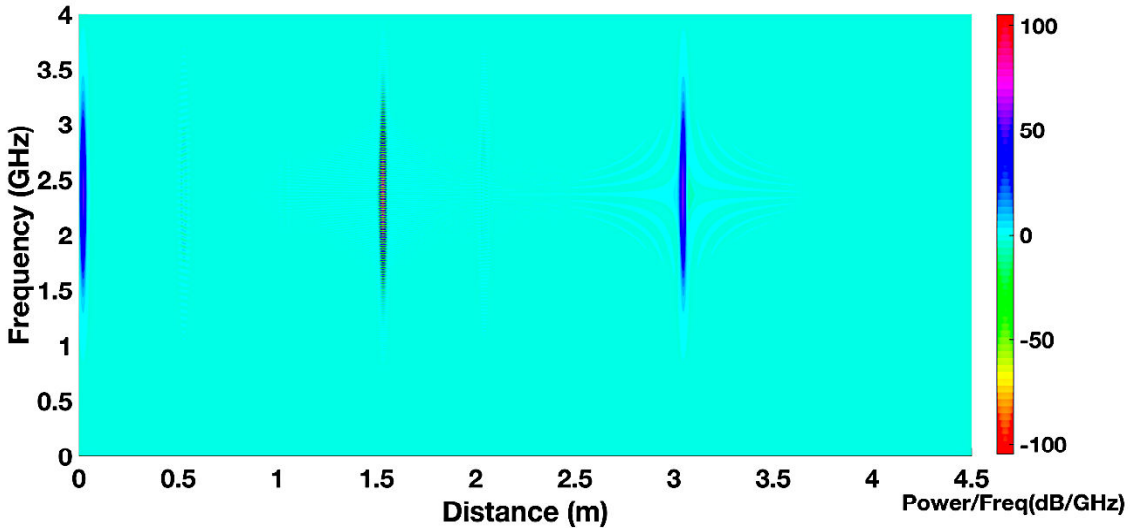

Figure 3-5. The Wigner–Ville transform applied on the reflected signal.

3.5 The Continuous Wavelet Transform (CWT)

In this section, we introduce the wavelet transform to overcome the limitations of the STFT and WVT. Some basic wavelet concepts have already been covered in Chapter 1.

The abrupt signal's changes contain the most interesting information in the data. To efficiently analyse these signals, they are analysed by a method called the continuous wavelet transform (CWT).

The outputs of CWT are coefficients (3.11), which are a function of scale or frequency and time.

$$\begin{aligned} CWT(s,u) &= \langle f(t), \psi_{s,u} \rangle \\ &= \int_{-\infty}^{+\infty} f(t)\psi_{s,u}^{*}(t)dt \\ &= \int_{-\infty}^{+\infty} f(t)\frac{1}{\sqrt{s}}\psi^{*}\left(\frac{t-u}{s}\right)dt \end{aligned} \tag{3.11}$$

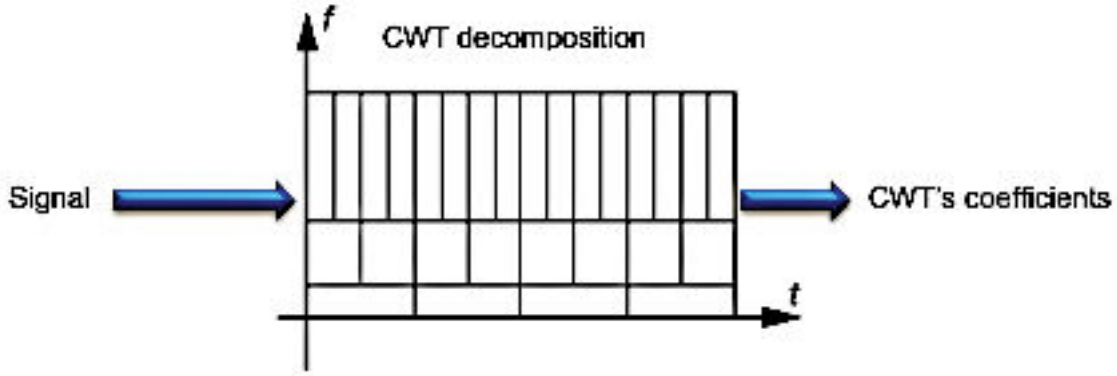

Figure 3-6. The continuous wavelet transform decomposition over the time and frequency domains [126].

Equation (3.11) and Figure 3-6 depict the transformation of one-dimensional signal $f(t)$ to two-dimensional function $CWT(s,u)$. The translation coefficient indicates which region is concerned, and the scaling coefficient eliminates the negative scales. For instance, the higher the number of scales per octave, the finer the scale discretization due to the relation between the equivalent frequency F_{eq} and the scale s (Figure 3-7) (2.17). For instance, a signal with 100 samples analysed with 10 scales results in 1,000 coefficients that better characterize oscillatory signal behaviour with the CWT.

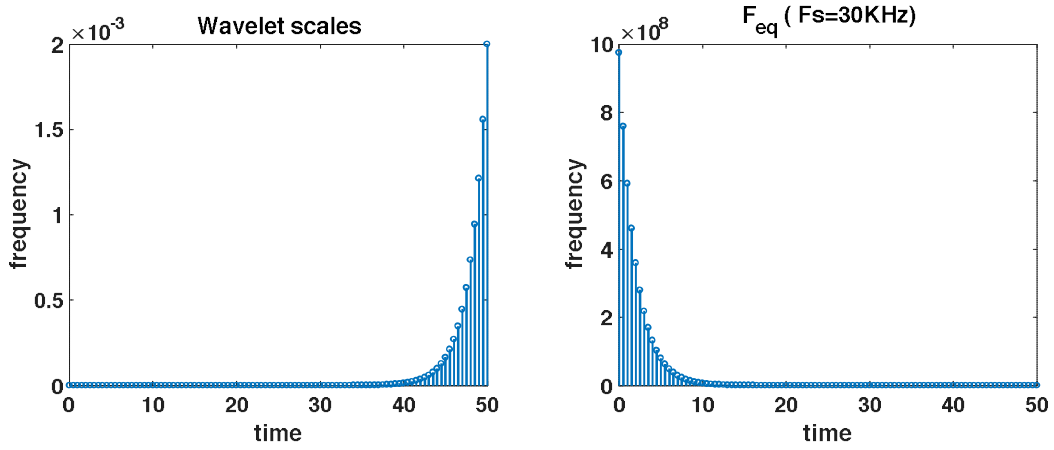

Figure 3-7. The relation between the equivalent frequency F_eq and the scale s.

In addition, the inverse continuous wavelet transform is defined as

$$f(t)=\frac{1}{C_\psi}\int_0^{+\infty}\int_{-\infty}^{+\infty} CWT(s,u)\frac{1}{\sqrt{s}}\psi\left(\frac{t-u}{s}\right)du\frac{ds}{s^2}. \quad (3.12)$$

where C_ψ is defined as

$$C_\psi=\int_0^{+\infty}\frac{|\psi(\omega)|^2}{\omega}d\omega<\infty. \quad (3.13)$$

where $\psi(\omega)$ is the FT of the mother wavelet $\psi(t)$.

The CWT will be more obvious with an illustrating example. The reflected signal at the cable with one fault denoised by the EMD ($SNR_{noisy\_f} = 10\,dB, SNR_{denoised\_EMD} = 13\,dB$) as defined in the chapter 2 (Figure 3-8) is considered. Before using the CWT, the daubechies wavelet with thirteen vanishing moments (db13) is chosen as a mother wavelet. The db13 wavelet gives accurate results that were not possible using FT techniques. It can show short signals with a clear start and end time for each signal. The CWT produces a time–frequency visualization of the input signal. In Figure 3-9, the magnitude of the wavelet coefficients returned by equation (3.11) are color-coded. The wavelet coefficient estimates are reliable. In addition, there are three wavelet coefficients convergence produced by the signal studied, at 0 m, 1 m and 3 m. However, the wavelet coefficients convergence requires to be at high frequencies. For instance, at [3-4] GHz, the CWT detects the chafing fault at 1 m which is more accurate than the STFT which localize the chafing fault interval [1-1.2] m and the WVT which does not detect the chafing fault for the same range frequency. As regards the hard fault which is the open circuit in this case, the CWT is able to detect its position at 3 m at 3 GHz. As a result, the CWT is more accurate than the STFT and the WVT regarding the hard fault.

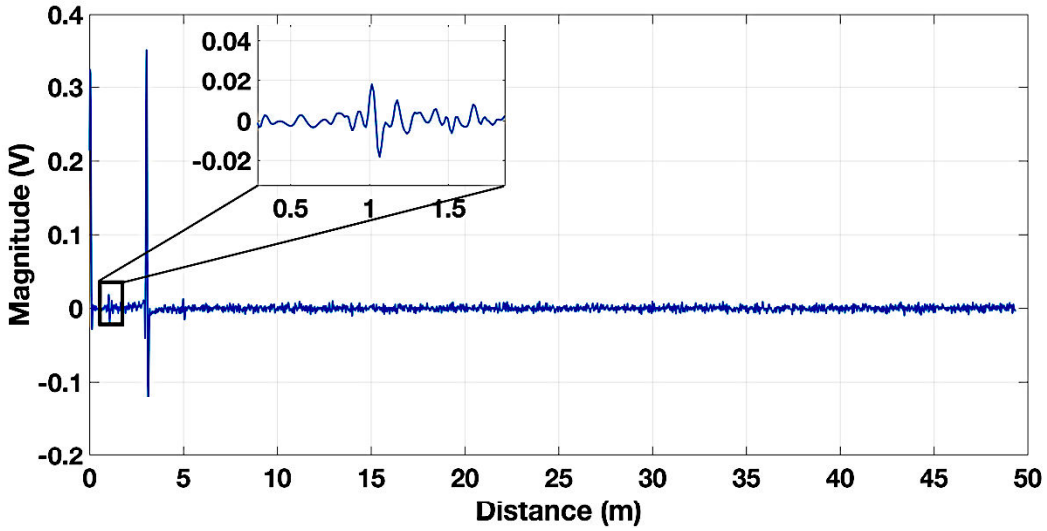

Figure 3-8. The denoised signal of 3 m coaxial cable with one chafing fault at 1 m via EMD method ($SNR_{noisy\_f} = 10\,dB, SNR_{denoised\_EMD} = 13\,dB$).

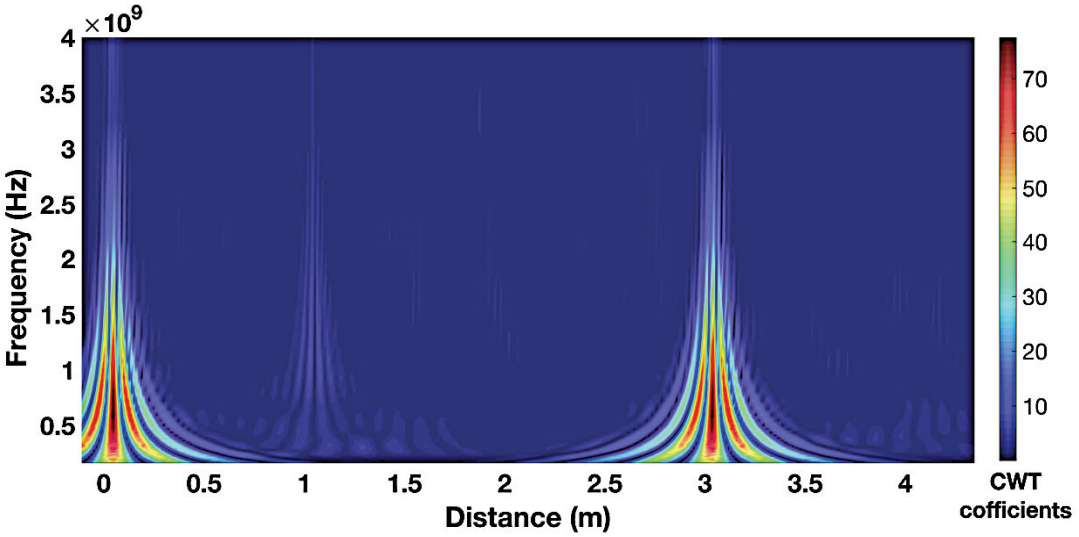

Figure 3-9. The sinusoidal signal and its scalogram via CWT.

3.6 Application

In this section, we will apply the time frequency method on the reflected signal at the cable with one fault denoised by the EMD ($SNR_{noisy\_f} = 10\,dB, SNR_{denoised\_EMD} = 15.32\,dB$) as defined in the chapter 2 (Figure 3-10) is considered.

First, STFT was used with the hamming window. The reflected signal at the cable with two faults (Figure 3-10) is divided into shorter sub-sequences, which often overlap, and the periodogram shown in is calculated for each one, giving frequency spectra for all sub-sequences which form a three-dimensional picture (distance, frequency, and power). In Figure 3-11, STFT was not able to localize the both chafing faults because of the sensitivity issues discussed previously. For 1 GHz, at 8 m, the power/frequency equals -14.65 dB/GHz and at 7 m, the power/frequency equals -15.2 dB/GHz. At 3 m, the power/frequency equals -3 dB/GHz and at 0.9 m, the power/frequency equals -9 dB/GHz. As a result, it is so confusing to distinguish between them and to conclude in which position the chafing fault is.

Second, as depicted in the section 3.4, the WVT failed to detect the chafing fault by applying it on the reflected signal at the cable with one fault because of the cross-terms. As a result, it is not necessary to apply it on the reflected signal at the cable with two chafing faults.

Finally, CWT was applied. The scalogram is produced from the reflected signal at the cable with two faults (Figure 3-10). Daubechies wavelet with thirteen vanished moments is used as an orthonormal basis. As depicted in Figure 3-12, CWT was able to detect the chafing faults even from our noisy signal. For high frequencies, for example at [2-3] GHz, the CWT detects the chafing faults at 3 m and 8 m which is more accurate and better than the STFT and the WVT which do not be able to detect the chafing faults.

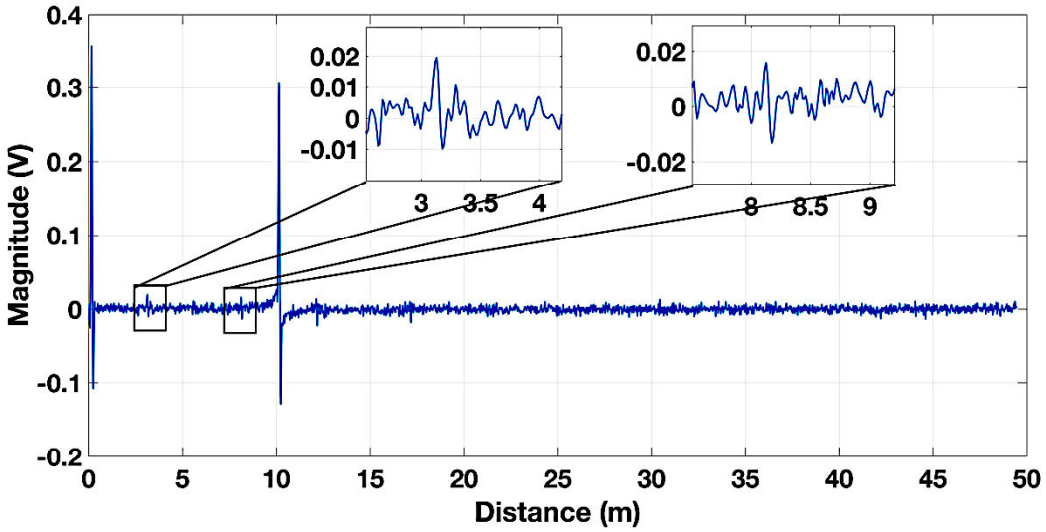

Figure 3-10. The denoised signal from 10 m coaxial cable with two chafing faults at 3 m and 8 m via EMD method ($SNR_{noisy\_f} = 10\,dB, SNR_{denoised\_EMD} = 15.32\,dB$).

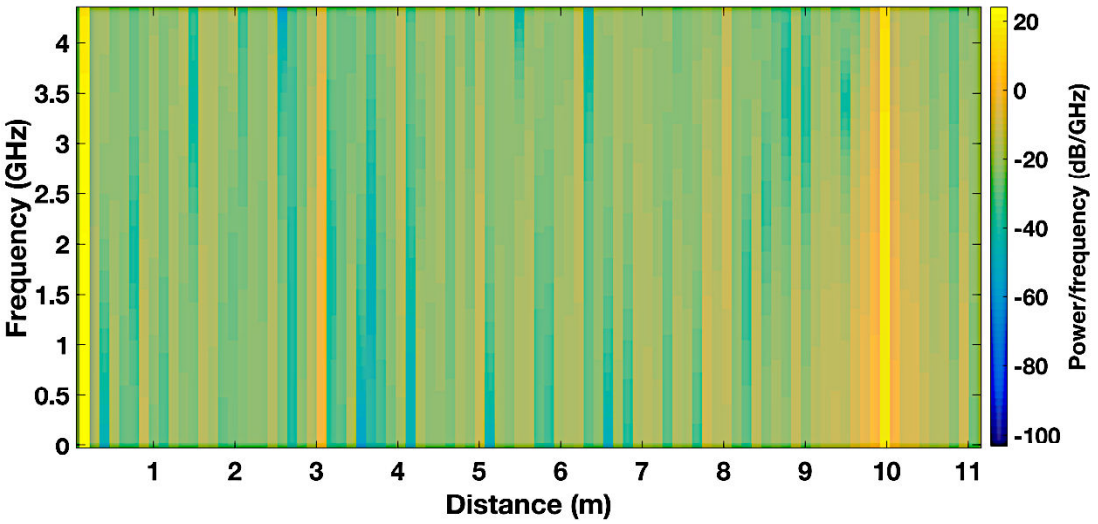

Figure 3-11. STFT spectrogram of the 10 m coaxial cable with two chafing faults at 3 m and 8 m.

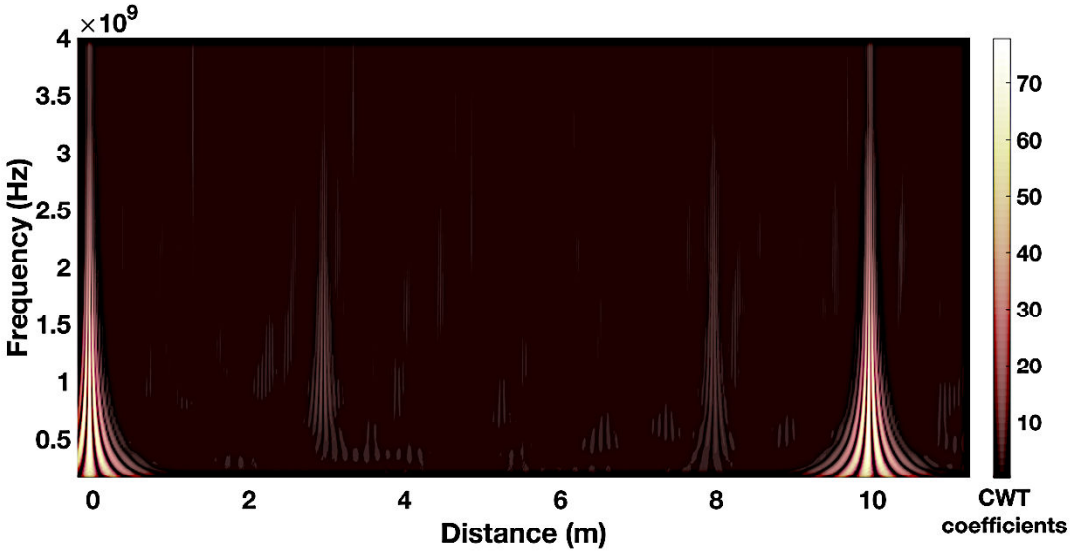

Figure 3-12. CWT of the 10 m coaxial cable with two chafing faults at 3 m and 8 m.

To sum up, in this section, as shown in Table 3-1, we applied the STFT, WVT and the CWT on the reflected signal of one-fault cable, and the reflected signal of two-faults cable. In the case of one-fault cable, we conclude that the STFT is able to detect the proposed chafing fault with the proposed denoised signal. Nevertheless, the best approximated fault's position cannot be determined because of the STFT's time resolution. As regards the WVT, it cannot be applied to detect the chafing fault. In addition, the most accurate method to detect this fault seems to be the CWT which is able to localize it at almost 1 m. However, it requires to be at a "high" frequency in order to obtain the wavelet coefficients convergence.
For the reflected signal of two-faults cable, for high frequencies [2-3] GHz, the CWT detects the chafing faults at almost 3 m and 8 m in contrast with the STFT and the WVT which do not detect the chafing faults.

Table 3-1. The comparison between the chafing fault position gotten by the STFT, the WVT, and the CWT in the frequency range [2-3] GHz.

	STFT	WVT	CWT
Chafing fault position estimated in coaxial cable with one chafing fault (accurate position is 1 m).	[1-1.2] m	Failed to detect the chafing fault.	Almost 1 m.
Chafing fault position estimated in coaxial cable with two chafing faults (accurate positions are 3 m and 8 m).	Failed to detect the chafing faults.	Failed to detect the chafing faults.	Almost 3 m, 8 m.

3.7 Conclusion

As discussed in the previous sections, time–frequency techniques involve a physical decomposition of signals acquired by a set of frequencies in a time domain and can be used for a host of applications. The analysis of hard faults is a fundamental task for time–frequency applications. This chapter employed the STFT, the WVT, and the CWT for time–frequency decomposition. This was done via the use of complementary temporal windows for the STFT, whereas the WVT employs local signal autocorrelation, and the CWT employs an orthonormal wavelet basis. Furthermore, both the STFT and WVT are approaches that fail to identify simple or multiple chafing faults.

The STFT uses a window to give the spectrum in the time domain, but the frequency and time resolutions are limited by the window length. A wide window gives better frequency resolution but poor time resolution, whereas a narrower window gives better time resolution but poor frequency resolution. Additionally, the STFT performance degrades if the noise level is high relative to the amplitude of the signal reflected from the chafing fault. The WVT can be interpreted as the power spectral density, and the propagation of a noisy signal creates overlapped signals which make difficult the fault detection and localization. On the other hand, the WVT needs to be combined by some temporal window to make the result smoother according to the inferences.

It was shown that for well-resolved point-like information on chafing faults, location information is partially encoded by the CWT. Backpropagation of the continuous wavelet coefficients in the Daubechies wavelet basis yields target chafing faults. The projection of any signal onto the wavelet basis via the CWT method provides better detection and location properties than the STFT and the WVT methods as shown in Table 3-2.

Since the problem of chafing-fault detection and location in cables is, to a great extent, a signal analysis problem, the STFT, WVT, and CWT methods were adopted. The CWT method showed promising results in locating single and multiple chafing faults in a simple cable but failed to give fault's characteristics as its width, and its length. With this in mind, the coming chapter recalls the basic principles of the Bayesian method and presents some of the simulation results that validated it. Limitations of the Bayesian approach in the face of different cable topologies are also illustrated.

Table 3-2. Comparison between the three time frequency methods.

	STFT	WVT	CWT
Advantages	Hard fault detection.	Hard fault detection.	Hard and chafing fault detection.
Inconvenient	Noise/resolution.	Interferences.	Fault's characteristics.

Chapter 4: Bayesian Approach

4 Bayesian approach

4.1 Introduction

The time–frequency analysis, although quite a sophisticated technique, left practically unresolved one of the most important objectives of the study – namely, whether the CWT can be used in the chafing fault detection. It is, therefore, clearly of interest to reanalyse the data with a different methodology, such as the Bayesian approach taken in this thesis. Bayesian data analysis has become more attractive to researchers in various disciplines [63]-[127]-[128]-[129]. The approach has been popular in econometrics, in astrophysical studies, in medical research, in image processing, and in many other areas. The values of unknown parameters entering the cable's model are constant, not random; hence, probability theory cannot be directly applied to them. To cope with this problem, mathematicians created a new statistical approach to estimate these parameters from data and other functions [130]-[131]. This statistical approach is used to derive conclusions about both the process which produces the observations and the expected behaviour in future instances of the same process. The approach is based on a probability model which describes the mechanism of the observed data Y as a function of a parameter θ.

Bayesian statistics, unlike most other statistical methods, reduces statistical inference to problems in probability theory, thereby involving three assumptions [132]. It first draws on prior knowledge to better estimate the posterior distribution of model parameters. Second, it chooses the answer that best explains the observations. Finally, it avoids making extra assumptions. In fact, it describes by means of probability distributions all uncertainties present in the problem. In particular, unknown parameters in probability models must have a joint probability distribution which describes the available information about their values; this is often regarded as the characteristic element of a Bayesian approach. Moreover, the parameters are treated as random variables within the Bayesian paradigm by using prior information that is subjective and objective. The Bayesian approach is based on accepted model assumptions and data. This is addressed to derive appropriate posterior distributions, defined to encapsulate inferential conclusions about the model, data, and parameters. The Bayesian inference presents an optimization problem solved by nested sampling (NS) or by the Gauss Newton (GN) algorithm.

Proposed by John Skilling in 2004 [133], NS has been used in many domains, including biology [134]-[135], astronomy, and cosmology [136]. NS is based on the Monte Carlo method [63]. In this work, we use the same NS used in [63] and we compare it to the GN method in order to conclude if the GN method can overcome some NS method limitations or not. The Gauss Newton (GN) algorithm [137] is used to solve non-linear functions. It is a modification of Newton's method to find an optimization solution of a function. NS and GN used in Bayesian evidence calculation bring two advantages. First, they give an accurate posterior distribution estimation. Second, they converge faster than the traditional Markov Chain Monte Carlo (MCMC) approach [138].

Chapter 4 briefly reviews the principles of Bayesian inference, with particular attention to parameter estimation and model selection. First, the Bayesian method is introduced with its properties. Second, cable's model used for the present study is described. Third, GN and NS are presented to determine their effectiveness in the soft fault detection. Finally, we conclude the chapter with a critical discussion of the results of the Bayesian analysis versus those of the time–frequency methods and point out future useful directions for application of the Bayesian methodology.

4.2 Bayesian approach

Bayesian inference is based on the forward model M (4.1) and probability theory to take into consideration measurement noise ς and to describe uncertainty, often about unknown parameters θ [139]. Data Y, which is the sum of the model and the noise as shown in the equation (4.1), is obtained via either the RF instrument or simulation. The prior distribution $P(\theta)$ for the unknown parameters is chosen based on prior information, along with a conditional distribution $P(\theta|M)$, which describes knowledge about the unknown model parameters θ before the simulation is made and the likelihood distribution $P(Y|\theta,M)$, which stands for the simulation's probability regarding the model's parameters [140]. By the product rule, this yields the Bayes' formula (4.2):

$$Y = M + \varsigma, \tag{4.1}$$

$$P(\theta|Y,M)=\frac{P(Y|\theta,M)P(\theta|M)}{P(Y|M)} . \tag{4.2}$$

In the Bayesian approach, posterior information is based on prior information. So, it is important to assign $P(\theta)$ properly. For this, there are two concepts:

1. In a real physical problem, prior information about the observed data or the observation procedure is known.
2. Prior information can be exactly represented by one certain probability distribution.

The first point shows that, in most problems, it is possible to determine a family of prior laws for specific parameters. The second point shows that the parameters are not fixed a priori. However, these parameters can be estimated, either from a set of training data or even posteriori from the observed data [141].

The Bayesian algorithm can be summarized as follows [142]:

1. Prior modelling: assign the prior probability distributions $P(\theta|M)$ and $P(\theta)$.
2. Compute the posterior probability: once $P(\theta|M)$ and $P(\theta)$ are assigned, equation (4.2) is used, which contains all the information from data and a priori information.
3. Use this posterior probability to infer the unknown θ.

To calculate the posterior information, equation (4.2) estimates the maximum posterior laws [63]:

$$\text{maximize } P(\theta|Y,M). \tag{4.3}$$

To do this, it is necessary to calculate the normalizing term in the equation (4.2), called the evidence, $P(Y|M)$, which, being an integral, can sometimes be problematic to evaluate.

$$P(Y|M) = \int P(Y|\theta,M)\,P(\theta|M)d\theta. \tag{4.4}$$

The idea is to generate a reference particle θ_n from the distribution $P(\theta)$. Then, a Bayesian approach run evolves a set of variables θ_n, n = 1:N, initially representing $P(\theta)$, tending to calculate the log-evidence. Nearness is defined using a distribution prior function and the likelihood distribution. The posterior parameters are chosen according to the log-evidence that is higher than a threshold r. If a different threshold is chosen, then this estimate of posterior

parameters will change. In the literature, there are many methods to solve equation (4.3); the approach depends on the model used and the desired results. We choose to solve it with the GN algorithm and NS because of their convergence, simplicity, and efficacy. These exposed methods are implemented in Matlab.

4.3 Theory

4.3.1 Gauss–Newton (GN)

The GN algorithm is a modification of Newton's method. It consists in finding the solution θ^* of the function $F(\theta) = 0$ for which the partial derivative $Df(\theta^*)$ is reversible.

$$F(\theta)=f(\theta)-J(\theta)*(\theta-\theta_0)\ . \tag{4.5}$$

where J denotes the Jacobian matrix of $f(\theta)$, and θ_0 is the vector of model's prior parameters. This method is well-known for its quick convergence if the function has one variable, but to ensure a quick convergence in the case of a multivariable function, the partial derivative Df calculation should be minimized. Otherwise, the approach will be slow and extremely costly. To solve equation (4.3), the points that zero out Df should be looked for. For that, a choice of prior parameters is made. In the case where $f = 0$ is the minimum, or when f varies almost as a linear function near to the minimum point, the approximation to the partial derivative is significant, and the convergence of the GN method is noticed [143]. Solving a function f using GN [144] is applying non-linear least-squares to fit the function f. As a result, the solution is θ^*.

The GN algorithm is used to solve non-linear systems. After modelling $S_{11\text{Model}}$ by a non-linear function with a set of the θ model's parameter, the square error ε between the $S_{11\text{TDR}}$ calculated by TDR and the S_{11} simulated by our model should be minimized.

$$\varepsilon(\theta) = \sum_i r_i^2 = \sum_i (S^i_{11_{TDR}} - S^i_{11_{Model}}(\theta))^2. \tag{4.6}$$

where $i \in [1, N]$ is the number of iterations.

The optimal parameters θ^* that minimize this $\varepsilon(\theta)$ have to satisfy the equation such that the gradient vector is equal to zero.

$$\frac{\partial \varepsilon(\theta)}{\partial \theta_j} = -2 \sum_i (S^i_{11_{TDR}} - S^i_{11_{Model}}(\theta_j)) J_{ij}. \tag{4.7}$$

where J_{ij} is the *ij*th component of the Jacobian matrix J.

$$J_{ij} = \frac{\partial S^i_{11Model}(\theta)}{\partial \theta_j}. \tag{4.8}$$

where *j* is the *j*th component of the θ model's parameter.

To find the optimal parameter, the iterations shown in the equation (4.9) are used.

$$\theta_{n+1} = \theta_n + \Delta\theta = \theta_n - J^-(S_{11TDR}(\theta) - S_{11Model}(\theta)). \tag{4.9}$$

where $J^- = (J^T J)^- J^T$ is the pseudo inverse of J.

To avoid the possibility that the iteration may not converge, a parameter $0<\zeta<1$ to reduce the step size is introduced.

$$\theta_{n+1}=\theta_n+\zeta\Delta\theta. \quad (4.10)$$

4.3.2 Nested sampling (NS)

A model has been used to develop and test the chosen parameters and their distributions. Running this model requires developing sampling algorithms to fully explore and calculate the posterior parameters. These algorithms are needed to overcome difficulties in a time-computing and the space of interest scale. Thus, a set of model parameters is proposed and is accepted or rejected using the standard Metropolis–Hastings acceptance criterion. Many sampling techniques have been developed, such as the metadynamics technique [145]-[146] and umbrella sampling [147], which is widely used in studying chemical reactions, originally tested on Lennard–Jones clusters. In addition, some sophisticated sampling algorithms have been developed that do not require prior knowledge about the model parameters [148]. One of the initial sampling algorithms is Monte Carlo sampling [149]. Recently, Skilling introduced the novel technique of NS [142], an algorithm specifically designed to sample high-dimensional spaces [150]. Its outputs are a set of samples and associated weights from which an estimated marginal likelihood and model variables are calculated, such as fault length and width. While initially developed for Bayesian statistical inference [142], the algorithm is well-established in the astrophysics community [136] and has also been successfully applied in a variety of other fields, including bioinformatics [151], systems biology [152], and data analysis. As a reminder, the objective of this section is to solve the Bayes' formula defined in (4.2). Noted Z the Bayesian evidence $P(Y|M)$, NS [150] - [134] which is a Bayesian sampling method, is used to estimate this Bayesian evidence Z as well as posterior distribution parameters of the faulty cable (4.2). The main step in NS is to create N samples $(\theta_1 \dots \dots \theta_N)$ from each point θ of a function interval. As a result the evidence for each point θ in this interval is a multidimensional integral (4.11).

$$Z = \int \dots \int P(Y|M(\theta_1 \dots \dots \theta_N))d\theta_1 \dots . d\theta_N. \quad (4.11)$$

However, NS converts a multidimensional integral to one dimension (4.13), which is easier to evaluate numerically. The posterior distribution is incrementally constructed by having a set of samples that evolves to high-probability regions X of the research area. Starting from the iteration index $j = 1$, $X_0 = 1$, and $Z = 0$, this Bayesian method could be formulated by sampling prior information using N samples and evaluating their likelihood.

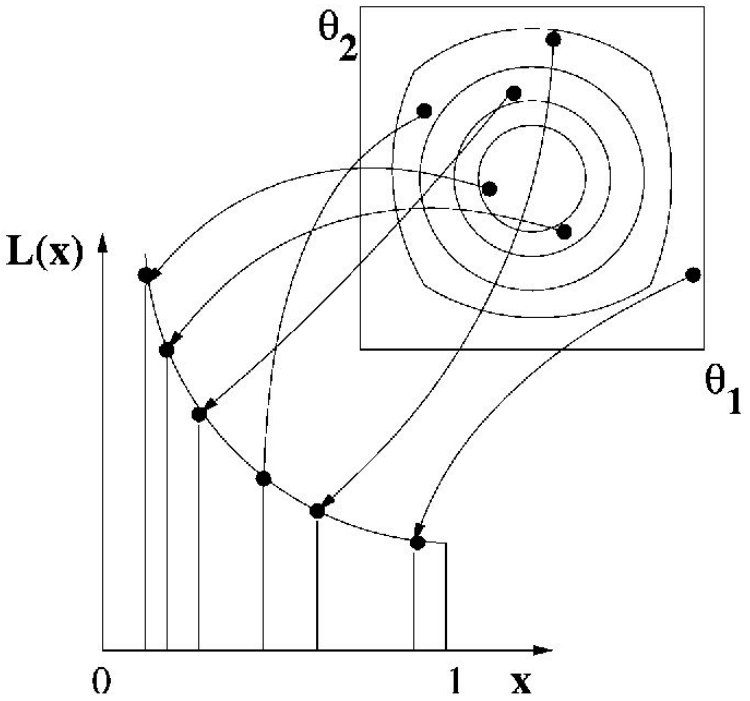

Figure 4-1. The NS algorithm integrates the likelihood over the prior volume by peeling away thin isosurfaces of equal likelihood [153].

These samples are called the 'active set'. Subsequently, the active set samples are evaluated in the high-probability region by an iterative replacement of the sample θ_{worst}, which has the lowest likelihood function $L(\theta_{worst})$, by a new sample θ_{new}, which has the highest likelihood: $L(\theta_{new}) > L(\theta_{worst})$ (Figure 4-1). While replacing the worst likelihood, the prior volume shrinks at each iteration. However, the uncertainty in this shrinkage gives rise to an error in *Z*. Besides, the shrinkage of this prior for a sequence of points from a two-dimensional parameter space is illustrated in Figure 4-1.

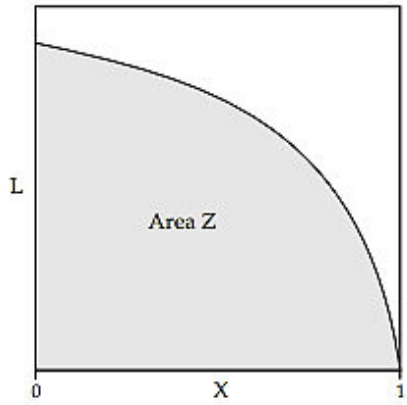

Figure 4-2. Likelihood function with area Z [125].

Then, the next iteration's volume can be estimated as

$$X_j = \exp(-\frac{j}{N}). \qquad (4.12)$$

The Bayesian evidence (Figure 4-2) is

$$Z=\sum_{j=1}^{m} Z_j, \quad Z_j=\frac{L_j}{2}(X_{j-1}-X_j). \tag{4.13}$$

After M iterations, the total Bayesian evidence (4.13) can be approximated by summing the contributions of each iteration. Furthermore, the active and rejected sets are used for the calculation of posterior distribution.

The NS's main difficulty lies in the sample replacement step, which requires the proposition of a new sample θ_{new} corresponding to $L(\theta_{new}) > L_j$. The problem becomes more difficult after a few iterations, when L_j reaches a high value and the research area which satisfies the constraint of the lower limit is reduced to a smaller region. As a solution, Skilling proposed NS based on the MCMC approach (Markov Chain Monte Carlo) [146]. Consider a sequence of a random variables $[\theta_1, \theta_2 \dots \theta_n]$ sampled from the distribution $P(\theta_{n+1}|\theta_n)$, which means that θ_{n+1} depends only on θ_n and not on the further variables $[\theta_1, \theta_2 \dots \theta_{n-1}]$. Such a sequence is called a Markov chain.

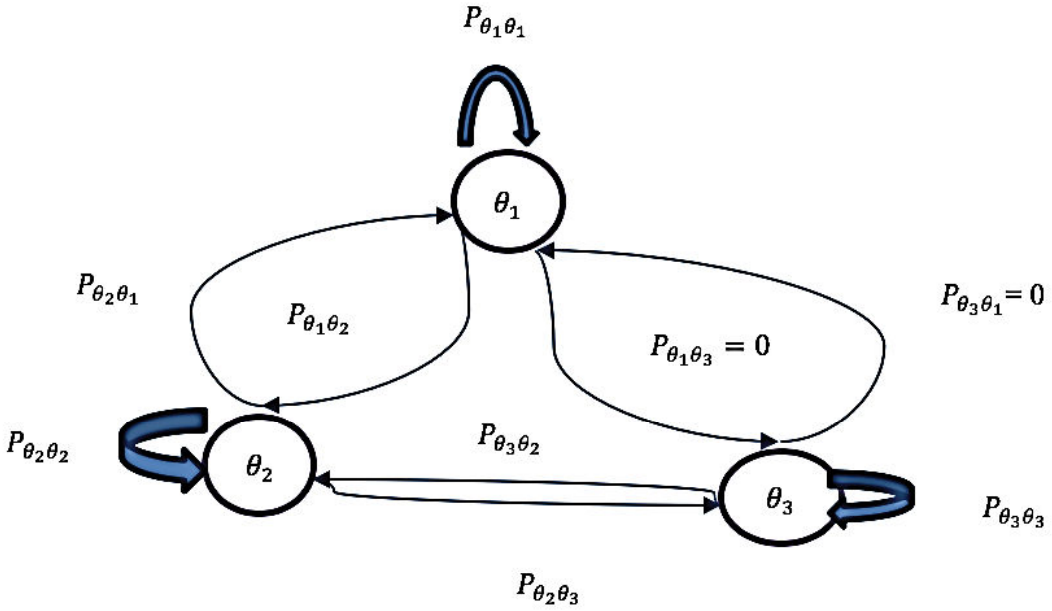

Figure 4-3. A Markov chain.

As illustrated in Figure 4-3, a Markov chain is a probabilistic way to traverse a random walk across a graph. It traces a series of transitions from one state to another. In addition, a Markov graph is used to formulate a problem. The nodes are formulated by including the node that must be predicted. Therefore, MCMC is used to make sampled chains which draw samples from the distribution. It is a sampling algorithm from probability distributions using Markov chains [154]-[155]. MCMC methods can be considered as special cases of the Metropolis algorithm (MH). The Metropolis algorithm is a random sampling that uses an acceptance and rejection rule to converge to the target distribution.

The MCMC algorithm is as follows:

1. Define a value for the prior variable.
2. For I iteration sampling variables θ_* from the prior distribution, calculate the ratio

$$r = \frac{p(\theta_*|Y)}{p(\theta_{i-1}|Y)}. \quad (4.14)$$

Consequently, the new variable is

$$\theta_i = \begin{cases} \theta_* \text{ with probability } \min(r,1) \\ \theta_{i-1} \text{ otherwise} \end{cases} \quad (4.15)$$

4.4 Application

Before moving on, to keep the idea clear:
Our process includes four parts:

- Model:
  - Create a TDR response model of the nominal and chafed cable.

- Simulation:
  - Concentrate on a chafing fault (Figure 1-14) in the coax cable
  - Simulate TDR response of the undamaged coax cable
  - Create a chafing fault on the coax cable
  - Simulate TDR response of the chafed coax cable

- Probabilistic approach:
  - Use the model and the simulated data.
  - Solve the Bayesian method by Nested Sampling or Gauss Newton.
  - Look for the evidence and the posterior parameters.

- Comparison between Gauss Newton and Nested Sampling.

For all this chapter, the research area represented is very limited. In fact, the analysis is made over the entire length of the cable but only the results corresponding to a short research area are represented. In addition, the chafing fault treated in this section is the same chafing fault shown in Figure 1-14 that we treated in the previous applications.
As discussed above, the key to the Bayesian inversion methods is to model some prior information of scattering coefficients and to recover the scattering coefficients under the Bayesian principle. In the context of this thesis, the Bayesian approach consists in calculating the reflected signal at the coaxial cable input. This requires identifying the S-matrix [62] of the fault and integrating it in the transmission line model so as to be more compatible with the simulated S-matrix over the whole frequency range of the injected signal. To provide clear evidence, the Bayesian model studied is the S_{11} parameter at the cable entry with regard to the model's parameters θ.

$$S_{11} = S_{11_{system}}(\theta) \quad . \quad (4.16)$$

where θ is a vector of unknown model parameters: $\theta = [d_f, L_F]$.

Table 4-1. Model's parameters and their distributions

Model's parameters	Distribution for GN or NS
Distance to fault (d_f)	Gaussian distribution. Its mean equals 0.1, and its standard deviation equals 50.
Fault's length (L_F)	Gaussian distribution. Its mean equals 0.005, and its standard deviation equals 2.5.

The Gaussian distribution is chosen for these parameters because it is symmetric, and it is denser in the centre and less dense in the tails.
Given a set of input variables vector θ_n, where n = [1: N], the non-linear model is written as

$$f_n = M(\theta_n). \tag{4.17}$$

The output variable is then given as a linear combination:

$$y_n = f_n(\theta) + \varsigma_n. \tag{4.18}$$

where θ is a column vector of coefficients, and ς is zero-mean Gaussian noise with the covariance β.
Given a data set Y, the likelihood is written as

$$\mathrm{P(Y|\theta}_n, \mathrm{M}) = (\frac{\beta}{2pi})^{N/2}\, e^{-\frac{\beta}{2}(Y-F\theta)^T(Y-F\theta)}. \tag{4.19}$$

where Y is a column vector of data, and F is the nth row of the matrix X containing f_n. The weights are drawn from a zero-mean Gaussian prior with an isotropic covariance α.

$$\mathrm{P(\theta}_n|\mathrm{M}) = (\frac{\alpha}{2pi})^{p/2}\, e^{-\frac{\alpha}{2}\theta^T\theta}. \tag{4.20}$$

The evidence is then

$$P(Y|M) = (\frac{\beta}{2pi})^{N/2}(\frac{\alpha}{2pi})^{p/2} \int e^{-\beta e^{-\frac{\beta}{2}(Y-F\theta)^T(Y-F\theta)} + \alpha e^{-\frac{\alpha}{2}\theta^T\theta}}\, d\theta. \tag{4.21}$$

The log of the evidence can then be written as

$$\begin{aligned}\log(P(Y|M)) = -\alpha e^{-\frac{\alpha}{2}\theta^T\theta} - \beta e^{-\frac{\beta}{2}(Y-F\theta)^T(Y-F\theta)} + \\ 0.5\log\left|\beta e^{-\frac{\beta}{2}(Y-F\theta)^T(Y-F\theta)} + \alpha e^{-\frac{\alpha}{2}\theta^T\theta}\right| + \frac{p}{2}\log\alpha + \frac{N}{2}\log\beta - \frac{N}{2}\log(2pi).\end{aligned} \tag{4.22}$$

As defined in the previous paragraphs, the chafing fault exists where the log evidence is higher than a threshold, which is the log evidence of the nominal cable data.
In brief, to infer the chafing fault parameters, the fault prior parameters (position and length) are defined. Afterward, the Bayesian approach is solved by NS or GN, as elaborated upon in Section 4.3, for the sake of the evidence and the model posterior parameters.
In this section, we validate our method by using the reflected signal at the cable entries denoised via EMD shown in Figure 2-22 and Figure 2-36. To substantiate the probabilistic approach, the fault's length and position should be identified using the Bayesian process. To accelerate the process for the first case, the cable with one fault in Figure 2-20, the Bayesian inference is applied either in a small interval referred to as the research area, or launching several searches on evenly spaced cable sections instead of browsing the entire cable in a single search which is more efficient for convergence. In fact, the analysis is made over the entire length of the cable but only the results corresponding to the research area [0.9–1.5] m are represented.

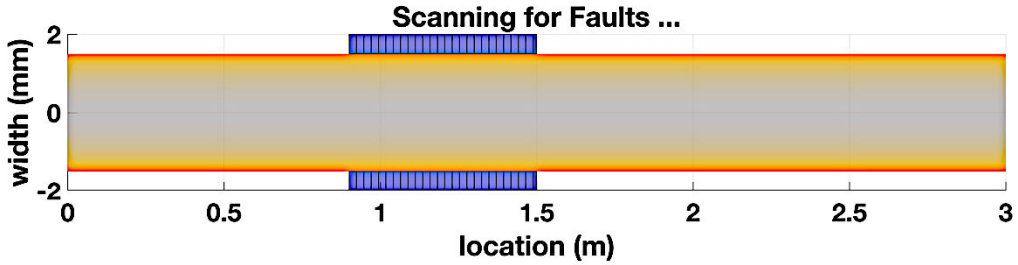

Figure 4-4. The 3-m coaxial cable is represented by the yellow section. The research area is the blue sections [0.9–1.5] m.

Using the Bayesian approach, evidence was generated via NS (Figure 4-7) and GN (Figure 4-6). The fault exists when the evidence is higher than the threshold for both methods. For the other research areas, there is no evidence higher than the threshold, meaning that there is no fault present.
In Figure 4-5, the NS generates almost 500 points from the fault's prior parameters (l_f=0.5 cm, d_f=0.1m). These samples are evaluated in the high-probability region by an iterative replacement of the sample θ_{f_worst}, which has the lowest likelihood function $L(\theta_{f\_worst})$, by a new sample $\theta_{f\_new} = [l_f = 1.39\,cm, d_f = 1.01\,m]$, which has the highest likelihood: $L(\theta_{f\_new}) > L(\theta_{f\_worst})$.

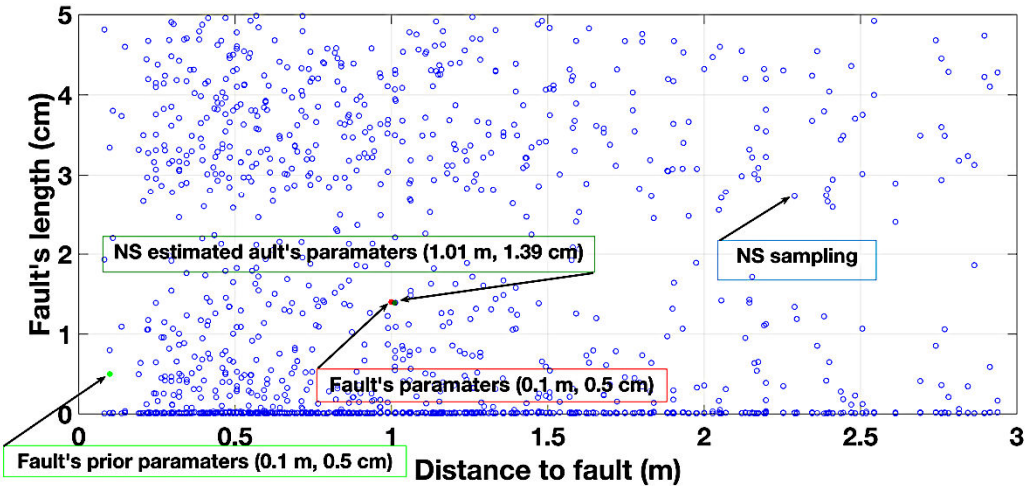

Figure 4-5. NS sampling.

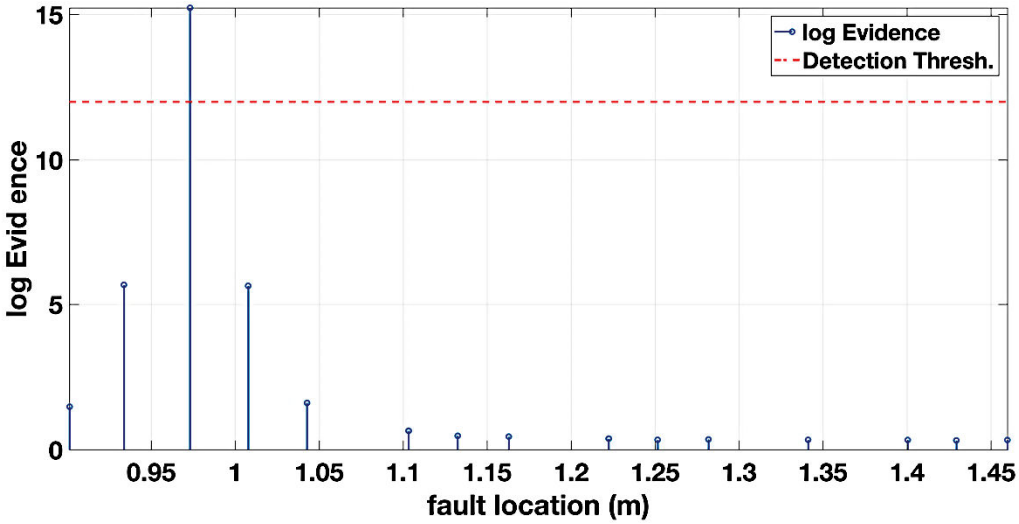

Figure 4-6. The evidence via GN (straight line with pentagram) is represented indicating the fault position in the research area [0.9–1.5] m. The threshold (dashed line) is 12.

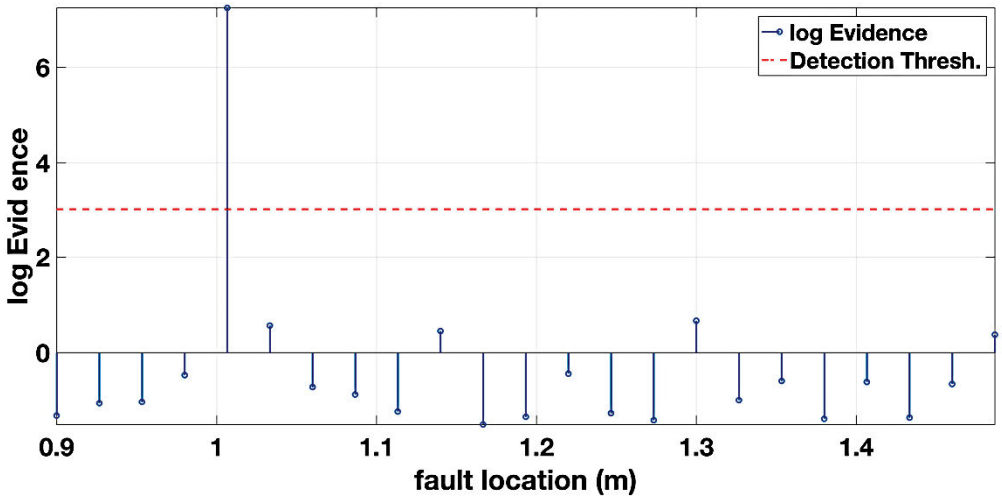

Figure 4-7. The evidence via NS (straight line with pentagram) is represented indicating the fault position in the research area [0.9–1.5] m. The threshold (dashed line) is 3.

In Figure 4-6 and Figure 4-7, we observe that there is only one value in the evidence that is higher than the threshold for both methods. This value indicates the existence of the fault and its position. The fault is marked at 0.98 m using GN but at 1.01 m using NS.

Table 4-2. Prior parameters vs Posterior parameters

Model's parameters θ	Fault's parameters	Prior parameters	Estimated posterior parameters Via NS	Estimated posterior parameters Via GN
Distance to fault (d_f)	1 m	0.1 m	1.01 m	0.98 m
Fault's length (L_f)	0.014 m	0.005 m	0.013 m	0.013 m
Sensitivity regarding fault's position			0.01	0.02

Table 4-2 depicts the model's prior and posterior parameters. Thanks to the probabilistic inference, these parameters are close for both methods.
To learn which method is more accurate, we calculated their sensitivities to the fault's position. As seen in Table 4-2, the NS sensitivity is better than the GN sensitivity, meaning that in this case NS is more accurate than GN in uncovering the chafing fault on the coaxial cable. Using the posterior parameters (Table 4-2), in Figure 4-8, we graph the reflected signal at the cable entry via GN (dotted red line) and via NS (solid blue line).

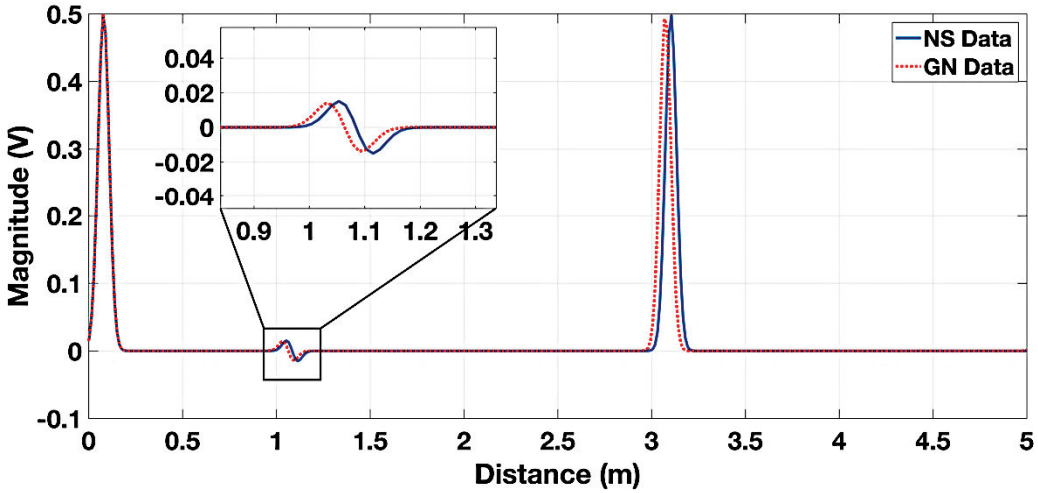

Figure 4-8. TDR response simulated signal via GN (dotted red line) and via NS (solid blue line). The first peak represents the Gaussian injected signal. The second peak is caused by the impedance discontinuities due to the chafing fault.

Thanks to the Bayesian approach, the solutions via NS or GN are pseudo-similar, and the fault prior and posterior parameters are much the same, which validates both methods. However, the fundamental flaw of solving the Bayesian approach via NS is the time required to calculate the posterior parameters. As an example, in the research area [0.9–1.5] m, it took almost 2 hours to detect one fault. However, the GN method took only 5 minutes to detect the

fault. Solving the Bayesian problem via GN made this algorithm less flexible and more sensitive to the prior parameters.
After proving the reliability of the Bayesian approach to detect one fault, the next step is to investigate its ability to detect multiple defects. In this section, a 10 m coaxial cable is considered, as shown in Figure 1-24. This time, our research area is divided into two small intervals. In each, we are looking for the Bayesian evidence. Indeed, the Bayesian evidence is calculated over the entire length of the cable but only the results corresponding to the research areas [2.9–3.5] m and [7.9–8.5] m are represented.
The first interval [2.9–3.5] m is considered.

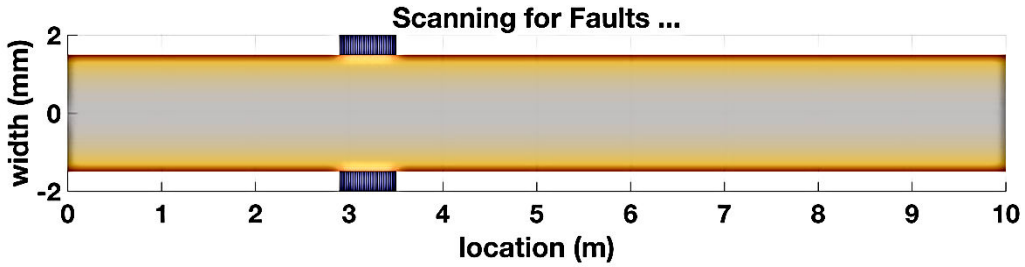

Figure 4-9. The 10 m coaxial cable is represented by the yellow section. The research area is the blue sections [2.9–3.5] m.

For each point in our first research area, the evidence using the Bayesian approach solved via NS and GN was calculated.

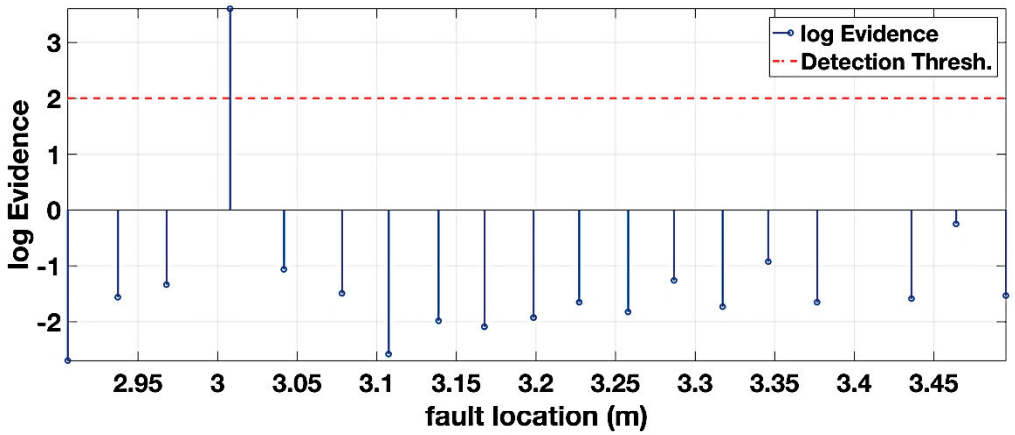

Figure 4-10. The evidence via GN (straight line with pentagram) is represented indicating the fault position in the research area [2.9–3.5] m. The threshold (dashed line) is 2.

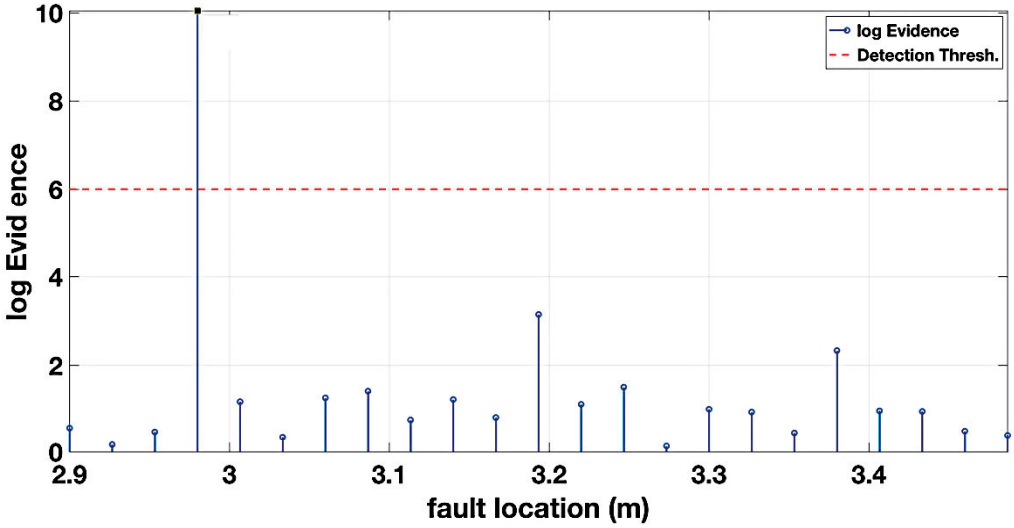

Figure 4-11. The evidence via NS (straight line with pentagram) is represented indicating the fault position in the research area [2.9–3.5] m. The threshold (dashed line) is 6.

Figure 4-10 and Figure 4-11 depict the existence of one fault which is inferred by the highest value among the evidence. The fault is marked at 2.98 m using NS but at 3.01 m using GN. The second interval is [7.9–8.5] m.

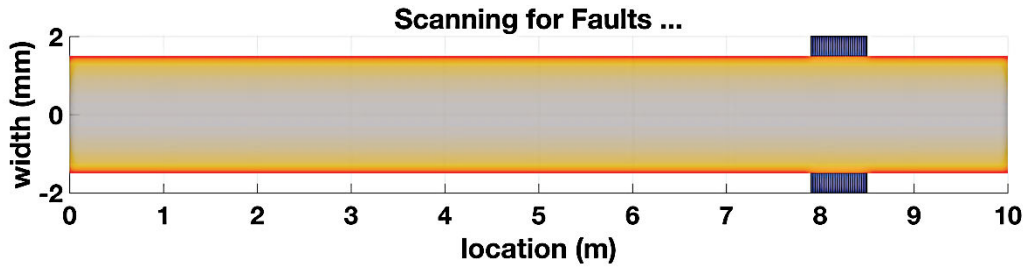

Figure 4-12. The 10 m coaxial cable is represented by the yellow section. The research area is the blue section [7.9–8.5] m.

Figure 4-13 and Figure 4-14 show the existence of the second chafing fault in the research area [7.9–8.5] m. It is indicated by the value that is higher than the threshold. Using NS, the fault was marked at 7.98 m but at 8.06 m using GN.

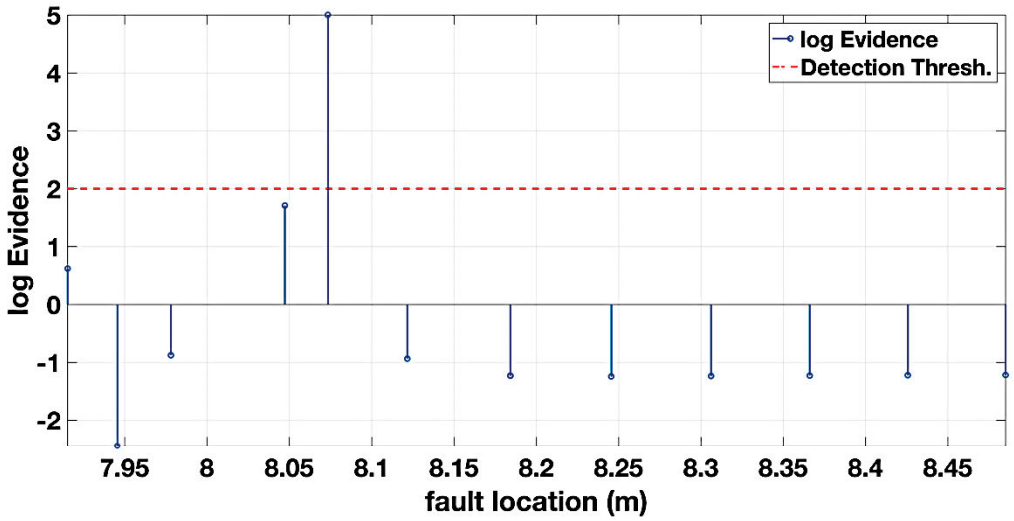

Figure 4-13. The evidence via GN (straight line with pentagram) is represented indicating the fault position in the research area [7.9–8.5] m. The threshold (dashed line) is 2.

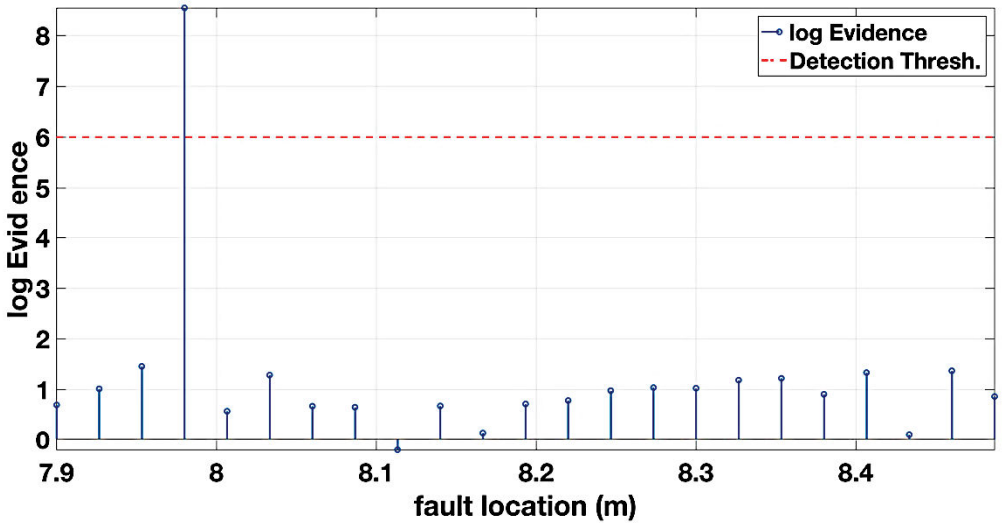

Figure 4-14. The evidence via NS (straight line with pentagram) is represented indicating the fault position in the research area [7.9–9.5] m. The threshold (dashed line) is 6.

For the other research areas, there was no evidence value higher than the threshold, meaning that no fault was found.

Table 4-3. Prior parameters vs posterior parameters.

Model's parameters θ	Fault's parameters	Prior parameters	Estimated posterior parameters Via NS	Estimated posterior parameters Via GN
Distance to fault (d_f)	3 m, 8 m	0.1 m	2.98 m, 3.01 m	7.98 m, 8.06 m
Fault's length (L_f)	14 mm	5 mm	13 mm	12.9 mm
Sensitivity regarding fault's position			0.02, 0.01	0.02, 0.06

Table 4-3 shows the model's prior and posterior parameters. To see which method is more accurate, we calculate their sensitivities to the faults' position. We find that GN is more sensitive to the fault's prior position changes than NS. As a result, the Bayesian evidence solved via GN is sufficient to detect both chafing faults, but it is less accurate than NS. Moreover, the process via NS took almost 2 hours to track down these chafing defects, while it took only 5 minutes via GN method which make it faster than the NS method.
Using these posterior parameters (Table 4-3), the reflected signal at the cable entry via GN (solid red line) and via NS (dotted blue line) are graphed in Figure 4-15.

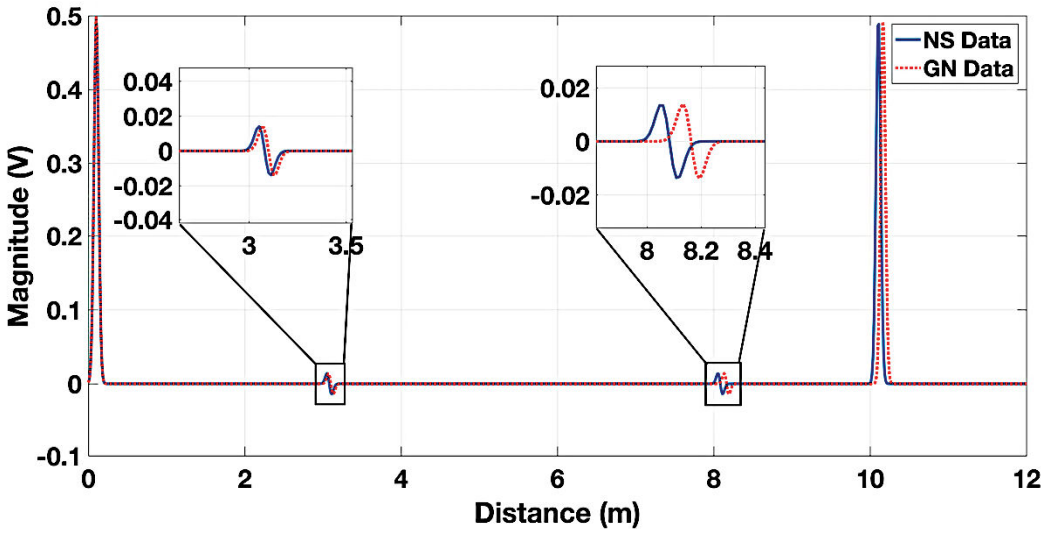

Figure 4-15. TDR response simulated signal via GN (dotted red line) and via NS (solid blue line). The first peak represents the Gaussian injected signal. The second and third peaks are caused by the impedance discontinuities due to the chafing fault.

In summary, the results of the present study demonstrate the efficiency of the probabilistic inference in detecting many chafing faults in a coaxial cable. Furthermore, we provided the first insight into detecting chafing faults via NS and GN. In the next section, we apply the probabilistic approach to a cable network.

4.5 Cable network application

4.5.1 Network modelling

Three sets of cables were designed for this research work. The cables were grouped into three types: Type A, Type B, and Type C. The cable C and B have one chafing fault at $d_f = 6\,\mathrm{m}$. This chafing fault is the same chafing fault as shown in Figure 1-14 that we treated in the previous applications.
Type A: nominal coaxial cable (L_1: 4 m).
Type B: nominal coaxial cable (L_2: 5m).
Type C: chafed coaxial cable (L_3: 3 m).

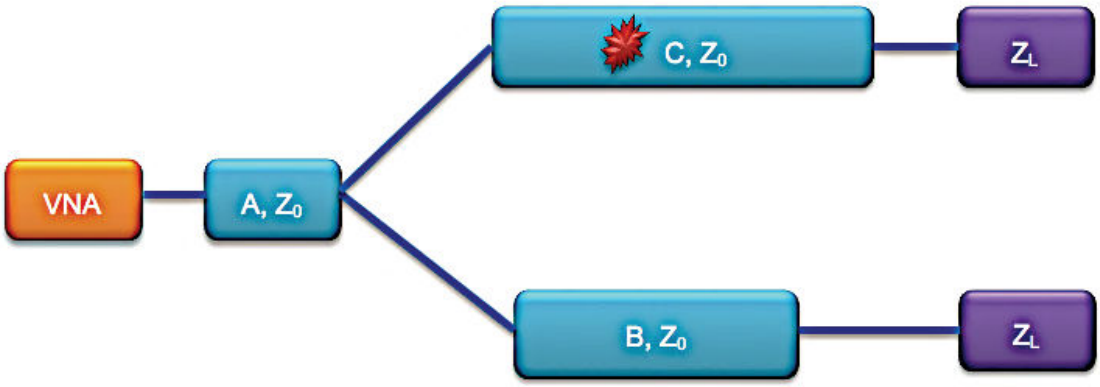

Figure 4-16. This network cable has two faults, placed in cable C and cable B. Z_L is equal to the cable impedance Z_0.

Using the model presented in Figure 4-16, the simulated reflected signal at this cable network entry whose $SNR_{noisy\_f} = 10\ dB$ is depicted in Figure 4-17.

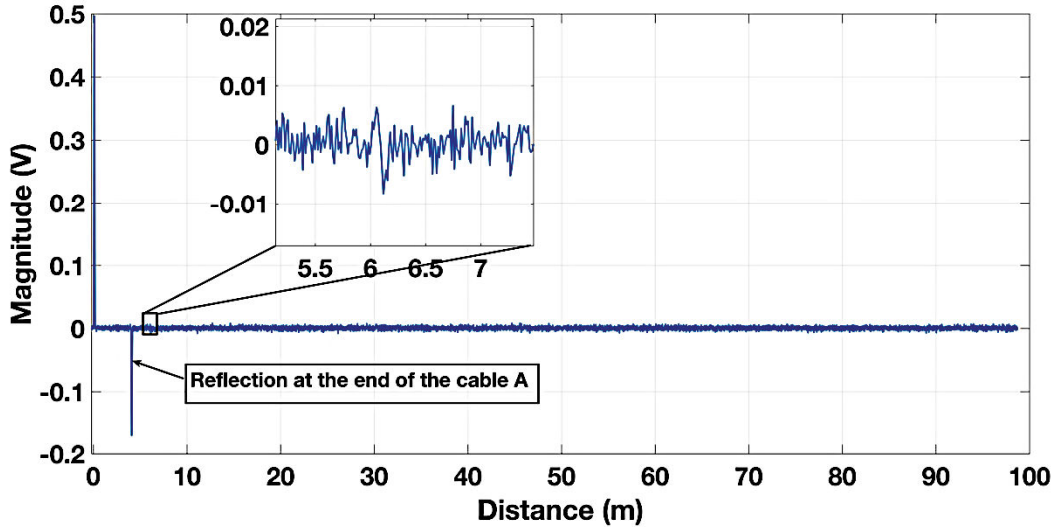

Figure 4-17. The reflected voltage in the 9 m cable network with one chafing fault at 6 m.

After comparing between the three denoising methods in the section 1, the evaluation methods indicated that the DWT and LMD failed to denoise properly the reflected signals of a simple coaxial cable with one and two chafing faults, while EMD shows promising results with some limitations. As a result, EMD is the method that we retain to denoise the signal depicted in Figure 4-17. Our input signal is the reflected signal (Figure 4-17) whose $SNR_{noisy\_f} = 10\ dB$. The EMD method decomposes the signal of Figure 4-17 into eleven Intrinsic Mode Function (IMFs). After eleven iterations, the residual is non-oscillating signal which stops the EMD algorithm. The first IMF corresponds to fast oscillation while the eleventh IMF corresponds to slow oscillation. As a reminder, the proposed method is divided into three steps. First, the signal is decomposed into different IMFs. Second, the first IMF is eliminated because it contains the maximum of the noise. Finally, the signal is reconstructed after removing the first IMF. Figure 4-18 displays the outcomes of applying the EMD denoising scheme to the one-fault reflected signal after eliminating the first IMF. Its

$SNR_{denoised\_EMD} = 12.1\,dB$ which is obviously higher than $SNR_{noisy\_f} = 10\,dB$. Therefore, using the EMD method, The SNR has 2.1 dB improvement. In addition, in order to examine and improve the EMD performances, we consider a 9-m nominal cable without any chafing fault which has the same topology as the one-fault cable illustrated in Figure 4-16. In this time, for the EMD decomposition, our input signal is the reflected signal at the entry of the three meters nominal cable. Its signal noise ratio SNR_{noisy} equals the signal noise ratio of the one-fault cable, $SNR_{noisy} = SNR_{noisy\_f} = 10\,dB$. Moreover, the generated noise is the same than the one with the one-fault cable. We apply the algorithm shown in Figure 2-1 to our new input signal. After that, we reconstruct the signal by removing the first IMF. Then, we subtract the reconstructed reflected signal at the entry of the 9 meters one-fault cable from this reconstructed signal. We obtain the signal shown in Figure 4-19. After that, we calculate the signal noise ratio SNR_{subs_EMD} of this signal only for the fault interval defined as [5.9-6.5] m in order to extract and detect the soft fault regarding the noise. The $SNR_{subs\_EMD} = 29\,dB$, as a result, the fault amplitude is higher than the noise level. Consequently, we detect the fault better than using only the time domain reflectometry without the denoising methods. Besides, the EMD method creates some side effects at the beginning and the end of each signal's peak. This subtraction is not realisable in real time because we could not generate the same noise for the both signals (nominal cable, and one-fault cable). Nevertheless, the solution could be measuring the reflected signal of the nominal cable several times. Then, we calculate the mean amplitude of the signal which is decomposed and reconstructed, after that, by the EMD algorithm. After that, we subtract it from the reconstructed reflected signal at the one fault cable entry.

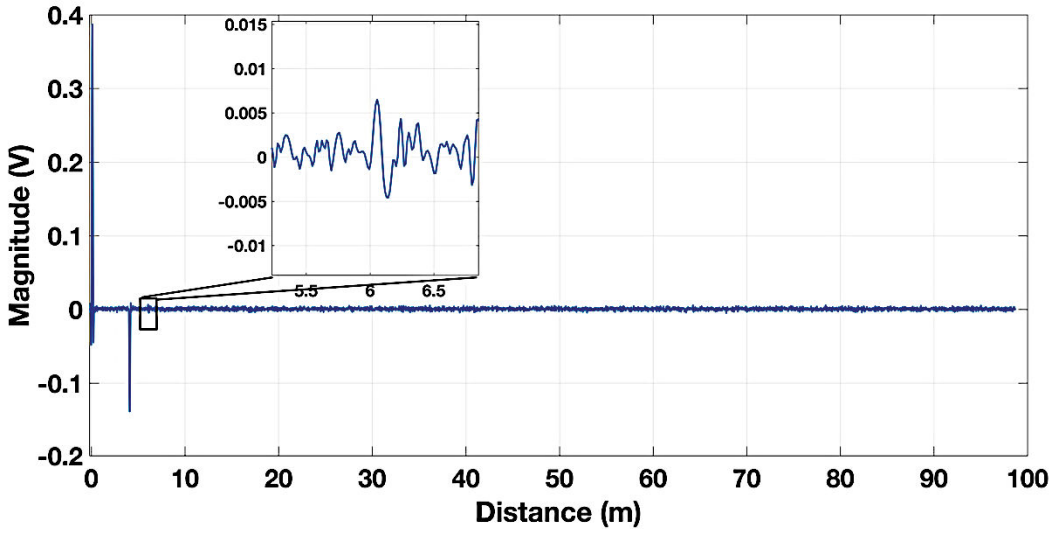

Figure 4-18. The denoised signal of 9 m coaxial cable with one chafing faults at 6 m via EMD method.

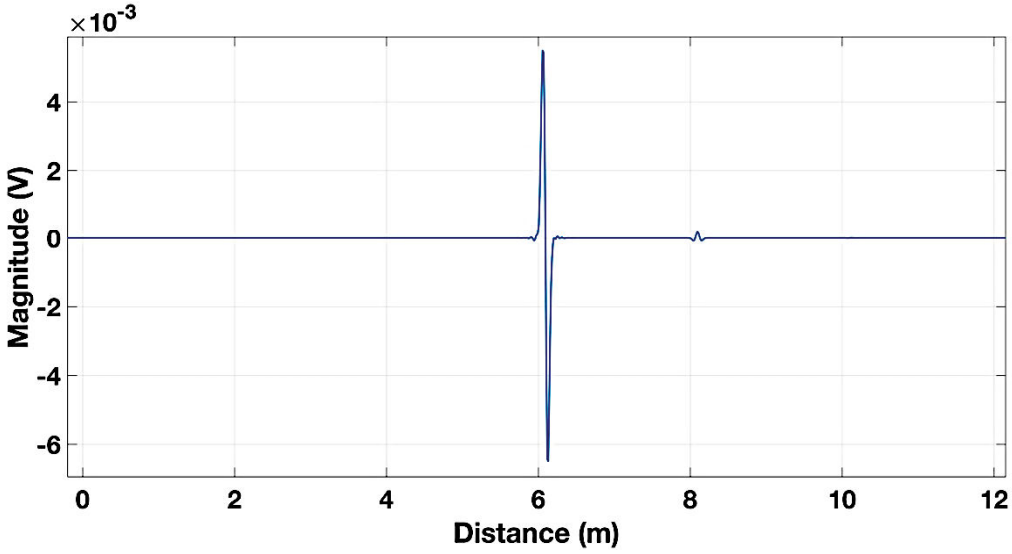

Figure 4-19. The subtraction between the reconstructed reflected signal at the entry of the 9 meters faulty cable and the reconstructed reflected signal at the entry of the 9 meters nominal cable ($SNR_{noisy\_f} = 10\ dB$).

Even denoising the signal with the EMD method, it is barely to detect the chafing fault at 6 m via the TDR. To overcome this, the time frequency analysis will be applied. The section 1 employed the STFT, the WVT, and the CWT for time–frequency decomposition. In the chapter 1, we conclude that both the STFT and WVT fail to identify simple or multiple chafing faults on a simple coaxial cable while the CWT method showed promising results. Consequently, the CWT will be applied on the denoised signal displayed in Figure 4-18. The scalogram is represented in Figure 4-20. We used a Daubechies wavelet with thirteen vanished moments for the tested signal. As depicted in Figure 4-20, CWT was able only to barely detect the chafing fault at 6 m.

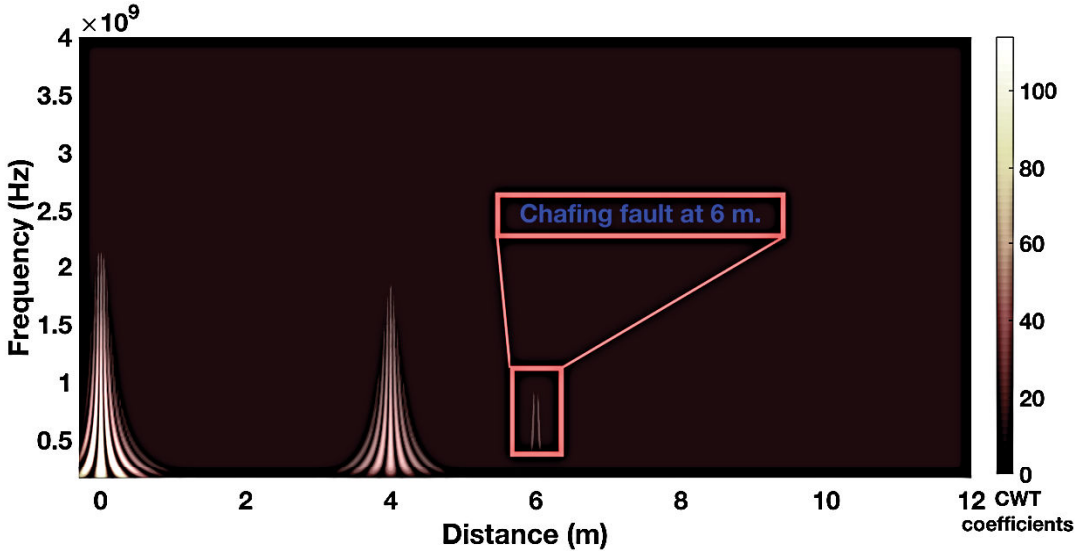

Figure 4-20. CWT of the 9 m cable network with one chafing faults at 6 m.

As a result, the CWT method, although quite a sophisticated technique, it can be used in soft fault detection only on a simple cable not on a cable network. It is, therefore, clearly of interest to reanalyse the data with a different methodology, such as the Bayesian approach

defined in this chapter. Using the model, we exposed in Figure 4-16, we applied the Bayesian approach solved via GN and NS.
To accelerate the process, the Bayesian inference is applied in a small interval referred to as the research area [5.9-6.5] m (Figure 4-21). In fact, the Bayesian evidence is calculated over the entire length of the cable but only the results corresponding to the research area [5.9-6.5] m are represented.

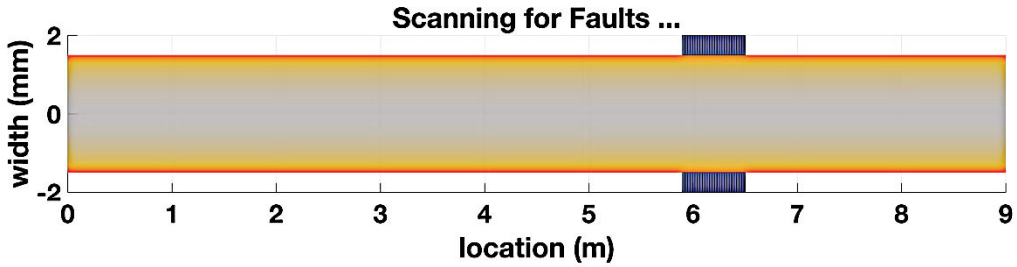

Figure 4-21. The 9-m cable network is represented by the yellow section. The research area is the blue sections [5.9–6.5] m.

For each point in our first research area, the evidence using the Bayesian approach solved via NS and GN was calculated.

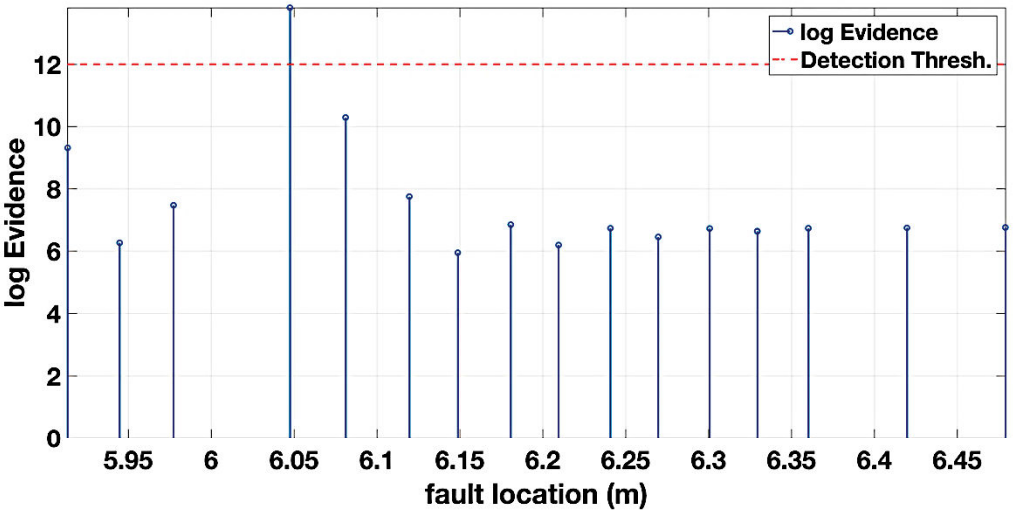

Figure 4-22. The evidence via GN (straight line with pentagram) is represented indicating the fault position in the research area [5.9–6.5] m. The threshold (dashed line) is 12.

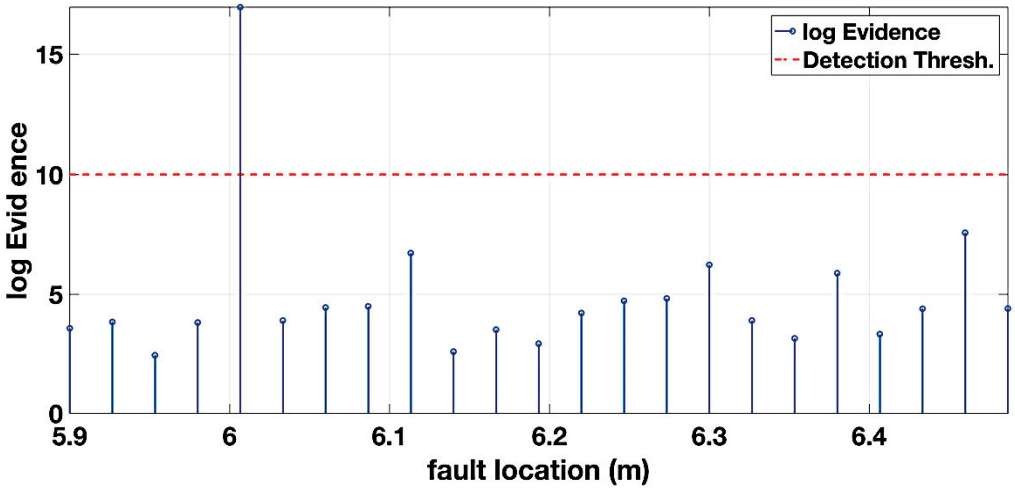

Figure 4-23. The evidence via NS (straight line with pentagram) is represented indicating the fault position in the research area [5.9–6.5] m. The threshold (dashed line) is 10.

The Figure 4-22 and Figure 4-23 depict the log evidence calculated by using GN and NS respectively. They show that only one evidence that is higher than the threshold for both methods which betokens the existence of the fault and its position. The fault exists at 6.01 m using Nested Sampling however it is at 6.05m using Gauss Newton.

Table 4-4. Prior parameters vs posterior parameters

Model's parameters θ	Fault's parameters	Prior parameters	Estimated posterior parameters Via NS	Estimated posterior parameters Via GN
distance to fault (d_f)	6 m	0.1 m	6.01 m,	6.05 m,
fault's length (L_f)	0.014 m	0.005 m	0.015 m	0.012 m
Sensitivity regarding fault's length			0.001	0.002

Table 4-4 depicts the model's prior and posterior parameters. Thanks to the probabilistic inference, these parameters are almost similar for both methods. To see which method is more accurate, we calculate their sensitivities to the fault's length. For choosing the more significant position, we calculate their sensitivities to the fault's prior length. As a result, NS is more accurate than GN because GN is more sensitive to the fault's prior length and position changes. In Figure 4-24, two curves are depicted indicating that the chafing faults are detected (the third peak), which validates our Bayesian approach solved via NS or via GN. The fault's amplitude calculated via GN is smaller than the one calculated via NS because the GN is more sensitive than NS to the prior parameters such as the fault's length and position. In the other hand, NS took almost 2 hours to identify the defect while GN took almost 5 minutes. In Figure 4-24, the second peak is due to impedance discontinuities at 4 m, at the end of cable A.

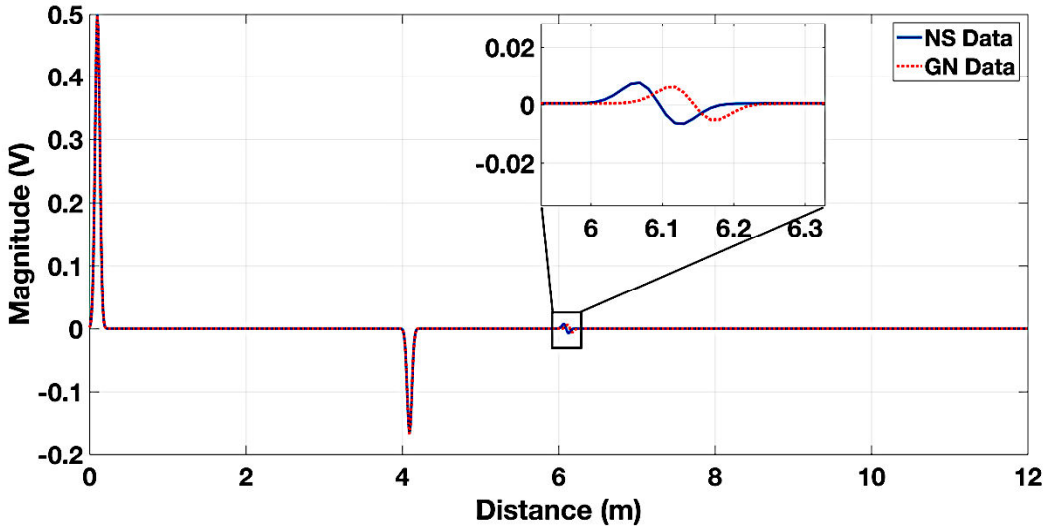

Figure 4-24. TDR response simulated signal via GN (dotted red line) and via NS (solid blue line). The first peak represents the Gaussian injected signal. The second peak matches the reflection at 4 m, the end of cable A. The third peak stems from the impedance discontinuity which is ascribable to the chafing fault at almost 6 m.

In summary, the results of the present study demonstrate the efficiency of probabilistic inference solved by NS and GN in detecting many chafing faults in a coaxial cable. Furthermore, the Bayesian approach is susceptible to prior parameters. Indeed, the Bayesian approach solved by GN is faster than the Bayesian approach solved via NS. Moreover, to identify which cable has the chafing fault in the cable network, the model of the cable used should be modified. To overcome this, the chaotic time domain reflectometry is discussed in the next chapter.

4.6 Conclusion

Recently developed methods of Bayesian approaches and models have been presented. The Bayesian approach can be ranked by evaluating the evidence and a model's ability to fit the data with its complexity. In addition, the model's posterior probabilities depend on the subjective priors that are assigned to them. For many cable problems, the prior parameters make it possible to perform the optimization of the Bayesian approach. In the examples discussed, the evidence was used to identify the wiring faults in the cable model and to indicate the fault position and length.

A solution has been obtained to maximize the optimization problem. The solution applies to a non–linear interpolation model but depends on the GN approximation and NS approach. Multiple simulations have been made. In each case, a function of x has been derived that predicts the information for a simulation at that x. This function can be used to search for an optimal value of x called the posterior parameters. This function, which has been made to lucidly discuss the Bayesian approach and how it helps to detect chafing faults in cable networks, has been solved via NS, although the solution process requires several hours, and via GN, which makes the method's convergence quicker, although it is more dependent on prior parameters and thus less flexible.

This chapter describes the basics of probabilistic inference and how Bayesian evidence can be employed in soft fault detection. The results validate the effectiveness of this approach solved via NS or GN. However, NS pinpoints the fault more accurately than GN. It is important to notice that the capacity for chafing fault detection using the Bayesian approach does not depend on how the cables are arranged or terminated, but it does depend on the fault dimensions and the prior parameters. Additionally, a possible weakness of the Bayesian

approach solved via either NS or GN is that it estimates the utility of a simulation assuming that the model is correct.
Further work is needed to formalize the relationship of this framework to the model. Using the Bayesian approach, it is possible to detect chafing faults in the underlying assumptions implicit in the data and model being used. For this reason, in the next chapter a new method termed chaotic time domain reflectometry is discussed and illustrated via different cable topology examples.

Chapter 5: Chaotic Time Domain Reflectometry

5 Chaotic time domain reflectometry

5.1 Introduction

In the previous chapters, different advanced methods have been studied and developed in simulation for the fault detection. In our last chapter, we propose to analyse a last method based on the chaos time domain reflectometry (CTDR). In particular, this chapter aims to propose a specific measurement bench for fault detection.

Some literature: 'The flap of a butterfly's wings in Brazil set off a tornado in Texas'. This disturbance created by the flight of a butterfly is known as 'the butterfly effect', which is the metaphor expression used by Lorenz to describe the idea of chaotic effects. The chaotic signal is a pseudo-noise signal generated from a deterministic system whose variations strongly depend on its initial conditions. Moreover, it is also non-periodic and unpredictable over the long term, which makes it highly useful in fields such as astrophysics, computer science, aerodynamics, and signal processing.

In the literature, we find several kinds of chaotic signal [156]-[163]. For instance, the Lorenz system, the logistic map, the Bernoulli map, the Van der Pol system, the Holling Tanner model, Volterra Lotka equations, Baker's map, the Bogdanov map, Rayleigh Benard convection, etc.. have been studied in various scientific domains [161]-[162]-[163]. In particular, we note the Lorenz system, the logistic map, and the Bernoulli map have been already studied for reflectometry-based applications, especially in fault detection [156]-[158]-[159]-[160].

In terms of fault detection, a method has been proposed in [159]. The chaotic signal is generated using a Colpitts oscillator. Indeed, it has been demonstrated than using a specific input current, this oscillator can produce an output behaviour. Measurements with different hard and soft faults leads to good results for the location of open circuits, short circuits, impedance discontinuities and other different damage on wires. Simulations have been also perform in order to prove the ability for real time diagnosis. This method is quite efficient for single cable topology, however, the oscillators must be well designed in order to propose a chaotic behaviour. Moreover, this chaotic behaviour cannot be managed as it depends on the oscillator design. As a further matter, an average measurement from 1000 measures must be performed in order to reduce the noise of the test bench. Thus, another method has been proposed in [156]-[158]. In [158], it has been demonstrated that a combination between the logistic map and the Bernoulli map leads to a chaotic behaviour "choosing properly" the parameters. Moreover, the orthogonality of the generated chaotic signals has been shown modifying slightly the parameters. Hence, simulations highlight the ability of the hard fault detection for complex wire network. Thus, this chaotic signal is used in [156] to demonstrate the efficiency of the method in a high noisy cable network, and, for real time measurements. From a measurement bench where the chaotic signal is generated with an arbitrary wave generator, the sensitivity analysis carried out in this article was promising for the soft fault detection. As a consequence, in our work, we focus on soft fault detection for more or less complex cables network. In particular, we propose to compare the efficiency of two chaotic signals (the one used in [156] and the Lorenz signal) in terms of soft fault detection. In another hand, we proposed to validate the proposed method in measurement from a specific measurement bench. The process for the fault detection has been improved in comparison with [156] and leads to demonstrate the ability to detect soft fault using the CTDR.

First a sensitivity analysis is carried out from simulations in order to compare the efficiency of two chaotic signals in terms of soft fault detection. Then, the measurement process is depicted and the experimental results are discussed.

5.2 Chaotic signals

5.2.1 Introduction

In this section, we introduce several chaotic signals. In particular, the choice of the use of two different chaotic signals is discussed in terms of fault detection.
First, we can define a chaotic signal with two general conditions:
- it must be sensitive to initial conditions, that means that small causes can have great effects and,
- it must be recurrent.
It exists different kind of chaotic signal as the ones illustrated in Figure 5-1.

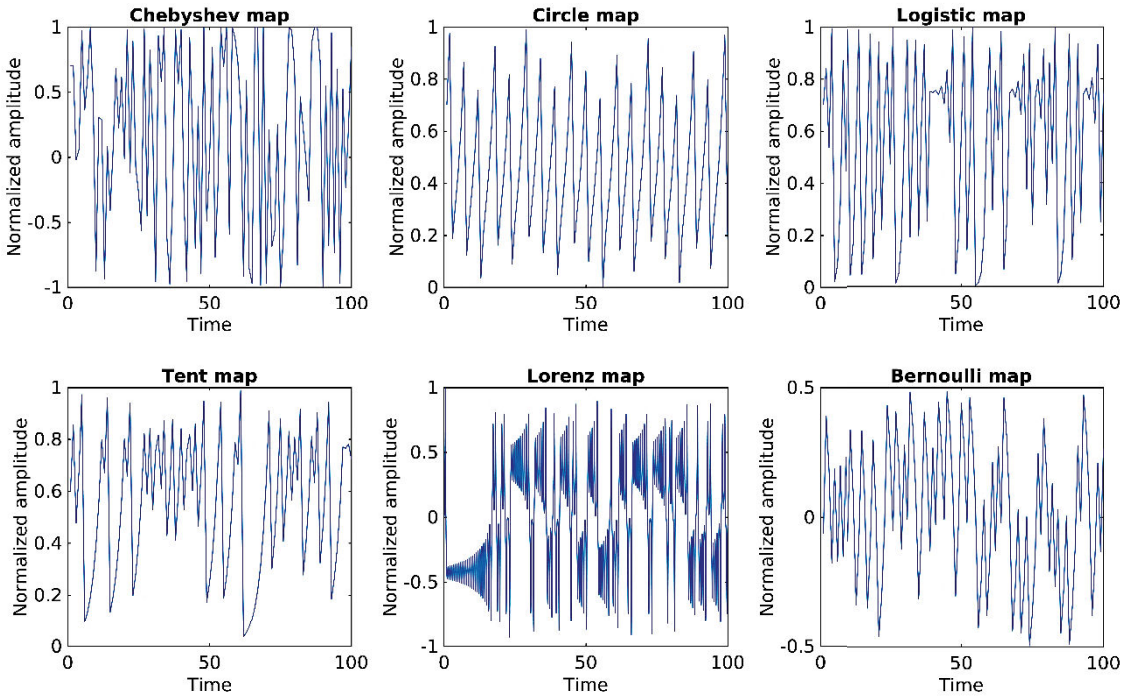

Figure 5-1. Different chaotic signals.

For the soft fault detection, we decide to use two different chaotic signals which are 1) a combination of the logistic map and Bernoulli map and 2) a Lorenz signal. First of all, a simulation analysis is carried out. For this, we choose the 3 meters length cable which a 14 mm length chafed fault at 1 meter as in the previous chapters in order to be consistent. Nevertheless, the manner to obtain the reflected signal is different in this chapter. Indeed, the previous proposed method required to use a Fourier transform which can lead to wrong results for chaotic signals. Therefore, we decide to build a code in the time domain based on the transmission line theory. The simulated cable is represented in Figure 5-2. Hence, the step mesh dx is fixed to 1 mm while the time step dt is equal to $\frac{dx}{2*c}$ with c the celerity. Indeed, for chaotic signals it is better to choose $dt < \frac{dx}{c}$ using the tansmission line theory. The number of iteration is $Nt = f\left(\frac{Tmax}{dt}\right)$ with, f the function which rounds the proposed ratio to the nearest integer less than or equal to that ratio, and, $Tmax \gg \frac{3000\mathrm{dx}}{c}$. The characteristic impedance Z_c of the cable 50 Ω and the one of the chafing fault Z_f is 62.5658 Ω. Each segment dx is defined as an inductance and a capacitance in parallel as shown in Figure 5-2. Between 1 m to 1.014 m the inductance is defined as $L_f = \frac{Z_f}{c}$ and the capacitance as $C_f = \frac{1}{Z_f * c}$. Outside this interval

we have $L = \frac{Z_c}{c}$ and $= \frac{1}{Z_c * c}$. Hence, the current and the voltage can be computed for each segment for the injected chaotic signal solving the following equations:

$$L\frac{\partial I}{\partial t} + RI + \frac{\partial V}{\partial x} = 0, \tag{5.1}$$

$$C\frac{\partial V}{\partial t} + \frac{\partial I}{\partial x} = 0 \tag{5.2}$$

These equations are solved using the finite difference process in the time domain as mentioned previously. Then, we do the correlation between the injected chaotic signal and the obtained signal. Finally, the convolution between the right-side of this signal and a Gaussian signal is carried out in order to filter our signal and to obtain a smooth reflected signal.
As the chosen chaotic signals are parameters dependent, the sensitivity about the parameters of each signal is studied in the next sections in terms of soft fault detections. Furthermore, the sensitivity on the fault detection against the used chaotic signal is also carried out in the next sections. In the next paragraphs, both used chaotic signals are depicted.

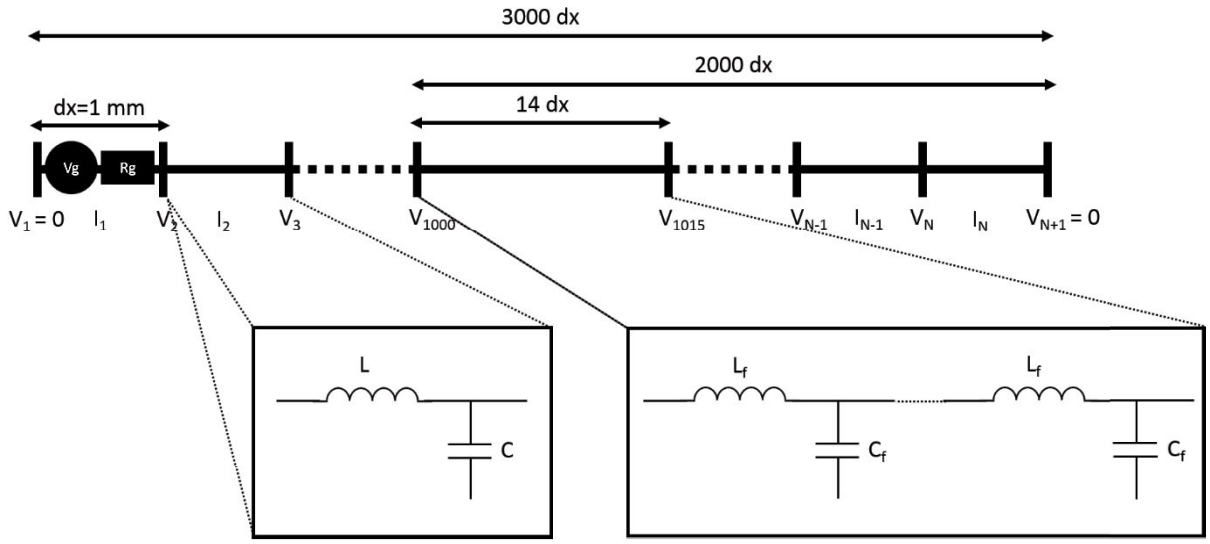

Figure 5-2. Transmission line model of the coaxial cable.

5.2.2 Combination of Logistic map and Bernoulli map

5.2.2.1 Definition

In this subsection, the combination between the logistic map and the Bernoulli map is presented.
The logistic map is a chaotic second-order polynomial (5.3) using non-linear dynamical equations.

$$x_{m+1} = kx_m(1 - x_m), m = 1, 2,...,M, \tag{5.3}$$

where $k \in [0,4]$, and M is the number of samples.
Usually, the Bernoulli map (5.4) is defined as follow:

$$y_{n+1} = \begin{cases} By_n + 0.5 & \text{if } y_n > 0 \\ By_n - 0.5 & \text{if } y_n < 0' \end{cases} \quad (5.4)$$

with B a constant value.
We decide to combine the both maps. Using initial conditions $\{x_0, y_{m,1}\}$, the logistic map generates the Bernoulli map (5.5) as follow:

$$y_{m,n+1} = \begin{cases} B_m y_{m,n} + 0{,}5 & \text{if } y_{m,n} < 0 \\ B_m y_{m,n} - 0{,}5 & \text{if } y_{m,n} > 0 \end{cases} \quad n = 1, 2, \ldots, N, \quad (5.5)$$

with

$$B_m = 1.4 + 0.6x_m. \quad (5.6)$$

where N is the number of samples. Therefore, the total number of samples of the chaotic signal is M × N. The chaotic signal is $S = [Y_1, Y_2, Y_3, \ldots, Y_M]$, where $Y_1, Y_2, Y_3, \ldots, Y_M = [Y_{m,1}, Y_{m,2}, Y_{m,3}, \ldots, Y_{m,M}]$ is generated using (5.3), (5.5) and (5.6). This kind of signal with these choices of parameters values ensures a chaotic behaviour as demonstrated in [145]. In particular, we note a specific property related to the number of sample which is that the noise level of this chaotic signal decreases as the number of the samples increases. Indeed, the noise level of the chaotic signal noted L can be calculated using (5.7) according to [147]. For instance, the S chaotic signal with 65000 samples has a −33.69 dB noise level, which is lower than the one with 10000 samples which has a -28.00 dB noise level as shown in Figure 5-3.

$$L = -7\log 10\,(NM) \quad (5.7)$$

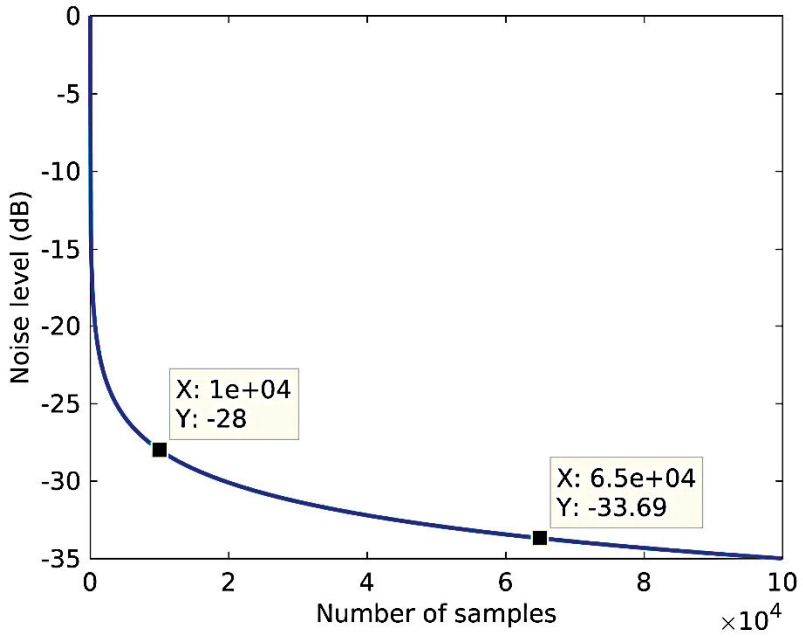

Figure 5-3. Noise level versus sample number.

Finally, the chaotic signal S has two parameters which are the number of samples and the value of k (in addition to the initial conditions). In the next subsection, a parametric study is carried out in terms of soft fault detection.

5.2.2.2 Parametric study

First, the sample number sensitivity is studied in terms of fault detection. Four chaotic signals are compared; 1) a 20000 samples signal noted 20k signal, 2) a 40000 samples signal noted 40k signal, 3) a 50000 samples signal noted 50k signal, and, 4) a 65000 samples signal noted 65k signal. For each signal, N is fixed to 100 while M takes the value 200, 400, 500 or 650 respectively for the 20k signal, 40k signal, 50 signal and 65k signal. These generated signals are illustrated in Figure 5-4 using $k = 3.9, x_0 = 0.1$ and $y_{m,1} = -0.4$. By definition, these signals are surrounded between -0.5 V and 0.5 V with the chosen parameters.

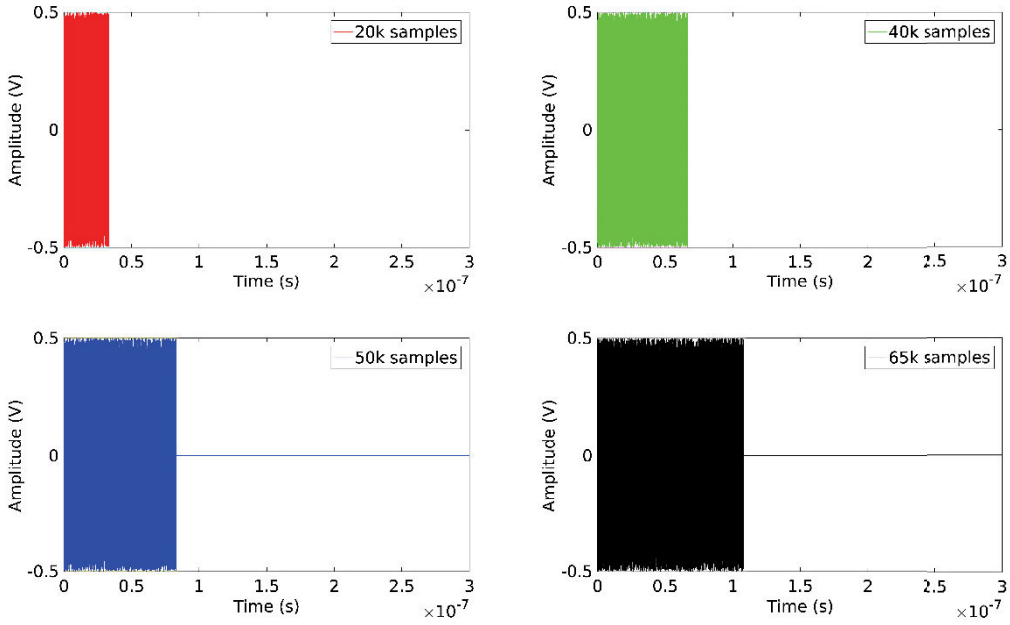

Figure 5-4. The different generated chaotic signals with k=3.9.

Then, each signal is the injected voltage V_g of Figure 5-2 and the reflected signal is computed using the iterative procedure presented in the subsection 5.2.1. The obtained reflected signals are illustrated in Figure 5-5. It appears clearly the peak related to the soft fault at 1 meter and the one related to the "hard fault" at 3 m. It seems that the peak-to-peak amplitude related to the soft fault at one meter increases with the number of samples of the injected signal. Moreover, as expected according to (5.7), the noise level seems to decrease with the number of samples of the injected signal. In order to quantify these assumptions, we define an indicator as follow:

$$\Delta = 20\log_{10}\left(\frac{A_{\text{soft default}}^{\text{peak-to-peak}}}{\sigma_{[0,0.95]}}\right), \tag{5.8}$$

with, $A_{\text{soft default}}^{\text{peak-to-peak}}$ the peak-to-peak amplitude related to the soft fault and $\sigma_{[0,0.95]}$ the standard deviation on the interval [0, 0.95] m. Thus, the indicator Δ can be understand as a signal to noise ratio which is hard to define for a chaotic signal because of its own structure. The higher the indicator Δ is, the better the soft fault detection is. For instance, we can considerer the fault detection acceptable while $\Delta > 6$ dB which lead to a signal more than twice than the "noise". The results are depicted in Table 5-1. Indeed, the standard deviation decreases with the increase of the number of samples of the injected signal. However, the peak-to-peak

amplitude related to the soft fault is higher for the 40k signal than for the 50k signal or 65k signal. Nevertheless, the "performance indicator" Δ can be considered better increasing the number of samples. As a consequence, for the next paragraph, we will keep the 65k signal and we will apply a variation on the k parameter in order to quantify the sensitivity in terms of soft fault detection.

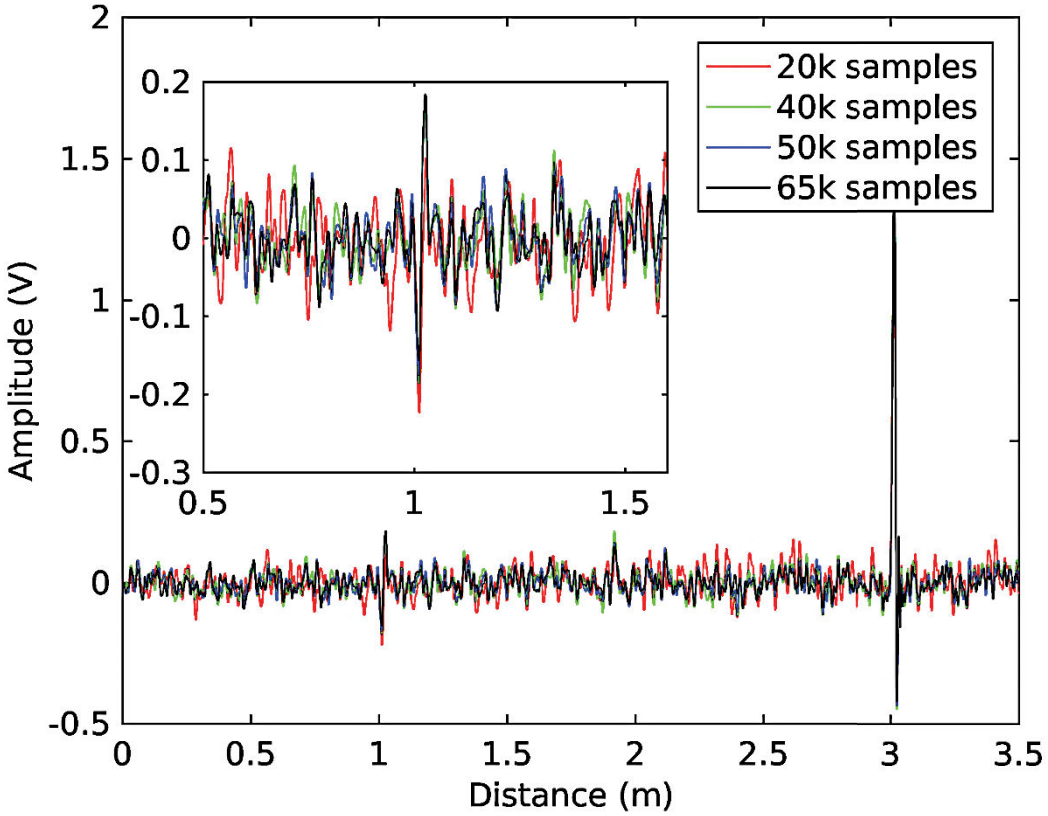

Figure 5-5. Reflected signals for several chaotic signals with different number of samples. The inset is a zoom of the signals on the interval [0.5,1.6] m.

Table 5-1. Performance indicators in terms of fault detection for several chaotic signals with different number of samples.

	20k signal	40k signal	50k signal	65k signal
$A_{\text{soft default}}^{\text{peak-to-peak}}$ (V)	0.3264	0.3521	0.3516	0.3411
$\sigma_{[0,0.95]}$ (V)	0.0389	0.0348	0.0323	0.0310
Δ (dB)	18.4866	20.1130	20.7277	20.8409

Now, the sensitivity analysis about the k parameter of the proposed chaotic signal is carried out. We note a small difference in the manner to generate the chaotic signals choosing to initialize y_m as follow:

$$y_{m,1} = X - 0.5 \; \forall m \in [1..M], \tag{5.9}$$

with, $X \sim U(0,1)$ which means that X is a uniformly distributed random number in the interval [0,1], and, M=650. Therefore, we must use the same $y_{m,1}$ initial vector for each generated signal in order to be consistent for comparison. This random initialization is important in order to ensure a chaotic behavior for some k values. Indeed, with a constant initial value the generated signal can be pseudo-periodic using k=2 for instance. We decide to analyze the

reflected signal with three different values of k. The generated signals are illustrated in Figure 5-6. Using the iterative procedure presented in the subsection 5.2.1, we obtain the reflected signals depicted in Figure 5-7. As previously, it appears the peak related to the soft fault at 1 meter and the one related to the "hard fault" at 3 m with a better dynamic increasing k. Thus, the peak-to-peak amplitude related to the soft fault increases with k. From this figure, conclusions about the noise level is not easy. Therefore, we compare the results with the "performance indicator" defined in (5.8). This time, the standard deviation decreases with the decrease of k. Nevertheless, the "performance indicator" Δ can be considered better by increasing k.

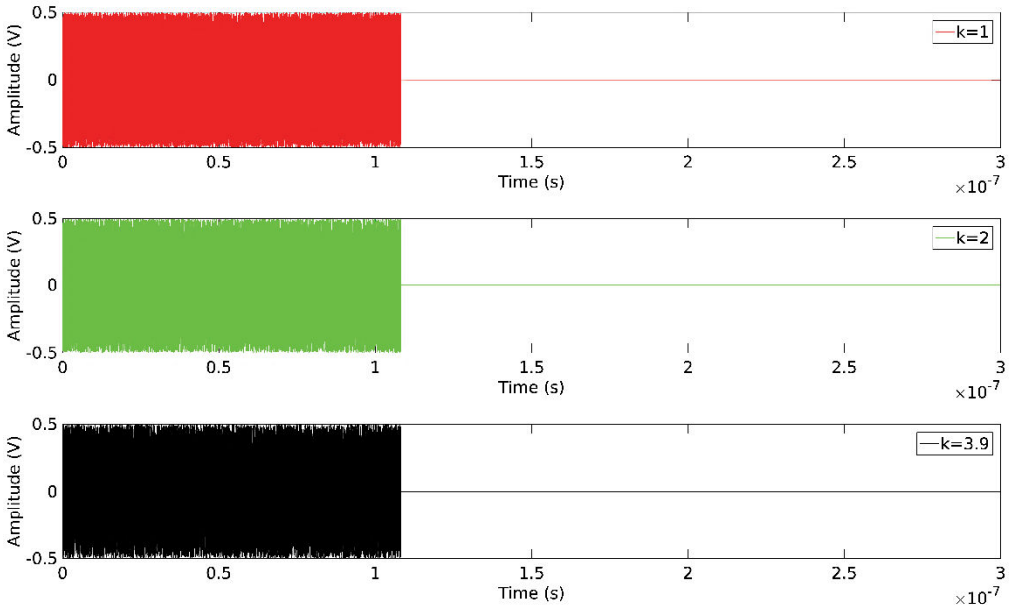

Figure 5-6. 65k signal with different values of k.

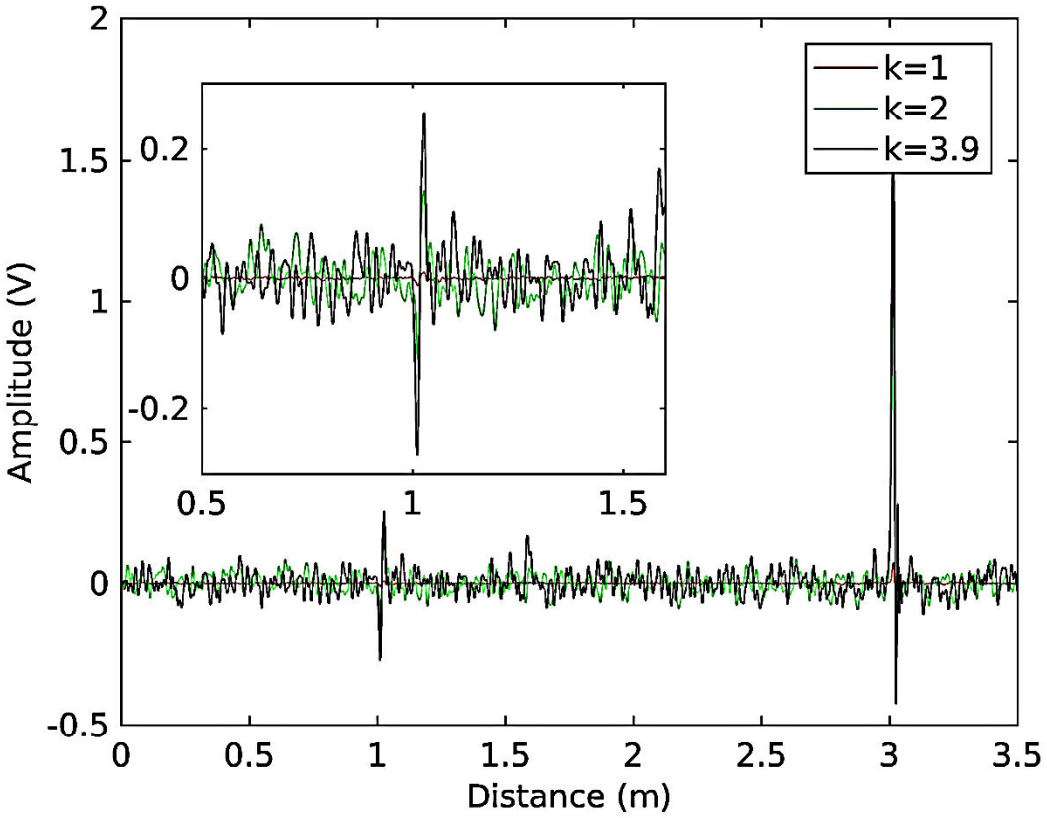

Figure 5-7. Reflected signals for several 65000 samples chaotic signals with different values of k. The inset is a zoom of the signals on the interval [0.5,1.6] m.

Table 5-2. Performance indicators in terms of fault detection for the 65k chaotic signal with different values of k.

	k=1	k=2	k=3.9
$A_{\text{soft default}}^{\text{peak-to-peak}}$ (V)	0.0215	0.2590	0.5259
$\sigma_{[0,0.95]}$ (V)	0.0024	0.0270	0.0344
Δ (dB)	19.1706	19.6304	23.6884

5.2.3 Lorenz chaotic signal

5.2.3.1 Definition

The second chaotic signal used is the Lorentz chaotic signal. Edward Lorenz discovered a three nonlinearly coupled ordinary differential equations called the Lorenz model. The dynamics of the Lorenz chaotic system can be described in the equations:

$$\frac{dx}{dt} = \sigma\big(y(t) - x(t)\big), \tag{5.10}$$

$$\frac{dx}{dt} = \sigma\big(y(t) - x(t)\big), \tag{5.11}$$

$$\frac{dz}{dt} = -bz(t) + x(t)y(t). \tag{5.12}$$

with σ, b and r three parameters. Usually, σ=10, b=8/3 and r is variable. Nevertheless, to obtain a chaotic behaviour the r parameter value must be higher than 24.3. Indeed, according to the Lorentz attractor plots in Figure 5-8, we note that under this threshold value the attractor converges to one value. As a consequence, for instance, the signal x(t) begins pseudo-periodic as shown in Figure 5-9. We note also that the chaotic behaviour can have some lags for r=28. It means that the signal is pseudo-periodic in the first 18 seconds, then, the signal has a chaotic behaviour. Increasing the r value, this lag is reduced. At r=40, the signal has a chaotic behaviour since zero second.

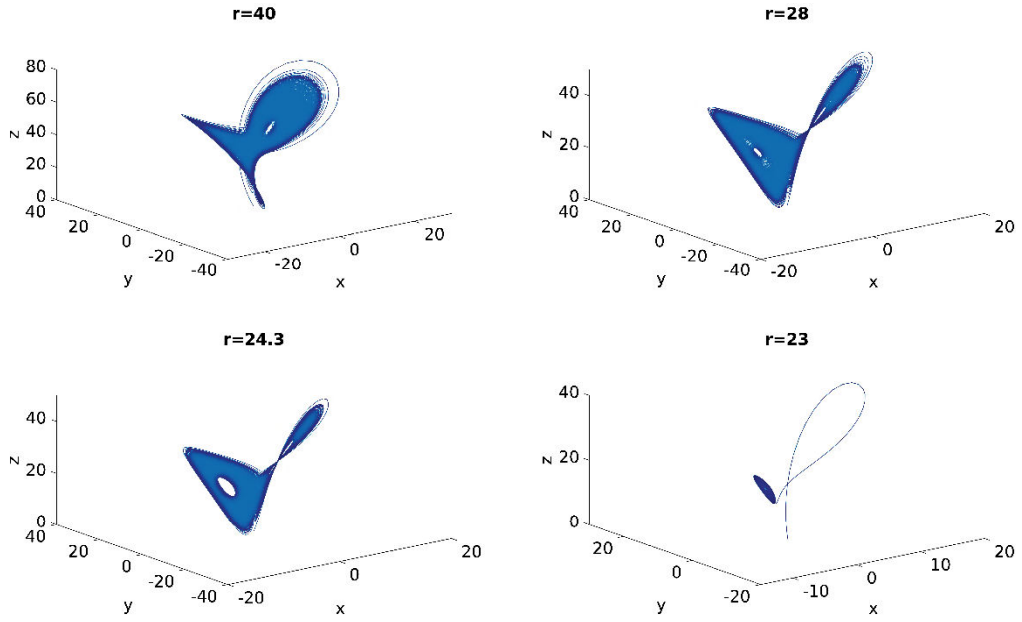

Figure 5-8. Lorenz attractors for different r values.

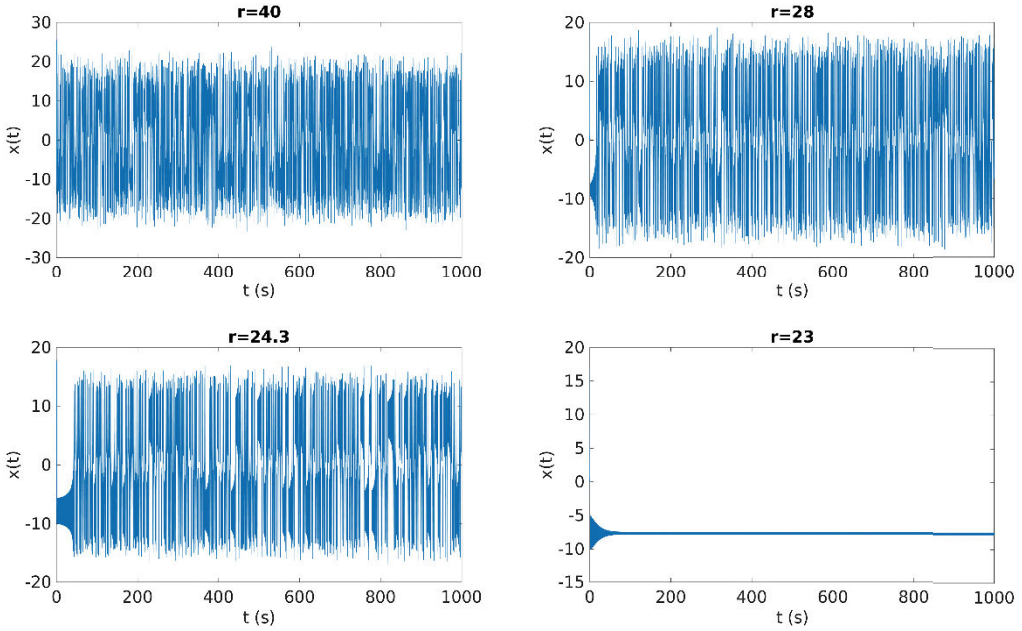

Figure 5-9. Solutions of x(t) for different r values.

Moreover, this discussion about the threshold value and the time lag is also related to the numerical solver of the Lorenz equations. The previous results (Figure 5-8 and Figure 5-9) has been produced solving these equations with a 4th order Runge-Kutta algorithm. We propose to study the impact of the ordinary differential equations (ODE) solver on the x(t) result. Therefore, we compare the result with the 4th order Runge-Kutta algorithm against the result from the forward Euler method which leads to more important errors. Hence, we define the initial conditions t_0=0, x_0=0.1, y_0=0.1 and z_0=0.1. Then, we apply the iterative process below:

$$x_t = x_{t-1} + dT\frac{dx}{dt}, \tag{5.13}$$

$$y_t = y_{t-1} + dT\frac{dy}{dt}, \tag{5.14}$$

$$z_t = z_{t-1} + dT\frac{dz}{dt}, \tag{5.15}$$

$$t_t = t_{t-1} + dT. \tag{5.16}$$

with dT the time step. The time step dT must be well chosen in order to obtain a stable numerical solution with this kind of solving method. In particular, it must be "enough short". We choose two different time steps; dT1=0.0013 s and dT2=dT1/1000. The results are displayed in Figure 5-10. First, it is obvious that the three manners to solve the ODE lead to three different results. We note that the time lag is slightly different from the different solvers. Furthermore, we expected that with a smaller time step (dT2), the solution could converge to the Runge-Kutta solution. Indeed, we can see a better convergence between 18 seconds and 22 seconds. Therefore, it is hard to conclude. We can only said than the time steps required to converge to the Runge-Kutta solution is not acceptable in terms of computation resources.

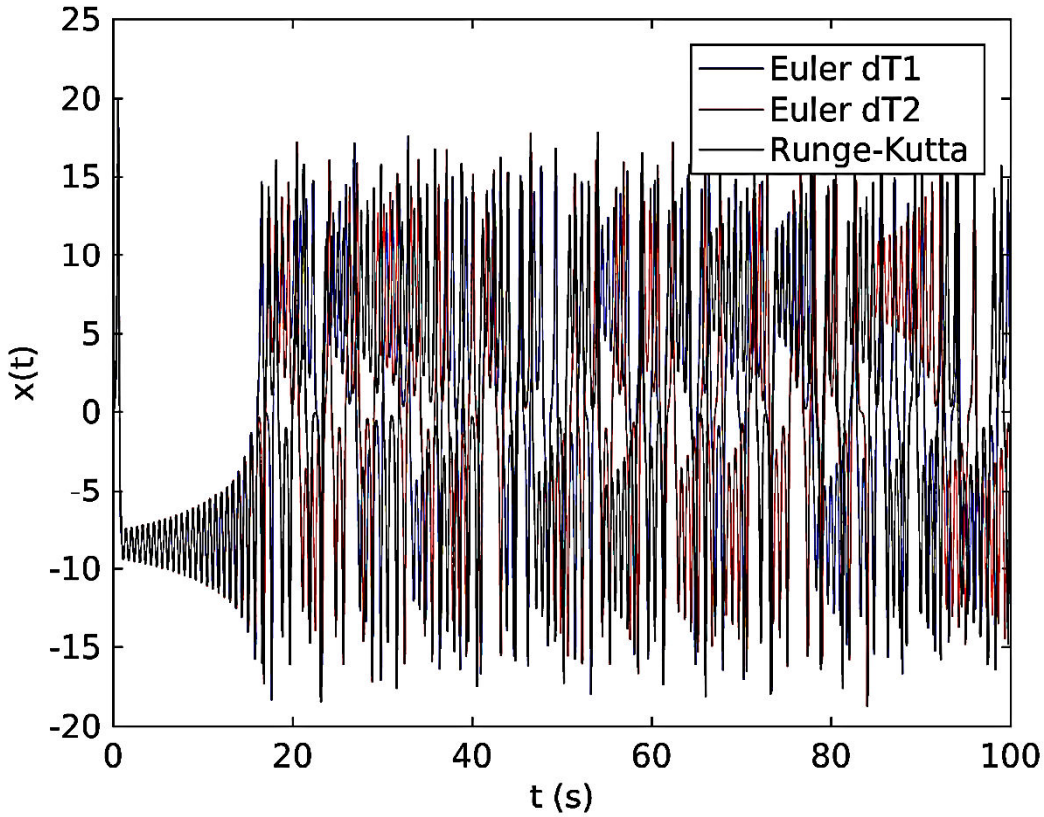

Figure 5-10. Solutions of x(t) with different solving methods.

To conclude, the chaotic Lorenz signal is three parameters signal. By setting σ=10, b=8/3 the third parameter r must be higher than a threshold value which depend on the ODE solver. Moreover, the time lag defined previously is reduced increasing the r value. As a consequence, we decide to compare, in the next subsection, the influence of the r value in terms of soft fault detection for r=40 and r=50 with the 4th order Runge-Kutta solver. Both signals are normalized between +0.5 V and -0.5 V in order to be consistent with the previous chaotic signal studied in the subsection 5.2.2.1. Moreover, for the same reason, the signal is compressed in the time scale with the same dt than previously.

5.2.3.2 Parametric study

First, as previously, the sample number sensitivity is studied in terms of fault detection. We fixe r=40 and we define four injected signals; 1) a 20000 samples signal noted 20k Lorenz signal , 2) a 40000 samples signal noted 40k Lorenz signal, 3) a 50000 samples signal noted 50k Lorenz signal, and, 4) a 65000 samples signal noted 65k Lorenz signal. These signals are the result of the x(t) solved with the 4th order Runge-Kutta solver (with t_0=0, x_0=0.1, y_0=0.1 and z_0=0.1 as initial conditions) are normalized between +0.5 V and -0.5 V and compressed in the time scale with the same dt than the used signals in the subsection 5.2.2.2. Figure 5-11 illustrates the proposed generated signals. Then, each signal is the injected voltage V_g of Figure 5-2 and the reflected signal that is computed using the iterative procedure presented in the subsection 5.2.1. Figure 5-12 displays the obtained reflected signals. As in the subsection 5.2.2.2, the peak related to the soft fault at 1 meter, and, the one related to the "hard fault" at 3 m, appear. We note that the amplitude of the peaks is considerably higher with this kind of signal. Nevertheless, the "noise" is also higher. Therefore, the "performance indicator" defined in (5.8) is used to compare the result in terms of soft fault detection. The results are

summarized in Table 5-3. Clearly, the higher the sample number, the better the soft fault detection.

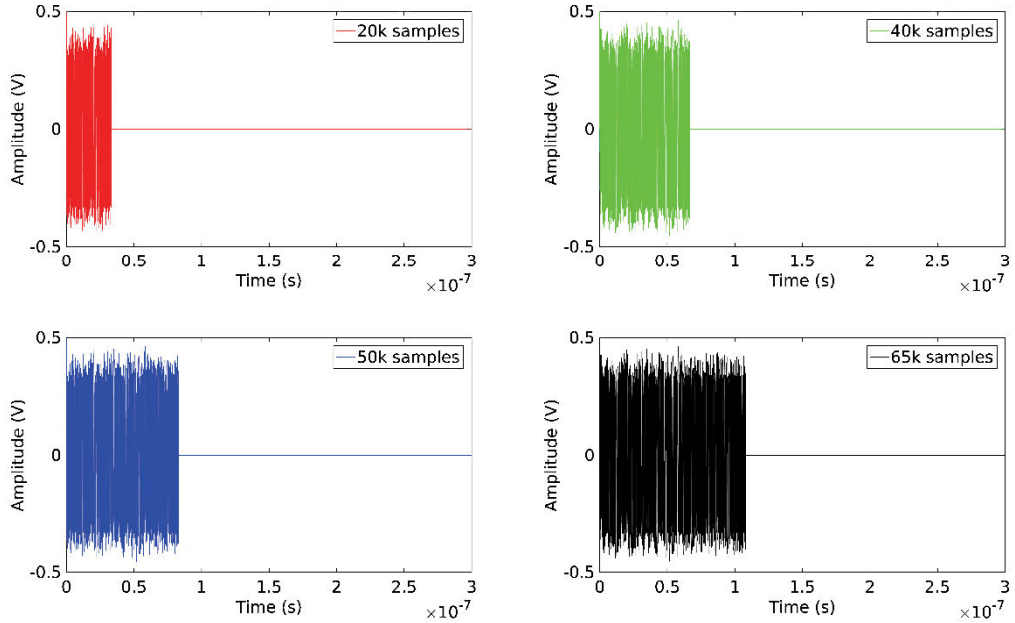

Figure 5-11. The different generated Lorenz signals with r=40.

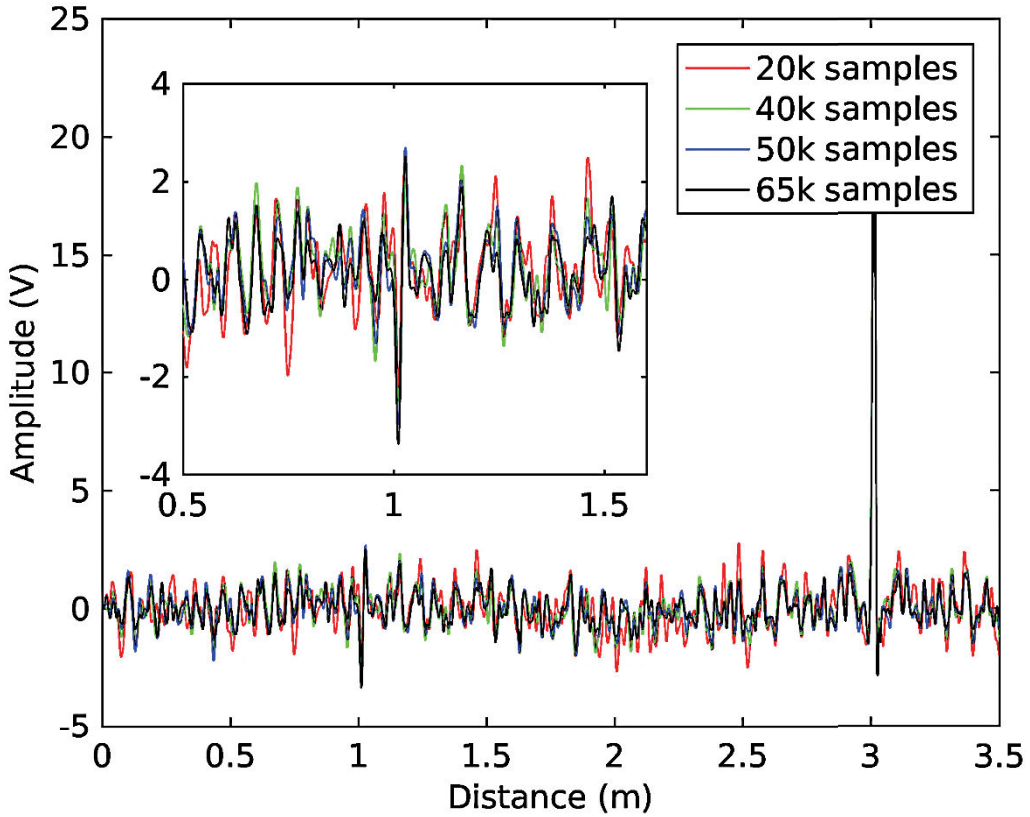

Figure 5-12. Reflected signals for several Lorenz signals with different number of samples. The inset is a zoom of the signals on the interval [0.5,1.6] m.

Table 5-3. Performance indicators in terms of fault detection for several Lorenz signals with different number of samples.

	20k signal	40k signal	50k signal	65k signal
$A_{\text{soft default}}^{\text{peak-to-peak}}$ (V)	4.6538	4.5931	5.6722	5.8960
$\sigma_{[0,0.95]}$ (V)	0.8171	0.6866	0.6813	0.5809
Δ (dB)	15.1111	16.5084	18.4087	20.1292

Now, the sensitivity analysis about the r parameter value of the 65k Lorenz signal is carried out. We decide to analyze the reflected signal with two different values of r (r=40 and r=50). The generated signals are illustrated in Figure 5-12. Using the iterative procedure presented in the subsection 5.2.1, we obtain the reflected signals depicted in Figure 5-14. Obviously, we two peaks related to the faults are highlighted. It seems that increasing the r value leads to a better fault detection. In order to verify this assumption, we use the "performance indicator". Indeed, the Table 5-4 confirms our assumption. The comparison between the 65k signal and the 65k Lorenz signal is carried out in the next subsection.

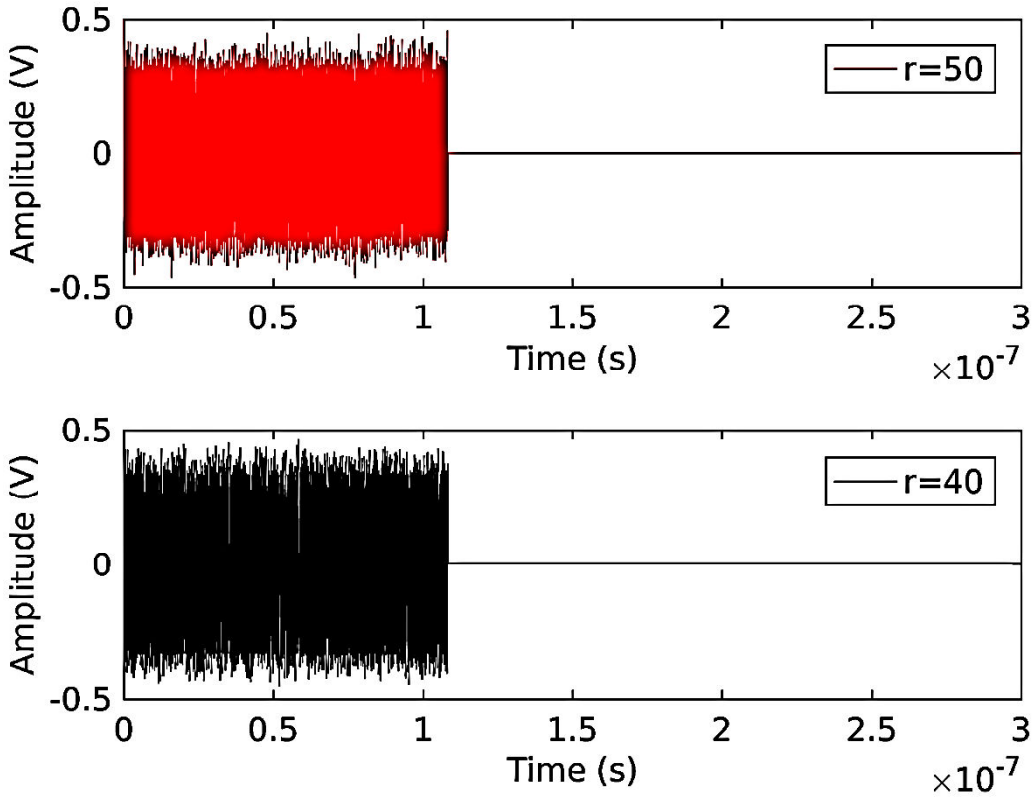

Figure 5-13. 65k Lorenz signal with different values of r.

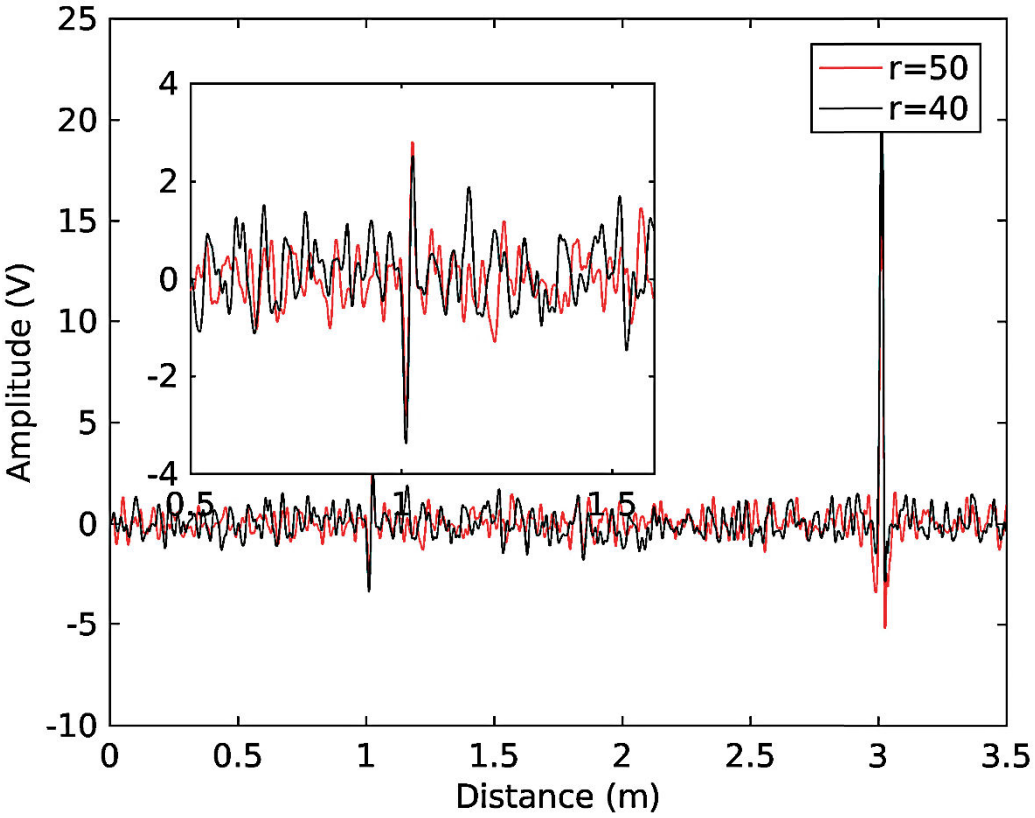

Figure 5-14. Reflected signals for 65k Lorenz signals with different values of r. The inset is a zoom of the signals on the interval [0.5,1.6] m.

Table 5-4. Performance indicators in terms of fault detection for the 65k Lorenz signal with different values of r.

	r=40	r=50
$A_{\text{soft default}}^{\text{peak-to-peak}}$ (V)	5.8960	5.6127
$\sigma_{[0,0.95]}$ (V)	0.5809	0.4465
Δ (dB)	20.1292	21.9860

5.2.4 Conclusions

Finally, we want to validate the chaotic signal in terms of soft fault detection with measurement. We had proposed in this section a simulation analysis with two signals 1) a combination of the logistic map and Bernoulli map and 2) a Lorenz signal. This analysis leads to increase the sample number of each chaotic signal in order to obtain better performances. Furthermore, a sensitivity analysis has been performed on the parameters of both signals. We conclude that for the combination of the logistic map and Bernoulli map, it is better to increase the parameter k. Similarly, for the Lorenz signal, it is better to increase the r value. Table 5-5 summarizes the results for the both signals. We can conclude that it should be better to use the combination of the logistic map and Bernoulli map with 65k samples and k=3.9 than the 65k Lorenz signal with r=50 while the measurement dynamic is acceptable. As a consequence, in the following, the measurement are performed with the combination of the logistic map and Bernoulli map with 65k samples and k=3.9.

Table 5-5. Performance indicators for the 65k signal and 65 Lorenz signal (with the "better parameters" in terms of fault detection)

	65k signal (k=3.9)	65k Lorenz signal (r=50)
$A_{\text{soft default}}^{\text{peak-to-peak}}$ (V)	0.5259	5.6127
$\sigma_{[0,0.95]}$ (V)	0.0344	0.4465
Δ (dB)	23.6884	21.9860

5.3 Measurement bench

The CTDR is based on the same concept as the TDR; the differences are in the exciting signal, which is the chaotic signal generated via a Matlab script from an arbitrary waveform generator AWG801 with a 8 GHz sampling frequency, and in the reflected chaotic signal, which is visualized and collected using a Tektronix DPO 7354 digital phosphor oscilloscope (DPO). The 8 GHz sampling frequency means that the time step $dt = \frac{1}{f_{max}} = 0.125$ ns. The arbitrary waveform generator AWG801 with the sampling frequency of 8 GHz has been chosen in order to stimulate in the good frequency range the coaxial cable under test which is a RG58 coaxial cable. First, the chaotic signal is injected into the arbitrary waveform generator through a T-junction loaded with a 50 Ω matched load and we measure the reflected signal $S_r(t)$ with the oscilloscope. This step may be associated to a calibration in a manner of speaking. Then, the 50 Ω load is replaced with the cable under test and we measure the reflected signal $S_C(t)$. Finally, we do the cross-correlated with the reference chaotic signal $S_r(t)$ measured previously to detect the wiring faults as below:

$$R_t(T_d) = S_C(t) \otimes S_r(t). \tag{5.17}$$

From the correlated result $R_t(T_d)$, the reflected signal can be computed using the right-side of the correlation as in simulation previously. This measurement process is depicted in Figure 5-15. Moreover, from the correlated result $R_t(T_d)$, the length of the fault can be find using (5.18) defined as follow:

$$L_f = cv_f T_d/2. \tag{5.18}$$

where, c the celerity, $v_f = 0.66$ the velocity factor of the cable, and T_d the round-trip time between the input signal and the first reflection.

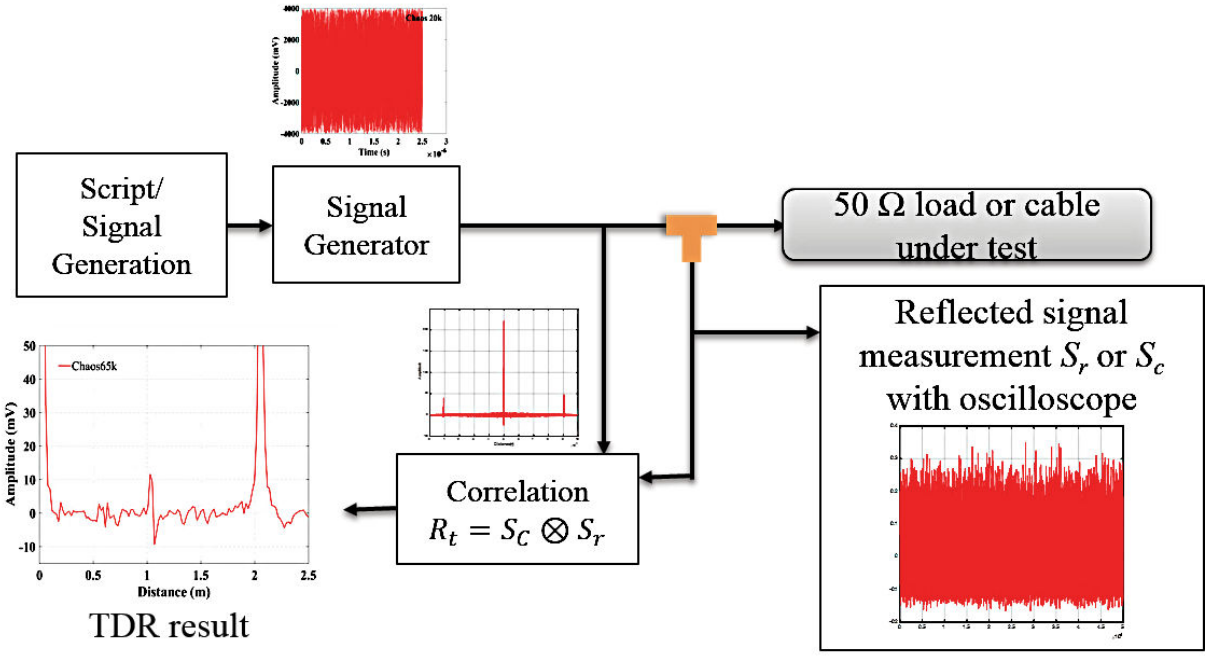

Figure 5-15. Measurement process.

Different cables under test are built with different soft faults. We note four different soft fault illustrated in Figure 5-16. The first one has a 2.5-cm length and 2.5-mm thickness (Figure 5-16 (a)). Figure 5-16 (c) represents a soft fault with a 4-cm length. Figure 5-16 (b) depicts a soft fault created by taking off the outer conductor at two positions separated by a length of 2 cm. Figure 5-16 (d) represents another soft fault with 2-cm length and a cut in the insulator and shield of less than 30° (Figure 5-16 (d)). All these faults are created in a RG-58/U type coaxial cable, with the characteristic impedance of 50 Ω. This type of coaxial cables often used for low-power signal and RF connections at moderately high frequencies. The signal attenuation depends on the frequency, e.g. from 10.8 dB per 100 m at 50 MHz to 70.5 dB per 100 m at 1 GHz.

Figure 5-16. Different types of soft faults: (a) 2.5-cm-long 90° cut in the insulator and shield of the coaxial, (b) cuts in the shield and insulator, (c) 4-cm-long 90° cut in the insulator and shield of the coaxial, and (d) 2-cm-long <30° long cut on the insulator and shield of the coaxial.

Four measurement setups are studied in the following. These setups are displayed in Figure 5-17. The first one is a 2 m coaxial cable with the soft fault of Figure 5-16 (a), (b), (c) or (d) located at a point 1 m from the T junction. This setup allows the comparison between the different soft faults. The second setup is a 2 m coaxial cable with simultaneously two faults;

the soft fault of Figure 5-16 (d) and the soft fault of Figure 5-16 (b) respectively located at 1 m and 1.5 m from the T junction. This setup is created in order to prove that the method can be applied for several soft faults in the same cable. The third setup is a 16 m coaxial cable with the soft fault of Figure 5-16 (a) or (d) located at a point 15.1 m from the T junction. The 16 m cable is created by connecting cables of 10, 3, 1, and 2 m. This setup allows a sensitivity analysis with the length of cable in comparison with the first setup. The last setup is a network composed with one cable c1 connected to two cables; one 3 m coaxial cable c3 without soft faults, and one 2 m cable c2 with the soft fault of Figure 5-16 (a) or (d) located at 2 m of the first T junction. This setup is built in order to study the feasibility of CTDR for different network topologies in comparison with the previous ones. As shown in Figure 5-17, all the cables are in open circuit.

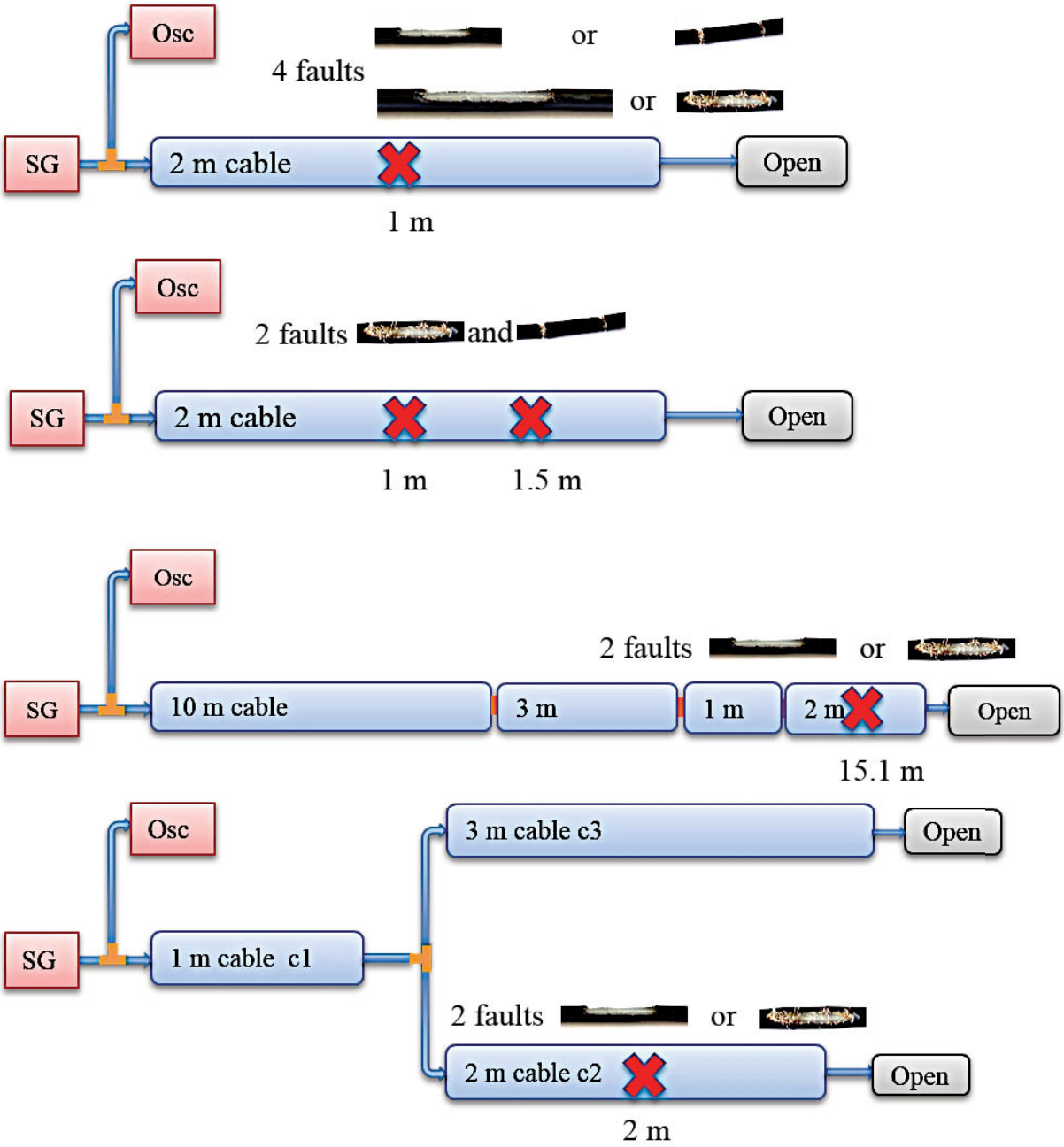

Figure 5-17. The different configurations of the measurement setup.

5.4 Experimental results

5.4.1.1 For the first setup

First, the chaos TDR is performed for the faulted RG-58 coaxial cable, in which the soft fault of 2.5 cm with 90° cut in the insulator (Figure 5-16 (a)) is located at 1 m (first setup of Figure 5-17). As a reminder, the injected signal is a 65k samples combination of Logistic map and Bernoulli map. The measurement process depicted in section 5.3 is performed. The obtained reflected signal is illustrated in Figure 5-18. The result shows that there is a visible and proper reflection at 1 m in the cable, which corresponds to the reflected signal from the soft fault.

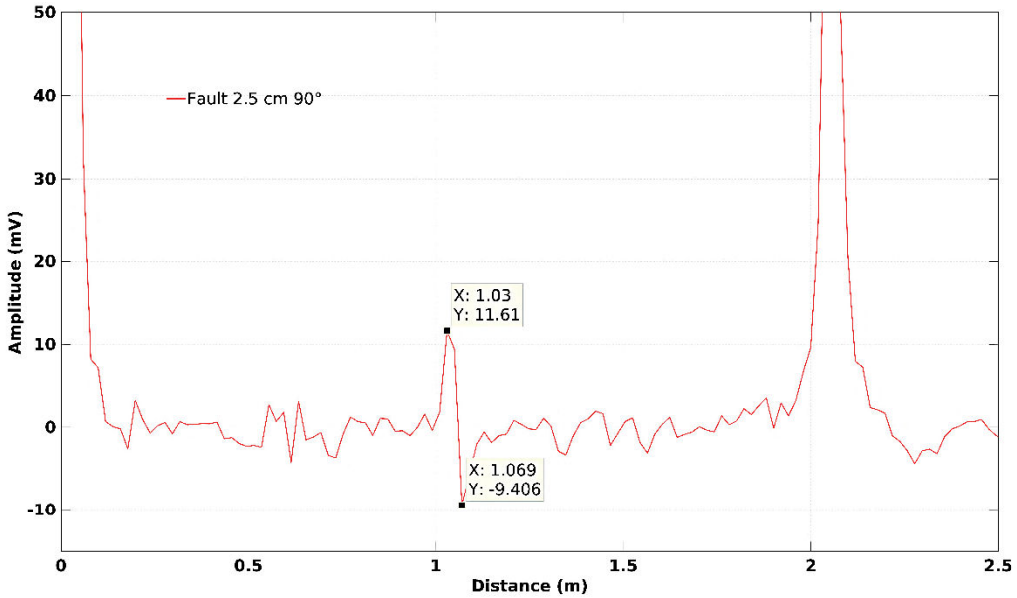

Figure 5-18. Reflected signal for the 2 m coaxial cable with the soft fault of Figure 5-16 (a) located at 1 m.

Table 5-6. Performance indicators for reflected signal due to the soft fault 2.5 cm 90° with first measurement setup.

	Fault 2.5 cm 90° with first measurement setup
$A_{\text{soft default}}^{\text{peak-to-peak}}$ (mV)	21.0118
$\sigma_{[0.009,0.99]}$ (mV)	1.9637
Δ (dB)	20.5877

As expected, the reflected signal is slightly noisy. This noise and the quality of the fault detection is therefore quantify using the "performance indicator" of (5.8). The results are summarized in Table 5-6. We will try to enhance this "performance indicator". The trick is to subtract the reflected signal from a cable without default called nominal cable and the reflected signal of the cable with the soft fault. Thus, the reflected signal of the faulted cable is computed from:

$$R_F(T_d) = S_{CF}(t) \otimes S_r(t). \tag{5.19}$$

with, $R_F(T_d)$ the cross-correlation between the reflected signal S_{CF} from the nominal cable and the injected signal S_r. Then, we subtract (5.19) from (5.17):

$$R_D = R_F - R_t. \tag{5.20}$$

From R_D, we obtain the reflected signal illustrated in Figure 5-19. Obviously, the nominal cable and the cable with a soft fault must have the same characteristics (dimensions, EM characteristics, etc…). We note that the length of the nominal cable used here must be slightly different in comparison with the cable with fault because of the peak obtained at 2 m. If the both cables have the same length, this peak can disappear. As, we are interested in the soft fault, it does not matter. Table 5-7 displays the performance indicators of the reflected signal due to the soft fault 2.5 cm 90° with first measurement setup from (5.19) and (5.17). Although the proposed enhancement reduce slighlty the peak-to-peak amplitude of the soft fault, it increases significantly the fault detection performance by reducing considerably the noise. As a consequence, all the following results come from (5.20).

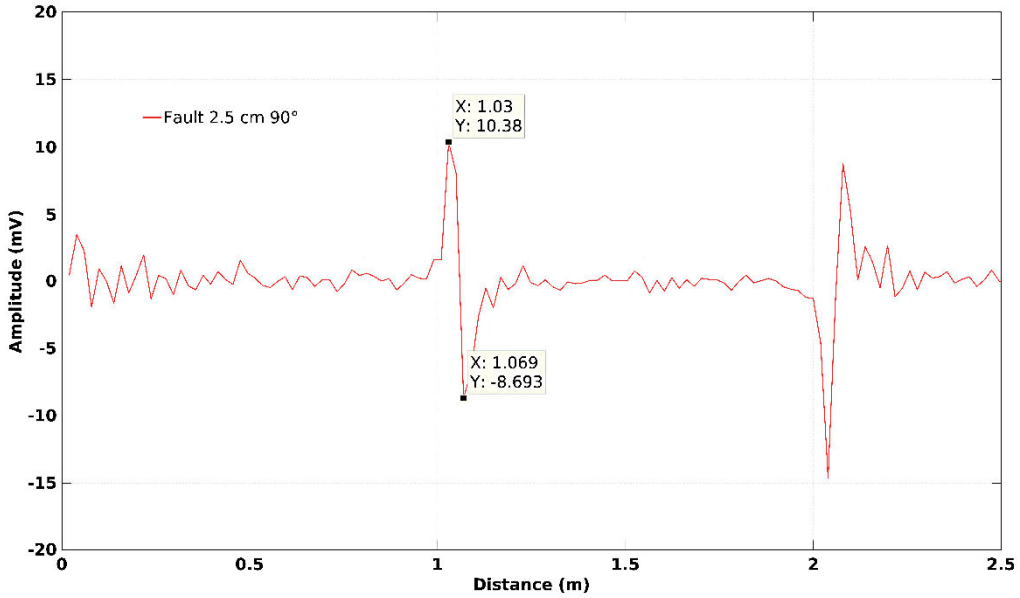

Figure 5-19. Reflected signal from (5.20) for the 2 m coaxial cable with the soft fault of Figure 5-16 (a) located at 1 m.

Table 5-7. Comparison of the performance indicators of the reflected signal due to the soft fault 2.5 cm 90° with first measurement setup from (5.20) and (5.17).

	Fault 2.5 cm 90° with first measurement setup from (5.17)	Fault 2.5 cm 90° with first measurement setup from (5.20)
$A^{\text{peak-to-peak}}_{\text{soft default}}$ (mV)	21.0118	19.0710
$\sigma_{[0.009,0.99]}$ (mV)	1.9637	0.7167
Δ (dB)	20.5877	28.5005

Now, we will compare the impact of the different soft faults presented in Figure 5-16 in the fault detection. Figure 5-20 displays the different reflected signals. We note, in particular, that the length of the soft fault seems to have a smaller impact than the extracted volume of insulator and shield. Indeed, the peak-to-peak amplitude due the 4 cm length fault with 90° cut in the insulator and shield seems to be really close to the one with 2.5 cm length fault with 90° cut in the insulator and shield. Moreover, these amplitudes are, clearly smaller than the one due to the 4.5 cm length fault with 120° cut in the insulator and shield, and, clearly higher

than the one due to 2 cm length fault with less than 30° cut in the insulator and shield. In order to quantify this, the performance indicators are presented in Table 5-8. The previous observations are confirmed according to the peak-to-peak amplitude. Nevertheless, the noise with the 2.5 cm length fault with 90° cut in the insulator and shield is noticeably smaller than the one with the 4 cm length fault with 90° cut in the insulator and shield. Thus, it leads to a better performance indicator for the 2.5 cm length fault with 90° cut in the insulator and shield which is close to the one of the 4.5 cm length fault with 120° cut in the insulator and shield. Furthermore, we note that the results of Table 5-8 are slightly different than the ones of Table 5-7 for the same fault. It can be explained by the fact that we did another measure leading to new results. In this thesis, the measurement uncertainties have not been studied. This topic could be an interesting perspective of the work proposed in this manuscript.

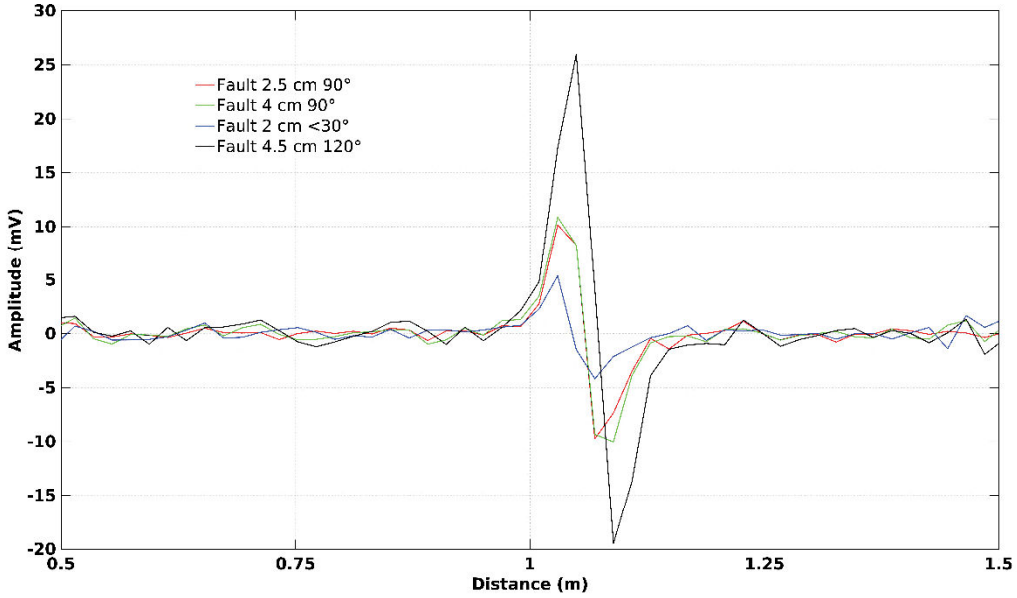

Figure 5-20. Reflected signal from (5.20) for the 2 m coaxial cable with the soft faults of Figure 5-16 located at 1 m.

Table 5-8. Comparison of the performance indicators of the reflected signals due to the soft fault of Figure 5-16 for the 2 m coaxial cable.

	Fault 2.5 cm 90° with first measurement setup from from (5.20)	Fault 4 cm 90° with first measurement setup from (5.20)	Fault 2 cm <30° with first measurement setup from (5.20)	Fault 4.5 cm 120° with first measurement setup from (5.20)
$A^{\text{peak-to-peak}}_{\text{soft default}}$ (mV)	19.8901	20.9076	9.5383	45.4478
$\sigma_{[0.009,0.99]}$ (mV)	0.4386	1.0689	0.7596	0.9878
Δ (dB)	33.1313	25.8275	21.9774	33.2572

5.4.1.2 For the second setup

In this section, we are interested in the second setup which is, as a reminder, a 2 m coaxial cable with simultaneously two different faults (Figure 5-16 (d) and (b)) respectively located at 1 and 1.5 m from the T junction. Figure 5-21 displays the obtained reflected signal. First, we note that the first fault seems to be hard to detect even considering the dynamic. Moreover,

we note a small shift of the first fault which must be located at 1 m. This shift can be explained by the fact that the nominal cable has, as previously, a different length in comparison to the cable under test. This measurement uncertainty leads to an uncertainty in the soft fault location unlike the previous results. Indeed, the error regarding the cable length is clearly higher than previously according to the peak at 2 m. We propose to analyze the results with the performances indicators of Table 5-9. Regarding the peak-to-peak amplitude versus the "noise" and the performance indicator of the first fault, we can consider the detection of this fault acceptable. Obviously, the second fault can be easily detected by the proposed method. This experiment highlights the performance of the proposed method applied on a coaxial cable with different soft fault regarding simultaneously an accuracy due to the impact of the soft faults and the measurement uncertainties.

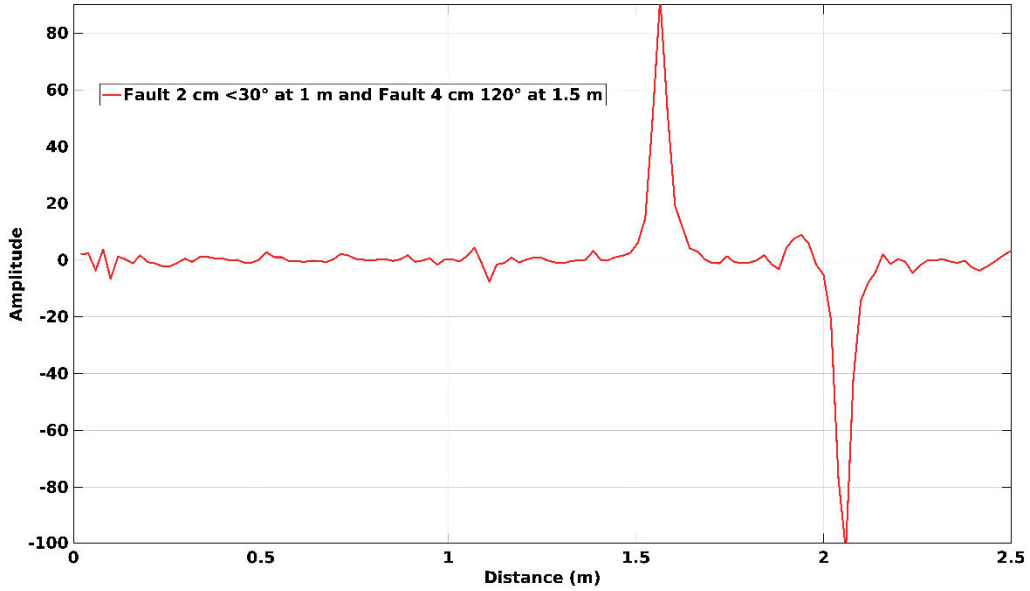

Figure 5-21. Reflected signals for the 2 m coaxial cable with the soft fault of Figure 5-16 (d) located at 1 m and the soft fault of Figure 5-16 (b) located at 1.5 m.

Table 5-9. Performance indicators of the reflected signals due to the soft fault of Figure 5-16 (d) and (b) for the second setup.

	Fault 2 cm <30° with second measurement setup from (5.20)	Fault 4.5 cm 120° with second measurement setup from (5.20)
$A^{\text{peak-to-peak}}_{\text{soft default}}$ (mV)	11.9704	93.5093
$\sigma_{[0.009,0.99]}$ (mV)	1.4343	1.4343
Δ (dB)	18.4292	36.2841

5.4.1.3 For the third setup

In this subsection, we are interested in the sensitivity with the length of the cable in terms of fault detection. Hence, we consider a 16 m coaxial cable with two different soft faults (Figure 5-16 (a) or (d)) located at 15.1 m from the T junction. As a reminder, the 16 m cable is created by connecting cables of 10, 3, 1, and 2 m. It is important to note that the lengths of the connectors between the cables can be considered as additional lengths for the fault location.

Figure 5-22 illustrates the both reflected signals with an inset which shows a zoom of both signals in the distance interval of the soft faults. Both peaks clearly appears. Once again, the nominal cable and the cables under test have a different length according to the peak close to 16 m. This time, it does not significantly affect the fault location. As previously, the performance indicator is chosen as a quantifier with a standard deviation computed in the interval [1.98, 9.90] m. The results are summarized in Table 5-10. The trend is the same as the one in Table 5-8, it leads to a better performance indicator for the 2.5 cm length fault with 90° cut in the insulator than for the 2 cm length fault with less than 30° cut in the insulator and shield. We note that for the 16 m coaxial cable the amplitudes related to the soft faults are smaller than the ones with the 2 m coaxial cable. However, the dynamic is better when the noise is smaller. To conclude, the length of the cable is not an obstacle for the soft fault detection using the proposed method.

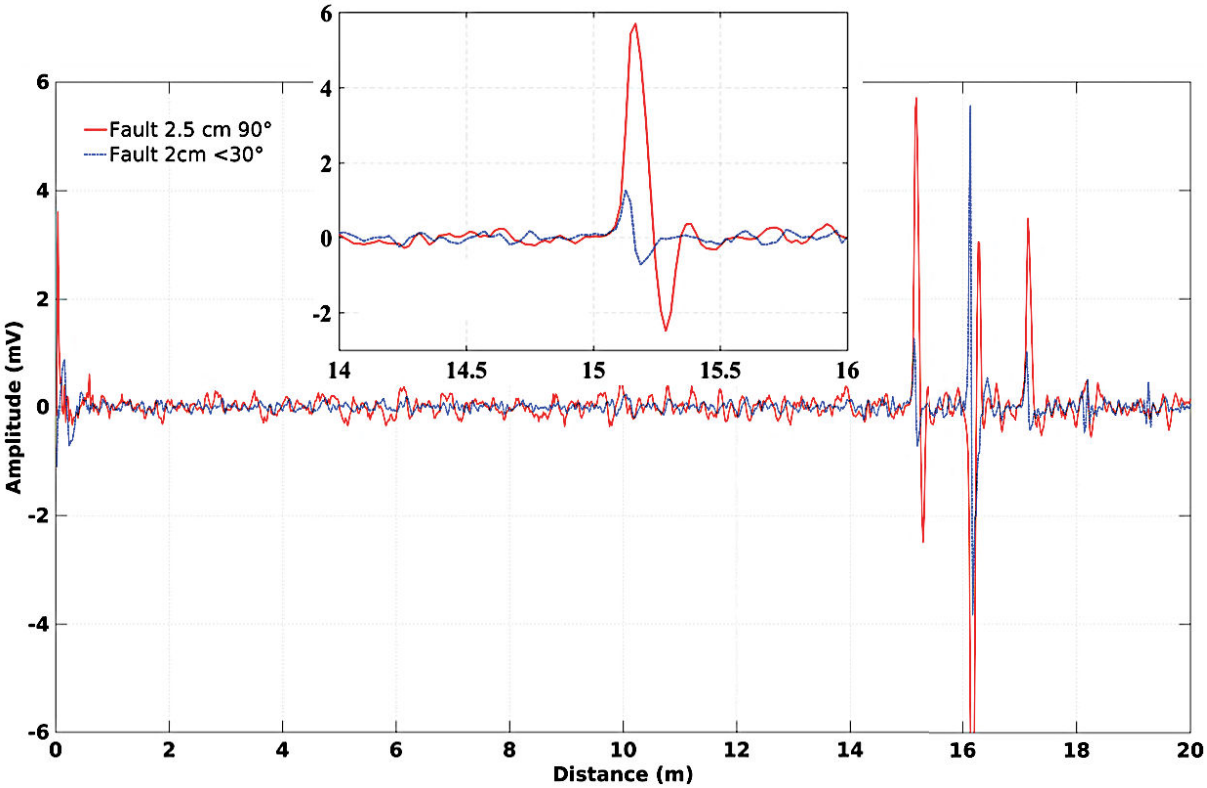

Figure 5-22. Reflected signals for the 16 m coaxial cable with the soft faults of Figure 5-16 (a) and (d) located at 15.1 m. The inset shows a zoom of both signals in the distance interval of the soft faults.

Table 5-10. Performance indicators of the reflected signals due to the soft fault of Figure 5-16 (a) and (d) for the third setup.

	Fault 2.5 cm 90° with third measurement setup from (5.20)	Fault 2 cm <30° with third measurement setup from (5.20)
$A^{\text{peak-to-peak}}_{\text{soft default}}$ (mV)	8.1960	1.9898
$\sigma_{[1.98,9.90]}$ (mV)	0.1417	0.0618
Δ (dB)	35.2470	30.1558

5.4.1.4 For the fourth setup

To study the feasibility of CTDR for different network topologies, the measurement of a cable with a single T-connection was performed, as shown in Figure 5-17. As a reminder, this setup correspond to one cable c1 connected to two cables; one 3 m coaxial cable c3 without soft faults, and one 2 m cable c2 with the soft fault of Figure 5-16 (a) or (d) located at 2 m of the first T junction. Two different faults (Figure 5-16 (a) and (d)) located in the middle of c2 are studied. To perform the subtraction (5.20), a topology similar to that of the nominal cable measurement was used to obtain the reference signal needed for the subtraction process. The obtained reflected signal is displays in Figure 5-23. The peaks at 1 m correspond to the T junction between the cables c1, c2 and c3, while the peak close to 2 m correspond to the soft fault, the peak close to 3 m is related to the end of the cable c2 and the one close to 4 m correspond to the end of the cable c3. Except for the peak related to the soft fault, the others are due to the measurement uncertainties as explained before. In any event, the soft fault might be detected with a small location error. The performance indicator is used to quantify our results with a standard deviation computed in the interval [1.485, 1.980] m. The results are presented in Table 5-11. The same conclusions as previously can be made. The performance indicator for the 2.5 cm length fault with 90° cut in the insulator is better than the one for the 2 cm length fault with less than 30° cut in the insulator and shield. Although, the dynamic is slighly lower in the cables networks than in the second or third setup, the faults are detectable. These results prove that CTDR can be used in multiple-cable networks.

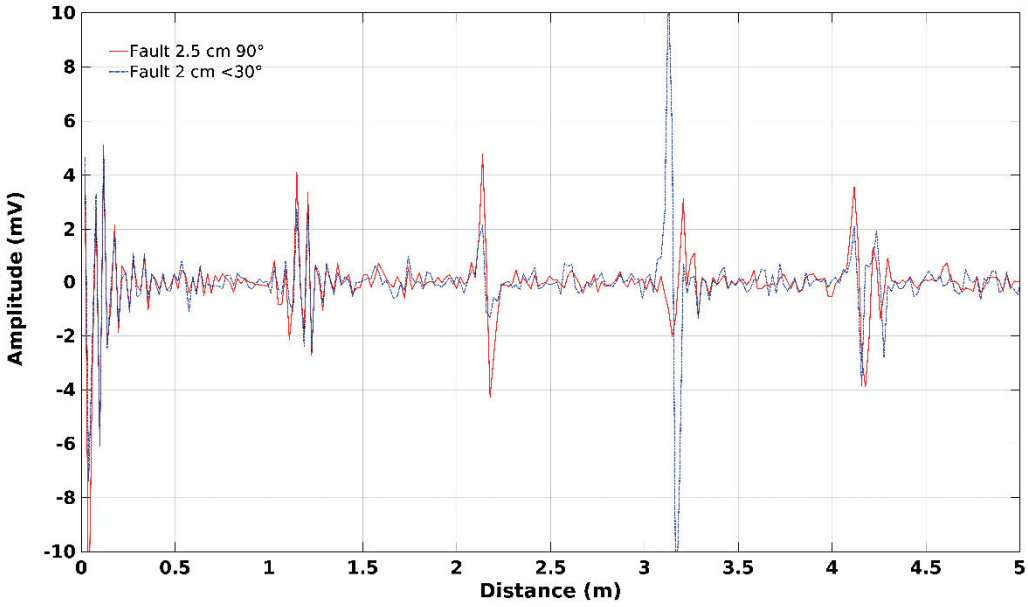

Figure 5-23. Reflected signals for the cables network with the soft faults of Figure 5-16 (a) and (d) located at 2 m.

Table 5-11. Performance indicators of the reflected signals due to the soft fault of Figure 5-16 (a) and (d) for the fourth setup.

	Fault 2.5 cm 90° with fourth measurement setup from (5.20)	Fault 2 cm <30° with fourth measurement setup from (5.20)
$A_{\text{soft default}}^{\text{peak-to-peak}}$ (mV)	9.0464	3.4697
$\sigma_{[1.98,9.90]}$ (mV)	0.2737	0.3313
Δ (dB)	30.3848	20.4019

5.4.1.5 Conclusions

An improved chaos TDR has been presented for wire diagnosis. Different measurements have been performed for four different setup with different soft faults. The different kinds of soft faults have been analyzed with the different topology of the cable. In all measurements, the chaos TDR assures an efficient performance with relatively accurate results for any kind of soft faults. In particular, it has been shown that the length of the soft fault seems to have a smaller impact than the extracted volume of insulator and shield. Moreover, we demonstrated that the length of the cable should not be an obstacle for the soft fault detection using the proposed method. Finally, we highlight that proposed CTDR can be used in multiple-cable networks.

5.5 Conclusions

The chaotic signal is only a recent advancement in science within the last few decades. Although the chaotic signal suffered from various disadvantages, mainly being vulnerable in the application, it can detect wiring faults because it is broadband, and sensitive to initial conditions. Different techniques exist to produce chaotic signals, such as chaotic masking. Thus, adaptive algorithms have been used to provide promising results.
In this chapter, we first perform a simulation analysis with two signals 1) a combination of the logistic map and Bernoulli map and 2) a Lorenz signal. The sensitivity analysis carried out on the parameters of both signals lead us to use the combination of the logistic map and Bernoulli map with 65k samples and k=3.9 for measurement. Indeed, it has been shown that this signal allows a better fault detection in comparison with the Lorenz signal, even if the Lorenz signal could be used. Hence, we proposed a measurement method based on the CTDR with an arbitrary waveform generator and an oscilloscope. The method has been improved doing in a manner of a calibration replacing the faulted cable with a nominal cable. In practice, it is not easy to perform this kind of calibration for industrial process as cable cannot be replaced. However, we can calculate the reference signal just after the certification of a device or another. Finally, the proposed method allows us to obtain promising results with a better dynamic. Furthermore, some limits about the measurement uncertainties of this method has been raised. This topic could be an interesting perspective of the work proposed in this manuscript. A sensitivity analyze has been performed with different kinds of soft faults and different setup of cables. The proposed measurement method provides efficient performance with relatively accurate results for any kind of soft faults or cables setups. In particular, it has been proved that the proposed method is efficient in multiple-cable networks in terms of soft fault detection. In the future, it could be interesting to investigate the limits of the method according to the soft faults and the cable topologies.
Furthermore, the chaos TDR is a promising method for the diagnosis of the complex cables networks because of its orthogonality. This point has not been studied in this manuscript. Nevertheless, it could be really interesting to investigate it in the future work. Moreover, the method is also promising for the real-time detection as the chaotic signals can be considered as a “noise”, and, thus, they should not disturb the useful injected signal. In addition, the chaotic signals can easily be generated by using arbitrary waveform generators (AWG), FPGAs or microcontrollers. These electronic devices and circuits are fairly less expensive to build than a TDR equipment or a VNA thus reduces the cost of implementation of chaos TDR.

Conclusions and Perspectives

Conclusions / Perspectives

The objective of this research was to examine whether a Bayesian approach, time–frequency analysis, and chaotic signal techniques could be used to make earlier chafing fault detection possible. The main challenge in model-based TDR is to diagnose incipient faults in non-linear dynamic systems under the assumption that input, and output measurements are affected by the disturbances caused by faults in a system. In the thesis, four approaches were introduced. These techniques were applied to coaxial cables with one or two faults and to a cable network. When different denoising tools were applied, the outputs of some of these diagnostic tools contained useful information for other treatment tools. In other words, integrating denoising methods and using their information in a hybrid framework will increase the accuracy of the fault diagnosis task. The EMD method is a more efficient method than LMD and the DWT to denoise the signal while conserving the fault signature. The EMD method suffers from a lack of a full, generally accepted theoretical framework. Thus, it is of immense importance that an analytical formulation for the so-called mean envelope be developed for characterization of this method. The main problems are associated with the fact that the local mean of a signal depends on its characteristic local time scales. The LMD method is developed from EMD and has the same drawbacks as EMD. However, it loses the fault signature while denoising the signal. The process of DWT is different from EMD and LMD, as it filters the signal with low-pass and high-pass filters. Although it thresholded the signal at each level, it was unable to maintain the fault information due to its weak amplitude.

Time–frequency analysis has been proposed for processing the signal after denoising. In these fault detection algorithms, it might use only output measurements, which might provide enough information to detect certain types of faults. Moreover, the time–frequency method can provide satisfactory results for certain non-linear signals. We can say that the proposed CWT method is robust compared to the other time–frequency methods STFT and WVT. Using the CWT method, we can detect wiring faults. However, due to the noise level and window length, the time–frequency methods are not able to localize and isolate these faults. Hence, intelligent techniques to isolate faults should be used. The Bayesian method can be used to extract information from data to construct posterior parameters. These parameters correspond to fault characteristics. This process can serve as a step towards earlier chafing fault detection in processes that do not necessarily operate at steady state. Using a coaxial cable model to simulate the reflected signal at its entry, the simulated signal can be converging to the reflected signal. This convergence is effected by solving the Bayesian approach via either NS or the GN algorithm. Although, the results show that NS performs better than GN in terms of stability, GN method converges faster than NS.

At the end, an improved chaos TDR is presented for real-time wire diagnosis. Different measurements of different topologies of the cable with different kinds of faults are performed for both hard and soft faults detections. In all measurements, the chaos TDR assures an efficient performance and accurate results for any kind of soft faults. In addition, the chaotic signals can easily be generated by using arbitrary waveform generators (AWG). These electronic devices are fairly less expensive to build than a TDR equipment or a VNA thus reduces the cost of implementation of chaos TDR. This thesis presents soft fault detection methods and assesses their feasibility for fault detection and location.

The following future work can be carried out to improve the potential of our proposed methods. In this thesis, the Bayesian approach is analysed on a coaxial cable based on prior parameters. This proposed method needs to be modified to better analyse faults and improve precision. To do so, the Maxwell equations should be used to predict the prior parameters, which will increase computational complexity. In addition, the soft fault used in this thesis is

modelled as an impedance. In upcoming work, the fault will be introduced as RLC parameters to increase accuracy and performance in soft fault detection. The last point invoked in Chapter 4 is the chafing fault detection using a Bayesian approach based on prior parameters. To go further in subsequent studies, temperature should also be taken into consideration as prior parameters. For Chapter 5, experiments using CTDR were conducted to detect different fault types via the Bernoulli map. The proposed methods can also be analysed with other chaotic maps. Moreover, the implementation of the chaos TDR for the live wire monitoring in a T-network.

Bibliography

Bibliography

[1] W. B. Hassen, "Études de stratégies de diagnostic embarque des réseaux filaires complexes," PhD thesis, Université de Toulouse, Toulouse, France, 2014.

[2] R. Collin, ''*Foundations for Microwave Engeneering,*'' Hoboken, NJ: Wiley-Blackwell, 2007.

[3] F. Auzanneau, "Wire Troubleshooting And Diagnosis: Review And Perspectives," *Progress in Electromagnetics Research*, vol. 49, pp. 253–279, Feb. 2013.

[4] P. Kuhn, "Wiring, Locating Hidden Hazards in Electrical," *Aged Electrical Systems Research Application Symposium*, 2006 .

[5] C. Furse and R. Haupt, "Down to the wire," IEEE Spectrum, vol. 38, pp. 34-39, 2001.

[6] U.S. NRC, nrc.gov [Online]. Available : //www.nrc.gov/reading-rm/doc-collections/nuregs/staff/.../appa-i.pdf/

[7] B. J. McPartland, J. F. McPartland and F. P. Hartwell, ''National Electrical Code,'' 26th ed. New York: McGraw-Hill Education, 2008.

[8] E. Lakervi and E. J. Holmes, ''*Electricity Distribution Network Design,*'' 2nd ed. Stevenage: Institution of Engineering and Technology, 1905.

[9] R. Yarlagadda, ''*Analog and Digital Signals and Systems,*'' Berlin: Springer, 2009.

[10] S. Y. King and N. A. Halfter, ''*Underground Power Cables,*'' Harlow: Longman, 1982.

[11] D. Noland and B. Peterson (2017, Aug. 4), ''*12 plane crashes that changed aviation*'' [Online]. Available: https://www.popularmechanics.com/flight/g73/12-airplane-crashes-that-changed-aviation/

[12] Materielelectrique.com (2017, Jan. 25), ''*Les différents types de câbles*'' [Online]. Available: https://blog.materielelectrique.com/differents-types-de-cables/

[13] U. A. Arefin, H. Hira, R. Hossen, and J. Prodhan, "Analysis of Conductive Materials, Wires and Cables for Using in a Commercial Complex," Book, Dept. of Elect. and Electr. Eng., Nothern University Bangladesh, Dhaka, Bangladesh, 2015.

[14] F. Binot, T. D. Le and M. Petit, "Modélisation de l'impédance des câbles: Étude de sensibilité et impact sur le réseau BT," *Symposium de Génie Électrique*, 2018.

[15] Nexans (2019), [Online]. Available: //www.nexans.fr/

[16] Cirris (2018), [Online]. Available: //www.cirris.com/testing/twisted_pair/twist.html/

[17] Anon (2013, Feb. 16), ''*Quelle différence entre les câbles et prises RJ45 - UTP - FTP-STP-CAT5-CAT6-N12*'' [Online]. Available: https://www.alliancelec.fr/blog/quelle-difference-entre-les-cables-prises-rj45-utp-ftp-stp-cat5-cat6-n12

[18] Electdirect (2018, Sept. 12), ''*Différence entre câbles UTP, FTP et STP*'' [Online]. Available: https://www.elecdirect.fr/blog/conseil-technique/difference-entre-cable-utp-ftp-et-stp.html

[19] L. Rochester, ''*Coaxial Cables Application Data,*'' Technical Publishers Incorporated, 1969.

[20] M. J. Wison, ''*The ARRL Handbook for Radio Communications*,'' 87th ed. Newington: The American Radio Relay League, 2010.

[21] M. J. Van-Der-Burgt, ''*Coaxial Cables and Applications,*'' Saint-Louis (Missouri): Belden, 2011.

[22] Anon (2015, Feb. 25), ''*Coaxial Cables Common Parameters,*'' [Online]. Available: https://qrznow.com/coaxial-cables-common-parameters/

[23] H. E. Green. "The Numerical Solution of Some Important Transmission Line Problems," *IEEE Transactions on Microwave Theory and Techniques*, vol. 13, pp. 676–692, 1965.

[24] N. I. Badler and A. S. Glassner, "3D Object Modeling," University of Pennsylvania, Pennsylvania, 1999.

[25] K. S. Yee, "Numerical solution of initial boundary value problems involving maxwell's equations in isotropic media," *IEEE Transactions on Antennas and Propagation*, vol. 14, issue 13, pp. 302–307, 1966.

[26] N. C. Knowles, "Finite element analysis," *Computer-Aided Design*, vol. 16, issue 13, pp. 134-140, May 1984.

[27] K. J. Bathe, ''*Finite Element Procedures,*'' Watertown, MA: K. J. Bathe, 2016.

[28] S. Yao (2016, Aug. 23), ''*HFSS Tutorial coaxial cables,*'' [Online video]. Available: https://www.youtube.com/watch?v=w9SA9LjRuPA/

[29] S. Rengang, Y. Haitian and L. Gao, "An adaptive time step FDTD method for Maxwell's Equations," *IEEE Antennas and Wireless Propagation Letters*, vol. 14, issue 11, 2015

[30] Anon, ''*Alter FEKO Overview,*'' [Online]. Available: https://altairhyperworks.com/product/FEKO.

[31] R. P. Clayton, ''*Analysis of Multiconductor Transmission Lines,*'' Hoboken: Wiley-Interscience, 1994.

[32] R. Scott, "Frequency-domain analysis," Addison-Wesley Series in the engineering sciences Addison-Wesley, 1960.

[33] K. Morita, ''*Applied Fourier Transform,*'' Japan: Ohmsha Ltd., 1995.

[34] J. Zhang, J. L. Drewniak, D. J. Pommerenke, M. Y. Koledinteva, R. E. Dubroff, Z. Yang, Q. B. Chen, and A. Orlandi, "Causal RLGC(f) Models for Transmission Lines From Measured S-Parameters," *IEEE Transactions on Electromagnetic Compatibility*, vol. 52, issue 11, pp. 189-198, 2010.

[35] F. Caspers, "RF engineering basic concepts: S-parameters," *CERN*, June 2010.

[36] F. Dolcini, "Introduction to the Scattering Matrix Formalism," Lecture notes for XXIII Physics GradDays, in Heidelberg, 5-9 October 2009.

[37] E. Cortright, "Report of the Apollo 13 Review Board," *NASA*, 1970.

[38] G. Slensky, "Aircraft Wiring System Integrity Initiatives," *Air Force Research Laboratory*, AFRL/MLSA WPAFB, OH 45433.

[39] K. R. Wheeler, "Model-based diagnostics for wire health management," NASA Ames Research Center, Moffett Field, CA, 2008.

[40] B. Calmet, "Protection des réseaux de transport et de répartition : présentation.," *Centre national d'expertise réseaux de RTE*, May 2009.

[41] M. Kafal, A. Cozza and L. Pichon, "Locating Faults with High Resolution Using Single-Frequency TR-MUSIC Processing," *IEEE Transactions on Instrumentation and Measurement*, vol. 65 , issue 110, pp. 2342 - 2348, 31 May 2016.

[42] L. Griffiths, R. Parakh, C. Furse and B. Baker, "The invisible fray: A critical analysis of the use of reflectometry for fray location," *IEEE Sensors J.*, vol. 6, pp. 697–706, 2006.

[43] R. Badi, "Effet des traitements thermomécaniques sur lespropriétés mécaniques et électriques du câbleélectrique (Cuivre et Aluminium)," PhD. Thesis, Biskra, 2016.

[44] H. Hashemian, and W. C. Bean, "State-of-the-Art Predictive Maintenance Techniques," *IEEE Transactions on Instrumentation and Measurement*, vol. 60, pp. 226–236, Jan 2011.

[45] F. Auzanneau, N. Ravot, "Diagnostic Filaire: Détection, localisation et caractérisation de défauts dans des réseaux filaires complexes," *Recherche et Innovation des Techniques de l'Ingénieur*, pp. 1–11, May 2010.

[46] R. Wheeler, D. A Timucin, I. X. Twombly, K. F. Goebel, P. F. Wysocki, "Aging Aircraft Wiring Fault Detection Survey," NASA Ames Research Center, Moffett Field, CA, June 2007.

[47] J. Schonfeld, "Wiring Integrity Research (WIRe) Pilot Study," Technical report, Design for Safety Initiative, August 2000.

[48] Y. C. Chung, N. N. Amarnath and C. M. Furse, "Capacitance and Inductance Sensor Circuits for Detecting the Lengths of Open- and Short-Circuited Wires," *IEEE Transactions on Instrumentation and Measurement,* vol. 58, issue 18, pp. 2495–2502, Augustus 2009.

[49] V. C. Camara and D. Laux, "Moisture content in honey determination with a shear ultrasonic reflectometer," *Journal of Food Engineering*, vol. 96, pp. 93–96, 2010.

[50] D. Santos, "Développement d'une nouvelle méthode de détermination des profils de teneur en eau dans les sols par inversion d'un signal TDR," PhD thesis, 1997.

[51] R. J. Woodward, "Using Frequency Domain Reflectometry for Water Level Measurement," Master's thesis, Dept. Elect. Comp. Eng., Utah State Univ., Logan, UT, 2000.

[52] C. Neus, P. Boets, L. V. Biesen, ''Channel capacity estimation of digital subscriber lines: a frequency domain approach,'' *2007 IEEE International Conference on Communications*, pp. 2676–2681, 2007.

[53] M. Kowalski, "A simple and efficient computational approach to chafed cable time-domain reflectometry signature prediction," *Annual Review of Progress in Applied Computational Electromagnetics Conference*, March 2009.

[54] M. Kafal, "Imaging Techniques for Soft Fault Detection and Location in Wiring Networks," PhD. thesis, Université Paris-Saclay, 2016.

[55] C. Furse, Y. C. Chung, R. Dangol, M. Nielsen, G. Mabey, and R. Woodward, "Frequency-Domain Reflectometry for On-Board Testing of Aging Aircraft Wiring," *IEEE Transactions on Electromagnetic Compatibility,* vol. 45, pp. 306–315, 2003.

[56] P. J. Medelius and H. J. Simpson, "Non-intrusive impedance-based cable tester," US Patent 59 7777 3A, 1999.

[57] C. Furse and N. Kamdar, "An inexpensive distance measuring system for navigation of robotic vehicles," *Microwave and Optical Technology Letters,* vol. 33, issue 12, pp. 84–87, 2002.

[58] Y. C. Chung, C. Furse, and J. Pruitt, "Application of phase detection frequency domain reflectometry for locating faults in an f-18 flight control harness," *IEEE Transactions on Electromagnetic Compatibility*, vol. 47, issue 12, pp. 327–334, 2005.

[59] F. Auzanneau, Y. Bonhomme, M. O. Carrion, F. Bouillault and N. Ravot, "Distributed Reflectometry-Based Diagnosis for Complex Wired Networks," *EMC: Safety, Reliability and Security of Communication and Transportation SysT*, 2007.

[60] V. Taylor, M. Faulkner, A. Kalam, and J. Haydon, "Digital simulation of fault location on ehv lines using wideband spread spectrum techniques," *IEEE Proceedings, Generation, Transmission and Distribution*, vol. 142, pp 73–80, 1995.

[61] P. Smith, C. Furse, and J. Gunther, "Analysis of spread spectrum time domain reflectometry for wire fault location," *IEEE Sensors Journal*, vol. 20, 2005.

[62] Y. C. Chung, N. Amarnath, C. Furse, and J. Mahoney, "Capacitance and inductance sensors for location of open and short circuited wires," *IEEE Trans Instrum. Meas*, pp. 604–613, 2009.

[63] S. Schuet, D. Timucin and K. Wheeler, "A Model-Based Probabilistic Inversion Framework for Characterizing Wire Fault Detection Using TDR," *IEEE Transactions on Instrumentation and Measurement*, vol. 60, issue 15, pp. 1654-1663, 2011.

[64] A. Ang, "SFG and Mason's Rule : A revision," Nov 2016. Available Online: https //https://www.eee.hku.hk/~msang/SFG_Mason.pdf/

[65] T. Ditchi, "Lignes de Transmission," Lecture Notes, Paris: UPMC-Sorbonne University, 2012.

[66] A Buades, B. Coll, and J. M. Morel, "On image denoising methods," SIAM Review, vol. 52, issue 1, pp. 113-147, 2010.

[67] N. Pierazzo and G. Facciolo, "Data Adaptive Dual Domain Denoising: A Method to Boost State of the Art Denoising Algorithms," *Image Processing*, vol. 7, pp. 93-114, 2017.

[68] [Online]. Available: https://www.bioss.ac.uk/people/chris/ch3.pdf/

[69] A. Bijaoui, "Wavelets, Gaussian mixtures and Wiener filtering," *Signal Processing*, vol. 82, issue 14, pp. 709-712, 2002.

[70] R. Bucy, "Linear and nonlinear filtering," *Proceedings of the IEEE*, vol. 58, issue°6, pp. 854-864, 1970.

[71] Y. Zhu and C. Huang, "An Improved Median Filtering Algorithm for Image Noise Reduction," *Physics Procedia*, vol. 25, pp. 609-616 , 2012.

[72] V. Kamalavenia, R. Anitha Rajalakshmi, K. A. Narayanankutty, "Image Denoising Using Variations of Perona-Malik Model with Different Edge Stopping Functions," *Procedia Computer Science* , vol. 58, pp. 673-682 , 2015.

[73] Tong-Zhang, "Image denoising algorithm via Wiener filtering with elliptic directional windows combine anisotropic diffusion in complex wavelet domain, " *International Conference on Computer Science and Service System (CSSS)*, Nanjing, China, June 2011.

[74] Y. Huang, F. G. Schmitt, Z. Lu and Y. Liu, "Empirical Mode Decomposition Analysis of Experimental Homogeneous Turbulence Time Series," *Colloque GRETSI*, pp. 450-452, 2007.

[75] J. S. Smith, "The local mean decomposition and its application to EEG perception data," *Journal of the Royal Society Interface,* vol. 2, issue°5, pp. 443–454, 2005.

[76] G. Padmavathi, "Performance Analysis of Non Linear Filtering Algorithms for Underwater Images," *Computer Science and Information Security,* vol. 6, issue 2, 2009.

[77] K. Friston, "Variational filtering," *NeuroImage,* vol. 41, pp. 747–766, 2008.

[78] L.I. Rudin, S. Osher, and E. Fatemi, "Nonlinear total variation based noise removal algorithms," *Physica D*, vol. 60, issue 1-4, pp. 259-268, 1990.

[79] C. Marselli, D. Daudet, H. P. Amann, F. Pellandini, "Application of Kalman filtering to noise reduction on microsensor signals, " *Proceeding of the Colloque indesciplinaire en instrumentation, C2I*, pp. 443-450, 1998.

[80] H. Ali, N. Ahmad, X. Zhou, K. Iqbal, and, S. Ali, "DWT features performance analysis for automatic speech recognition of Urdu," *SpringerPlus,* vol. 3, issue 204, 2014.

[81] K. Kisman, "Spectral analysis of doppler ultrasonic decompression data," *Ultrasonics*, vol. 15, issue 3, pp. 105-110, 1977.

[82] K. Tufan, A. Ademoglu, E. Kurtaran, G. Yildiz, S. Aydin, and S. M. Egi, "Automatic Detection of Bubbles in the Subclavian Vein Using Doppler Ultrasound Signals," *Aviation Space And Environmental Medicine*, vol. 77, issue 9, pp. 957-962, 2006.

[83] G. Rilling, and P. Flandrin, P. Gonçalvès, "On empirical mode decomposition and its algorithms," *Proceedings of the 6 th IEEE/EURASIP Workshop on Nonlinear Signal and Image Processing,* Volume 37, Issue 3, pp. 315-320, 2015.

[84] P. Flandrin, G. Rilling, and P. Gonçalvès, "Empirical mode decomposition as a Filter bank," *IEEE Transactions on signal processing,* vol. 11, pp. 112–114, 2004.

[85] G. Rilling, and P. Flandrin, "On the influence of sampling on the empirical mode decomposition," chez *IEEE International Conference on Acoustics Speech and Signal Processing Proceedings*, vol. 3, pp. 4, 2006.

[86] G. Rilling, "Décompositions modales empiriques: contributions à la théorie, l'algorithmie et l'analyse de performances," PhD. thesis, Ecole Normale Supérieure de Lyon, Lyon, 2007.

[87] G. Rilling, and P. Flandrin, "One or Two Frequencies, the Empirical Mode Decomposition Answers," *IEEE Transactions on Signal Processing*, vol. 56, Issue 1, pp. 85–95, 2008.

[88] P. Abry, G. Rilling, P. Flandrin and P. Goncalves, "Fractal dimension estimation: empirical mode decomposition versus wavelets," *IEEE Acoustics, Speech and Signal Procesing*, vol. 3, pp. 1153–1156, 2007.

[89] Y. Yang, J. Cheng, and K. Zhang, "An ensemble local means decomposition method and its application to local rub-impact fault diagnosis of the rotor systems," *Measurement*, vol. 45, issue 3, pp. 561–570, 2012.

[90] C. Valens. (1999). *A Really Friendly Guide to Wavelets* [Online]. Available: https://www.cs.unm.edu/~williams/cs530/arfgtw.pdf

[91] A. Graps, "An Introduction to Wavelets," *IEEE Computational Science and Engineering*, vol. 2, issue 2, pp. 50-61, 1995.

[92] S. Mallat, "A Theory for Multiresolution Signal Decomposition: The Wavelet Representation," *IEEE Transactions on Pattern Analysis and Machine Intelligence*, vol. 11, issue 7, pp. 674-693, 1989.

[93] N. E. Huang, Z. Shen, S. R. Long, M. C. Wu, H. H. Shih, Q. Zheng, N.-C. Yen, C. C. Tung, and H. H. Liu, "The empirical mode decomposition and the Hilbert spectrum for nonlinear and non-stationary time series analysis," *Proceedings of the Royal Society of London A: Mathematical, Physical and Engineering Sciences*, vol. 454, issue 1971, pp. 903-905, 1998.

[94] P. Flandrin, P. Gonçalvès and G. Rilling, "Detrending and Denoising with Empirical Mode Decomposition," Wien: EUSIPCO-04.

[95] A. Linderhed, "Adaptive Image Compression with Wavelet Packets and Empirical Mode Decomposition," Phd thesis Studies in Science and Technology, Linkopings university, 2004.

[96] J. C. Nunes, Y. Bouaoune, E. Delechelle, O. Niang, and P. Bunel, "Image Analysis by Bidimensional Empirical Mode Decomposition," *Image and Vision Computing*, vol. 21, pp. 1019-1026, 2003.

[97] J. Nunes, "Analyse Multiéchelle d'image. Application à l'Angiographie Rétinienne et à la DMLA," PhD Thesis, Université Paris 12, Paris, 2003.

[98] N. Di-Palma, A. Batailly, and M. Legrand, "Méthodes de traitement du signal par décomposition en modes empiriques," HAL, 2018.

[99] X. Hu, S. Peng, and W.-L. Hwang, "EMD revisited: A new understanding of the envelope and resolving the mode-mixing problem in AM-FM signals," *IEEE Trans. Signal Processing*, vol. 60, pp. 1075-1086, 2012.

[100] Y. Wang, Z. He, and Y. Zi, "A comparative study on the local mean decomposition and empirical mode decomposition and their applications to rotating machinery health diagnosis," *Journal of Vibration Acoustics*, vol. 132, pp. 1-10, 2010.

[101] K. Zhang, J. Cheng, and Y. Yang, "The product function criterion in local mean decomposition method," *Journal of Vibration and Shock*, , vol. 30, issue°9, pp. 84–88, 2011.

[102] J. Cheng, Y. Yang, and Y. Yang, "A rotating machinery fault diagnosis method based on local mean decomposition," *Digital Signal Process*, vol. 22, issue°2, pp. 356-366, 2012.

[103] J. C. Goswami, and A. K. Chan, ''*Fundamentals of Wavelets Theory, Algorithms and Applications*''. Hoboken, NJ: John Wiley & Sons, Chap. 3, 1999.

[104] V. Strela, "Multiwavelets: Theory and Application," PhD Thesis, MIT, Cambridge, 1996.

[105] Anon. (2017, May 03). *Thresholds for wavelet 1-D using Birgé-Massart strategy* [Online]. Available: www.mathworks.com

[106] X. Zhang, W. Qi, Y. Cen, H. Lin, and N. Wang, "Denoising vegetation spectra by combining mathematical-morphology and wavelet-transform-based filters," *Journal of Applied Remote Sensing*, vol. 13, issue°1, 2019.

[107] G. Strang. and V. Strela, "The Application of Multiwavelet Filter Banks to Image Processing," *IEEE Transaction on Image Processing*, vol. 8, issue°4, pp. 548-563, 1993.

[108] V. Strela, "Multiwavelets: Theory and Application," PhD Thesis, MIT, Cambridge, June 1996.

[109] G.Strang and T. Ngyuen, *Wavelets and Filter Banks*. Wellesley: Cambridge Press, 1996.

[110] M. Vicek, "Stationary and non-stationary signals," Dept. of applied mathematics, Faculty of Transportation Sciences CTU, 2009.

[111] B. Osgood, "The Fourier Transform and its Applications," Electrical Engineering Department, Stanford University, 2011.

[112] M. Sandsten. (2018). *Time-Frequency Analysis of Time-Varying Signals and Non-Stationary Processes* [Online]. Available: http://www.maths.lu.se/fileadmin/maths/personal_staff/mariasandsten/TFkompver2.pdf

[113] Y. J. Shin, "Theory and Application of Time-Frequency Analysis to Transient Phenomena in Electric Power and Other Physical Systems," PhD Thesis, University of Texas, 2004.

[114] Y. J. Shin, E. Powers, T. S. Choe, C. Y. Hong, E. S; Song, J. G. Yook, and J. B., Park, "Application of time-frequency domain reflectometry for detection and localization of a fault on a coaxial cable," *IEEE Transactions on Instrumentation and Measurements,* vol. 54, no. 6, pp. 437-441, 2008.

[115] M. Franchet, N. Ravot, and O. Picon, ''The use of the pseudo Wigner Ville transform for detecting soft defects in electric cables," *IEEE/ASME International Conference on Advanced Intelligent Mechatronics*, 2011.

[116] M. Franchet, N. Ravot, and O. Picon, ''Soft Fault Detection in Cables using the Cluster Time-Frequency Domain Reflectometry,'' *IEEE Electromagnetic Compatibility Magazine,* vol. 2, pp 54-68, 2013.

[117] E. Song, Y. Shin, P. E. Stone, J. Wang, T. Choe, J. Yook,; Jin Bae Park,'' Detection and Location of Multiple Wiring Faults via Time–Frequency-Domain Reflectometry,'' *IEEE Transactions on Electromagnetic Compatibility,* vol. 59, n°1, pp 131-138, 2009.

[118] S. Qian and D. Chen, "Joint Time Frequency Analysis, methods and applications," Prentice Hall, 1996.

[119] I. Bzikha, C. Guiffaut and A. Reineix, "Time-Frequency analysis for wiring soft faults detection," *IEEE EMC Europe conference*, Barcelona, pp. 481-485, 2019.

[120] Notes de cours. [Online]. Available: http://faculty.nps.edu/rcristi/EO3404/B-Discrete-Fourier-Transform/text/3-STFT.pdf

[121] P. Flandrin, "Principe et mise en œuvre de l'analyse temps fréquence par transformation de Wigner-Ville," *Traitement de signal,* vol. 2, issue°12, pp. 143-151, 1985.

[122] [Online]. Available: https://royalsocietypublishing.org/doi/full/10.1098/rsta.2017.0258.

[123] A. Schuster, "On the investigation of hidden periodicities with application to a supposed 26-day period of meteorological phenomena," *Terrestrial Magnetism,* vol. 3, pp. 3–41, 1898.

[124] J. W. Cooley and J. W. Tukey, "An algorithm for the machine calculation of Fourier series," *Mathematics of Computation,* vol. 19, issue°90, pp. 297–301, 1965.

[125] I. W. Selesnick. (2009). *Short-Time Fourier Transform and Its Inverse* [Online]. Available: http://eeweb.poly.edu/iselesni/EL713/STFT/stft_inverse.pdf

[126] Letwave7 (Sep 17, 2018), [Online]. Available: https://letswave.cn/tu_ch1_5.html/

[127] D. J. MacKay, ‘’Bayesian Methods for Adaptive Models. Pasadena’’, PhD Thesis, California Institute of Technology, 1992.

[128] Grimaldi, C. and Marcy, G. W., “Bayesian approach to SETI,” *Proceedings of the National Academy of Sciences*, 115(42), E9755-E9764. [Online]. Available: https://www.pnas.org/content/115/42/E9755.

[129] N. S. Burkoff, C. Varnai, S. Wells, and D. Wils, "Exploring the energy landscapes of protein folding simulations with Bayesian computation," *Biophysical Journal,* vol. 102, issue 14, pp. 878–886, 2012.

[130] S. Kou, "Equi-energy sampler with applications in statistical inference and statistical mechanics," *Annals of Statistics,* vol. 34, issue 14, pp. 1581–1619, 2006.

[131] M. Bonomi and M. Parrinello, "Enhanced sampling in the well-tempered ensemble," *Physical Review Letters,* vol. 104, issue 119, pp. 190 - 601, 2010.

[132] D. Spiegelhalter, "Bayesian statistics," *Scholarpedia,* vol. 4, issue 18, pp. 5230, 2009.

[133] S. Schuet, D. Timucin, and K. Wheeler, “Physics-Based Precursor Wiring Diagnostics for Shielded-Twisted-Pair Cable,” *IEEE Transactions on Instrumentation and Measurement,* vol. 64, issue 12, pp. 378-391, February 2015.

[134] S. Aitken, “Nested Sampling for parameter inference I systems biology: application to an exemplar circadian model,” *BMC Systems Biology,* July 2013.

[135] N. S. Burkoff, R. J. N. Baldock, C. Varnai, D. L. Wild, and G. Csanyi, “Exploiting molecular dynamics in Nested Sampling simulations of small peptides,” *Computer Physics Computation,* vol. 201, pp. 8-18, April 2014.

[136] P. Mukherjee, D. Parkinon, and A. R. Liddle, “A Nested Sampling algorithm for cosmological model selection,” *Astronomy Centre,* vol. 638, 2008.

[137] A. H. Phan, P. Tichavsky, and A. Cichoki, “Damped Gauss-Newton algorithm for nonnegative Tucker decomposition,” *IEEE Statistical Signal Processing Workshop (SSP)*, pp. 665-668, 2011.

[138] U. Hansmann, Y. Okamoto, and F. Eisenmenger, "Molecular dynamics Langevin and hydrid Monte Carlo simulations in a multicanonical ensemble," *Chemial Physics Letters*, vol. 259, issue 13, pp. 321–330, 1997.

[139] R. Van de Schoot, D. Kaplan, J. Denissen, J. B. Assendorpf, F. J. Neyer, and M. A. Van Aken, "A Gentle Introduction to Bayesian Analysis: Applications to Developmental Research," *Child Development*, vol. 85, issue 13, pp. 842–860, 2013.

[140] C. Farmington, "Bayesian Inference," *Statisticat LLC*, 2005.

[141] S. Adithya, “An Introduction to Bayesian Inference a mathematical venture”. [Online]. Available: https://towardsdatascience.com/an-introduction-to-bayesian-inference-a-mathematical-venture-9919a2937f28.

[142] G. Verdoolaege, "Bayesian inference and maximum entropy methods in science and engineering," *AIP Conference Proceedings*, vol. 735, pp. 395–405, 2004.

[143] M. Cosovic, and D. Vukobratovic, "Distributed Gauss-Newton Method for State Estimation Using Belief Propagation," *IEEE Transactions on Power Systems*, 2018.

[144] M. Hernandez, and S. Olmos, "Gauss-Newton optimization in Diffeomorphic registration," *IEEE International Symposium on Biomedical Imaging*, pp. 1083-1086, 2008.

[145] A. Barducci, G. Bussi, and M. Parrinello, "Well-tempered metadynamics: A smoothly converging and tunable free-energy method," *Physical Review Letters*, vol. 100, 2008.

[146] K. Walczewska-Szewc, E. Deplazes, and B. Corry, "Comparing the ability of enhanced sampling molecular dynamics methods to reproduce the behavior of fluorescent labels on proteins," *Journal of Chemical Theory and Computation*, vol. 11, issue 17, pp. 3455–3465, 2015.

[147] G.M. Torrie, and J. Valleau, "Nonphysical sampling distributions in Monte Carlo free-energy estimation: Umbrella sampling," *Journal of Computational Physics*, vol. 23, issue 12, pp. 187–199, 1977.

[148] D. Hamelberg, J. Mongan, and J. McCammon, "Accelerated molecular dynamics: a promising and efficient simulation method for biomolecules," *Journal of Chemical Physics*, vol. 120, issue 124, pp. 11919–11929, 2004.

[149] B. Berg, and T. Neuhaus, "Multicanonical ensemble: A new approach to simulate first-order phase transitions," *Physical Review Letters*, vol. 68, issue 11, pp. 9–12, 1992.

[150] J. Skilling, "Nested Sampling for general Bayesian computation," *Bayesian Analysis*, vol. 1, issue 14, pp. 833–859, 2006.

[151] M. Doğruel, T. Down, and T. Hubbard, "NestedMICA as an ab initio protein motif discovery tool," *BMC Bioinformatics*, vol. 9, issue 11, pp. 19–31, 2008.

[152] N. Pullen, and R. Morris, "Bayesian model comparison and parameter inference in systems biology using nested sampling," *PLOS ONE*, vol. 9, issue 12, pp. 1-11, 2014.

[153] P. Mukherjee, D. A. Parkinson, and A. R. Liddle, "A nested sampling algorithm for cosmological model selection," *The Astrophysical Journal Letters*, vol. 638, issue 12, 2006.

[154] C. Andrieu, N. De Freitas, A. Doucet, M. Jordan and, "An introduction to MCMC for machine learning," *Machine Learning*, vol. 50, 2003.

[155] C. Robert and G. Casella., "A short history of Markov Chain Monte Carlo: Subjective recollections from incomplete data," *Statistical science - STAT SCI*, vol. 26, pp. 102-115, 2008.

[156] F. Auzanneau, N. Ravot, and L. Incarbone, "Chaos Time Domain Reflectometry for Online Defect Detection in Noisy Wired Networks," *IEEE Sensors Journal*, vol. 16, issue 122, pp. 8027-8034, 2016.

[157] K. Araki, and K. Akiyama, "Nonlinear oscillation modes in the 3rd order Josephson junction circuits," *IEEE Transactions Magnetics*, vol. 27, issue 12, p. 2732–2735, March 1991.

[158] F. Auzanneau, "Chaos time-domain reflectometry for distributed diagnosis of complex topology wired networks," *Electronics Letters*, vol. 52, pp. 280-281, 2016.

[159] H. Xu, B. Wang, J. Li, A. Wang, and Y. Wang, "Location of Wire Faults Using Chaotic Signal Generated by an Improved Colpitts Oscillator," *International Journal of Bifurcation and Chaos*, vol. 24, pp. 1450-053, 2014.

[160] Q. Yang, Y. Zhang, and X. Gu, "A Signal Model Based On Combination Chaotic Map For Noise Radar," *Progress in Electromagnetics Research*, vol. 28, pp. 57-71, 2013.

[161] B. Jovic, ''*Synchronization Techniques for Chaotic Communication Systems,*'' 1st ed. Heidelberg: Springer, 2011.

[162] D. Arrowsmith, ''*Dynamical Systems: Differential Equations, Maps, and Chaotic Behaviour,*'' 1st ed. London: Chapman Hall/CRC Mathematics Series, 1992.

[163] D. Driebe, ''Fully Chaotic Maps and Broken Time Symmetry'', Nonlinear Phenomena and Complex Systems, vol. 4, pp. 19-110, 1999.

[164] S. Bumelienė, A. Tamaševičius, G. Mykolaitis, A. Baziliauskas, and E. Lindberg, "Numerical investigation and experimental demonstration of chaos from Colpitts oscillator in the Ultrahigh frequency range," *Nonlinear Dyn* , vol. 40, pp. 91-92, 2004.

[165] Z. Wang, R. Goh, K. Bazargan, A. Scheel, and N. Saraf, "Stochastic Implementation and Analysis of Dynamical Systems Similar to the Logistic Map," *IEEE Transactions on Very Large Scale Integration (VLSI) Systems*, vol. 25, issue 2, pp. 747-759, February 2017.

[166] M. Boubekeura, A. K. Ntichi, and L. Pichon, "Modeling of thin heterogeneous sheets in the discontinuous Galerkin method for 3D transient scattering problems," *IEEE Transactions on Magn*etics, vol. 50, issue 2, pp. 493-496, 2014.

Abstract

In this thesis, we present new approaches of soft fault detection and location in simple and complex wire networks. The idea is to find a new approach to overcome the difficulties with standard reflectometry techniques. We prove that before applying post-treatment methods, denoising techniques should be applied, such as empirical mode decomposition (EMD), local mean decomposition (LMD), or the discrete wavelet transform (DWT). These three methods decompose a signal into multiple levels to threshold them before signal reconstruction. Testing several applications shows that EMD is the most efficient method, although it has some limitations as side effects. After the denoising step, the wiring faults can be detected. Time–frequency analysis is employed at this step. This approach, based on the Fourier Transform, is able to detect wiring faults only if the noise level is low. To overcome this difficulty, the Bayesian approach is beneficial when system complexity increases. Its response is based on estimation of prior parameters and prior distributions. In this work, the Bayesian approach is applied via a formal mathematical study followed by simulation results validating the proposed approach, with analysis of the parameters that affect the method's performance. In the domain of soft fault location, we derive a chaos time domain reflectometry approach based on chaotic signal properties. Our simulation and experimental results prove that this method can synthesize signals and localize the soft fault position without the need for supplemental methods.

Résumé

Dans cette thèse, nous présentons de nouvelles approches pour la détection de défauts sur des structures filaires plus ou moins complexes. L'idée est de trouver une nouvelle approche pour surmonter les difficultés des techniques de réflectométrie standards. Tout d'abord, des techniques de débruitage doivent être appliquées, telles que la décomposition en mode empirique (EMD), la décomposition moyenne locale (LMD), ou la transformée des ondelettes discrète (DWT). Ces trois méthodes décomposent un signal en plusieurs niveaux de reconstruire un signal utile. On montre dans ce manuscrit que l'EMD est la méthode la plus efficace, bien que limitée par les effets de bords. Ensuite, l'analyse temps fréquence est utilisée afin de détecter et localiser les défauts sur le câblage. Cette approche, basée sur la transformation de Fourier, ne permet de détecter les défauts de câblage que si le niveau de bruit est faible d'où l'intérêt de la première étape de débruitage. Par ailleurs, on propose aussi une approche bayésienne utile notamment lorsque la complexité du système augmente. Sa réponse est basée sur l'estimation des paramètres et des distributions à priori. Dans ce manuscrit, l'approche bayésienne est décrite mathématiquement puis les résultats validant l'approche sont présentés en analysant en particulier les paramètres qui affectent la performance de la méthode. Enfin, nous utilisons une approche de la réflectométrie chaotique temporelle basée sur les propriétés du signal chaotique. Les résultats montrent que cette méthode est capable de synthétiser des signaux et de localiser les défauts de câblage sans prétraitement ou informations a priori.